DEFORMATION ~~AND FRACTURE~~ BEHAVIOUR and life prediction OF SOME ~~NICKEL-BASED~~ GAS TURBINE ALLOYS

- by -

G F HARRISON

Thesis submitted through the Faculty of Engineering
to the University of London for degree of
Doctor of Philosophy

Mech Eng Dept
Imperial College
London

May 1975

SUMMARY

The mechanical deformation behaviour of the three typical gas turbine alloys, Nimonic 90, Nimonic 108 and Mar M246, are investigated. Effect of casting processes on resistance to deformation of Mar M246 is included.

In the wrought alloys, tensile and compressive creep tests show close correlation in deformation rates during initial stages of creep, however tertiary creep in compression is delayed relative to the tensile case and appears to be associated with strain induced phase transformation. In cyclic stress tests on Nimonic 90 anelastic recoveries do not affect subsequent damage. Periodic compressive loading is investigated in triangular and rectangular cycle push-pull fatigue tests. Strain hardening theory and the Graham and Walles creep equations give satisfactory predictions of all cyclic results from static tensile creep data.

Conventionally cast Mar M246 is slightly stronger in compression than in tension, however, no further improvement in compressive creep resistance is obtained with directionally solidified or single crystal forms of the material. In contrast under tensile loading, although minimum creep rates for the three types of material are similar, directionally solidified and single crystal forms have lives twice those of conventionally cast material and rupture strains three or four times greater.

A friction stress, σ_o, is measured by a progressive stress reduction technique. Using a net effective stress concept, both for Mar M246 and for Nimonic 90, calculated activation energies are close to those for self diffusion in a simple nickel-chromium solid solution. Initial and steady-state creep rates superimpose at equivalent effective stresses. Inherent material friction stress levels are temperature dependent and allow determination of the γ' solvus temperatures. A normalised effective stress enables creep rates for Nimonic 90, Mar M246 and various other materials to be superimposed.

Applying strain hardening theory, basic creep laws developed for static creep are modified to analyse simple thermal fatigue results on Nimonic 108.

CONTENTS

		Page
1.0	Introduction	6
2.0	Theories of creep	7
2.1	Empirical equations of creep	7
2.1.1	Static creep	7
2.1.2	Stress dependence of creep	10
2.1.3	Temperature dependence of creep	11
2.1.4	Creep under variable stress	14
2.1.5	Summary of the requirements of empirical theories of creep	18
2.2	Physical approaches to creep	21
2.2.1	General structural characteristics of creep	21
2.2.2	Glide theories of creep	22
2.2.3	Recovery theories of creep	28
2.2.4	Application of internal stress concepts to theories of creep	36
2.3	The effect of material composition on high temperature creep strength	42
2.3.1	Solid solution alloys	42
2.3.2	Two-phase alloys	42
2.3.2.1	Creep theories of two-phase alloys	45
2.4	Application of alloy theory to gas turbine materials	47
2.4.1	Solid solution hardening of γ phase	47
2.4.2	Precipitation hardening by γ' phase	47
2.5	Relevance of the findings of the literature survey to the current research programme	49
3.0	The research programme	50
3.1	Programme objectives	50
3.2	Choice of materials	51
3.3	Experimental programme	53
3.4	Equipment and test technique	57
3.5	Metallographic technique	62
4.0	Results	62
4.1	Static and cyclic creep properties of wrought Nimonics	63
4.1.1	Tensile and compressive creep of Nimonic 90 and Nimonic 108	63
4.1.2	Tensile and rectangular creep of Nimonic 90	64
4.1.3	Frequency effects in triangular tensile creep of Nimonic 90	66
4.1.4	Rectangular push-pull creep of Nimonic 90	66

CONTENTS (cont'd)

		Page
4.2	Static and cyclic creep properties of conventionally cast, directionally solidified and single crystals of Mar M246	66
4.2.1	Tensile and compressive creep	66
4.2.2	Tensile and rectangular creep	67
4.2.3	Triangular tensile creep	68
4.2.4	Triangular push-pull and rectangular push-pull creep	68
4.3	Stress changes on subsequent creep of Nimonic 90 and Mar M246	68
4.3.1	Instantaneous stress reductions	68
4.3.2	Progressive stress reductions	69
4.3.3	Stress changes during anelastic recovery	70
4.4	Metallographic examination	70
4.4.1	Metallographic observations on Nimonic 90 and Nimonic 108	70
4.4.2	Metallographic observations on Mar M246	72
5.0	Analysis of results	73
5.1	Analysis of results based on the Graham and Walles equations of creep	74
5.2	Tensile and compressive creep	78
5.3	Rectangular creep	81
5.4	Triangular tensile creep	86
5.5	Push-pull triangular creep	89
5.6	Push-pull rectangular creep	90
5.7	Main findings and conclusions on empirical life prediction	92
6.0	Discussion	94
6.1	Effect of static and cyclic stressing on strain accumulation and rupture of Nimonic 90 and Nimonic 108	94
6.1.1	Comparison of tensile and compressive creep	94
6.1.2	Comparison of tensile and rectangular creep properties	94
6.1.3	Effects of frequency on triangular tension	100
6.1.4	Effect of rectangular push-pull cycling on creep	101
6.2	Effect of static and cyclic stressing on strain accumulation and rupture of three forms of cast Mar M246	101
6.2.1	Comparison of tensile creep properties	101
6.2.2	Comparison of tensile and compressive creep properties	102
6.2.3	Comparison of triangular and rectangular creep properties of Mar M246	103

CONTENTS (cont'd)

		Page
6.2.4	Triangular tensile creep	103
6.2.5	Push-pull triangular and rectangular creep	103
6.3	The effect of stress changes on subsequent creep deformation	104
6.3.1	Assessment of the validity of using stress reduction measurements in developing theories for creep	104
6.3.2	Significance of stress reduction results	106
6.3.3	Implication of stress reduction observations to current physical theories of creep	112
6.4	Implications of friction stress concepts to variable stress creep	119
6.5	Main findings and conclusions	123
7.0	Relevance of the current research programme to the practical problem of thermal fatigue	124
7.1	Choice of materials	125
7.2	Experimental technique	125
7.3	Analysis of thermal fatigue damage	126
7.4	Discussion of thermal fatigue analysis and comparison with experimental results	128
7.5	Main findings and conclusions	130
Acknowledgements		130
References		131

CONTENTS (cont'd)

TABLES

No.	Title	Page
I	Chemical composition and heat treatment	139
II	Schematic illustration of test programme	54
III	Electron-probe microanalysis of the distribution of elements in Nimonic 90 after high compressive strain	140
IV	Summary of metallographic examination of selected test specimens	141
V	Statistical analysis of Nimonic 90 creep data	142
VI	Summary table of transition stress levels in Nimonic 90	117
VII	Life predictions for various time intervals	143
VIII	Life predictions for several assumed damage regions	144
IX	Comparison of life predictions based on final stress and temperature and peak damage stress and temperature	145

APPENDICES

No.	Title	Page
I	The Graham and Walles method for analysis of creep data	146
V	Strain accumulation under rectangular stress cyclic creep using time hardening assumptions	152

1.0 Introduction

In this section it is hoped to present the broad objectives of this thesis in a manner which will indicate their relevance within the field of gas turbine technology. Specific objectives will be set out in Section

The drive to obtain increased thrust has resulted in aero engines showing a steady rise in operating temperatures. This places an increased requirement on turbine components where metal temperatures in excess of 1273K are now experienced. The situation has resulted in the development of complex nickel-based alloys in which by alloy additions, both the γ solid solution strength and the γ' precipitation hardened strength have been increased progressively. The latter is more effective, improvements in alloy strength resulting from

(a) increasing the strength of the γ'

(b) increasing the volume fraction of the γ' that is present

and (c) raising the γ' solvus temperature.

The improved high temperature strength of the latest alloys has been gained at the expense of formability and so some forged blades are being replaced by cast blades of alloys such as Mar M002 and Mar M246. These casting alloys are more dense than conventional alloys but have superior specific (density corrected) strengths. However the lower ductilities and the proposed longer service lives of blades in these materials could well make cyclic deformation an even more critical limiting property than in wrought alloys. The current test programme should provide basic data on the effect of casting method (conventional casting, directional solidification and single crystal casting) on the high temperature mechanical properties of cast alloys.

Under operational conditions, the leading and trailing edges of cooled blades are subjected to transient tensile and compressive strains and hence tensile and compressive stresses are developed. In the absence of any firm evidence, designers have been forced to assume that compressive creep accumulates in a similar way to tensile creep. It is hoped either to confirm this assumption or to provide a more suitable replacement.

The laws of material behaviour are not sufficiently developed to allow the designer to estimate accurately lives under cyclic conditions and although it is known that metallurgical and mechanical effects such

as creep, anelastic recovery, material overaging, cast to cast variation and etc, influence the rate of accumulation of damage, these cannot be numerically quantified. One of the aims of this programme is therefore to obtain sufficient theoretical understanding of the laws of material behaviour to allow the development of analytical methods which are able to quantify material damage under transient conditions. It is hoped to apply this understanding to the practical problem of thermal fatigue such that the lives of components subjected to this type of damage can be predicted more accurately.

2.0 Theories of creep

The complex nature of creep is indicated by the period over which it has been investigated and the concentration of effort which has been spent in attempts to obtain a satisfactory understanding of the phenomenon. The diverse opinions and contradictory theories (at least in part) show that although this effort has not been wasted, neither has the fundamental solution of the problem been realised. The present literature survey will be limited to a selection of classical papers responsible for the development of current theories, consideration of recent review articles and selected recent papers, the object being to indicate the main streams of current opinion.

Studies of creep have taken two directions,

(a) creep as a fundamental concept where the interest is in unravelling the mystery of the actual deformation mechanisms

and (b) the consequences of creep as this might affect life, performance or operating conditions of components.

Within this broad division there must be a large region of overlap since it is difficult to relate some aspects to one or other category. Also since creep encompasses several distinct phenomena, each of varying importance depending on the particular situation, investigators have tended to concentrate on their own particular 'problem area'.

2.1 Empirical equations of creep

2.1.1 Static creep

There is a lack of detailed understanding of creep mechanisms and this has meant that in order to predict deformation in any practical situation the designer is forced to employ a phenomenological approach based on empirical equations.

One of the first studies was made by Andrade[1] who postulated that two stages existed,

(i) a Beta-flow region where the strain rate is proportional to the cubed root of time, and

(ii) a region of viscous flow where the strain rate is directly proportional to time.

Combining these two ideas, extension can be expressed by the equation

$$\ell = \ell_0 \left(1 + \beta' t^{\frac{1}{3}}\right) \exp \kappa' t \qquad \ldots.(1)$$

where ℓ_0 is the initial length, ℓ is the length at time t, β' and κ' are constants.

Under conditions of constant stress and converting to true strain ε

$$\varepsilon = \varepsilon_0 + \beta t^{\frac{1}{3}} + \kappa t \qquad \ldots.(2)$$

where $\beta t^{\frac{1}{3}}$ is small, and $\log e \left(1 + \beta t^{\frac{1}{3}}\right) \simeq \beta t^{\frac{1}{3}}$ and ε_0 is the initial loading strain.

Later workers have suggested expressions similar to Equation (2) but with varying time exponents, for example[2]

$$\varepsilon = a + bt^{\frac{1}{3}} + ct^{\frac{2}{3}} + dt \qquad \ldots.(3)$$

where a, b, c, and d are all constants

or the more general form of de Lacombe[3]

$$\varepsilon = a + bt^{p} + ct^{q} \qquad \ldots.(4)$$

where $p < 1$ and $q > 1$.

Many investigators have stated that the drawback to the more general use of these equations is the theoretical limitation of an infinite creep rate at zero time and also non-linear steady state[4,5].

The common method which has been adopted to overcome the apparent shortcomings above has been to use exponential expressions of the form proposed by McVetty[6]

$$\varepsilon = \varepsilon_0 + \varepsilon_T \left(1 - e^{-mt}\right) + \dot{\varepsilon}_s t \qquad \ldots.(5)$$

where ε_T is the total transient strain and $\dot{\varepsilon}_s$ the steady-state creep rate. m is a constant related to the exhaustion of transient creep.

One advantage stated by users of this type of equation is that by differentiating and setting the time equal to zero, initial creep rates can be calculated. However, evidence indicates measured values 10 to 1,000 times larger than predicted[7].

Comparing the fit obtained with the three types of equations, namely Equations (2), (3) and (5), it was found that the third degree polynomial gave a slightly better fit than the McVetty and Andrade equations (as might be expected from the use of an additional term). There was little difference between the latter two[8,9].

Evans[10] carried out a computer analysis of accurately controlled creep tests and found there was little to choose between polynomial and exponential expressions, however the former had the advantage of giving a much better fit over the first 10 to 15 per cent where the exponential had its greatest errors.

Kennedy[11], in his review of creep, makes the valid observation that the most detailed investigation of creep empiricism is that carried out by Graham et al[12]. This is based on a summation of terms of a type originally proposed by Nutting, such that

$$\varepsilon = \Sigma c \sigma^{\beta} \phi^{\kappa} \qquad \ldots.(6)$$

where σ is the stress, ϕ is the time-temperature function $t\,(T' - T)^{-A}$, T is temperature and T' is a temperature constant, c, β and κ are constants such that κ follows the series $\frac{1}{3}$, 1, 3 which broadly represents the primary, secondary and tertiary stages of creep. $\frac{\kappa}{\beta}$ follows the series $-\frac{1}{16}$, $-\frac{1}{8}$, $-\frac{1}{4}$. The constant A can vary within wide limits with little effect on ε and a value of 20 is used as a general solution.

This expression allows virtually any stress or temperature dependence which might be described by power, exponential or hyperbolic functions, to be represented if sufficient terms are employed. However, for constant stress and temperature it reduces to the familiar form

$$\varepsilon = at^{\frac{1}{3}} + bt + ct^3 \qquad \ldots.(7)$$

There appears to be little to choose between the accuracy of fit obtained with power functions and exponential functions, however

(a) both neglect creep during the initial loading period,

(b) power functions apparently predict infinite creep rates on application of load and exponential functions show their greatest errors in this region.

2.1.2 Stress dependence of creep

In the intermediate temperature region power functions are generally used to describe strain accumulation. These were originally proposed by Norton[13] and by Bailey[14] such that

$$\varepsilon = B\, f\,(t)\, \sigma^n \qquad \ldots.(8)$$

where B and n are constants at constant temperature. This is also the type of function used by Graham.

Exponential functions are generally used at high stresses and lower temperatures, that of Dorn[15] being typical

$$\varepsilon = B'\, f\,(t)\, \exp\,(m\sigma) \qquad \ldots.(9)$$

Various people have used hyperbolic functions, for example Feltham[16], Weertman[17], however Garofalo[18] has illustrated that the equation

$$\varepsilon = B''\, (\sinh\, \alpha\sigma)^n\, f(t) \qquad \ldots.(10)$$

reduces to Equation (8) at low stresses where $\alpha\sigma < 0.8$, and Equation (10) at high stresses where $\alpha\sigma > 1.2$ and hence $n\alpha = m$. (Garofalo used the steady-state creep rate form of these equations.)

2.1.3 Temperature dependence of creep

The temperature dependence of creep is generally introduced through an activation energy term, Q, such as illustrated by Dorn[15] or by Larsen and Miller[19]. The difference between these two approaches is that in the original basic Arrhenius equation, $\dot{\varepsilon} = A' e^{-Q/RT}$, Dorn considers A' to be a function of stress whereas Larsen and Miller consider A' to be independent of stress, the resulting equation derived by Dorn being of the form

$$\varepsilon = g\left[t \exp\left(-Q/RT\right)\right]^n \qquad \ldots.(11)$$

The expanded re-arranged form of Larsen and Miller[19] being

$$\varepsilon = f\left[T\,(c + \log t)\right] \qquad \ldots.(12)$$

A modified form has been proposed by Manson and Haferd[20] where

$$\varepsilon = f\left[(T - T_a)/(\log t - \log t_a)\right] \qquad \ldots.(13)$$

In this case when $T_a = 0$ and $\log t_a = -c$, Equation (13) reduces to Equation (12). In all three cases above, the equations can be written in the form $f(t) = \left[t_\varepsilon, f(T)\right]$, ie variables are separable. t_ε is the time to any specified strain.

The one major exception to the general approach based on activation energies is that due to Graham[21], who initially and just prior to Larsen and Miller, proposed an almost identical expression. However he later modified this to a $(T' - T)^{-A}$ concept[12], where T' relates to a critical temperature which best represents the previous history prior to creep, and so incorporates an alternative material aspect to that given by activation energy.

Clauss[22] has compared the Larsen and Miller, Dorn and Manson-Haferd parameters with reference to stress rupture results. He started from the assumption of an equation of state which can be represented by the explicit expression

$$\log t_\varepsilon = \Psi\,(\log \sigma, T) \qquad \ldots.(14)$$

Differentiating this expression

$$d \log t_\varepsilon = (\partial \psi / \partial \log \sigma)_T \, d \log \sigma + (\partial \psi / \partial T)_\sigma \, dT \qquad \ldots.(15)$$

where the partial differential $(\partial \psi / \partial \log \sigma)_T$ is the rate of change of $\log t_\varepsilon$ with respect to $\log \sigma$ and is the slope of the isothermal line of the plot of $\log t_\varepsilon$ versus $\log \sigma$. $(\partial \psi / \partial T)_\sigma$ is the rate of change of $\log t_r$ with respect to temperature and is a measure of the separation of the isothermal lines.

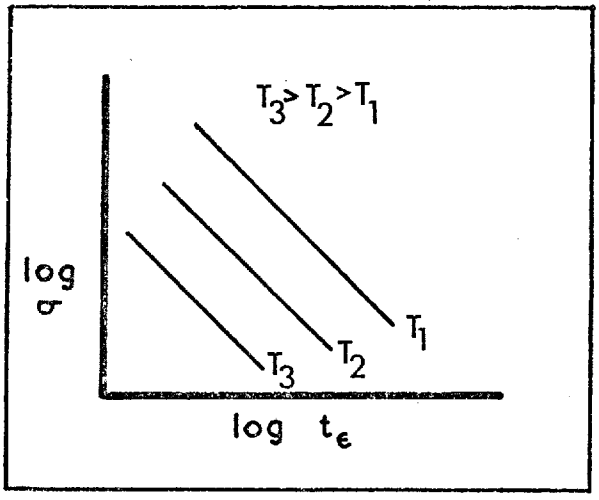

Figure 1

In the Larsen and Miller analysis $(\partial \psi / \partial \log \sigma)_T$ is assumed to be constant and so, as shown in Figure 1, in stress time cross-plots lines will be parallel and straight and evenly spaced with respect to temperature.

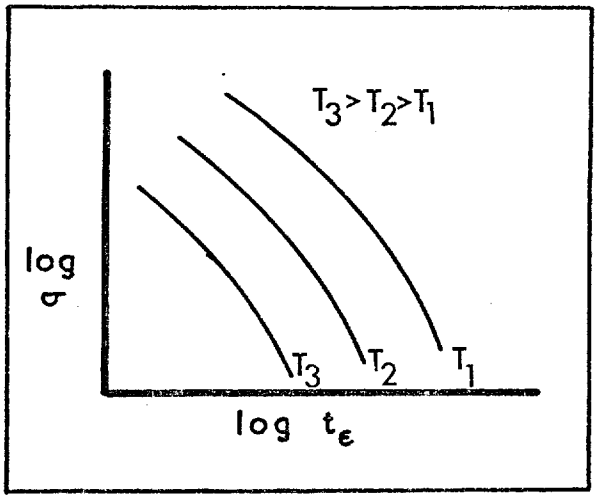

Figure 2

The Dorn analysis assumes $(\partial \psi / \partial \log \sigma)_T$ to be a function of stress and can therefore deal with curved isothermal lines evenly spaced. This is illustrated in Figure 2.

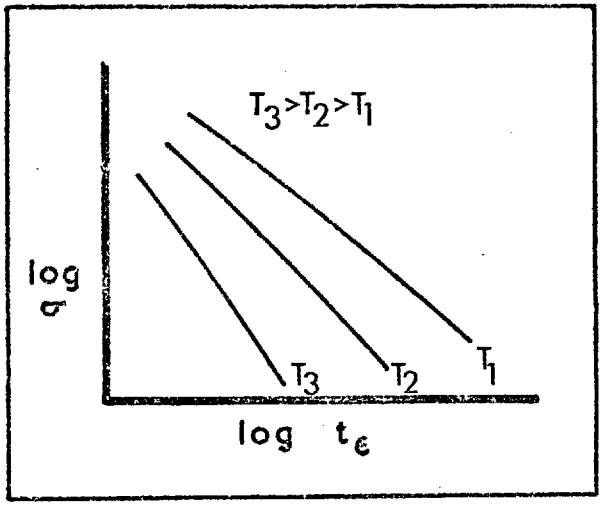

Figure 3

The Manson-Haferd parameter is based on the approximate linearity between lines of log t_ε against T for constant stress and so can successfully deal with log σ versus log t_ε curves which are straight but fan out as illustrated in Figure 3.

Recently Raut and Clough[23] carried out a computer analysis of creep data using seven time-temperature parameters to correlate and extrapolate rupture. These parameters included the three discussed above together with those of Goldhoff and Sherby, Manson and Succop, Conrad and Korchynsky. They concluded that apart from Korchynsky the other time-temperature parameters can compete almost equally although the Manson-Haferd and Goldhoff-Sherby parameters have general superiority. They found that no single standard parameter is ideally suited for use with all Ni-base alloys and 'an open mind (should be) kept as to the best equation'.

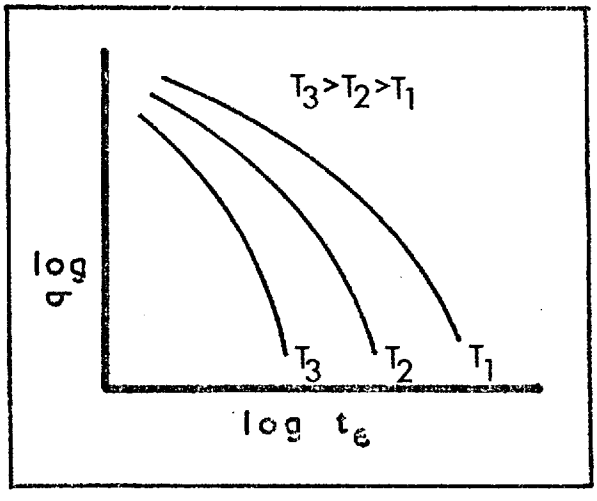

Figure 4a

Although not considered by Clauss or Raut and Clough, the Graham and Walles analysis can deal successfully with the general case, Figure 4a, since curvature of isothermal cross-plots is accounted for through change in stress and time exponents of Equation (6) and also the ratio of these exponents predicts the slope of the isothermal cross-plots. Change of curvature is obtained

since each κ/β region can have a different temperature function due to a change in the constant T'. Simplification of this analysis to the cases above would mean fewer terms, ie larger range of applicability for particular κ/β ratios and/or more than one region having similar T' temperature constants.

2.1.4 Creep under variable stress

Under conditions of varying stress and temperature two choices are available to describe creep behaviour. One is based on the assumption that material damage is hereditary such that present behaviour depends on the entire past history. The second possibility invokes the concept of an equation of state such that

$$\phi\ (\dot{\varepsilon},\ \sigma,\ T,\ S)\ =\ 0 \qquad \ldots.(16)$$

where S is a parameter defining the state of the material. This theory defines behaviour in terms of current value of various parameters.

In the equation of state concept, general expressions used are

(i) Time hardening hypothesis

Here it is considered that the state of a material is governed solely by the time under stress, t_e. Using the Graham and Walles expression for creep, the basic time hardening equation is given by

$$\dot{\varepsilon}\ =\ \Sigma\ c\ \kappa\ \sigma^{\beta}\ \eta^{\kappa}\ t_e^{\kappa-1} \qquad \ldots.(17)$$

where $\eta\ =\ T' - T$

A limitation of time hardening is that if a small preload is applied for a time greater than the time to fracture at a subsequent test condition, then the theory predicts that failure should occur immediately on application of load.

(ii) Life fraction hypothesis

In this proposal it is considered that the state of the material depends on the fraction of life expended and so,

$$S = \Sigma \frac{t}{t_{r,n}} \qquad \ldots.(18)$$

where $t_{r,n}$ is the time to rupture at stress σ_n and temperature T_n, t is the actual time spent at σ_n , T_n and S is the damage fraction. At rupture the value of S is unity.

Converting to an equivalent time t_e, at stress σ_e and temperature T_e it follows that

$$t_e = t_{r,e} \sum_{r=1}^{r=e} \frac{t}{t_{r,n}} \qquad \ldots.(19)$$

where $t_{r,e}$ is the time to rupture at σ_e, T_e. Expressed in this simple form life fraction assumes that creep damage is linear, ie for a particular stress and temperature $\frac{t}{t_r}$ produces a constant damage contribution, independent of when in the life of the test the particular stress and temperature are applied.

Life fraction is in effect an attempt to normalise time hardening and to overcome its limitations cited above. Expressed as this more general concept the equation for creep rate can be written

$$\dot{\varepsilon} = \Sigma\, c\, \sigma^{\beta}\, \kappa\, \eta^{\kappa} \left(\frac{t}{t_r}\right)^{\kappa-1} \qquad \ldots.(20)$$

where $\dot{\varepsilon}$ is the instantaneous creep rate, and the other terms are defined in the Graham and Walles analysis. This form of presentation predicts the characteristic creep shape and allows separate contributions from primary, secondary and tertiary stages of creep.

(iii) Strain hardening hypothesis

Here the material state is considered to be uniquely defined by the strain accumulation and hence S is equivalent to ε[24,25]. Using the Graham and Walles expression for creep, the basic strain hardening equation is given by

$$\dot{\varepsilon} = \Sigma\, \kappa\, c^{1/\kappa}\, \sigma^{\beta/\kappa}\, \eta^{\kappa}\, \varepsilon^{\left(\frac{\kappa-1}{\kappa}\right)} \qquad \ldots.(21)$$

Strain hardening suffers from an equivalent type of disadvantage to time hardening. If rupture ductilities are widely different, change of test conditions to those under which the rupture ductility is less than the current value of creep strain would predict immediate failure. This is not as serious a limitation as that for time hardening since the condition will generally arise only in the final stages of testing when strain accumulation is controlled by time raised to a high power. If the time index is 9, as is frequently found close to rupture, calculation shows that doubling the rupture ductility increases the test life only by about 10 per cent.

(iv) Strain fraction

Similar forms of equations to those presented for life fraction can be obtained by normalising strain such that

$$S = \Sigma \frac{\varepsilon}{\varepsilon_{r,n}} \qquad \ldots.(22)$$

where $\varepsilon_{r,n}$ is the strain at rupture at stress σ_n and temperature T_n, ε is the actual strain accumulation at σ_n, T_n and, as before, S is the damage fraction.

In the more general form, to overcome the limitation of strain hardening, the creep rate equation can be written

$$\dot{\varepsilon} = \Sigma\, \kappa\, ^{1/\kappa}\, \sigma^{\beta/\kappa}\, \eta^{\kappa} \left(\frac{\varepsilon}{\varepsilon_r}\right)^{\frac{\kappa-1}{\kappa}} \qquad \ldots.(23)$$

The limitation of simple expressions of life fraction and strain fraction (Equations (18) and (22)) is their assumption of linear damage with strain or time. Freeman and Voorhess[26] noted that if strain or time were used for rupture predictions, answers were generally opposite, ie one greater and the other less than 1 for values of S. They found that combined together a much closer approximation to 1 was obtained and so they proposed the equation

$$\Sigma \left(\frac{t}{t_r} \frac{\varepsilon}{\varepsilon_r}\right)^{0.5} = 1 \qquad \ldots.(24)$$

Despite the apparent differences in conception between strain hardening and time hardening, Leckie[27] amongst others, has shown that under steady load, structural constraints result in there being little difference between the two predictions.

All four laws fail to predict creep recovery on unloading. Thermal/mechanical recovery and metallurgical instability indicate the need for some hereditary theory to take account of the stress/temperature history. However strain hardening theory is not generally seriously in error and it might be possible to modify the theory to accommodate this aspect. The alternative is to develop a purely rheological theory and most of this work has involved Superposition Theory.

Superposition Theory

This is an attempt to incorporate "past history" by using a generalisation of Boltzmann's Superposition Theory, a convenient expression being

$$\varepsilon = \int_0^t \theta\,(t - t_1) \frac{d\,F\,(\sigma)}{d\,t_1}\, d\,t_1 \qquad \ldots.(25)$$

where $\varepsilon = F(\sigma)\ \theta(t)$ at constant stress.

Graham[12] proposed a form of this equation such that

$$\varepsilon = \Sigma\, c \int_0^t \kappa\,(t - t_1)^{K-1}\, \sigma^{\beta}\, d\,t_1 \qquad \ldots.(26)$$

Since κ is from the series $\frac{1}{3}$, 1, 3, if used for conditions of unloading this predicts complete recovery for $\kappa < 1$, no recovery for $\kappa = 1$ and increasing creep for $\kappa > 1$. Evidence has shown that more generally only a fraction of the transient creep might be recoverable[28,29,30].

Disadvantages of this approach are that

(i) it is cumbersome and requires all previous stress and temperature histories to be carried forwards separately and not as a net effect

and (ii) without modification, it cannot be applied to the tertiary stages of creep since it predicts eventual rupture even if a test is completely unloaded.

The whole field of anelastic behaviour has recently been reviewed by Norwick and Berry[31].

2.1.5 Summary of the requirements of empirical theories of creep

For the purposes of predicting strain accumulation, it is generally considered that creep behaviour can be expressed as a function of time, t, temperature T, and stress σ, such that for any particular set of these values

$$\varepsilon = f(\sigma, t, T) \qquad \ldots.(27)$$

the main objective of the various phenomenological creep theories being to define explicitly the form of Equation (27). Under conventional creep testing conditions the experimental strain-time creep curves are described by a re-arrangement of Equation (27) into two-variable component equations such that

$$(\varepsilon)_{\sigma,T} = g(t) \qquad \ldots.(28)$$

a common solution being

$$(\varepsilon)_{\sigma,T} = \varepsilon_o + at^{\frac{1}{3}} + bt + ct^3 \qquad \ldots.(29)$$

A typical example of this approach is given in Figure 4b.

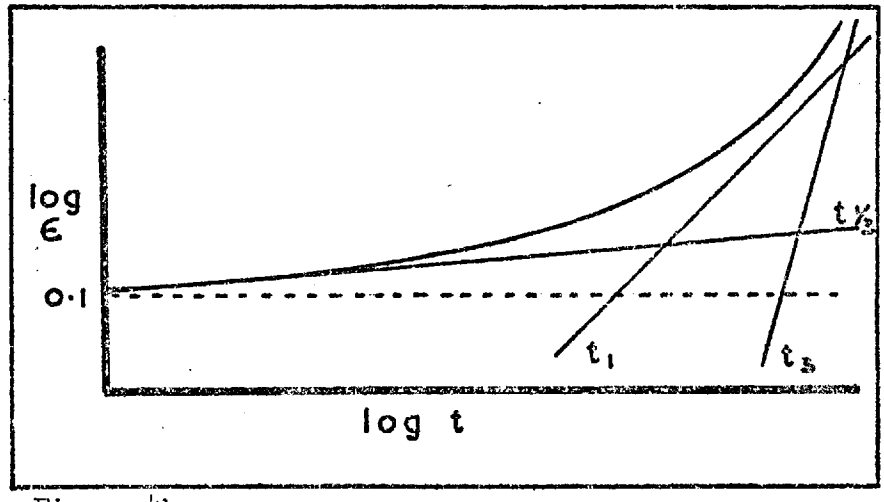

Figure 4b

An alternative method of presenting creep test data uses logarithmic functions so as to achieve solutions in the form of times required to attain specific strains, the equation being

$$\log(t)_\varepsilon = \psi(\log \sigma, T) \qquad \ldots.(30)$$

This is the form used for the conventional rupture plots of log σ against log t as shown in Figures 1 to 4a. In general, if test results are compiled over a sufficiently wide range of testing conditions it is found that

(i) for any one temperature the results show downwards curvature and

(ii) for a series of temperatures the curves fan out.

This curvature of the isothermal data and its separation with temperature can be expressed mathematically by the differential form of Equation (30) such that

$$d \log(\sigma)_\varepsilon = \left(\frac{\partial \psi}{\partial \log t}\right)_T d \log t + \left(\frac{\partial \psi}{\partial T}\right)_\sigma dT \qquad \ldots.(31)$$

In stress-rupture cross-plots for example the isothermal curves give graphical solutions of $\left(\frac{\partial \psi}{\partial \log t}\right)$, this being the shape of the isothermal

line and $\left(\frac{\partial\psi}{\partial T}\right)$ being a measure of the separation of these lines with temperature.

From Observation (i) it follows that, in general, stress-time cross-plots are non-linear and therefore stress dependent and from (ii) each isothermal cross-plot must also be temperature dependent. The many empirical equations of creep must in effect include solutions of the partial differentials $\left(\frac{\partial\psi}{\partial \log t}\right)$ and $\left(\frac{\partial\psi}{\partial T}\right)$. Most of the available equations are adequate for particular materials over limited ranges of test conditions and, where specific equations break down, this is generally due to an incorrect solution being given by one of the partial differential terms outside the region of its original derivation.

Simple solutions of the differentials exist where the experimental data can be split up into parallel straight line segments because within any set of lines $\left(\frac{\partial\psi}{\partial \log t}\right)$ is independent of time. Most stress-rupture data can be presented in this way. However solutions for specified strains are not easily converted to this form and so equations capable of predicting accumulated strain throughout the life of a creep test are more difficult to achieve and more complex in form. Examination of the various conditions under which the Graham and Walles analysis has been applied shows that it works well over wide ranges of stress and temperature. It is mathematically simple and there is physical evidence to support the temperature function employed since the T' constant generally relates to heat treatment temperatures, precipitate resolution temperatures or melting temperatures. It would appear therefore that the Graham and Walles analysis offers

(a) the greatest flexibility

and (b) when applied with strain hardening hypothesis, potential application to variable stress situations.

Possible errors may occur

(i) in predicting initial creep rates

(ii) where metallurgical recovery can occur, or where the deformation depends on the creep rate/temperature history

(iii) where anelastic recovery mechanisms can influence subsequent creep behaviour.

Another inconvenience of this method is its reliance on graphical methods of analysis and regeneration. A brief outline of the Graham and Walles method of graphical analysis is given in Appendix I.

2.2 Physical approaches to creep

Although the empirical approach gives the best short-term solution to the designer who has the immediate problem of predicting component life, it does little to improve fundamental understanding or material development.

One method of combining these two different aims, understanding of fundamental mechanisms and description of physical experience by mathematical equations, does this by attempting to attach some physical significance to the terms derived empirically. The difficulty is that different equations can adequately represent the data within a given range but might well lead to the deduction of different controlling mechanisms. The use of theories developed within particular regions, outside these regions can sometimes be used as a test of the more general validity of the theories.

2.2.1 General structural characteristics of creep

Since stress and temperature are constant, normal transient creep rates must be a reflection of net substructural change. The initial substructure closely resembles that developed during strain hardening and can be described as a complex three-dimensional network of dislocations[32]. It has been shown[33] that dislocations re-arrange themselves and entanglements disperse as the transient stage progresses. The changes which occur are extremely complex and Dorn et al state[5] that available data suggests a slight decrease in dislocation density during transient creep. This is in direct contrast to Lagneborg[34] who suggests that dislocation densities gradually increase during primary creep. However it is clear that formation of subgrains leads to drainage of dislocations from the interior of the subgrain. Dorn[35] suggests that the best term to describe the net effect is 'recovery strengthening due to dispersal of entanglements by dislocation climb'.

It has been shown[36] that subgrain interior density and subgrain size are functions of the applied stress, and that sub-boundaries act as sinks for dislocations generated in the network thus reducing the internal stresses associated with the network. Ishida[37] showed from stress change experiments that, on lowering the stress, creep rate is more sensitive to dislocation density within subgrains than to subgrain size, the implication being that the former term is the important one during creep.

General theories can be split into two categories,

(1) those based on dislocation glide concepts

and (2) those based on dynamic recovery through dislocation climb. In the former case the rate controlling event is considered to be some glide process such as the motion of screw dislocations or the movement of nodes and in the latter case it is considered to be some process such as the climb of edge dislocations.

It is readily apparent that both processes must be operating since the observed strain is the result of dislocation movement within the crystal lattice. During this movement the total length of dislocations increases causing materials to strain harden and consequently some recovery mechanism must operate to limit the total dislocation length and thus prevent the strain rate decaying to zero.

2.2.2 Glide theories of creep

Various obstacles are considered to hinder dislocation motion and hence their rate of flow is dependent on frequency of thermal fluctuations sufficiently large to aid movement from one equilibrium position to another. Within any system there will be a distribution of energies of thermal fluctuation and from statistics and thermodynamics[38]

$$\frac{d\varepsilon}{dt} = A\, e^{-E/KT} \qquad \ldots.(32)$$

where E is the potential energy barrier or activation energy for a single occurrence, and K is the Boltzmann constant. The exponential E/KT represents the fraction of the atoms having an energy E at any moment. A is a frequency factor, ie the number of atoms/unit time having energy greater than the activation energy.

If E and K are multiplied by Avogadro's number Equation (34) is obtained

$$\dot{\varepsilon} = A\, e^{-Q/RT} \qquad \ldots.(33)$$

where Q is the activation energy/gm mole.

The applied stress can be assumed to aid the motion of dislocations in one direction by lowering the activation energy by $v'\sigma$, where v' is the activation volume, whilst raising it in the opposite direction by the same amount. The net rate of flow can then by given by an equation of the form

$$\dot{\varepsilon}_s = \varepsilon_o \left[\exp\left(-\frac{Q - v'\sigma}{KT}\right) - \exp\left(-\frac{Q + v'\sigma}{KT}\right)\right] \qquad \ldots.(34)$$

$$= 2\,\varepsilon_o \exp\left(-\frac{Q}{KT}\right) \sinh\left(\frac{v'\sigma}{KT}\right) \qquad \ldots.(35)$$

Mott[39] considered a rate controlling process to be the glide of jogged screw dislocations since jogs are small segments of edge dislocations which cannot move with the dislocation by glide on the slip planes. Movement can then occur only by climb of these jogs either through emission or absorption of vacancies. If the work done by the applied shear stress, γ, in moving the dislocation line in the neighbourhood of the jog one atomic distance, is considered to be $\gamma L b_1^2$ where L is the average spacing of the jogs on the dislocation, Mott considered the activation energy of the dislocations to be reduced by this amount in the direction of the stress but increased by the same amount in the opposite direction. The form of Equation (35) is

$$\dot{\varepsilon}_s = 2v\left(\frac{b_1}{d}\right) \exp^{-Q/KT} \sinh\left(\frac{Lb_1^2\sigma}{2KT}\right) \qquad \ldots.(36)$$

where Q is the activation energy for self-diffusion and d is the distance between active slip planes and b_1 is the burgers vector.

Minor variations to this equation can be obtained by considering the different ways that jogs can affect the flow rate[40-42]. In a more detailed analysis of the diffusion controlled motion of jogged screw dislocations Barrett and Nix[43] considered that the local vacancy concentration around moving screw dislocations containing a vacancy, either increases or decreases depending on whether the jog is of emission or absorption type. This gives rise to a chemical force which counteracts or promotes dislocation motion and from the laws of diffusion it follows eventually that if the chemical force is balanced by a force due to the applied stress then

$$\dot{\varepsilon}_s = B' D_s \rho_m \sinh \frac{\sigma b_j^2 L}{2KT} \qquad \ldots.(37)$$

where B' is a constant of about 20, ρ_m is the mobile dislocation density, D is the lattice diffusion coefficient and L is the average spacing between the jogs. The limitations of jog dislocation models are

(1) the uncertainty of ρ_m with respect to stress dependence

and (2) no consideration has been given to the stress dependence of L.

Weertman[44] has criticised the model of Barrett and Nix on the grounds that flow of vacancies between producing and absorbing regions has not been established and indeed Cottrell[45] has found that conditions can exist where screw dislocations have an excess of vacancy absorbing jogs. McLean and Hale[46] have shown that at high temperatures, equations in which the influence of stress is through its effect on activation energy are less suitable than power law equations of the form (σ^n).

Clauer Wilcox and Hirth[33] have thrown further doubt on jogged screw theories as being the rate controlling reaction as in an electron microscopic study they found that dislocations were of edge orientation, which suggests that screw dislocations move rapidly and are annihilated by cross slip.

Li[47] proposed that steady-state creep might be controlled by the co-operative movement of atoms at dislocation nodes. From transmission

electron microscopic observations of stainless steel, it was found that dislocation networks consist of two sets of dislocations joined by short nodal segments. One set was observed to bow out between the nodes and was considered capable of slip in that plane except at the node, the other set being considered immobile. Hence, for slip to continue, mobile dislocations will have to drag the node along by a climb process. This is considered to be limited by the emission or absorption of vacancies. Since atoms in the node cannot move independently, it is assumed that they move successively with a jump probability p^n where n is the number of atoms in the node and p is the jump probability when n = 1. It is considered that the applied stress will aid this process such that the activation energy is reduced in the direction of the stress. Applying these assumptions and reaction rate theory the final steady-state creep rate is

$$\dot{\varepsilon}_s = \frac{\rho 2^n KTb_i^2 \sin\phi}{h'} \sinh\left(\frac{\sigma b_i^2 x \sin\phi'}{2nKT}\right)^n \exp\left(\frac{-\Delta Fv + n\,\Delta Fm}{KT}\right) \quad \ldots.(38)$$

where ρ is the dislocation density, h' Plancks constant, ϕ' the angle between two sets of dislocations, $-\Delta Fv$ is the free energy of formation of vacancies and ΔFm is the free energy of motion of atoms at the node. x is the dislocation length between the nodes. This equation can be reduced to the empirical equation derived by Garofalo, Equation (10). The objections to drag theory can also be applied to this analysis, also the mobile dislocation density is assumed independent of applied stress which is at variance with measurement.

Considering the reaction rates for specific dislocation processes Li has also suggested[48] multiplication of dislocations follow first order reaction kinetics and immobilisation second order kinetics such that

$$\frac{d\rho_m}{dt} = K_1\rho_m - K_2\rho_m^2 \quad \ldots.(39)$$

where ρ_m is the dislocation density of mobile dislocations, K_1 and K_2 are rate constants.

The dislocation velocity and rate constants are considered to be independent of immobilised dislocations. Assuming creep rates can be expressed as[49]

$$\dot{\varepsilon} = \rho b_1 \bar{v} \qquad \ldots.(40)$$

where $\bar{v}$ is the average mobile dislocation velocity, from Equations (39) and (40) it is found that

$$\dot{\varepsilon} = \dot{\varepsilon}_s \left(1 - \frac{\dot{\varepsilon}_o - \dot{\varepsilon}_s}{\varepsilon_o} e^{-K_1 t}\right)^{-1} \qquad \ldots.(41)$$

where $\dot{\varepsilon}_o$ is the initial creep rate and $\dot{\varepsilon}_s$ the steady-state creep rate

and where $$\rho_s = \frac{K_1}{K_2}$$

Integration of this equation gives

$$\varepsilon = \varepsilon_o + \frac{\dot{\varepsilon}_s}{K_1} \log \left[1 + \frac{\dot{\varepsilon}_o - \dot{\varepsilon}_s}{\dot{\varepsilon}_s}\left(1 - e^{-K_1 t}\right)\right] + \dot{\varepsilon}_s t \qquad \ldots.(42)$$

and using logarithmic expansion, at intermediate to high temperatures where initial and steady-state creep rates are close in value, this equation reduces to

$$\varepsilon = \varepsilon_o + \frac{\dot{\varepsilon}_o - \dot{\varepsilon}_s}{K_1}\left(1 - e^{-K_1 t}\right) + \dot{\varepsilon}_s t \qquad \ldots.(43)$$

where ε_o is the initial strain. This is in fact Equation (5) with $(\dot{\varepsilon}_o - \dot{\varepsilon}_s)\, K_1 = \varepsilon_T$ and $K_1 = m$.

Assuming the average velocity of dislocations is independent of time, Akulov[50] has derived a similar equation to (41) based on

$$\frac{d\rho}{d\varepsilon} = \alpha_o + \beta'' \varepsilon \qquad \ldots.(44)$$

where α_o and β'' are constants independent of strain.

From this equation the relationship between the mobile dislocation density and the strain at any time can be obtained as

$$\rho_t = \rho_s + (\rho_o - \rho_s) \exp -\beta'' \varepsilon_{(t)} \quad \ldots.(45)$$

where $\rho_s = a_o/\beta''$ and $\rho_t = \rho_o$ at $t = 0$ and ρ_s at $t \to \infty$

By substituting into Equation (40) and assuming that the average dislocation velocity is independent of time, Equation (45) becomes

$$\dot{\varepsilon} = \dot{\varepsilon}_s + (\dot{\varepsilon}_o - \dot{\varepsilon}_s) \exp (-\beta'' \varepsilon) \quad \ldots.(46)$$

which can be differentiated with respect to time to eliminate strain and re-integrated to give Equation (43). Li has shown that the two approaches are equivalent only if constancy of average mobile dislocation density is assumed and the first order multiplication constant $K_1 = a_o \bar{v}$ and the second order immobilisation constant $K_2 = \beta'' b_1 \bar{v}$.

It has been shown[51] that ρ may decrease during primary creep and that the average dislocation velocity also decreases making the validity of Equation (44) suspect. However in an extension of this approach, Webster[52] pointed out that the rate of collision is proportional to $\bar{v}\rho^2$ but the probability of immobilisation increases as the velocity decreases and so, to a first approximation, the rate of immobilisation of dislocations by pairwise interaction can be assumed to be independent of velocity. More recently Webster, Dorn and Cox[53] proposed that if the motion of a dislocation segment is controlled by vacancy diffusion, the speed of dislocations will depend on a flux of vacancies to and from suitable sites on dislocations. This flux is given by first order chemical kinetics and if re-arrangement also obeys first order kinetics, then rates of change of the product, $\bar{v}\rho$, in Equation (40) should be proportional to the difference between its current and steady-state values and expressed in terms of strain rates

$$\frac{d\dot{\varepsilon}}{dt} = -(\dot{\varepsilon}_o - \dot{\varepsilon}_s)/\tau \quad \ldots.(47)$$

where τ is the relaxation time for the re-arrangement of dislocations during transient creep. Double integration gives

$$\varepsilon = \varepsilon_o + \varepsilon_T \left\{1 - \exp(-t/\tau)\right\} + \dot{\varepsilon}_S t \qquad \ldots.(48)$$

where $\varepsilon_T = (\dot{\varepsilon}_o - \dot{\varepsilon}_S)\,\tau$. This is again equivalent to Equation (5) if $\tau = \frac{1}{m}$.

The approach depends on the assumption that one diffusion controlled process only is governing deformation. The good correlation found between the various constants in Equation (48) is convincing evidence in support of its general validity, however since it does not give good correlation between predicted and experimental initial creep rates, this may suggest that early creep processes are controlled by a different mechanism to that applying throughout the remainder of the creep life.

The various models proposed in reaction rate - glide approaches to creep consider that, when the stress is reduced by a small amount, forwards creep continues immediately on unloading since the rate controlling event is not the emission from the dislocation source, but the glide of the emitted dislocation through the lattice. However, for a large number of materials, incubation periods of zero creep rate have been observed after small reductions in stress. Models of creep have been developed to account for these experimental observations. In these models it is considered that the strain rate is based on a balance between the rate of strain hardening due to dislocation interaction processes, and the rate of softening due to recovery mechanisms such as dislocation growth. These processes will be discussed in the next section.

2.2.3 Recovery theories of creep

In these cases it is considered that the emission of a dislocation strains the lattice locally, and this local strain must be reduced by recovery prior to the emission of another dislocation from the source. This concept is based on an original proposal by Bailey[54] and developed into a more rigorous form by Orowan[55] who considered that during creep, the flow stress σ_f of a material is controlled by the relative magnitudes of the recovery rate, r $(= -\partial\sigma/\partial t)$ and the rate of strain hardening h $(= \partial\sigma/\partial\varepsilon)$ such that

$$d\sigma_f = \frac{\partial\sigma_f}{\partial\varepsilon}\,d\varepsilon + \frac{\partial\sigma_f}{\partial t}\,dt \qquad \ldots.(49)$$

The recovery rate can be calculated from the incubation period following a small reduction in applied stress. It is considered to be the time taken for the flow stress to fall to a value corresponding to the new applied stress such that $r \approx \Delta\sigma/\Delta t$. The strain hardening coefficient can be obtained either from a similar small increase in applied stress related to the instantaneous non-elastic strain, $h \approx \Delta\sigma/\Delta\varepsilon$, or from the slope of a stress-strain curve of a room temperature tensile test on a previously creep tested specimen.

When steady-state is reached a constant mechanical state exists, the flow stress remains constant and so $d\sigma_f = 0$ and hence

$$\dot{\varepsilon}_s = \frac{d\varepsilon}{dt} = \frac{\partial\sigma_f/\partial t}{\partial\sigma_f/\partial\varepsilon} = \frac{r}{h} \qquad \ldots.(50)$$

Cottrell and Aytekin[56] pointed out that the flow stress is not only affected by strain hardening and recovery, dynamic effects such as strain hardening rate sensitivity must be taken into account. They propose that strain hardening will cause the flow stress σ_f to rise above the applied stress, σ_a, creating an energy barrier to flow, $u(\sigma_f\ \sigma_a)$. Thermal fluctuations are then considered necessary to overcome these barriers and so the rate of flow will be controlled by a Boltzmann relationship

$$\frac{d\varepsilon}{dt} = \nu \exp\left(-\frac{u(\sigma_f\ \sigma_a)}{RT}\right) \qquad \ldots.(51)$$

The effect of recovery is to reduce the level of this energy barrier and it follows that steady-state creep will occur at a value of σ_f such that $d\sigma_f/dt = 0$.

An important prediction of this theory is that following small reductions in applied stress an incubation period should be observed whilst the internal stress falls to a value appropriate to the new applied stress. Cottrell and Aytekin have shown that these periods do exist as have many other authors[57-59]. Subsequent theories have incorporated their ideas but added to the theory by postulating specific dislocation models.

Using Mott's dislocation climb model[60], Weertman[61] assumed that the dislocations generated by a Frank Read source piled-up on the slip plane against Lomer-Cottrell barriers, and eventually caused sufficient back stress to prevent the source from operating. Reactivation is considered to occur only after the dislocation closest to the barrier has escaped by climb, this dislocation being replaced immediately by a dislocation newly generated from the source.

To determine the creep rate it is necessary to calculate the rate of escape of dislocations from the Lomer-Cottrell barriers in terms of the height that the dislocations must climb, and their rate of climb. The rate controlling process is considered to be determined by diffusion of vacancies between dislocations which create vacancies and those which destroy them. The equation which results from this analysis is

$$\dot{\varepsilon}_S = c(\sigma^n/KT) \exp - \frac{H_D}{KT} \qquad \ldots.(52)$$

where n equals a constant of the value about 3 or 4, and H_D is the activation energy for self-diffusion. In order to evaluate n, Weertman assumed the edge portion of a dislocation loop moves the average dimension of the dislocation array when it escapes from the barrier, whereas the screw component moves a distance equal to the grain dimensions. The number of Frank Read sources/unit volume was taken to be independent of stress and this is not generally true[62].

This model cannot be applied to hexagonal close-packed structures because even if Lomer-Cottrell interaction could occur the resultant dislocations would be mobile. A subsequent analysis was proposed which was based on climb between piled-up dislocations in parallel slip systems[63]. Dislocation loops emitted from a Frank Read source are assumed to expand until they come into the stress field of other sources on parallel slip planes. Eventually these stress fields prevent further motion and piled-up arrays are formed. Annihilation occurs through climb of leading edge dislocations, this allowing further operation of the source and giving

$$\dot{\varepsilon}_S = \frac{G\pi^2 \nu' \sigma^3}{G} \sinh \left(\frac{3\sigma^2 b_1^3}{2K^2 T^2 G^3 M} \right)^{\frac{1}{2}} e^{S/K} e^{-Q_D/KT} \qquad \ldots.(53)$$

The average velocity of climb for each dislocation in the group is given by

$$V_c = \left[\frac{\nu' n' \sigma b_1^4}{KT}\right] \exp\left[\frac{S}{K}\right] \exp\left[-\frac{Q_D}{KT}\right] \quad \ldots.(54)$$

where V_c is the velocity of climb, ν' is the vibrational frequency of a vacancy and S and Q_D are the entropy and activation energy for self diffusion. The average area swept out by a dislocation loop is $4\pi L^2$, where 2L is the average distance between Frank Read sources. The climb distance is $\frac{1}{2}h_1$, where h_1 is the minimum distance for dislocations to glide past one another. The creep rate is given by

$$\dot{\varepsilon}_S = \left[\frac{M 4\pi L^2 b_1}{\frac{1}{2}h_1}\right]\left[\frac{\nu n \sigma b_1^4}{KT}\right] \exp\left[\frac{S}{K}\right] \exp\left[-\frac{Q_D}{KT}\right] \quad \ldots.(55)$$

Substituting $2\sigma L/Gb_1$ for the number of dislocations n', in a piled-up group, where the source separation distance 2L is $(K/Mh_1)^{\frac{1}{2}}$, and the climb distance $\frac{1}{2}h_1$ is greater than $Gb/8\pi\sigma$, gives

$$\dot{\varepsilon}_S = \frac{K' \sigma^{4.5}}{G^{3.5} T} \exp\left[-\frac{Q}{KT}\right] \quad \ldots.(56)$$

where

$$\text{constant } K' = \frac{3(6)^{\frac{1}{2}} \pi^2 \nu b_1^{1.5}}{M^{\frac{1}{2}} K} \exp\left[\frac{S}{K}\right] \quad \ldots.(57)$$

Although a major step forward in understanding creep processes several objections have been noted:-

(a) Dorn[66] pointed out that the activation energy is assumed independent of the jog energy. This assumption is based on a proposal that an excess of mechanically produced jogs of the appropriate sign might account for the absence of jog energy in the observed activation energies.

(b) The assumption of constancy of sources independent of stress is doubtful.

(c) There is evidence to indicate that the interaction between edge dislocations of opposite sign on parallel slip planes does not impede their motion[67,68].

(d) McLean[69] has pointed out that the derivation is based on an incomplete hardening model and considers only long range stress fields. If contributions from intersection processes and defect production are included, a re-analysis would give a creep rate proportional to σ^3.

(e) Generally Frank Read sources and pile-ups are not found in transmission electron microscopy, dislocation tangles and dipoles, tilt and twist boundaries and cellular structures being more common.

McLean and Hale[46] considered creep behaviour could be explained by the occurrence of a three-dimensional network. It is assumed that strength is provided by the attractive and repulsive junctions of the network. Those junctions of longest link length will break away under the action of thermal fluctuations. The released dislocations travel until they are again held up by the network and, since the moving dislocations increase in length, this gives an increase in the dislocation density, ie strain hardening. Simultaneously, recovery of the network occurs by growth of the larger meshes and absorption of the smaller ones by a method analogous to grain growth. This causes a reduction in dislocation density. McLean[72] analysed this model mathematically by incorporating Friedel's theory of network growth[73] and assuming the dislocation line energy is proportional to x^{-2} where x is the average mesh size. To reduce energy, the dislocations will try to decrease in length, thus giving the network a natural tendency to coarsen. The driving force for growth is approximately inversely proportional to x such that

$$\frac{\partial x}{\partial t} \propto \frac{1}{x} \qquad \ldots.(58)$$

The flow stress σ_f is found to be inversely proportional to x, and so the rate of recovery, r, can be expressed[57] by

$$r = -\frac{d\sigma_f}{dt} = -\left(\frac{d\sigma_f}{dx}\right)\left(\frac{dx}{dt}\right) \propto \frac{1}{x^3} \qquad \ldots.(59)$$

and hence

$$r \propto \sigma_f^3 \qquad \ldots.(60)$$

Since network growth involves climb of edge dislocations and migration of jogs on screw dislocations, the speed of both being controlled by the diffusion coefficient D, r must be proportional to D and hence

$$r \propto \sigma_f^3 D \qquad \ldots.(61)$$

During steady state when equilibrium is achieved, substitution into Equation (50) gives

$$\dot{\varepsilon}_s = \frac{A\sigma_f^3 D}{h} \qquad \ldots.(62)$$

It follows that for creep rate stress exponents of 4.5, the work hardening coefficient should be inversely proportional to the stress raised to the power 1.5. Mitra and McLean[74] have had reasonable agreement with Equation (62) for nickel and aluminium alloys.

This theory has been applied to primary creep[75]. It is considered that on initial loading some of the links formed are able to break free with the aid of very small thermal fluctuations, thus giving rise to rapid creep rates. These easily activated links are gradually used up so that progressively during primary creep it is necessary to break stronger links and so greater thermal fluctuations are required to maintain flow and hence the creep rate is reduced. McLean quantified this in terms of strain hardening and recovery by means of reaction rate theory such that

$$\dot{\varepsilon} = \dot{\varepsilon}_o \exp\left[-\frac{b_1 A\,(h\varepsilon - rt)}{KT}\right] \qquad \ldots.(63)$$

where A is the area swept out by the dislocation. Integration of the above equation gives

$$\varepsilon = \frac{KT}{b_1 Ah} \ln\left[\frac{\varepsilon_o h}{r}\right] + \frac{r}{h}\, t \qquad \ldots.(64)$$

$(h\varepsilon - rt)$ is the activation energy for creep at any time, and is the net increase in internal stress.

In a later formulation he derived a slightly different equation[86]

$$\varepsilon = \varepsilon_0 \dot{\theta} \exp\left[(\sigma_2 - \sigma_1) - h\varepsilon + rt\right] \qquad \ldots.(65)$$

where σ_1 is the basic flow stress, σ_2 the obtained flow stress and $(\sigma_2 - \sigma_1)$ the frictional force from alloy additions. On integration, after long times this gives

$$\varepsilon = \frac{1}{h}\left[\ell n \frac{A\dot{\theta}h}{r} + \sigma_2 - \sigma_1\right] + \frac{r}{h} t \qquad \ldots.(66)$$

Objections to McLean's theories can be made in that it is an over-simplification to treat h and r as constants. Lagneborg[4] points out that recovery rates should increase during creep since increased dislocation density and decreased mesh size should provide a larger driving force for recovery. He regards dislocation density as a primary variable determining creep rate, and proposes an equation for the dislocation density such that

$$\frac{d\rho_t}{dt} = \frac{1}{b_1 L}\frac{d\varepsilon}{dt} - 2M\tau_D'\rho^2_{(t)} \qquad \ldots.(67)$$

The first term on the right hand side gives the dislocation production per unit time if no recovery occurs. If this is true, any increment in dislocation density produces a corresponding increment in strain, and $d\varepsilon = b_1 L\, d\rho$, where L is the mean free path of the dislocation, and so for a strain rate $\frac{d\varepsilon}{dt}$, the dislocation production is $\frac{1}{b_1 L}\frac{d\varepsilon}{dt}$. The second term accounts for the reduction in dislocation density due to recovery by growth of the average mesh size x, the equation being

$$\frac{dR_M}{dt} = M\frac{\tau_D'}{x} \qquad \ldots.(68)$$

where $\frac{\tau_D'}{x}$ is the driving force for climb caused by the line tension τ_D'. M is a term to account for mobility of climbing dislocations and contains the self-diffusion coefficient. If $x \approx \rho^{-\frac{1}{2}}$, then Equation (68) reduces to $-2M\frac{\tau_D'}{x}$ and for constant ρ, as in steady-state creep, it follows from Equation (66) that

$$\dot{\varepsilon}_s = 2bL\, M\tau_D'\rho_s^2 \qquad \ldots.(69)$$

Lagneborg also proposed that, by analogy with normal plastic deformation, strain hardening coefficients should decrease with increased dislocation density. With these assumptions and the classical Arrhenius equation, he obtained an expression[76]

$$\frac{d\varepsilon}{dt} = \dot{\varepsilon}_o \exp\left\{-bA\left[\frac{\alpha G b_1 \rho_t^{\frac{1}{2}} - \sigma}{KT}\right]\right\} \qquad \ldots.(70)$$

which is similar to Equation (63). $\alpha G b_1 \rho^{\frac{1}{2}}$ is the average internal stress and $\left(\alpha G b_1 \rho_t^{\frac{1}{2}} - \sigma\right)$ represents the height of the internal stress barrier.

This approach is closely similar to that of Li given in Equations (27) to (31), however in the former case K_1 and K_2 cannot be determined. In order to compare the models, Lagneborg forced them to coincide at very short and very long times, the result being that Li's model approached steady-state much faster than the refined recovery model since during primary creep increase in ρ causes a decrease in Equation (70) whilst $K_1\rho$ of Li's model increases. In Lagneborg's model the current dislocation density is lower than in Li's model since it equals the total number of dislocations generated minus those annihilated by recovery.

Unfortunately, application of recovery theory to primary creep has shown, from experimental determinations of r and h, that r decreases from a maximum at the beginning of primary to a minimum at the commencement of secondary and $\dot{\varepsilon} = \frac{r}{h}$ holds throughout[58]. Extending this theory to tertiary creep, it has been found that h remains approximately constant but that the recovery rate increases to failure[77].

The extension of the basic recovery creep rate equation to primary and tertiary regions of creep deformation has been criticised by several authors[76,78]. It is suggested that if dislocation density increases, then the theoretical recovery rates should also increase. This has been supported by transmission electron microscopy work which purported to show that recovery under reduced stresses leads to coalescence and migration of sub-grain boundaries, thus making recovery measurements meaningless[78]. However in these experiments the stress reductions were very much greater than 10 per cent of the original applied stress.

Considering available experimental evidence, if in a creep test for very short periods during primary creep, small increases in stress are made, it is found that the strain increment decreases as primary creep proceeds. This indicates that h is increasing. Also, if an instantaneous small reduction in stress is made, the structure must remain close to that developed by the higher stress and for criticisms of strain hardening-recovery theory to be valid, the initial creep rates after a reduction should correspond closely to the original creep rate. If creep is dominated by dislocations within the body of sub-grains or a similar type of mechanism, the creep rate should be zero during the period of transition in structure. As stated, the references above give many examples of this latter situation occurring after stress reductions. In detailed observations of structural changes, it has been shown[79] that a marked increase in dislocation density and dislocation interaction occurs when h is increasing, but once it has attained a constant value subsequent changes are more difficult to detect. As the secondary creep stage is approached it is frequently found that tangle density increases and the number of dislocations not associated with tangles decreases. This indicates that decrease in creep rate during primary creep can be attributed to dislocations within sub-boundaries, and so the pertinent recovery parameter should decrease during primary creep. This is confirmed by experimental measurement.

2.2.4 Application of internal stress concepts to theories of creep

Gasca-Neri Alquist and Nix, in a series of recent papers[64,65,80], have proposed a model of creep based on combined glide-recovery mechanisms and the concept of internal stress. It is at present

probably the most widely accepted theory, and is therefore worthy of detailed consideration.

Strain rate is considered to be controlled by a dynamic interaction between the development of internal stresses through glide, and reduction of internal stress through recovery. The maintenance of a positive strain rate is the result of recovery events preventing the internal stress reaching the applied stress. It is proposed that the driving force for recovery is the internal stress, and the driving force for glide and strain hardening the effective stress, such that at any time the applied stress is opposed by the mean internal stress, $\bar{\sigma}_i$, and the average effective stress, $\bar{\sigma}_e$, such that

$$\sigma_a = \bar{\sigma}_i + \bar{\sigma}_e \qquad \ldots.(71)$$

Changes in the mean internal stress reflect variations in the structural parameters which control the creep processes.

The model of Gasca-Neri Alquist and Nix is based on the Orowan[81] equation

$$\dot{\varepsilon} = \phi \rho_m b_1 \bar{v} \qquad \ldots.(72)$$

where ρ_m is the mobile dislocation density, b_1 the Burgers vector and $\bar{v}$ the average dislocation velocity, ϕ is an orientation factor, usually about 0.5.

Direct measurement of total dislocation density, ρ_t, indicate that it is approximately proportional to the square of the applied stress[82]. Although it is not clear how ρ_m is related to ρ_t, Gasca-Neri et al have followed the assumption of Dorn[42] and of others[51] in considering it to be a constant fraction of ρ_t, and hence

$$\rho_m = \frac{\sigma_i \ell}{(\alpha G b_1)^2} \qquad \ldots.(73)$$

where ℓ is a constant about 2.

Considering alternative expressions for dislocation velocity depending on the deformation mechanism operating,

(a) In a variety of metals, a power law velocity-stress relationship is commonly applied[83] and hence

$$\bar{V} = V_o \bar{\sigma}_e^{n} \qquad \ldots.(74)$$

This type of expression is generally found when dislocation motion is controlled by solute diffusion.

(b) When dislocation velocity is controlled by diffusion processes such as jog drag, the following expression is satisfactory[84]

$$\bar{V} = V_o \left[\exp \bar{\sigma}_e \lambda b_i^2 / KT - 1 \right] \qquad \ldots.(75)$$

where λ is the jog spacing.

Considering the conventional phenomenological approach to creep,

$$\dot{\varepsilon}_s = B\,(T)\, \sigma_A^{P} \qquad \ldots.(76)$$

This can be written in terms of the internal stress concept as

$$\dot{\varepsilon}_s = B'\,(T)\, \bar{\sigma}_e^{n}\, \bar{\sigma}_i^{\ell} \qquad \ldots.(77)$$

This concept can also be applied to recovery theories of creep, if in the Bailey-Orowan model the strain hardening and recovery parameters $\left(\frac{\partial \sigma_A}{\partial \varepsilon}\right)$ and $\left(\frac{\partial \sigma_A}{\partial t}\right)$, are expressed in terms of the internal stress, $\bar{\sigma}_i$, instead of the applied stress, $\bar{\sigma}_A$.

It follows from Friedel's theory of recovery, if r is defined as $-(\partial \bar{\sigma}_i / \partial t)$ and recovery involves the annihilation of dislocations of opposite sign, the recovery rate can be expressed as

$$r = r_o \bar{\sigma}_i^{m} \qquad \ldots.(78)$$

where r_o and m are constants, and for simple network growth m = 3.

If, as found experimentally, the rate of strain hardening is inversely proportional to the mean internal stress, then

$$h = \frac{h_o}{\bar{\sigma}_i} \qquad \ldots.(79)$$

and if steady-state creep can be presented as given in Equation (45), namely

$$\dot{\varepsilon}_s = \frac{r}{h}$$

then again expressed in terms of the internal stress concept

$$\dot{\varepsilon}_s = \frac{r_o \, \sigma_i^{\,m}}{h_o/\bar{\sigma}_i} \qquad \ldots.(80)$$

and in the form of Equation (78)

$$\dot{\varepsilon}_s = B'' \, (T) \, \bar{\sigma}_i^{\,m+1} \qquad \ldots.(81)$$

Considering the relationship between the conventional stress dependence of the applied stress with respect to steady-state creep rate, p, and the internal stress parameters m, n and ℓ it follows from the equation above that

$$p = \left(\frac{\partial \, \ell n \, \dot{\varepsilon}_s}{\partial \, \ell n \, \sigma_A} \right)_T ; \qquad m + 1 = \left(\frac{\partial \, \ell n \, \dot{\varepsilon}_s}{\partial \, \ell n \, \bar{\sigma}_i} \right)_T ;$$

$$n = \left(\frac{\partial \, \ell n \, \dot{\varepsilon}_s}{\partial \, \ell n \, \bar{\sigma}_e} \right)_{T, \, \bar{\sigma}_i} ; \qquad \ell = \left(\frac{\partial \, \ell n \, \dot{\varepsilon}_s}{\partial \, \ell n \, \bar{\sigma}_i} \right)_{T, \, \bar{\sigma}_e}$$

From Equations (76), (77) and (81)

$$p \frac{d\sigma_A}{\sigma_A} = (m + 1) \frac{d\bar{\sigma}_i}{\bar{\sigma}_i} = \ell \frac{d\bar{\sigma}_i}{\bar{\sigma}_i} + n \frac{d\bar{\sigma}_e}{\bar{\sigma}_e} \qquad \ldots.(82)$$

and since $d\sigma_A = d\bar{\sigma}_e + d\bar{\sigma}_i$ it follows that

$$p = \frac{(\bar{\sigma}_e/\bar{\sigma}_i + 1)\ (m + 1)}{\left(\frac{m - \ell + 1}{n}\right)\frac{\bar{\sigma}_e}{\bar{\sigma}_i} + 1} \qquad \ldots.(83)$$

The experimentally observed stress dependence of the creep rate is considered by the authors to be related to the stress dependences of processes linked through a glide recovery balance. The authors have achieved a means of linking these two processes phenomenologically. Figures calculated from the equations are in reasonable agreement with measured values.

The model assumes

(i) incubation periods occur for one level of stress reduction

(ii) strain hardening is inversely proportional to internal stress

(iii) recovery rate is proportional to $\bar{\sigma}_i^3$.

In several recent papers[85-88] the network growth model has been modified such that it is considered that once a dislocation link of sufficient length has formed, a burst of local slip will take place generating dislocation pile-ups which increase the local dislocation density, and so the next slip event is likely to take place elsewhere. Hence the rate of deformation is controlled by the rate of growth of the network and not by recovery in the vicinity of a pile-up. From progressive stress reduction tests it was found that the incubation period following each consecutive small reduction in stress increased until a limiting value was reached, at which creep did not recommence within a reasonable period of time. The corresponding value of current applied stress is termed the friction stress σ_0. It is considered to be related to the stress level which can be supported by the relaxed dislocations, and so creep deformation does not occur under the full applied stress but under $\sigma_A - \sigma_0$. In a variety of materials for which stress-steady state creep rate graphs show relationships of the form $\dot{\varepsilon}_s \propto \sigma^4$ at low stresses and relationships of the form $\dot{\varepsilon}_s \propto \sigma^8$ at high stresses, the approach is found to remove the break in the curves such that $\dot{\varepsilon}_s \propto (\sigma_A - \sigma_0)^4$ applies over the whole range. The concept has been shown to reduce calculated high activation energy

values obtained for complex alloys, to values close to those for diffusion in the matrix material.

Although conceptually simple, the idea would appear to be of potential fundamental significance to the understanding of creep processes. Comparing this σ_o internal stress with that of Nix and Co, $\bar{\sigma}_i$, $(\sigma_A - \sigma_o)$ is considered to be responsible only for determining the mesh size of the dislocation network developed during creep, whereas $\bar{\sigma}_i$ is considered to be a back stress which opposes dislocation movement in the forwards direction. Also, in the Nix approach, incubation periods should occur only when the stress is reduced to the internal stress level $\bar{\sigma}_i$. In the above model however, incubation periods should occur for all stress reductions up to a critical level.

Recently some evidence by McElroy[89] has thrown doubt on the internal stress and recovery interpretations of material response to stress reductions. It is considered that experimental observations can be explained on the basis of an interaction between forwards creep at the reduced stress level and concurrent anelastic recovery. It is suggested that anelastic recovery always accompanies stress reductions. The recovery rate r is defined as $r = \Delta\sigma \cdot \dot{\varepsilon}_L/\varepsilon_a$, where $\dot{\varepsilon}_L$ is the creep rate after the stress change and ε_a is the anelastic strain. The work hardening term, h, is considered to be equal to $\Delta\sigma/\varepsilon_a$. It is suggested that after small reductions in stress are made during a creep test, the internal stress concept of a continuous forwards creep rate and the recovery concept of the occurrence of incubation periods can both be explained by the anelastic approach. On this basis it is stated that stress reduction techniques are invalid for determining the rate controlling mechanisms during creep. However, the occurrence of incubation periods over a range of stress reductions would appear to require a fortuitous relationship between forwards and backwards deformation. Also since these incubation periods are proportional to the stress drop, the rate of recovery (defined as $r = \Delta\sigma/\Delta t$) is constant. In the anelastic model the rate of recovery is dependent on $\dot{\varepsilon}_L$, the creep rate after the stress reduction, and since this depends on the new applied stress, the predicted rate of recovery (defined as $r = \Delta\sigma\ \dot{\varepsilon}_L/\varepsilon_a$) is not constant.

The present research programme should allow the assumptions of the three models to be tested and hence should provide some indication of the general validity of the various models.

2.3 The effect of material composition on high temperature creep strength

High temperature strength depends on the manner in which alloying elements modify the rates of strain hardening and subsequent recovery. In order to attain commercial alloys with improved creep resistance it is necessary that attempts be made to understand the mechanisms of creep in complex alloy structures. In simple solid solution alloys, a number of strengthening mechanisms have been noted and these serve as pointers in attempting to isolate the more obscure mechanisms in complex alloys.

2.3.1 Solid solution alloys

Since hardening arises through interactions between dislocations, solid solution elements may further impede dislocation movement by introducing a friction stress. Although a variety of mechanisms are known to contribute to solid solution strengthening[90-96,100-104], in general, solid solution alloying produces only minor improvements in creep resistance. Most high temperature materials deriving their strength from a dispersion of precipitates or insoluble particles and in an 80/20 nickel/chromium solid solution alloy for example, the addition of about 15 per cent Ni_3 Al γ' precipitate has been shown[58] to increase the creep resistance of the basic alloy by a factor of about 10^6. Evidence is accumulating to indicate that the strengthening which does occur from alloy additions is through reduction in recovery rates, by hindering climb through solute atoms attaching themselves to jogs and thereby retarding movement[96], by reducing the stacking fault energy and hence making cross-slip more difficult[97] or by large quantities of solute atoms altering the binding strength as has been found for nickel-chromium alloys[98].

2.3.2 Two-phase alloys

The strengthening of two-phase alloys depends on either

(a) second phase particles acting as inpenetrable barriers to dislocation motion and so forcing glide dislocations to bow-out and by-pass particles by Orowan mechanisms[99] (or climb over particles by Weertman mechanisms)

or (b) second phase particles being cut or sheared by dislocations below the Orowan stress, the strengthening effect being due to the additional work required to force the dislocations to cut the particles.

For either case the theoretical treatment is based on the model shown in Figure 5.

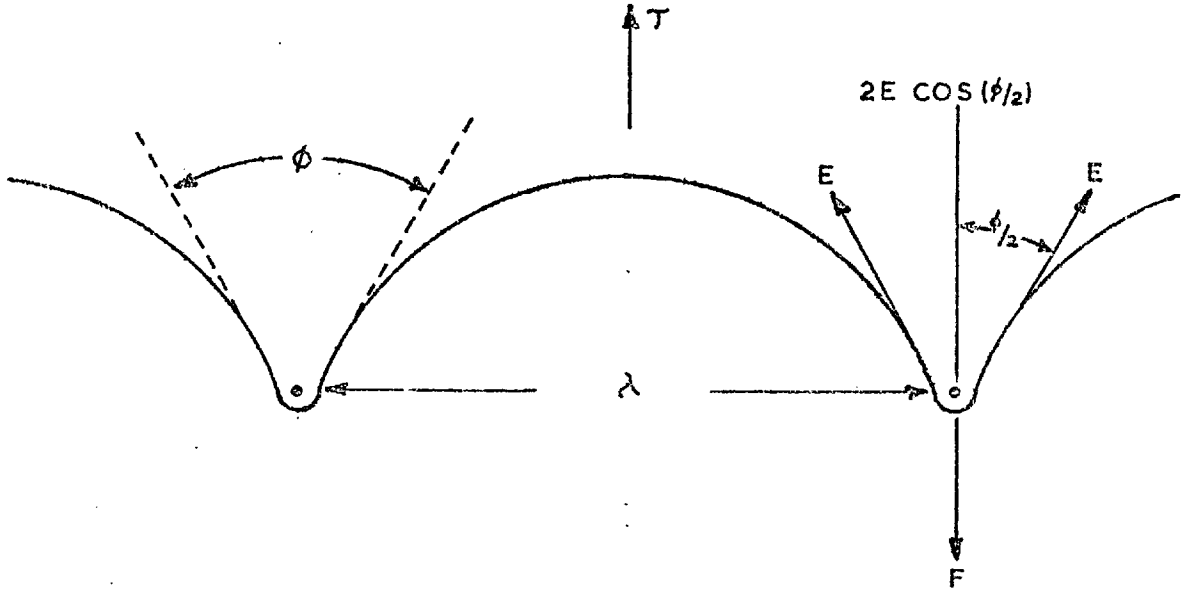

Figure 5

When the included angle reaches a critical value the dislocation breaks away from the obstacle allowing the obstacle strength, F, to be calculated from the dislocation line tension by the equation

$$F = 2E' \cos(\theta/2) \qquad \ldots.(84)$$

where E' is the energy/unit length of dislocation. If $\theta = 0$ the particle acts as an inpenetrable obstacle - ideal Orowan hardening.

Since for $\theta > 0$ the shear stress is given by $F = \tau b_1 \lambda p$, it follows that

$$\tau = \frac{2E' \cos(\theta/2)}{b_1 \lambda p} \qquad \ldots.(85)$$

where λp is the effective interparticle spacing. Macroscopic flow occurs at a value of τ for which the majority of the particles are sheared or by-passed by glide. Since in practice a distribution of

values will exist, an average must be selected and the interparticle spacing most suitable appears to be the Planar value[100]. When related to N_A, the number of particles intersecting a slip plane, this gives

$$\lambda_p = \beta/(N_A)^{\frac{1}{2}} = \beta L \qquad \ldots.(86)$$

where β = constant generally $\simeq 1.2$

and $L = 1/(N_A)^{\frac{1}{2}}$

When a particle is sheared the effective interparticle spacing is increased because the dislocations do not bow out so much before breaking away. An appropriate relationship is[73]

$$\lambda_p = \left(\frac{2E' L^2}{\tau_F b_1}\right)^{\frac{1}{3}} \qquad \ldots.(87)$$

which gives

$$\tau_F = \frac{2E'}{b_1 L}\left[\cos\left(\frac{\theta}{2}\right)\right]^{\frac{2}{3}} \qquad \ldots.(88)$$

where τ_F is the stress required to cause the dislocation to break through an array of particles. Foreman and Makin[101] showed this to be a good equation except when $\theta \to 0$ and so they suggested an empirical equation which could be applied over the whole range, this equation being

$$\tau_F = \frac{2E'}{b_1 L}\left[\cos\frac{\theta}{2}\right]\left[0.8 + \frac{\theta}{5\pi}\right] \qquad \ldots.(89)$$

Orowan hardening has been modified

(a) to take account of particle size d' by replacing λ_p by $(\lambda_p - 2d')$ and converting L to the effective interparticle spacing

(b) by using more refined values for line tension

(c) by considering the mutual interactions of two bowed out arms of dislocations on either side of a particle.

These assumptions lead to

$$\tau = \frac{0.83\ Gb_1}{2\pi\ (1 - \nu'')^{\frac{1}{2}}} \frac{\text{Log}\ (2d'/r_c)}{(\lambda - 2d')} \qquad \ldots.(90)$$

where r_c is the dislocation core radius and ν'' is Poisson's ratio. This gives good agreement with the data. Further modifications can be made for elongated particles.

2.3.2.1 Creep theories of two-phase alloys

In grain growth theories it is considered that particles impede grain growth due to a back stress from the particles[105]. Applying this concept to creep, Lagneborg[106] considered that dislocation network growth would be retarded by dispersed particles and proposed

$$\dot{\varepsilon}_s = \frac{\sigma^2}{\alpha G b_1} (\sigma - \sigma_0)^3 \qquad \ldots.(91)$$

where α is a constant and σ_0 in this case is related to the impeding effect of particles during creep. This leads to the conclusion that in the creep equation, $\dot{\varepsilon}_s = A\sigma^n$, n should be greater than 5 as stress is reduced. However in many cases n has values less than 5.

A qualitative theory for creep of two-phase alloys has been proposed by Ansell and Weertman[70,71]. At low stresses when $\sigma_A < Gb_1/\lambda p$, where G is the shear modulus, b_1 is the Burgers vector and λp interparticle spacing, it is considered that the rate controlling process is the climb of dislocations over particles with no pile-up or bowing of dislocations at the particles, and so the steady-state creep rate should be linearly proportional to applied stress, the equation being

$$\dot{\varepsilon}_s = \frac{\pi\ \sigma\ b^3\ \exp\ (-\ Q_m/KT)}{2KT\ d^2} \qquad \ldots.(92)$$

At stresses above $Gb_1/\lambda p$, dislocations are considered to bow round particles leaving pinched-off loops, until the back stress from the loops prevents further bowing. Creep rate is then proportional to the

rate at which the loop nearest the particle climbs and is annihilated, allowing further dislocations to bow between the particle and form another loop. They concluded that at high stresses, creep rate should vary as σ^4, the full expression being

$$\dot{\varepsilon}_s = \frac{2 \pi \sigma^4 \lambda_p^2 \exp (- Q_m/KT)}{d G KT} \quad \ldots.(93)$$

where Q_m is the activation energy for matrix self diffusion. Shearing of second phase particles was not considered.

Although these predictions are not in agreement with experimental observations on the stress dependence of steady-state creep rate of two-phase alloys, the theory has been the basis of recent investigation by Wilshire et al[86-88].

The model for creep of solid solution alloys considered previously in Section 2.2.4 can be extended to two-phase alloys. The friction stress, σ_o, relates to the limiting size of the dislocation network, however in this case σ_o it includes a combined particle-dislocation interaction effect.

Also, although the apparent activation energy for two-phase alloys, determined from creep rates using the equation

$$\dot{\varepsilon}_s = A \sigma^n \exp (- Q/RT) \quad \ldots.(94)$$

is markedly higher than that for the matrix material, using the equation

$$\dot{\varepsilon}_s = A (\sigma - \sigma_o)^4 \exp (- Q/RT) \quad \ldots.(95)$$

the value obtained for Q is close to that for creep and for self diffusion of the basic matrix material. This indicates that the rate controlling processes are due to matrix deformation and that the anomalously high values generally obtained in determining activation energies are due to their calculation under conditions in which $(\sigma_A - \sigma_o)$ is not constant, ie under variable structural conditions.

These creep theories confirm that improved creep resistance will be obtained by decreasing the self diffusion coefficient of the matrix and by increasing the particle size and volume fraction of the precipitated second phase.

2.4 Application of alloy theory to gas turbine materials

Most turbine blades and discs are based on variations of the basic nickel-chromium matrix hardened by γ' (Ni_3 Al Ti) but with further additions of Co, Fe, W, Mo, V, Nb, Ta, B, Zr, C and Mg. These alloys are used for thousands of hours at up to 0.8 T_M where T_M is the absolute melting temperature, their endurances being attributed to

(1) the high tolerance of nickel for alloying without instability, due to its nearly-filled 3d electron shell

(2) the protective $Cr_2 O_3$ rich scale which restricts diffusion rates of oxygen and sulphur in, and metallic elements out,

(3) the stability of the γ' dispersion hardened precipitate, and its effectiveness in restricting creep.

2.4.1 Solid solution hardening of γ phase

The solid solution elements added to the γ matrix include Co, Fe, Cr, Mo, W, V, Ti and Al[107]. From well-established alloy theory, hardening can be related to the atomic diameter and electron valancy number. The above elements differ from nickel by 1 to 13 per cent in atomic diameter and 1 to 7 per cent in electron valancy number. They also reduce its stacking fault energy. From these factors it is found that the potent solid solution hardeners are Al, W, Mo and Cr whereas Fe, Ti, Co and V are weak hardeners only. However under high temperature creep conditions, γ' strength is diffusion dependent and slow diffusing elements like Mo and W will be most potent. These elements can also lower the diffusivity of Ti and Cr hence enhancing their effect.

2.4.2 Precipitation hardening by γ' phase

γ' has an ordered L12 structure contributing anti-phase boundary strength. A theory of anti-phase boundary hardening has been developed based on coherent ordered γ' in disordered γ (Reference 108). It is considered that dislocations glide in pairs because the leading dislocation is impeded and creates disorder in cutting γ' particles, the trailing dislocation is assisted since it annihilates this disorder. However the contributions of second phase strengthening must also depend on stability,

and a critical factor is the transition from dislocation cutting to by-passing. As γ' coarsens above $0.6T_M$, this increases interparticle spacing making by-passing easier. Fleetwood[109] applied Wagner's theory of Oswald ripening to γ' particles and obtained for particle size, d, the equation

$$d = \left[\frac{64\ \gamma_e\ D\ C_e\ V_m^2\ t}{9RT}\right]^{\frac{1}{3}} \qquad \ldots.(96)$$

where γ_e is the specific γ'/γ interfacial free energy, D is the diffusion coefficient of the γ' solutes in γ, C_e is the equilibrium molar concentration of γ' solute in γ, and V_m is the molar volume of γ'. Composition causes significant changes in γ_e, C_e and D terms and for Ni-Al-Ti-Cr alloys, γ' coarsening decreases as the chromium increases from 10 to 37 per cent. This is due partly to the reduced C_e but also to a reduction in coherency strain, and consequent reductions in γ_e and D. Fell[102] found coarsening increased as strain decreased, but Mitchell[103] found no effect of Co, Mo and Fe, although increasing Nb from 2 to 5 per cent markedly reduced the rate of coarsening despite the concurrent increase in coherency strain due to Nb partitioning to the γ'.

When by-passing of particles occurs, dislocations do so either by looping around particles or by climbing over them[110]. Molybdenum additions to wrought alloys such as Nimonic 108 for example, and molybdenum and tungsten additions to cast alloys such as Mar M246, decrease the creep rates by their effects on diffusion rates. Cobalt additions to Nimonic 90 increase the γ' volume fraction. Massive additions of aluminium to Mar M246 increase the volume fraction of γ' in this alloy.

The transition from cutting to by-passing depends on particle size and temperature, but from the evidence available the size varies widely, depending on the particular alloy and operational temperatures. In alloys with about 20 per cent volume fraction γ', dislocation by-passing has been found with particles greater than 300 Å even with room temperature deformation. Since γ' rapidly coarsens at temperatures above 1023K, it is necessary to try to reduce this effect as much as possible. Mitchell[103] has shown that the transition size increases with volume percentage of γ', this giving a method of delaying by-passing

and illustrating part of the reason for the increased strength of Nimonic 108 as compared to Nimonic 90. No data is available for advanced super alloys, but the increased volume fraction of γ' is a trend in a similar direction.

Comparing these new casting alloys with wrought alloys, it can be seen that the greater volume fractions of γ' will make the cast alloys much stronger and the presence of slow diffusing elements such as niobium and tantalum will make them much more stable.

Since the friction stress σ_0 is a structural term related to second phase particles, it should be possible to relate the strength of the various γ' hardened wrought alloys and the cast alloys through their various σ_0 values and also within any alloy it should be possible to indicate changes in mechanisms of dislocation flow from changes in the structural internal stresses. These points will be investigated in the current research programme.

2.5 Relevance of the findings of the literature survey to the current research programme

The findings of the literature survey can be summarised under three general aspects.

1 Using Graham and Walles equations of creep it should be possible to develop empirical laws for compressive creep. Further applying strain hardening theory to the Graham and Walles equations, it should be possible to develop empirical laws for transient stress cycling and, possibly, transient stress and transient temperature cycling.

2 If friction and/or internal stress levels control the level of the effective stress causing deformation, it should be possible (a) to compare and (b) to predict deformation characteristics of different complex alloys from an evaluation of their friction and/or internal stress levels.

3 Although physical theories of creep are not yet comprehensive enough to be of use to the designer, it should he possible to bring the physical and empirical approaches closer together by quantifying structural or friction stress effects on rates of deformation. For example, the use of equations of state in variable stress situations are inadequate since after stress changes the structural state is unknown. Investigation of

changes in friction stress may give a clearer understanding of the 'state of the material' and hence lead to improved equation of state predictions.

3.0 The research programme

3.1 Programme objectives

In the introduction brief reference has been made to the main problems associated with material behaviour in gas turbines. These problems can be placed in two broad groups, the first relating to component life prediction and the second relating to methods of improving component life.

Although life prediction encompasses the fields of cooling and combustion technologies, the scope of this research programme will be limited to materials technology. In empirical life prediction crude linear damage laws are frequently employed in assessing transient stress effects. For instance, in gas turbines it is not known conclusively whether damage arising from transient stress and temperature (ie thermal fatigue) is due to fatigue, creep, stress corrosion, a combination of all three, or an entirely unique process.

Previously little accurate materials data has been compiled, the bulk of available information being in the form of small groups of tests at selected stresses and temperatures. Generally these tests have been conducted solely for purposes of quality control. Furthermore the lack of compressive creep information has necessitated the use of tensile data in design calculations. The evidence for the assumption of tensile and compressive damages being equal is based mainly on the fact that predictions are in reasonable agreement with practice.

With wrought alloys the gradual increase in engine operating temperatures has provided some safeguard to off-set a lack of understanding of specific deformation mechanisms. However although the introduction of cast alloys presents many potential advantages, such as increased operating temperatures and longer component lives, these are accompanied by a higher proportion of transient damage and the full benefits of cast alloys cannot therefore be derived until components can be lifed accurately.

The present programme has been conceived with two related themes, the first being aimed at

(1) providing information on the high temperature deformation and fracture behaviour of Nimonic 90, Nimonic 108 and Mar M246

(2) developing methods of quantifying cyclic deformation from static data

(3) applying the laws developed under simple testing conditions to the practical problem of thermal fatigue.

Since new materials for gas turbines cannot be developed as efficiently or effectively as possible if the mechanisms of high temperature deformation are not completely understood, the second theme is aimed at

(i) examining current physical laws for creep, assessing their validity and attempting to develop them to a point where they can be used to predict material behaviour and hence reduce the amount of testing required to prove new alloys

(ii) bringing physical and empirical laws closer together such that life predictions based on empirical concepts can be improved.

The test programme has been devised to achieve limited improvement in understanding of high temperature creep over a broad front rather than to achieve (possibly) a greater depth of progress on a restricted topic within this field. The two main themes can be combined in an overall objective to provide a phenomenological theory of high temperature deformation such that from a knowledge of material behaviour under one set of simple test conditions, predictions can be made of the behaviour to be expected under other conditions, possibly of increased test complexity.

3.2 Choice of materials

The test programme was conducted on the wrought alloys Nimonic 90 and Nimonic 108, which are characteristic of many current aero gas turbine disc and blade materials used for example in Spey, Avon and Conway engines, and on Mar M246 which is typical of those casting alloys being introduced in new technology engines such as the RB211 and RB199 engines. The thermal fatigue programme was conducted on Nimonic 108.

The chemical compositions and heat treatments are given in Table I.

Nimonic 90 was chosen because

(1) it is typical of the Nimonic series of alloys used generally in aero gas turbines

(2) static creep properties are known over a wide range of test conditions and hence if necessary findings could be related to previous work

(3) if at a later date extension of the work makes necessary the use of a different cast of material, cast to cast variations are easily quantified.

After the heat treatment given in Table I the structure of this material consists of a very fine intra-granular coherent precipitate of γ' (Ni_3 Al, Ti) in a γ solid solution together with grain boundary MC carbide. The titanium and aluminium concentrations are controlled so as to produce about 30 volume percent of γ' which has a size of about 0.02μ and an interparticle spacing of about 0.01μ. Figure 6a shows a typical microstructure for this material. With exposure to temperature carbide transformation to M_6C can occur together with coarsening of the γ' precipitate. With prolonged exposure to temperature, titanium and chromium can diffuse to the grain boundary carbides leading eventually to zones denuded of γ' precipitate.

Nimonic 108 was chosen for the compressive creep and thermal fatigue programmes because it was necessary to relate the imposed damage cycles to theoretically calculated damage experienced by a specific blade in service, and available damage cycles related to turbine blades in Nimonic 108 material.

After the heat treatment shown in Table I, Figure 6b shows that this alloy contains an intermittent grain boundary film of massive γ' together with fine intra-granular γ' of about 0.06μ and an interparticle spacing of about 0.01μ. Due to higher titanium and aluminium concentrations than in Nimonic 90 this alloy contains a greater volume fraction of γ', about 40 per cent, and the basic carbide is of the M_{23} C_6 type. The matrix is stronger than in Nimonic 90 due to the presence of the solid solution strengthener molybdenum. This element also helps to delay the onset of denudation.

Mar M246 was chosen because

(1) it is typical of the high strength, cast superalloys, whose increased use in aero gas turbines is envisaged

(2) successful techniques have been developed to enable directionally solidified and single crystal forms of this material to be obtained relatively easily and with the correct orientation for the best combinations of blade properties.

The alloy contains both tungsten and molybdenum and has a γ' volume fraction of just over 60 per cent. This is present in two sizes, large cuboids up to 0.8μ and much finer interspersed particles which are about 0.01μ. A typical microstructure is given in Figure 6c. The presence of tungsten and molybdenum atoms strain the matrix lattice structure, slow down diffusion rates and hence help to prevent coalescence of γ'. Complex $M_{23}C_6$ and M_2C carbides are formed at the grain boundaries where they effectively slow down creep rates.

3.3 Experimental programme

The full experimental test programme is presented in Table II.

TABLE II

Schematic illustration of test programme

TYPE OF TEST	MATERIAL		
	NIMONIC 90	NIMONIC 108	MAR.M. 246
TENSILE CREEP	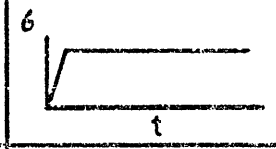	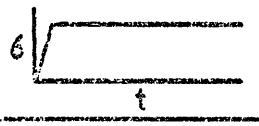	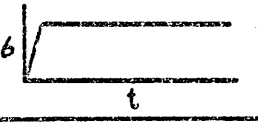
COMPRESSIVE CREEP	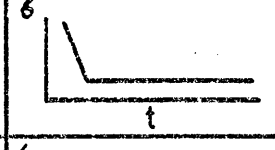	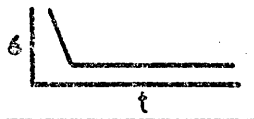	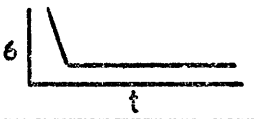
RECTANGULAR CREEP	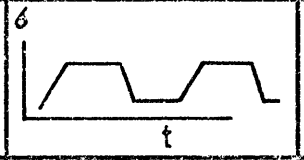		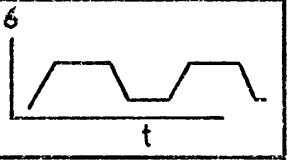
TRIANGULAR CREEP (VARIABLE FREQUENCY)	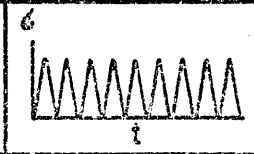		
TRIANGULAR PUSH-PULL	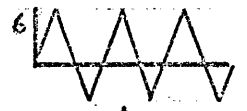		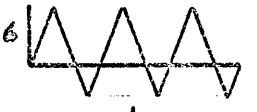
RECTANGULAR PUSH-PULL			
STRESS REDUCTION	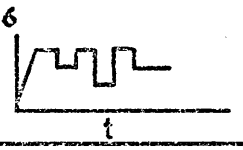		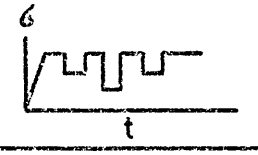
PROGRESSIVE STRESS REDUCTION	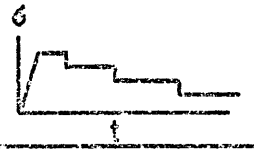		
VARIABLE STRESS AND TEMPERATURE (THERMAL FATIGUE)		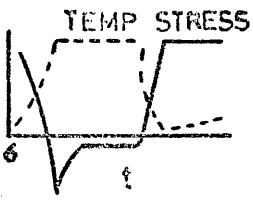	

Since turbine blades frequently experience peak damage during the initial start-up and shut-down of the engines, this will occur over a small number of seconds in an operational cycle of several hours. The significance is that current laboratory test conditions, chosen to produce failure in less than about 250 hours, are equivalent to several thousands of hours of flight. There is no necessity to enhance damage by increasing stress or temperature.

Considering the individual tests

Tensile creep

Constant stress tensile creep tests on Nimonic 90 were carried out over the temperature range 1073K to 1173K, stresses being chosen so as to give rupture in up to 250 hours.

On Nimonic 108, tests were carried out over the range 973 to 1173K for durations up to 250 hours. Some of these tests were unbroken after this time but stresses were selected to provide creep data for general gas turbine calculations.

Conventionally cast, directionally solidified and single crystals of Mar M246 were tested at 1123K and 1173K, stresses again being chosen so as to produce rupture in up to 250 hours.

Compressive creep

Compressive creep tests were carried out under equivalent conditions of stress and temperature as in the tensile case. Tests were discontinued after 250 hours or 2 per cent strain, whichever occurred first. The strain limit was imposed to ensure axiality was maintained throughout the test. However this strain level is considerably greater than the limit imposed on turbine blades.

A small number of compressive creep tests were taken to much higher limits of strain in order to investigate the occurrence of eventual cracking or structural change.

Rectangular creep

Rectangular creep tests having 360 second hold times at peak and minimum stress levels were carried out on Nimonic 90 over the temperature range 1073K to 1173K. These tests were compared with complementary tensile creep tests. At 1123K, tests were also conducted with hold times of 6 seconds, 1.8 ks and 11.2 ks. Stresses were chosen such that the total test durations were up to 400 hours.

Rectangular creep tests were also conducted on directionally solidified Mar M246 at the single hold time of 360 seconds. Again stresses were chosen to allow comparison with complementary monotonic creep tests.

Triangular tensile creep

Triangular tensile creep tests were carried out on Nimonic 90 at 1123K and a frequency of 1 CPM. Stresses were chosen to give rupture times of up to 500 hours. At 1173K, tests were conducted over a range of frequencies from 1 CPM to 10^3 CPM.

Both conventionally cast and directionally solidified forms of Mar M246 were tested at 1123 and 1173K. Frequencies of 1 CPM and 0.05 CPM were employed.

Triangular tension tests were conducted on Nimonic 108 in the temperature range 623 to 973K. These tests were simply to ensure that the low cycle fatigue lives obtained were very much greater than thermal fatigue lives predicted solely from creep damage considerations.

Triangular push-pull creep

Because of lack of machine capacity, to date this type of cycle has been applied only to conventionally cast Mar M246 specimens. It is hoped to confirm the findings on Nimonic 90.

Rectangular push-pull creep

Rectangular push-pull creep tests having 360 second hold times at peak tensile and peak compressive stress levels, were conducted on Nimonic 90 at 1123K and 1173K and on directionally solidified Mar M246 at 1173K, stresses being chosen to give rupture in up to 250 hours.

Stress decrement

Stress decrement tests were carried out on Nimonic 90 in the temperature range 1123K to 1173K and on Mar M246 in the range 1173K to 1273K, in order to obtain values of internal stress levels in these materials. Initial stress levels were chosen to give steady-state creep rates in the range 10^{-3}%/hr to 10^{-1}%/hr. These experiments were divided into two separate series of tests. The first involved determining the stress drop for which negative creep just occurred immediately following the stress reduction, and is illustrated in Figure 7a.

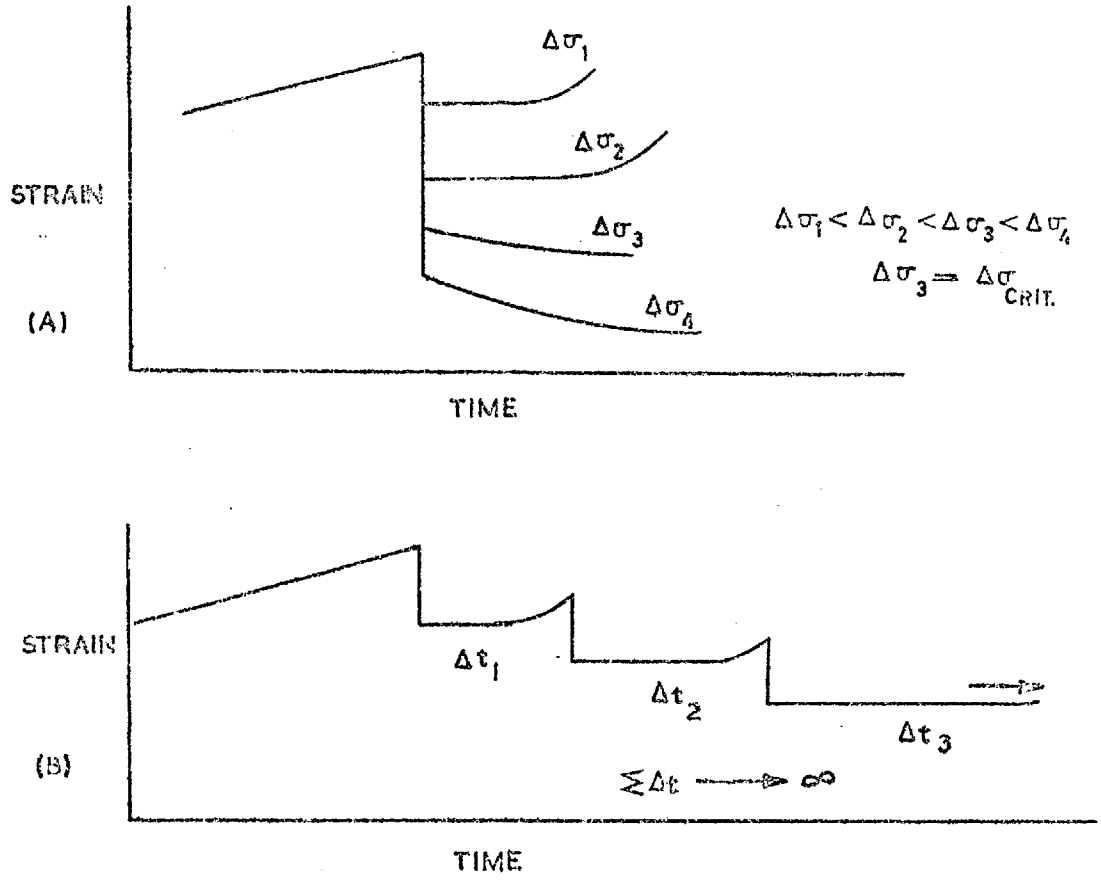

Figure 7

In the second series of tests a friction stress was determined by progressive stress reductions to a level at which the incubation time prior to forwards creep at the reduced stress level, was excessive. This is illustrated in Figure 7b.

Cyclic stress - cyclic temperature creep

These tests were conducted on Nimonic 108 and involved heating and cooling rates up to 30 K/s and loading rates of 50 MN/m^2 s^{-1}. The conditions were chosen to simulate thermal fatigue experienced by the leading edge of a turbine blade.

3.4 Equipment and test technique

Both tensile and compressive creep tests were conducted under conditions of constant stress. The necessity for this has been discussed previously in a recent paper[111] in which it was calculated that where ε_t and ε_c are the nominal tensile and compressive strains under constant load, and ε_s is the true strain under constant tensile or compressive stress, then, for each term in the Graham and Walles creep equation,

$$\varepsilon_t - \varepsilon_c = \beta \varepsilon_s^2$$

where β is the stress exponent. In a more general application, if secondary creep only is being considered, β is equal to the stress exponent n in the equation

$$\dot{\varepsilon}_s = A\sigma^n$$

If the typical value of 8 applies for the stress exponent in the secondary creep region, then for a true strain of 2 per cent, nominal values will differ by 0.3 per cent. If the comparison were made in the tertiary creep region then the corresponding stress exponent would be 24 and the nominal strain difference would be 1 per cent, ie an error of 50 per cent. This illustrates the importance of stress control rather than load control when characteristics of deformation are being investigated and compared under tension and compression.

The method devised to maintain constant stress has been discussed previously[111,112]. For the case of constant compressive stress the system is shown schematically in Figure 8. Briefly, load is sensed by a transducer sited across a proving ring whilst strain is measured from extensometer arms located on specimen ridges. As compressive creep occurs, load decreases and so the voltage proportional to load, V_{DE}, also decreases. This reduces the voltage across the preset 'constant voltage' unit, V_{DE}, so that a microswitch activates the load motor to restore, V_{DE}, to its preset value. The relationship between stress and load is controlled by a fixed resistance, R, and a variable resistance, r, which has a variable tapping proportional to strain. The proportionality is according to a scale factor, S, which is the strain to give full movement of the sliding contact.

At the commencement of a test, load is W_0 and $V_{AC} = V_{DE}$. As the specimen is compressed, the contribution from the variable resistance is altered such that

$$V_{DE} = V_{AC}\left[\frac{R + \left(1 - \frac{\varepsilon}{S}\right) r}{R + r}\right]$$

Since V_{AC} is proportional to the load W sensed on the proving ring and since V_{DE} is maintained constant at a value proportional to the initial load W_o then

$$W_o = W\left[\frac{R + \left(1 - \frac{\varepsilon}{s}\right) r}{R + r}\right]$$

such that $$R = r\left(\frac{1}{s} - 1\right)$$

and so $$W = \frac{W_o}{1 - \varepsilon}$$

which is the condition for constant stress. This assumes constant volume and uniform deformation along the gauge length. It gives a stress correction based on engineering strain defined as $\frac{\ell - \ell_o}{\ell_o}$, as opposed to true strain $\log\left(\frac{\ell - \ell_o}{\ell_o}\right)$. However for small strains the error is negligible, being 0.002 per cent for a true strain of 5 per cent.

The tensile machine was modified to allow specimens of various gauge lengths to be tested under constant stress conditions. The modification applied a factorising correction to the strain measuring system. In both tensile and compressive testing machines, load could be adjusted by the method described so as to maintain stress constant to ±0.25 per cent.

Comparative tensile creep tests using 12.5 mm, 25 mm and 50 mm gauge lengths exhibited no differences in creep characteristics and typical specimen dimensions are given in Figure 9a. When a high degree of accuracy was required the 50 mm gauge length specimen was used and, in conjunction with a linear displacement transducer, allowed strain discrimination of 5×10^{-6} (other gauge lengths giving proportional discrimination). A trizone furnace and controller allowed test piece temperatures to be maintained at set values ±0.5K. Three thermocouples placed along the gauge length of the specimen monitored temperature to ensure a gradient of not more than ±0.5K. The load control system of the tensile creep machine allowed either tensile, triangular or rectangular creep tests to be carried out.

When testing under compressive damage conditions several additional factors have to be considered, such as

(1) it is necessary to prevent 'bedding in' effects being included in any strain measurements and so strain must be measured directly off a gauge length rather than indirectly via movement of loading bars etc

(2) if results have to be compared with tensile data the specimen shape should be similar to tension in order to remove any possible differences due to geometric effects

(3) good axial alignment must be maintained to avoid buckling.

While the first point can be achieved comparatively easily the second and third points are more difficult to satisfy since tensile creep generally involves relatively slender specimens and these would tend to buckle under compressive loading. In this programme of tests a compromise solution was used in which, if compressive phases were to be experienced, specimens were used with parallel section to diameter ratios of 3 to 1. Small ridges 12.5 mm apart were incorporated within these sections to allow the location of axial extensometers. The end sections were waisted to the same shape as the tensile specimens, Figure 9b gives details of compressive specimen dimensions and Figure 9c of push-pull specimen dimensions. With this arrangement it was found that buckling could be minimised to less than 0.05 mm lateral movement at 2 per cent compressive strain. Tests were not normally taken above this value, to avoid buckling and because higher values are unlikely to apply in gas turbine applications. Some high stress tests were conducted to examine metallurgical effects of high compressive strain.

In the majority of the cyclic tests the minimum stress levels were set at a nominal value of about 25 MN/m^2 and loading rates of 30 $MN/m^2/s$ were employed. Peak stress and minimum stress levels were maintained for 360 seconds (6 minutes), 1.8 ks (30 minutes) and 14.4 ks (4 hours). For certain specific cycles a special technique was adopted in the measurement of anelastic recovery strains during the off-load periods. This involved using the finest strain discrimination and a recorder chart speed of 60 mm/min. It meant that zero strain on the recorder had to be suppressed prior to measurement of the recovery strain.

In order that a direct comparison could be made between static creep and rectangular creep results a technique was adopted in analysing the data such that if, in the cyclic tests, the total on-load/off-load cycle lasted 2τ, then the creep strain increment $\Delta\varepsilon$ occurring over the on-load period τ, was obtained by subtracting the off-load anelastic recovery from the total on-load plastic strain. During the secondary creep stage, the creep rate $\dot{\varepsilon}_s$ was then given by $\Delta\varepsilon/\tau$, however a more accurate figure could be obtained by measuring the net strain over several cycles and dividing by the total on-load time over the period considered.

Anelastic recoveries were further investigated as part of an exercise to improve understanding of deformation processes. In this exercise it is hoped to use stress decrement tests to investigate current theories on internal stress.

In the first series of tests the sign of the creep rate immediately following a stress reduction was noted. If an incubation period, ie a period of zero creep was observed the specimen was reloaded to the original stress level and once steady-state creep has been re-established a slightly greater stress reduction was made. This procedure was continued with increasing stress reduction until negative creep rates were observed. Several stress reductions were then made at values close to this level and the critical value of stress, at which the creep rate just went negative following a stress reduction, were determined. The initial applied stresses were chosen to cover this steady-state creep rates in the range 10^{-3}%/hr to 10^{-1}%/hr.

In some cases the critical stress was measured throughout the whole life of the specimen, although in general measurements were made in the steady-state region only.

In determining the friction stress the applied stress was reduced by about 10 per cent and the incubation period to recommencement of forwards creep monitored. As soon as forwards creep was re-established a further stress reduction was made. It was found that incubation periods increase progressively until a stress level is reached at which the incubation period is very great. This is considered to be the level of the friction stress relating to the original applied stress. The tests were conducted over an applied stress range similar to that discussed above.

3.5 Metallographic technique

In the main programme on compressive creep, tests were discontinued after about 2 per cent strain. No cracking was observed at this stage, however to determine whether cracking could occur at a later stage, additional tests were conducted on simple cylindrical specimens, deformation being measured approximately by the relative movements of the top and bottom loading bars. With this method high compressive strains could be produced so that specimens deformed to levels comparable to tensile fracture could be examined metallographically.

In examination of ruptured tensile specimens it is sometimes difficult to be certain whether small cavities are due to crack initiation during creep or pull-out of cracked grain boundary carbides during polishing. In order to remove this uncertainty notches were filed in some creep specimens at positions just below the fracture surface. The specimens were cooled in liquid nitrogen and then subjected to shock impact. This caused a transgranular fracture front to progress from the notch. Stereoscan examination of these new surfaces revealed internal creep cavities and hence allowed crack initiation sites to be positively identified.

4.0 Results

In the execution of this research project various different types of tests have been conducted. The results are presented graphically, in tabular form, or as micrographs.

Nimonic 90

Stress/strain curves are presented in Figure 10.

Tensile and compressive creep properties are compared in Figures 11, 13 and 15.

Tensile and rectangular creep properties are compared in Figures 17 and 23.

Anelastic recovery observations are presented in Figures 24 to 28.

Triangular tensile creep results are presented in Figures 16 and 30.

Rectangular push-pull creep results are presented in Figure 31.

Stress decrement results to determine the critical stress prior to backwards creep, σ_c, are presented in Figures 47 and 49.

Stress decrement tests to determine the friction stress level, σ_0, are presented in Figure 50.

Metallographic observations are presented in Figures 54 to 58 and Figure 60.

Nimonic 108

Tensile and compressive creep properties are presented in Figures 12, 14 and 16.

Thermal fatigue results are presented in Figure 87

Mar M246

The effects of casting method on tensile and compressive creep properties are presented in Figures 32 to 41.

Specimen size effects are presented in Figure 37.

Tensile and rectangular creep results are compared in Figure 42.

Anelastic recovery observations are presented in Figure 43.

Triangular tensile creep results are presented in Figure 44.

Triangular push-pull results are presented in Figure 45.

Rectangular push-pull results are presented in Figures 45 and 46.

Stress decrement results to determine the critical stress σ_c are presented in Figure 48b.

Stress decrement tests to determine the friction stress, σ_c, are presented in Figure 50b.

Metallographic observations are presented in Figures 61 to 64.

4.1 Static and cyclic creep properties of wrought Nimonics

4.1.1 Tensile and compressive creep of Nimonic 90 and Nimonic 108

Prior to commencing this investigation stress/strain curves under tensile and compressive loading were obtained for Nimonic 90 at the three selected temperatures. The modulus values obtained from the curves are given in Figure 10. Although the tensile and compressive modulii are identical, small but progressive deviations between tension and compression occurred in the plastic regions as shown in this figure. Insufficient material was available to carry out a similar exercise on Nimonic 108.

Typical tensile and compressive creep curves are shown in Figures 11 to 14. Figures 11 and 12 illustrate creep curves obtained over a range in temperature for Nimonic 90 and Nimonic 108 respectively, Figures 13 and 14 illustrate creep curves for each material, obtained

over a range of stresses at constant temperature. These experimental curves show that compressive creep damage is closely similar to tensile damage and that tertiary creep does occur in compression. Minimum creep rates are plotted against applied stress in Figures 15 and 16. For Nimonic 90 the stress exponent n, in the equation $\dot{\varepsilon}_s = A\sigma^n$ is 8 at higher stresses and 4 at lower stresses. For Nimonic 108 a value of 8 suffices for all conditions.

4.1.2 Tensile and rectangular creep of Nimonic 90

In Figure 17 it can be seen that tensile creep times to rupture are about half as long as times to rupture of cyclic creep tests having an equivalent upper stress level. The cyclic results are therefore presented also as times at peak stresses.

The effects of cycle hold times on cumulative damage was investigated and the results are presented in Figure 18, both as times to failure and number of cycles to failure. In this series, zero hold time tests (low cycle fatigue), 6 second, 1.8 ks and 14.4 ks hold times were also investigated. In Figure 19 applied stress is plotted against minimum creep rate, both for static and cyclic tests. Most of the cyclic test data was obtained from tests with on and off-load times of 360 seconds, although additional data at hold times of 1.8 ks and 14.4 ks are included. Similar stress exponents to those illustrated previously in Figure 15 are obtained.

In certain tests, fast chart speeds were used for recording strain, allowing initial strain rate, $\dot{\varepsilon}_i$, to be measured, and these results are shown in Figure 20. It can be seen that the stress exponent n in the equation $\dot{\varepsilon}_i = A\sigma^n$ is 4 irrespective of stress level. Over this period rectangular tests are identical to tensile creep.

The similarity between tensile and rectangular creep results is again evident from the measured times to the onset of tertiary deformation and to fracture, see Figure 21. In the rectangular creep tests the times are the sum of the on-load periods. It is apparent from Figure 22 that both the time to tertiary and the time to rupture are related to minimum creep rates by expressions of the form

$$\dot{\varepsilon}_s \times \text{time} = \text{a constant}$$

where the constant is dependent on the material and has the dimensions of strain. The full similarity between the cyclic tests and the monotonic tests is illustrated in Figure 23 where the cumulative strains are plotted against the times at peak stress.

In the cyclic tests anelastic recoveries were measured during each reduced load period and compared with creep strain accumulation during each corresponding on-load period. The differences between on-load strain accumulation and corresponding off-load anelastic recovery are shown for a typical set of results in Figure 24 for an on-load stress of 170 MN/m^2, a temperature of 1123K and a hold time of 360 seconds. The secondary creep stage occurs between about 100 and 700 cycles. These results are used in Figure 25 where the creep strain per cycle and anelastic recovery per cycle are each plotted against the cumulative time at peak stress. As might be expected, the on-load creep strain per cycle is initially high, quickly falls to a minimum constant value during the secondary creep deformation stage and then progressively increases until failure occurs. In contrast to this anelastic recovery during off-load periods is initially low but rises to an approximately constant value before eventually increasing to failure. During the initial stages of the test the on-load strain was about five times greater than the anelastic recovery. In the secondary creep region the ratio approached unity and at fracture the ratio had extended to about 8/1. The anelastic recoveries over the whole stress and temperature range are summarised in Figure 26. Each strain value refers to the total anelastic strain at the end of a 360 second hold period and is plotted against the cumulative on-load time. It can be seen that for each rectangular creep test there is a time t_I after which the anelastic recovery per cycle progressively increases. From Figure 27 the time t_I can be seen to lie between the times to tertiary and rupture. For the 360 second hold time tests the 'steady-state' anelastic strain per cycle is plotted against applied stress for temperatures of 1073, 1123 and 1173K in Figure 28. At 1123K data from tests with hold times of 1.8 ks and 14.4 ks are included. Although the amounts of anelastic recovery at any stress level vary with hold time, the intercept, σ', is independent of hold time and at 1123K has a value of 68 MN/m^2. Since the cyclic tests were conducted with a minimum stress level of 23 MN/m^2, if the data were plotted in terms of stress decrease the modified intercept would be

45 MN/m^2. Some additional stress reduction experiments were conducted during the secondary creep stage of 'static' creep tests. These involved both full stress removals, for example from 150 MN/m^2 to zero and also partial stress removals, for example from 300 to 150 Mn/m^2. The results are presented in Figure 29. Again a linear relationship is obtained, however the intercept on the stress axis is now 45 MN/m^2 independent of hold time.

4.1.3 Frequency effects in triangular tensile creep of Nimonic 90

In Figure 30 the monotonic creep rupture results are compared with triangular tensile creep tests conducted over a range of frequencies from 0.1 CPM to 10^3 CPM. It can be seen that increasing the frequency of cycling not only increases the number of cycles to failure but also the time to failure.

4.1.4 Rectangular push-pull creep of Nimonic 90

The effect of rectangular push-pull cycling on strain accumulation is given in Figure 31. The strain value plotted is the net strain at the end of the push-pull cycle. It can be seen that the rectangular push-pull lives are equal to those of the equivalent static creep tests, however strain accumulation occurs in a different manner.

4.2 Static and cyclic creep properties of conventionally cast, directionally solidified and single crystals of Mar M246

4.2.1 Tensile and compressive creep

(a) Tensile creep

The creep rupture times for the three forms of the alloy are shown in Figure 32. It appears that there is little difference between the directionally solidified and single crystal results, both of which have lives two to three times longer than conventionally cast material. To help quantify the relative strength of casting alloys, creep rupture data for a typical wrought alloy, Nimonic 108, is given for comparison. Figure 33 shows that the rates of strain accumulation of directionally solidified and single crystal forms are similar throughout the whole of their lives, rupture ductilities are 15 to 25 per cent. The directionally solidified and conventionally cast materials are compared in Figure 34 where it can be seen that the rupture strains of the latter materials are typically 3 to 6 per cent. In contrast minimum creep rate is unaffected by alloy form as is illustrated in Figure 35.

For each material a good correlation was obtained between minimum creep rates and tensile times to fracture as can be seen in Figure 36. The conventionally cast material exhibits less scatter in this relationship than do single crystal and directionally solidified materials.

The effect of specimen size on tensile creep properties was investigated for both conventionally cast and single crystal materials using a common gauge length of 25 mm and a range of diameters from 2.2 to 6.4 mm. In Figure 37 it can be seen that in the single crystal tests, specimen size had no effect whereas for the conventionally cast materials the smaller size produced a reduction in life of about one-third.

(b) Compressive creep

There is little difference in rates of deformation for the three cast forms when tested under compressive loading. This is illustrated in Figure 38 for conventionally cast and directionally solidified materials at 1123K. It is emphasised in Figure 39 where minimum creep rates for the three forms of material are compared. Also included in this figure are the tensile creep rates presented earlier. It can be seen that the minimum creep rates in compression are about half those in tension although the former results show slightly more scatter. Differences in strain accumulation under tension and compression occur throughout the whole of the creep life as can be seen in Figure 40 for conventionally cast material and Figure 41 for directionally solidified material.

4.2.2 Tensile and rectangular creep

The basic trends in the results are similar to those found for the wrought alloy Nimonic 90. Under cyclic conditions with hold times of 360 seconds, creep rates, based on time at peak stress, were found to be identical to those under tensile conditions, as were the times to fracture. The latter case is illustrated for directionally solidified material in Figure 42.

Anelastic recovery during the off-load period (360 seconds) was found to show similar trends to those for Nimonic 90, namely that initially it was small but built up rapidly to an approximately steady value, eventually increasing in magnitude prior to failure. The steady-state level is stress dependent as can be seen in Figure 43. However from the rupture results, although most of the time dependent

strain incurred during a hold time at maximum stress is recovered during the subsequent off-load period, this has little effect on net accumulation of damage.

4.2.3 Triangular tensile creep

These tests were conducted at frequencies of 3 c/h and 300 c/h. The times to rupture of the directionally solidified and the conventionally cast materials are given in Figure 44, static creep data being included for comparison. In both cases the higher frequency tests resulted in shorter lives to failure. Since fracture occurred close to the ridges in these shorter life tests, unridged directionally solidified specimens were also tested. Due to lack of material only ridged specimens were tested in the conventionally cast form.

4.2.4 Triangular push-pull and rectangular push-pull creep

The push-pull tests were conducted on a different cast of Mar M246 and it was necessary to conduct tensile creep tests to evaluate the basic creep properties. The triangular push-pull tests consisted of peak tensile and compressive stresses being applied at a constant frequency of 3 c/h. The rectangular push-pull tests also consisted of equal tensile and compressive stress levels but with a 360 second hold at maximum and minimum stresses. The rupture data for both the triangular and rectangular cycles are given in Figure 45. It can be seen that the rectangular push-pull lives are close to those of the equivalent static creep tests and the triangular push-pull lives are about four times as long as the static test. Strain accumulation under rectangular push-pull cycling is illustrated in Figure 46.

4.3 Stress changes on subsequent creep of Nimonic 90 and Mar M246

The major proportion of the testing was conducted on Nimonic 90 and the main findings confirmed on Mar M246.

4.3.1 Instantaneous stress reductions

The effects of large stress changes have been illustrated earlier under rectangular creep results. However, in an attempt to understand the mechanisms controlling deformation, additional stress reduction tests were carried out. The results show that for instantaneous stress reductions of up to 25 per cent of the original applied stress, periods of zero creep rate occur immediately after the

stress reductions have been made. The length of the incubation periods depends on

(i) the original applied stress and temperature

(ii) the stage in the creep curve at which the reduction is carried out

(iii) the magnitude of the stress reduction employed.

With larger stress reductions incubation periods increase in magnitude until at a critical stress level, σ_c, a maximum incubation period was obtained. For stress reductions to values of applied stress slightly lower than σ_c, immediate negative creep extension or anelastic recovery occurs even although a large proportion of the original applied stress still remains on the specimen. The general change in deformation behaviour with increasing stress decrement has been illustrated in Figure 7. For Nimonic 90, over a wide range of stresses and temperatures, values of σ_c were determined during the secondary creep stage and, as shown in Figure 47a, it is apparent that at low stresses the value of σ_c is proportional to the applied stress. A similar relationship is obtained for Mar M246 at 1173K as illustrated in Figure 47b. Deviation from this relationship occurs at high stresses, the particular values depending on the test temperature. The trends in the σ_c measurements are in general agreement with previous findings on other materials, see Section 2.2.4. However also plotted in this figure are the critical stress reductions $\Delta\sigma_c$ to cause anelastic recovery. It can be seen that for any temperature $\Delta\sigma_c$ is initially independent of stress although after a specific applied stress it increases progressively. This has not been reported previously. Variation in the critical stress throughout the creep life is illustrated in Figure 49.

For stress reductions to levels above and below σ_c, the creep rates on recommencement of forwards creep are compared with the minimum creep rates of static creep tests at equivalent stresses in Figure 48a for Nimonic 90 and Figure 48b for Mar M246.

4.3.2 Progressive stress reductions

In these tests the applied stress was reduced progressively in increments of 10 per cent. After each reduction an incubation period was experienced and the next stress reduction was not effected until positive creep had recommenced. The process was continued until a stress level was reached at which no further creep occurred. The friction stress, σ_c, was determined by plotting the accumulated stress reduction (the sum of $\Delta\sigma$) against the total incubation time (the sum of Δt) as illustrated in Figure 50. All tests were allowed to creep to the steady

state prior to the commencement of stress reductions. Both for Nimonic 90, as shown in Figure 51a and for Mar M246 as shown in Figure 51b, it can be seen that for low values of applied stress the friction stress is proportional to the applied stress but eventually achieves a maximum value. Following previous authors as discussed in Section 2.2.4, σ_0 was subtracted from the applied stress and the resultant stress term plotted against minimum creep rate as illustrated for Nimonic 90 in Figure 52a and for Mar M246 in Figure 52b. Although the original stress-creep rate graphs for Nimonic 90 show changes in stress exponent for each temperature, as illustrated in Figure 15, the entire stress range can now be described by a single expression of the form

$$\dot{\varepsilon}_s = A (\sigma - \sigma_0)^4$$

A similar expression was found to apply to Mar M246, although for the same temperatures the value of the constant A different from that for Nimonic 90.

4.3.3 Stress changes during anelastic recovery

These tests were limited to Nimonic 90. It was found that all stress increases made during periods of anelastic recovery resulted in subsequent periods of zero creep rate. For large increments of stress, or for small increments made after much of the anelastic recovery had been exhibited, the alloy did not recommence anelastic recovery within the measured period (600 seconds). However, for other conditions incubation periods eventually gave way to further negative deformation. The incubation time increased with the magnitude of the stress change and with the length of the anelastic recovery period prior to the stress change being effected. These points are shown in Figure 53 which illustrates a typical chart trace.

4.4 Metallographic examination

4.4.1 Metallographic observations on Nimonic 90 and Nimonic 108

In Nimonic 90, neither tensile nor compressive damage produced any significant changes in microstructure at strains up to 1 per cent. Surface oxidation caused some grain boundary zones to be depleted of chromium and hence of γ' precipitate. This resulted in intergranular surface cracking which eventually contributed to tensile failure but did not grow under compression, except at very high strains, greater than about 50 per cent, where cracks develop parallel to the direction of

the applied stress. Steroscan micrographs of tensile fracture surfaces are illustrated in Figure 54.

Wedge and cavity type intergranular cracks were evident in ruptured tensile specimens. Wedge cracks, Figure 55, tended to be prevalent in higher stress, shorter life specimens and cavity cracks, Figures 56 and 57, in lower stress, longer life specimens. Both longitudinal and transverse sections were examined. Cracking was similar to that found in earlier work by McLean[113].

In Nimonic 108 some massive grain boundary γ' was present at the commencement of testing. Again wedge and cavity cracking occurred although to a lesser extent than for Nimonic 90. For compressive strains up to 30 per cent no internal cracks were observed but growth of massive grain boundary γ' occurred.

In both materials the principal strengthening constituent is the γ' (Ni_3 Al, Ti) precipitate. In Nimonic 90 this was typically 0.02μm in size when tests commenced at 1173K. Progressive aging of the γ' precipitate occurs throughout the life of the test. However, coarsening of the precipitate does not appear to be strongly dependent on strain and, for example, the precipitate size was 0.02μm in a specimen taken to 150 per cent compressive strain in 60 hours at 1173K, and 0.05μm in a specimen taken to 15 per cent strain in 315 hours. This is in good agreement with the theoretical prediction[118] that growth rates are proportional to the cube root of time at temperature.

Under the action of strain and temperature, regions around grain boundaries accommodate severe distortion and in the case of Nimonic 90, denuded zones develop as γ' precipitates are taken into solution. Although this was observed to occur in tension, it occurs to a much greater extent in compression. Electron probe micro analysis was carried out to determine the distribution of elements across these zones. The results given in Table III show that the major change is in the distribution of titanium. Initially the growth of denuded regions tends to occur at areas of high strain concentration such as triple points but more general growth in zones adjacent to the grain boundaries follows. At 1173K after 10 per cent strain in 400 hours denuded zones up to 12μm were observed. In a plain cylindrical specimen taken to 28 per cent compressive strain in 27 hours the material close to the plattens incurred considerably less deformation than the remainder and there was

little change in the amount of denudation, as can be seen in Figure 58a. On the other hand highly deformed material at the specimen centre exhibited marked denudation, as can be seen in Figures 58b and 58c. It is difficult to represent the growth rates at different times and at various regions in the grain boundaries. However for Nimonic 90 at 1173K averaged measurements of zone widths, presented in Figure 59a, show that at short times and high strains, tertiary creep in compression is accompanied by growth of denuded zones. At longer times greater amounts of denudation were observed to occur under tension, probably due to the influence of cracks on recovery processes. In Figure 59b the data are correlated with a simple multiple of strain and time, indicating that increased compressive denudation is accumulated during the longer times to reach the same strain as in tension.

Under high compressive strains it was found that in Nimonic 108 the massive grain boundary γ' coarsened markedly, although insufficient tests were carried out for a quantified analysis to be made.

In comparing rectangular creep and tensile creep results, the former tests have been at elevated temperatures for much greater periods than the latter and might be expected to show greater oxide penetration and surface cracking, together with more severe over-aging of the γ' precipitate. In Table IV surface crack distribution, surface crack length and γ' precipitate size are compared for both types of testing. It can be seen that under rectangular tension the amount of surface cracking is slightly greater than for tensile creep.

Under triangular creep of Nimonic 90, at low cycle frequencies fractures are identical to those observed in tensile creep tests. At higher frequencies transgranular fatigue initiation is observed. This is most obvious in the high stress tests as shown in Figure 60a but lower stress tests also showed definite evidence of fatigue damage. Figure 60b illustrates oxidised striation markings. In all cases fatigue damage gave way to creep damage as illustrated in Figure 60c.

4.4.2 Metallographic observations on Mar M246

Little evidence of internal cracking was observed in ruptured tensile specimens of the three cast forms. In conventionally cast material some cracking did occur, but this tended to be concentrated

close to the fracture surface and to be associated with large grain boundary carbides. The absence of transverse boundaries in the directionally solidified and single crystal materials tends to remove this major source for the development of conventional creep cracks and under the current test conditions, which were selected to give relatively short durations, little cracking was observed. However in a series of longer life tests conducted at the higher temperature more general internal cracking did occur. In Figures 61b and c it can be seen that much larger cracks are incurred in both the directionally solidified and single crystal materials as compared to the conventionally cast material illustrated in Figure 61a. In all cases surface cracking, either intergranular or interdendritic, contributed to final failure.

Examination of high strain compression specimens revealed strain induced coarsening of the γ' precipitate had occurred in regions of severe deformation as shown in Figure 62.

As discussed earlier, the triangular creep results presented in Figure 44 show, both for conventionally cast and directionally solidified materials, that the higher frequencies resulted in somewhat shorter lives to failure than predicted. However, rupture occurred close to the extensometer ridges and examination revealed fatigue damage. For the directionally solidified material, unridged specimens were then tested at the higher frequency and found to give lives close to those obtained at the lower frequency. These tests also failed by fatigue as illustrated in Figure 63a which shows several initiation sites. Lower stress tests showed larger fatigue regions, Figure 63b.

The push-pull triangular tests on the conventionally cast material also showed several initiation sites, as can be seen in Figure 64, but final rupture appeared to be creep controlled.

5.0 Analysis of results

The Graham and Walles analysis is used to quantify tensile and compressive creep. Applying the concepts of strain hardening theory, the analysis is developed to assess damage incurred under cyclic loading conditions. It is then extended such that these cyclic cases can be predicted from tensile creep data.

Since the mathematics of the analysis is independent of material, any equations evolved must apply jointly to Nimonic 90 and to Mar M246.

However it is pointed out that the values of the constants in the equations are dependent on the material.

5.1 Analysis of results based on the Graham and Walles equations of creep

The Graham and Walles creep equation

$$\varepsilon = \Sigma\, c\sigma^{\beta}\, t^{\kappa}\, (T' - T)^{-20\kappa} \qquad \ldots.(101a)$$

has been used as a basis for analysing the results obtained from the various parts of this research programme.

For most engineering materials κ has the values of $\frac{1}{3}$, 1 and 3 progressively through the creep curve and so, for a given stress and temperature, the equation can be presented as

$$\varepsilon = at^{\frac{1}{3}} + bt + ct^{3} \qquad \ldots.(101b)$$

From Section 2 however it would appear that two main criticisms have been levelled against this form of analysis

(i) the reliance on graphical methods of analysis and regeneration

and (ii) the prediction of infinite creep rates immediately on loading.

These two limitations have been studied and overcome in the present research programme. Considering them in order:-

(i) Graphical analysis

The necessity of using graphical methods of analysis is created partly from the use of the series 2^{-n} for values of $\frac{\kappa}{\beta}$ and partly from the necessity of employing bi-modal terms. For example the full expression for $at^{\frac{1}{3}}$ in the equation above is

$$\left[c_1\sigma^{\beta_1}\, (T_1' - T)^{-\frac{20}{3}} + c_2\sigma^{\beta_2}\, (T_2' - T)^{-\frac{20}{3}} \right] t^{\frac{1}{3}} \qquad \ldots.(102)$$

If an averaged linear value of slope $\left(\frac{2\kappa}{\beta_1 + \beta_2}\right)$ can be employed in these bi-modal regions, this would be a known constant reducing the unknown constants (c_1, c_2, T_1' and T_2') from four to two (c and T') and allowing one component term to be used.

In a preliminary investigation to assess the validity of the Graham and Walles analysis to the present results, the equations were re-arranged in an attempt to apply a computer analysis to the Nimonic 90 rectangular creep tests in the range 1073 to 1173K.

Initially a least squares multiple regression method was employed using the equation

$$\varepsilon = at^{\frac{1}{3}} + bt + ct^{3} \qquad \ldots.(103)$$

This was successful in producing accurate fits to experimental data but had two drawbacks, (i) negative values for a, b and c could occur making further analysis impossible and (ii) the errors were the same order for each term of the equation, this meaning that at low initial strains the errors were a greater proportion of the accumulated strain. Although techniques could be employed to remove these limitations it was felt that a method more akin to previous graphical solutions would allow better assessment of the accuracy of analysis. Consequently the strain data were initially fitted with a $t^{\frac{1}{3}}$ expression, the remaining powers t' and t^{3} being used progressively as required to enable accurate fit to the data. The programme to achieve this is given in Appendix II.

For all terms the 0.1 per cent strain-time intercepts were plotted against stress, as discussed in Appendix I. From these isothermal curves the $\frac{\kappa}{\beta}$ values were obtained graphically and the various T' and c constants evaluated from $t^{\frac{1}{20}}$ against T cross plots.

The present results show a (dt^{9}) term which could be added to Equation (103) and it seems reasonable as a corollary that $\kappa = 9$ also controls rupture, assuming constant rupture strain of 15 per cent. The advantages of this are that rupture is uniquely specified and has the lowest scatter factor.

Figure 65 illustrates values of the 0.1 per cent strain intercepts for the various terms in Equation (101) for 1073K data. In Figure 65a log σ - log $t_{\frac{1}{3}}$ cross-plots have a shallow curve asymptotic to $\frac{\kappa}{\beta} = \frac{1}{16}$ at high stresses and short durations and $\frac{\kappa}{\beta} = \frac{1}{4}$ at low stresses and longer durations. However the method has been adopted of limiting the $t_{\frac{1}{3}}$ expression to a single component rather than a summation of terms. In this case therefore the value of $\frac{\kappa}{\beta} = \frac{1}{8}$ was chosen. This is illustrated in Figure 65.

For t_{1} terms (Figure 65) transition is found to occur between $\frac{\kappa}{\beta} = \frac{1}{8}$ and $\frac{\kappa}{\beta} = \frac{1}{4}$ and again to obtain single components an average value of $\frac{\kappa}{\beta} = \frac{3}{16}$ was chosen.

For t_3 terms although $\frac{K}{\beta}$ again changes from $\frac{1}{3}$ to $\frac{1}{4}$ the large time exponent means effectively that for any stress a single term dominates.

Further modifications were introduced by applying stress exponent β and constant c corrections so as to obtain a single master curve for all terms such that

$$\sigma = \left[\left(\frac{\varepsilon}{c}\right)^{\frac{1}{K}} \frac{(T' - 1)}{t}\right]^{\frac{K}{\beta}} \qquad \ldots.(104)$$

A computer program, given in Appendix III, was written to test the modifications by analysing creep curves to produce the various component terms. To illustrate the accuracy of fit the individual terms are plotted separately in Figures 66a-f and combined in Figure 66g. These figures give linear plots of the data. The use of averaged constants together with combined time-temperature functions is termed stage I extension. It can be seen from a statistical analysis of scatter, as illustrated by standard deviations in log time for the various terms, that the combined time-temperature function has not increased the degree of scatter over conventional analysis (see Table V). In the t_3 and t_1 component curves illustrated in Figures 66a and 66b, divergences from zero intercept or from slopes of unity are due to the approximations made in the modified analysis by the use of monotonic averaged terms. This would affect only creep curves regenerated from the single curve in Figure 66g since a best fit through the data of the individual terms in Figures 66a and b would compensate for errors made in calculating 'averaged' monotonic values. (It is pointed out that all previous graphical solutions in effect employed this error compensating technique.) The computer program used to regenerate the creep curves from the data is given in Appendix IV. The predicted creep curves are shown in Figure 67 where they are compared with the original creep data. They are typical of the accuracy of regenerating any creep curve in the temperature range 1073 to 1173K in which rupture occurs within 250 hours.

The master curve analysis, Figure 66g, can also be used to illustrate scatter conditions for all terms and it can be seen, for example, that poorest conditions at 85 MN/m^2 and 1173K can be predicted

from average conditions at 108 MN/m^2 and 1173K. This method allows minimum properties to be predicted from a large number of data points.

(ii) Initial creep rates

The other main criticism levelled in general against all power law equations for creep and against the Graham and Walles equation in particular is that they predict infinite creep rates at the commencement of a creep test. However Tilly[114] has illustrated that time should commence from the instant of first application of any part of the load. He derived an equation relating the sum of the transient damage during loading and the static damage immediately after full load is applied, to an instantaneously loaded test commencing at some equivalent time t_*, the final equation being

$$\varepsilon = \Sigma \left[c\sigma^{\beta} \, t^{\kappa+\beta} \right]_{0}^{t_*} + \Sigma \left[c\sigma^{\beta} \, t^{\kappa} \right]_{t_*}^{t_*+t} \qquad \ldots.(105)$$

where t_* is not the loading time, τ, but the time required for an instantaneously loaded test to acquire an amount of damage equivalent to that incurred during loading, and so

$$t_* = \left(1 + \frac{\beta}{\kappa}\right)^{-1} \tau \qquad \ldots.(106)$$

Using the full Graham and Walles form of this equation, including a temperature function, and differentiating it so as to obtain the initial creep rates on application of full load, the following expression is obtained

$$\frac{d\varepsilon}{dt} = \Sigma \, \kappa \, c\sigma^{\beta} \, t_*^{\kappa-1} \, (T' - T)^{-20\kappa} \qquad \ldots.(107)$$

since $\kappa = \frac{1}{3}$ dominates in this region the single term approximation can be used and so

$$\frac{d\varepsilon}{dt} = \frac{c\sigma^{\beta}\left(1 + \frac{\beta}{K}\right)^{\frac{2}{3}}}{3\tau^{\frac{2}{3}}\,(T' - T)^{-20K}} \qquad \ldots\ldots(108)$$

where τ is the loading time.

In certain of the tests, fast chart speeds were employed for recording strain thus allowing instantaneous creep rates to be measured. Using the appropriate values for the various constants in this equation, namely that $c = 3.2 \times 10^{10}$, $T' = 1208^{\circ}C$ and $\beta = \frac{8}{3}$, instantaneous creep rates can be calculated. Measured and calculated values are compared in Figure 68.

It has been shown that the two main criticisms of the Graham and Walles analysis have been overcome and it is proposed therefore to use this analysis as the basis for empirical equations to be derived to predict the various cyclic test results from monotonic creep data.

5.2 Tensile and compressive creep

(i) Nimonic 90 and Nimonic 108

In the present investigation the analysis developed for tensile creep has been extended to describe compressive deformation. The derived equations enable a comprehensive comparison of tensile and compressive creep since it is possible to study systematic differences for each stage of life, and to regenerate average strain-time curves for a series of stresses and temperatures.

The 0.1 per cent strain intercepts made by the individual components of Equation (103) were plotted against stress so as to allow the stress exponents (β in Equation (101a)) to be identified and hence to enable regenerated curves to be plotted against the original data. Stress-time cross-plots for Nimonic 90 and Nimonic 108 are given in Figures 69 and 70. Curves regenerated from these cross-plots are in effect averaged for the whole family of data and so failure of specific test results to fit the regenerated curve is indicative of material scatter. In practice very good correlation was obtained as evidenced by the regenerated curves shown in Figures 10 to 14.

Tertiary type deformation is found to occur under compressive creep. It is illustrated by the ct^3 component (Equation (101b)) of the curves and is shown in Figures 71 and 72 for Nimonic 90 and Nimonic 108 respectively.

From the stress-time cross-plots it is clear that experimental scatter is high for the $t_{\frac{1}{3}}$ terms but progressively reduces for the t_1 and t_3 terms. A statistical analysis of the degree of scatter confirms these trends and shows that standard deviation in log time cycles is invariant with temperature. The results given in Table V show also that there is no significant difference in scatter between tension and compression and that the t_3 terms have deviations closely similar to the figures for tensile rupture.

Examination of the stress-time cross-plot diagrams for the various terms in the Graham and Walles analysis (Figures 69 and 70) shows that the stress dependence of the rupture times, t_f, is similar to that for t_1. Since t_1 relates closely to the minimum creep rate this implies that the time to fracture, t_f, is related to the minimum creep rate. Such an equation has been proposed by Grant and Monkman[115] where

$$\dot{\varepsilon} \times t_f = \text{constant} \qquad \ldots.(109)$$

This equation is applicable to the present results as shown in Figure 22 for both monotonic and cyclic creep. It can be seen that at short endurances cyclic effects result in a slight strengthening relative to monotonic creep, and that exposure effects are the probable cause of a slight weakening when long endurance tests are being compared. A similar relationship between minimum creep rate and time to tertiary creep is also included in this figure. The form of relationship is identical to that for rupture.

The constant in Equation (109) has the dimensions of strain and in the results shown in Figure 22 it has a value of 0.62 per cent with one standard deviation of 0.22 per cent. The constant is independent of stress, temperature, static or cyclic loading and so would appear to be a possible damage criterion under conditions of variable stress or temperature histories. The basic equation predicting rupture would be

$$6 \times 10^{-2} = \sum \left(t_f \, \dot{\varepsilon}_s \right)_{\sigma, T} \qquad \ldots.(110)$$

where the remaining life at any constant set of conditions is

$$t_{(\sigma,T)} = \frac{6 \times 10^{-3} - \sum \left(t_f \, \dot{\varepsilon}_s \right)}{\dot{\varepsilon}_{min}} \qquad \ldots\ldots(111)$$

These equations should be generally applicable, the value of the constant varying for different materials. In order to reduce the constant to unity it can be seen from Equation (109) that

$$\dot{\varepsilon}_{s1} \, t_{f1} = \text{constant} = \dot{\varepsilon}_{s2} \, t_{f2}$$

$$\therefore \quad \dot{\varepsilon}_{s1} \, t_{f1} + \dot{\varepsilon}_{s2} \, t_{f2} = \text{const}$$

$$\therefore \quad \frac{\dot{\varepsilon}_{s1} \, t_{f1} + \dot{\varepsilon}_{s2} \, t_f}{\dot{\varepsilon}_s \, t_f} = 1$$

where $\dot{\varepsilon}_s \, t_f = \dot{\varepsilon}_{s1} \, t_{f1} = \dot{\varepsilon}_{s2} \, t_{f2} = \ldots$ etc

ie $$\frac{t_1}{t_{f1}} + \frac{t_2}{t_{f2}} = 1$$

Thus Robinson's life fraction rule[116] is a special case of Equation (110).

(ii) Mar M246

A typical set of stress-time cross-plots is given for the conventionally cast material in Figure 73 and the regenerated strain-time curves are compared with the experimental points in Figure 74.

The t_3 cross-plot shown in Figure 73 illustrates the delayed tertiary contribution to creep in compression relative to tension. Comparison of the tensile and compressive t_1 data with the corresponding minimum creep rate data indicates displacement of the compression results, with respect to the tensile results in the former case but not in the latter. To derive minimum creep rates from the present type of analysis the equation required is[111]

$$\dot{\varepsilon}_s = \sigma^{\beta_2} \left(c_3 + \frac{4}{3} \left(\frac{c_1^3 \, c_3}{3} \right)^{\frac{1}{4}} \right)$$

This contains a small contribution from the tertiary component and

predicts that minimum creep rates under tension should be slightly higher than under compression, however, the effect generally is small relative to experimental scatter. Insufficient results were available for the determination of meaningful scatter values.

5.3 Rectangular creep

1. Nimonic 90

It can be seen from Figure 67 that the Graham and Walles analysis and the convention of time at maximum stress provide a suitable method for analysing the rectangular creep tests. Standard deviations under rectangular tension are almost identical to monotonic creep, as shown in Table V.

Although time at peak stress is an obvious damage assumption, for more complex loading cycles a suitable convention becomes more obscure and so it was considered that the various hypotheses for analysing damage under variable stress should be examined relative to this simple case. When stress changes are made the basic tensile creep equations can be modified using

(1) the assumption of a mechanical equation of state in which strain rate is considered to be a function of current stress, temperature and condition of the material

or (2) the assumption of a superposition integral in which the strain rate is considered to be a function of the total previous history.

(i) Application of mechanical equation of state

This approach can be classified into (a) strain hardening, (b) time hardening and (c) life fraction assumptions where the further distinction is made in defining the condition of the material.

Applying these various assumptions to the Graham and Walles expression

(a) Strain hardening

In this case the condition of the material is considered to be totally defined by the current value of strain

thus $$\left(\frac{d\varepsilon}{dt}\right)_T = c\,\kappa\,\varepsilon^{1-\frac{1}{K}}\left(\cos\beta\right)^{\frac{1}{K}} \qquad \ldots.(112)$$

for each term in Equation (101a). Integration and cycle by cycle analysis of strain accumulation gives

$$\Delta\varepsilon_i = \Sigma\, c\sigma^{\beta} \left[(n\lambda)^{\kappa} - \left\{ (n-1)\,\lambda \right\}^{\kappa} \right]$$

where $\Delta\varepsilon_i$ is the creep strain during ith load cycle and $n\lambda$ is the time at maximum stress.

Summing this for the whole creep range gives

$$\Sigma\Delta\varepsilon_i = \varepsilon_r = \Sigma\Sigma\, c\sigma^{\beta}\, (n\lambda)^{\kappa} \qquad \ldots.(113)$$

$$\therefore \qquad \varepsilon_r = \Sigma\, c\sigma^{\beta} \left(t_r' \right)^{\kappa} \qquad \ldots.(114)$$

where ε_r and t_r' are respectively the strain accumulation and time at maximum stress in a rectangular creep test (t and ε being the time and strain of a tensile creep test). Equating this with Equation (101a) for monotonic creep, it follows that

$$t \equiv t_r'$$

but the total time of test

$$t_r = (2n\lambda) = 2\, t_r' = 2t$$

In terms of a static creep test it follows that

$$\varepsilon_r = 2^{-\kappa}\, \varepsilon \text{ and } t_r = 2t$$

(b) Time hardening

The condition for the material is considered to be totally defined by the total time of the test and thus

$$\left(\frac{d\varepsilon}{dt} \right)_T = \Sigma\, c\kappa\sigma^{\beta}\, t^{\kappa-1} \qquad \ldots.(115)$$

for each term of Equation (101a). Integration and cycle by cycle analysis of strain accumulation gives

$$\Delta\varepsilon_i = c\sigma^{\beta}\left[\left\{(N-1)\lambda\right\}^{\kappa} - \left\{(N-2)\lambda\right\}^{\kappa}\right]$$

where $\Delta\varepsilon_i$ is defined as above and N is the number of $\frac{1}{2}$ cycles (= 2n).

Again, summing $\Delta\varepsilon_i$ over the whole creep range gives

$$\Sigma\Delta\varepsilon_i = \varepsilon_r = \Sigma\Sigma\, c\sigma^{\beta}\left[\left\{(N-1)\lambda\right\}^{\kappa} - \left\{(N-2)\lambda\right\}^{\kappa} + \left\{(N-3)\lambda\right\}^{\kappa} - \left\{(N-4)\lambda\right\}^{\kappa} \ldots\right] \quad \ldots.(116)$$

A method of solving this series summation is given in Appendix V, the result being

$$\varepsilon_r = \Sigma\, 2^{-1}\, c\sigma^{\beta}\, (N\lambda)^{\kappa} = \Sigma\, 2^{-1}\, c\sigma^{\beta}\, t_r^{\kappa} \quad \ldots.(117)$$

Equating this with Equation (101a) for monotonic creep it follows that

$$t_r = 2^{\frac{1}{\kappa}}\, t \quad \ldots.(118)$$

for rupture $\kappa = 9$ and therefore

$$\varepsilon_r = 2^{-1}\, \varepsilon_e$$

and

$$t_r \approx t \quad \ldots.(119)$$

(c) Life fraction

This is a modification of time hardening in which the time function is normalised and hence creep rate is considered to be a

a function of current stress and normalised time $\left(\frac{t}{t_f}\right)$, where t_f is the time to fracture. Thus for rupture the prediction becomes

$$1 = \left(\frac{n\lambda}{t_f}\right)_{\sigma max} + \left(\frac{n\lambda}{t_f}\right)_{\sigma min} \qquad \ldots.(120)$$

which for near zero minimum stress simplifies to

$$\left(t_f\right)_{\sigma max} = n\lambda \qquad \ldots.(121)$$

and equating this with Equation (101a)

$$t_r = 2t \qquad \ldots.(122)$$

Predictions of strain and time from life fraction assumptions are identical to strain hardening predictions.

(ii) Superposition hypothesis

In this case strain is considered to be dependent on the sum of the continuing contributions made from each stress level employed, stress changes being made by the addition of further tensile or compressive stresses at the specific time.

$$\varepsilon = \int_0^t \phi\,(t - \gamma)\,\frac{dF(\sigma)}{d\tau}\,d\tau \qquad \ldots.(123)$$

Cycle to cycle analysis of strain accumulation gives

$$\Delta\varepsilon_i = \Sigma\, c\sigma^{\beta}\left[(N\lambda)^K - \left\{(N-1)\lambda\right\}^K + \left\{(N-2)\lambda\right\}^K \ldots\right] -$$

$$\Sigma\, c\sigma^{\beta}\left[\left\{(N-1)\lambda\right\}^K - \left\{(N-2)\lambda\right\}^K + \left\{(N-3)\lambda\right\}^K \ldots\right]$$

which gives

$$\Sigma\Delta\varepsilon \quad = \quad \varepsilon \quad = \quad \Sigma\Sigma \; c\sigma^{\beta} \left[(N\lambda)^{K} - \left\{(N-1)\lambda\right\}^{K} + \left\{(N-2)\lambda\right\}^{K} \ldots \right] \qquad \ldots\ldots(124)$$

This equation can be made equivalent to Equation (116) and hence it follows that strain and rupture predictions are identical to those produced from a time hardening analysis.

The initial assumption of time at maximum stress, being the most relevant time for strain analysis, is in agreement with strain hardening and life fraction predictions.

(iii) Analysis of anelastic recovery during off-load periods

In order to determine an expression describing anelastic recovery during off-load periods, a set of results are plotted logarithmically against time in Figure 75a. Although exponential or logarithmic expressions could be used to fit anelastic data as they can for primary creep, for recovery times greater than 30 seconds an adequate expression can be obtained from a $t^{\frac{1}{3}}$ power function. As this is the type of expression used in the analysis of creep strain in the forwards direction, it is considered more consistent to use it in the backwards direction. The initial discrepancy is due to the fact that some anelastic recovery must occur during unloading and this should manifest itself in an ε_o correction. Thus:

$$\Delta\varepsilon_n' \quad = \quad \varepsilon_o' + at^{\frac{1}{3}} \qquad \ldots\ldots(125)$$

This would appear to be a suitable expression for describing the whole of the anelastic recovery obtained during an off-load period. Values of ε_o' should be able to be determined from a quantitative assessment of the anelastic recovery during unloading. By analogy with strain accumulation during loading, it follows that the full Graham and Walles form of Equation (125), including anelastic strain recovered during unloading should be

$$\Delta\varepsilon = \left(\frac{\kappa}{\kappa + \beta}\right)^{\kappa} c \left[\Delta\sigma^{\beta}\ t^{\kappa\ \beta}\right]_{0}^{\tau} + c\ \Delta\sigma^{\beta} \left[t^{\kappa}\right]_{\tau}^{\tau+t} \qquad \ldots.(126)$$

where $\Delta\sigma$ is the stress reduction incurred in time τ. From the first term in the right hand side of Equation (126) it follows that the amount of anelastic recovery incurred during unloading is $\left(\frac{\kappa}{\kappa + \beta}\right)$ of the full anelastic strain recovered during the same period for a test in which the stress is instantaneously removed. This gives a value of about 10 per cent of the full anelastic recovery for $\frac{\kappa}{\beta} = \frac{1}{8}$ and about 20 per cent of the full anelastic recovery for $\frac{\kappa}{\beta} = \frac{1}{4}$. When these values are added as ε_o' it is found that a much better correlation to a $t^{\frac{1}{3}}$ power function is obtained as is shown in Figure 75b. Since anelastic recovery is an exhaustion process the above equations eventually break down as is obvious by consideration of the recovery as $t \to \infty$.

2. Mar M246

It was found that for Mar M246 results the convention of time at peak stress could also be used to quantify strain accumulation and rupture characteristics. For the simple stress cycle currently employed, this is in effect a statement validating the use of the strain hardening concept. Considering the correlation between minimum creep rates and time to fracture shown in Figure 36 the constant in Equation (110) is 1.92×10^{-2} for conventionally cast material and 4.4×10^{-2} for directionally solidified and single crystal materials.

5.4 Triangular tensile creep

(i) Nimonic 90

Recently Tilly[117] has applied strain hardening theory in combination with the Graham and Walles analysis to obtain an expression for the accumulated strain ε_f under repeated tensile loading such that

$$\varepsilon_f = \Sigma\ c\sigma^{\beta}\ t_*^{\kappa} \qquad \ldots.(127)$$

where $$t_* = \frac{2n\tau}{\left(1 + \frac{\beta}{\kappa}\right)}$$

and is the equivalent time of a monotonic creep test at the peak stress σ. This expression can be re-arranged and compared with the basic creep equation such that the time to any specific strain $t_{t\varepsilon}$ can be compared with the time of a monotonic creep test $t_{c\varepsilon}$ through the expression

$$t_{t\varepsilon} = \left(1 + \frac{\beta}{\kappa}\right) t_{c\varepsilon} \qquad \ldots.(128)$$

Both Equations (127) and (128) were found to satisfy accurately the low cycle fatigue results obtained in this investigation, as can be seen by a comparison of experimental and predicted values given in Figure 18. However the equations do not contain a frequency term and so for higher frequencies, as can be seen from Figure 30, these give pessimistic predictions.

Examination of Tilly's analysis shows that it assumes damage is occurring throughout the whole of the loading and unloading phases. This can only be the case if full recovery can occur and therefore the equation predicts the maximum damage criterion, ie one limiting condition. The evidence from internal stress measurements presented in Section 4.3 leads to the assumption that as frequency increases, a stage is eventually reached where damage is incurred only during part of the loading cycle. Leaving the proof of this till later but accepting its validity for purposes of analysis, it follows that for the first damage cycle

$$\Delta\varepsilon_1 = \Sigma \left\{ \left(\frac{\kappa}{\kappa + \beta}\right)^{\kappa} c \left[\sigma^{\beta} t^{\kappa+\beta}\right]_0^{\tau} - \left(\frac{\kappa}{\kappa + \beta}\right)^{\kappa} c \left[\sigma^{\beta} t^{\kappa+\beta}\right]_0^{\tau-\psi} \right\}$$

where ψ is the damage part of the cycle

$$= \Sigma \left(\frac{\kappa}{\kappa + \beta}\right)^{\kappa} c\sigma^{\beta} \tau^{\kappa} \psi \left(\frac{\beta + \kappa}{\tau}\right) \qquad \ldots.(129)$$

Therefore the equivalent time at maximum stress, t_*, is given by

$$t_* = \left(\frac{\kappa}{\kappa + \beta}\right) \tau \left[\frac{\psi (\beta + \kappa)}{\tau}\right]^{\frac{1}{\kappa}}$$

and hence $$\Delta\varepsilon_n = \Sigma\, c\sigma^{\beta} \left[t^{\kappa}\right]_{(n-1)t_*}^{nt_*}$$

$$\therefore \quad \Sigma\Delta\varepsilon_n = \varepsilon_f = \Sigma\, c\sigma^{\beta} (nt_*)^{\kappa} \qquad \ldots.(130)$$

But total time to fracture,

$$t_f = 2n\tau$$

$$= 2\, t_c \left(1 + \frac{\beta}{\kappa}\right) \left[\frac{\psi}{\tau}(\beta+\kappa)\right]^{-\frac{1}{\kappa}}$$

$$= 2\, t_c \left(1 + \frac{\beta}{\kappa}\right) F^{-\frac{1}{\kappa}} \qquad \ldots.(131)$$

where F is the frequency effect and $F = \frac{\psi}{\tau} (\beta + \kappa)$.

By re-arrangement to obtain an equation for the accumulation of strain

$$\varepsilon_f = \Sigma\, \varepsilon_c \left(1 + \frac{\beta}{\kappa}\right)^{-\kappa} 2^{-\kappa} F \qquad \ldots.(132)$$

(ii) Mar M246

Apart from tests in which failures occurred at the extensometer locating ridges, the equations derived for triangular tension were found to satisfy the current data on conventionally cast and directionally solidified materials. This is illustrated in Figure 44 by the agreement obtained between the predicted rupture line and the experimental points. This line is based on static creep rupture data only.

5.5 Push-pull triangular creep

In an attempt to predict the cyclic creep rupture results presented in Figure 45 from monotonic creep data, strain hardening theory has been applied to the Graham and Walles creep equations. Although it has been shown that differences can occur between tensile and compressive deformation, for the purposes of this analysis compressive cycling is considered to be equally damaging as tensile. However, since it causes flow in the negative direction, if it is applied after a tensile damage phase it will tend to reduce specimen length.

At the end of the first cycle

$$\Delta\varepsilon_1 = \Sigma \left\{ c\sigma^{\beta} \tau^{\kappa} \left(\frac{\kappa}{\kappa+\beta}\right)^{\kappa} - c\sigma^{\beta} \left(\frac{\kappa}{\kappa+\beta}\right)^{\kappa} \left[(2\tau)^{\kappa} - (\tau)^{\kappa}\right] \right\}$$

and hence it follows that after the nth loading cycle

$$\Sigma\Delta\varepsilon = \Sigma \left(\frac{\kappa}{\kappa+\beta}\right)^{\kappa} c\sigma^{\beta} \tau^{\kappa} \left[N^{\kappa} - 2\left\{(N-1)\tau\right\}^{\kappa} + 2\left\{(N-2)\tau\right\}^{\kappa} - \ldots.\right]$$

where N is the number of $\frac{1}{2}$ cycles.

$\therefore$ $$\Sigma\Delta\varepsilon = \varepsilon$$

$$= \Sigma \left(\frac{\kappa}{\kappa+\beta}\right)^{\kappa} \frac{\kappa}{N} c\sigma^{\beta} t^{\kappa} \qquad \ldots.(133)$$

assuming N large.

This can be related to the strain produced under static conditions at maximum stress σ to give

$$\varepsilon_{Pt} = \varepsilon_c \frac{\kappa}{N\left(1+\frac{\beta}{\kappa}\right)^{\kappa}} \qquad \ldots.(134)$$

where ε_{Pt} is the strain under push-pull triangular stress cycling and ε_c is the strain under monotonic creep. The time to develop a

particular value of net tensile strain (or the time to rupture) can be obtained from

$$t_{Pt} = \left[t_c \left(1 + \frac{\beta}{K}\right)\right]^{\frac{K}{K-1}} \left[\tau K\right]^{\frac{1}{1-K}} \quad \ldots.(135)$$

It follows using the constants derived for Mar M246 at 1173K that in this case

$$t_{Pt} = 4.6\ t_c^{1.1}/\tau^{0.12} \quad \ldots.(136)$$

5.6 Push-pull rectangular creep

Rupture results for Mar M246 are presented in Figure 45 and strain accumulation for Nimonic 90 and Mar M246 in Figures 31 and 46 respectively. In predicting strain accumulation and rupture from static creep data, similar assumptions were made as for push-pull triangular loading.

It follows that at the end of the nth cycle

$$\Sigma\Delta\varepsilon = \Sigma\ c\sigma^{\beta}\ (N\lambda)^{K} \left(\frac{K}{N}\right) \quad \ldots.(137)$$

But the total time $t_{Pr} = N\lambda$

$$\therefore \quad \Sigma\Delta\varepsilon = \Sigma \frac{K}{N} c\sigma^{\beta}\ t_{Pr}^{K} \quad \ldots.(138)$$

Comparing this with monotonic tensile creep it follows that

$$\varepsilon_{Pr} = \varepsilon_c \frac{K}{N} \quad \ldots.(139)$$

and

$$t_{Pr} = t_c^{\frac{K}{K-1}} (\lambda K)^{\frac{1}{1-K}} \quad \ldots.(140)$$

and for the same time constants as above

$$t_{Pr} = 0.76\ t_c^{1.1}\ \lambda^{-0.12} \qquad \ldots.(141)$$

Using the relationships developed in Sections 5.5 and 5.6 gives slightly optimistic predictions for strain behaviour of both Nimonic 90 and Mar M246 as shown in Figure 46 and also optimistic predictions of rupture time as shown for Mar M246 in Figure 45. These rupture times were similar in value to the complementary all tensile cycle and an alternative analysis based on compressive stresses being treated as tensile gives a lower bound to the estimates, ie

$$t_{Pr} = t_c \qquad \ldots.(142)$$

and

$$t_{Pt} = t_c \left(1 + \frac{\beta}{\kappa}\right) \qquad \ldots.(143)$$

These equations give improved rupture correlations but pessimistic estimates of strain.

From the above it can be seen that cyclic strain develops more rapidly than is predicted by the reversible strain hardening concept but slower than the equivalent tensile lower bound. In consequence the alternative modified strain hardening analysis has been adopted in which it is considered that compressive phases cause damage but have little influence on the development of strain. It follows that for triangular push-pull cycles

$$\Sigma\Delta\varepsilon_{Pt} = \left(\frac{\kappa}{\kappa + \beta}\right)^{\kappa} c\sigma^{\beta}\ \tau^{\kappa} \left[N^{\kappa} - (N - 1)^{\kappa} + (N - 2)^{\kappa} \ldots.\right]$$

where N is the number of $\frac{1}{2}$ cycles

and hence $\Sigma\Delta\varepsilon_{Pt} = \Sigma\ \frac{1}{2} \left(\frac{\kappa}{\kappa + \beta}\right)^{\kappa} c\sigma^{\beta}\ \tau^{\kappa}\ N^{\kappa}$

or in terms of monotonic tensile creep test

$$\varepsilon_{Pt} = \tfrac{1}{2}\,\varepsilon_c \left(1 + \frac{\beta}{\kappa}\right)^{\frac{1}{\kappa}} \qquad \ldots.(144)$$

and

$$t_{Pt} = 2^{\frac{1}{\kappa}}\, t_c \left(1 + \frac{\beta}{\kappa}\right) \qquad \ldots.(145)$$

For push-pull rectangular loading from similar assumptions to those above

$$\varepsilon_{Pr} = \varepsilon_c/2 \qquad \ldots.(146)$$

and

$$t_{Pr} = 2^{\frac{1}{\kappa}}\, t_c \qquad \ldots.(147)$$

This concept is found to give the closest estimates of strain accumulation and rupture. The strain accumulation and rupture predicted by these equations are also compared with experimental findings in Figures 45 and 46.

5.7 Main findings and conclusions on empirical life prediction

(1) The Graham and Walles creep equation can be used in computer analysis and regeneration of creep curves.

(2) The empirical equations derived to fit tensile creep data can be applied to compressive creep.

(3) An equivalent time concept, developed previously to account for effects of loading rate on subsequent creep, has been extended so as to predict accurately initial creep rates. The resulting equation is

$$\dot{\varepsilon}_i = \frac{c\sigma^{\beta}\left(1 + \frac{\beta}{\kappa}\right)^{\frac{2}{3}}}{3\tau^{\frac{2}{3}}\,(T' - T)^{-20\kappa}}$$

(4) Using strain hardening theory and the Graham and Walles creep equations, accurate predictions of strain accumulation and rupture under rectangular tensile creep can be obtained from static creep data, the equations being

$$\varepsilon_r = 2^{-\kappa}\ \varepsilon_c \text{ and } t_r = 2\ t_c$$

(5) Equations used to predict strain accumulation under triangular tensile creep have been extended to include frequency terms, the equations being

$$\varepsilon_f = \varepsilon_c \left(1 + \frac{\beta}{\kappa}\right)^{-\kappa} 2^{-\kappa} F \text{ and } t_f = \Sigma\ 2\ t_c \left(1 + \frac{\beta}{\kappa}\right) F^{-\frac{1}{\kappa}}$$

where $F = \frac{\psi}{\gamma} (\beta + \kappa)$.

(6) The equivalent time concept has been extended to the prediction of triangular push-pull and rectangular push-pull strain accumulation and rupture, the equations derived being

(a) for triangular push-pull

$$\varepsilon_{Pt} = \Sigma\ \tfrac{1}{2}\ \varepsilon_c \left(1 + \frac{\beta}{\kappa}\right)^{\frac{1}{\kappa}} \text{ and } t_{Pt} = \Sigma\ 2^{\frac{1}{\kappa}}\ t_c \left(1 + \frac{\beta}{\kappa}\right)$$

and (b) for rectangular push-pull

$$\varepsilon_{Pr} = \Sigma\ \varepsilon_c/2 \text{ and } t_{Pr} = \Sigma\ 2^{\frac{1}{\kappa}}\ t_c$$

(7) Robinson's linear damage rule, $\Sigma \frac{t}{t_f} = 1$, follows as a direct consequence of the Grant and Monkman equation $\dot{\varepsilon}_s\ t_f$ = constant. However a more general expression is $\Sigma\ (t_f\ \dot{\varepsilon}_s)$ = constant, where for Nimonic 90 for example, in the range 1023 to 1123K the constant has a value of 6×10^{-2}.

6.0 Discussion

6.1 Effect of static and cyclic stressing on strain accumulation and rupture of Nimonic 90 and Nimonic 108

6.1.1 Comparison of tensile and compressive creep

The Graham and Walles analysis has been shown to apply to compressive deformation. It enables a comprehensive comparison of tensile and compressive creep behaviour since it is possible to study systematic differences for each stage of creep deformation, and to regenerate average strain time curves for a series of stresses and temperatures. Using this method the strain time curves shown in Figures 11 to 14 were regenerated and compared with the experimental data.

Although in the preliminary stress-strain curves, Figure 10, a strength differential effect[119] was obtained showing that Nimonic 90 is slightly more resistant to compression than to tension, this difference is not reflected in subsequent primary creep strain accumulation. Both for Nimonic 90 and for Nimonic 108 there are no differences between tensile and compressive creep which exceed experimental scatter.

Examination of the secondary creep rates, Figures 15 and 16, shows that the data can be expressed by the relationship $\dot{\varepsilon}_s = A\sigma^n$, where A and n are constants over specified ranges. It is apparent that the constants are identical under tensile and compressive loading. For Nimonic 90 the value of the stress exponent n is shown to be 4 at low stresses and 8 at higher stresses. In the Nimonic 108 tests n is found to be 8 for all conditions.

Tertiary deformation occurs at relatively small strains and is well developed even in compressive creep tests stopped at 2 per cent strain. For Nimonic 90 at temperatures above 973K, the onset of tertiary deformation under compressive loading is delayed relative to tensile loading, the t_a intercept being a factor of 2 later than for tension. In terms of the Graham and Walles analysis this is equivalent to a shift in temperature of about 12K and is significantly greater than the experimental scatter figures of about ±25 per cent in time. The extent of the tertiary contribution to compressive creep damage of Nimonic 90 at 1073K is shown in Figure 71. For Nimonic 108 within the times tested, there is no significant tertiary creep at 973 and 1073K,

but tensile and compressive contributions were almost identical at 1173K as shown in Figure 72.

Although the γ' particles in Nimonic 90 create high coherency strain, differences between tension and compression occurred at endurances too short to involve significant coarsening of the γ' precipitate. Therefore at these short times the γ' particles are still coherent, are present as randomly distributed spheroids and deformation does little to alter the general precipitation characteristics of the γ' phase. Under high tensile stresses wedge-type cracking occurs at highly stressed triple points (see Figure 55) and leads to redistribution of localized stresses and an accelerated accumulation of strain. Under compression the stress system is complementary to tension but cracking cannot be a means of local stress relaxation because the compressive normal stress would cause plastic collapse. Coherent γ' phase causes a misfit strain of about 0.3 per cent (Reference 120) and application of compressive stress may therefore provide a driving force for the development of denuded regions, see Figure 60, since this will remove the strain and also reduce the local flow stress. The shear associated with grain boundary sliding under compressive stressing is therefore accommodated by the nucleation and growth of denuded areas. The eventual structure obtained may be described as partly recovered, ths large carbide particles acting as barriers to impede recrystallization.

The longer durations of tests at lower stresses relative to high stress tests, allows more time for structural instability to develop and so denudation can occur even under tensile loading as can be seen in Figure 56. In this case, when a sufficient area of denudation is present, the reduced flow stress of these regions allows rapid strain accumulation and hence the onset of cracking. In compression the strain accumulation occurs uninfluenced by cracking, however, once significant amounts of denudation have occurred, the alloy essentially becomes single phased (see Figure 59c), has less resistance to creep and so rapid strain accumulation can be accommodated. The greater similarity in structure between low stress tension and compression specimens relative to higher stress specimens is in agreement with the experimental results which show that differences between tertiary creep under tension and compression decrease as stress is reduced. The

correlation of denuded growth with a multiple of strain and time (Figure 60) appears to give reasonable agreement between high compressive strain short time tests, low compressive strain long time tests, and also denudation occurring under tensile creep where cracking is contributing to tensile strain accumulation. A strain time multiple has been used successfully to describe damage in other investigations[121].

It is generally considered that grain boundary carbides inhibit grain boundary sliding but are potential sites for crack growth[122,123]. If surrounded by a single-phase region this should redistribute more easily the local shear associated with grain boundary sliding and hence delay the onset of fracture processes. The present results indicate that this is only partly true, that is if this type of structure is developed prior to high tensile stress/low temperature applications. If however denudation occurs under the conditions of service, initially this may accommodate local stress concentrations, but this will be followed by a net weakening of the structure. The results presented in Figure 58 are used to illustrate this point schematically in Figure 58a. The change in slope of the rupture curves from a gradient of 8 to a gradient of 4 is considered to be related, at least partly, to structural degradation (denudation) reducing potential life. Since at high stress denudation is delayed relative to wedge cracking, this may be part of the reason for delayed tertiary deformation. At lower stresses since denudation occurs in tension as well as in compression the added influence of tensile cracking on recovery processes would be expected to be less significant.

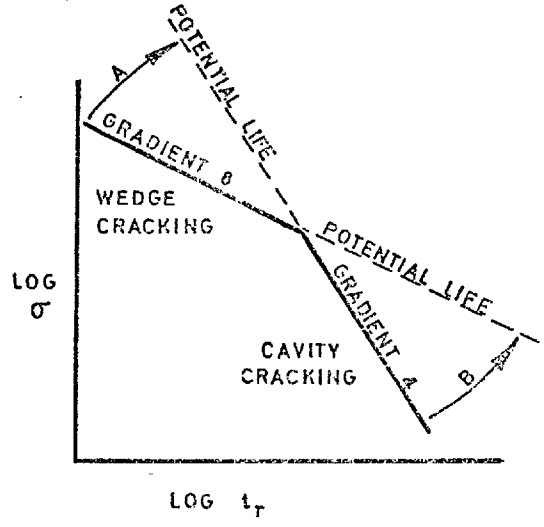

Figure 58a

Region A indicates potential improvement in life if high local stresses can be redistributed by denudation. A trend in this direction is shown in the high stress compressive creep results. This could possibly be obtained in tension if a suitable prior heat treatment could be employed and the testing temperature maintained at a low level.

Region B indicates the reduction in potential life which occurs due to the onset of denudation during testing. Since this occurs under both tensile and compressive testing, less difference would be expected in experimental results. It follows that heat treatments or alloy additions to delay denudation should improve both tensile and compressive lives.

The short time grain boundary denudation which occurs under high compressive stresses is in agreement with previous observations where, for an H46 martensitic steel tested under high compressive stresses, it was found that the centre of the specimens were about 40 Vickers hardness points softer than material from the dead zones at the specimen/platten interface[111]. In this former case the microstructures showed that this was due to strain induced tempering being developed to a greater extent at the centre relative to the end.

Considering Nimonic 108, under the conditions chosen for this test programme, a stress exponent of 8 was observed for the minimum creep rate correlation, even at 1173K. However, prior to the commencement of testing, the grain boundary region was found to contain massive γ' regions, see Figure 6b. This single phase can more easily accommodate local deformation than can two-phase areas[124] and acts in a similar fashion to the single γ phase regions which develop in Nimonic 90 during testing. Metallographic examination showed that tensile cracking tends to be inhibited relative to Nimonic 90. As tertiary creep deformation under both tensile and compressive loading will be partly or wholly controlled by growth of γ' precipitation regions, tertiary creep should be more closely related than is found for Nimonic 90. This is found to be the case as is shown in Figure 72.

6.1.2 Comparison of tensile and rectangular creep properties

The extension of the use of the equation,

$\varepsilon = \Sigma\, c\sigma^{\beta}\, t^{\kappa}\, (T' - T)^{-20\kappa}$, to describe strain accumulation during the on-load periods of a rectangular stress creep test has been found to be successful, as can be seen in Figure 68. However, for non zero minimum stress levels the method fails to take account of any damage which may be incurred at the lower value and to overcome this lack of flexibility it is necessary to use the concept of a mechanical equation of state or of a super position integral. The experimental results show that, under the present testing conditions, the value for the time to rupture of a rectangular creep test is twice the time of a monotonic creep test at the same stress.

Comparing predictions from the various equation of state concepts which have been presented in Section 5, it is found that close agreement with the experimental results is achieved using strain hardening and life fraction hypothesis. Time hardening and modified super position theory give rupture predictions that are both in error by a factor of 2.

For any specific stress level, illustrating the differences in predicted strain, at a total time equal to the time to monotonic creep rupture, strain hardening and life fraction analyses predict a value of strain equal to that of the monotonic test at half its life whereas time hardening and super position both predict a value of strain equal to half the strain of a monotonic creep test. The former prediction is found to be confirmed experimentally.

In utilising equations of state for variable stress calculations, no consideration is taken of the effects of anelasticity. Although not a serious omission in the current predictions, anelasticity is associated mainly with primary creep processes and in the present tests primary and secondary creep damage accounted for less than about 20 per cent of the lives. It follows that slight trends could be masked in the general analysis and so detailed measurements of anelasticity and of its effects have been carried out. It can be seen in Figures 24 and 25 that at the beginning of a creep test anelastic effects are small but increase rapidly during primary creep. Figure 28 illustrates that if stress is removed during the secondary creep stage, a critical value of

original applied stress exists below which anelastic recovery effects should not be observed on unloading. Results presented in Figure 29 show that for all applied stresses a critical value of stress reduction must be exceeded prior to anelastic recovery being observed.

Quantitatively, for periods greater than about 30 seconds, anelastic recovery can be adequately expressed using a $t^{\frac{1}{3}}$ power law. Early deviation is due, at least in part, to the time taken in unloading since recovery will commence as soon as the stress has been reduced to the critical value σ_c associated with the original applied stress, see Figure 29. During further unloading, the driving force for recovery will increase progressively until the full load has been removed. It follows that the initial discrepancy between predicted and experimental results is dependent on loading rate. The application of a loading rate correction, see Equation (126), allows a $t^{\frac{1}{3}}$ equation to be used from times greater than about 5 seconds. These results indicate that the laws governing primary creep and anelastic recovery are very similar.

An alternative way of considering the amount of anelastic recovery occurring during any reduced load period can be obtained from re-examining Figure 29. It can be seen that anelastic recovery is linearly related to the stress reduction through an equation of the form

$$\Delta\sigma_A - \sigma_o' = K \varepsilon_a$$

The value of K is dependent on the time over which anelastic recoveries are measured whereas σ_o', the intercept on the $\Delta\sigma_A$ axis is independent of hold time and appears to be related to a critical stress reduction which must be exceeded prior to anelastic recovery effects being observed during stress reduction tests. The increase in anelastic recovery during the later stages of tertiary creep, Figure 26, has not been reported previously. It has been correlated with reduction in area measurements to ensure that the effects observed are greater than might be expected from increased stresses at localised necked regions. For example at 154 MN/m^2 and 1123K, 15 per cent reduction in area occurred at fracture; this results in a maximum stress increase to 180 MN/m^2 which would increase anelastic recovery to twice its secondary value, as calculated from data available in Figure 26, whereas anelastic recovery at rupture was almost five times the secondary value.

It has been shown[125] that the secondary creep rate ends when voids grow to such a size that they become stable and can influence creep rates. The increase in anelastic recovery per cycle at time t_I occurs between about 0.3 to 0.5 per cent creep strain. Stable cavities were not observed until 1 to 2 per cent strain. However as the tests were not cooled down under load, and positive identification of cavities in this type of material is difficult, the correlation is probably satisfactory. Also it is reasonable to suppose that during the unloaded parts of the cycle, steady-state anelastic recovery will be upset when voids can influence recovery processes. At the commencement of tertiary creep, cavities are stable only under the applied stress, sinter on unloading and so although able to influence creep damage at the applied stress level, they are not available to influence rates of anelastic recovery. The time t_I, may therefore be related to the stage at which cavities that are stable under the maximum applied stress condition become stable under conditions of reduced stress.

In considering the practical significance of t_I, it has been shown in Figure 27 that for $\frac{K}{\beta}$ equal to $\frac{1}{4}$, the time t_I indicates that about 50 per cent of the test life has been reached, and for $\frac{K}{\beta}$ equal to $\frac{1}{8}$, t_I indicates that about 85 per cent of the life has been reached. A new technique for increasing component life is based on intermediate heat treatments annealing out previous damage[126]. This process is becoming a more attractive proposition as blade costs increase and in this context the time t_I indicates the maximum useful life that can be obtained prior to achieving full benefit (sintering of grain boundary cavities) from an intermediate heat treatment.

6.1.3 Effects of frequency on triangular tension

The results in Figure 30 indicate that limiting conditions exist at very high and very low frequencies. The equations developed in Section 5.4 give good prediction of these lives from static creep data.

Metallographic examination of failed specimens showed that at low frequencies specimens exhibit creep damage similar to that shown in Figure 54 whereas at high frequency damage is typical of that experienced during fatigue (Figure 61a). However (i) the limits in both cases are time dependent and not cycle dependent and (ii) since the creep is increased and the fatigue life decreased due to creep fatigue interaction, it

follows that life predictions of cyclic damage at elevated temperatures should be based on creep damage to obtain at worst pessimistic life estimates.

6.1.4 Effect of rectangular push-pull cycling on creep

Examination of tensile and compressive creep curves, Figures 11 to 14, shows that it is not strictly true to assume compressive damage equal to tensile damage, however prediction of strain accumulation using the basic strain hardening concept, Equation (139), gives a reasonable correlation with the data and the modified analysis, Equation (144), an improved correlation. Both indicate that the approximation seems justified, see Figure 31.

6.2 Effect of static and cyclic stressing on strain accumulation and rupture of three forms of cast Mar M246

Although insufficient tests were carried out for a full statistical assessment, the results show that the Graham and Walles analysis can be used to describe high temperature deformation of the three forms of cast Mar M246. This analysis allows accurate prediction of strain accumulation and rupture under cyclic stress conditions from monotonic creep data.

6.2.1 Comparison of tensile creep properties

In Figure 35 it can be seen that under constant tensile stress the minimum creep rates of the three forms of Mar M246 are similar. The improved lives of the directionally solidified and single crystal specimens over conventionally cast specimens (see Figure 32), appear therefore to be due to delayed onset of tertiary creep deformation and to an increased contribution from this stage. Tertiary creep is usually considered to be the stage at which cavities become stable, however the absence of general transverse boundaries in directionally solidified and single crystal materials removes the major source for the development of internal creep cracks. This does not eliminate completely internal cracking since it can occur at large carbides and dendritic arms, and at small transverse segments within longitudinal boundaries. The major source of cracking appears to be grain boundary carbides, see Figure 61.

The size effect results, Figure 37, show that a reduction in the cross-sectional area of the conventionally cast materials by a factor of 2 reduces the time to failure by about one-third. On the other hand the single crystal times to rupture are unaffected by reductions in cross-sectional areas by factors of up to 8.

The results of Figure 39 show that the original proposal of Grant and Monkman[115]

$$\dot{\varepsilon}_s \, t_c = \text{constant}$$

is reasonable for this alloy although the conventionally cast material has a different constant from the directionally solidified and single crystal materials. This type of relationship was also noted in the work on tensile creep of Nimonic 90 (Figure 22).

6.2.2 Comparison of tensile and compressive creep properties

The compressive creep properties of the directionally solidified and conventionally cast materials are very similar, as illustrated in Figure 38. In general, the onset of tertiary deformation in compression is not due to stable cavities but to overageing, recovery, or recrystallisation mechanisms[111]. It has been shown that while large carbides are desirable to inhibit grain boundary sliding[122], they are potential nucleation sites for cracking. The formation of blocky γ' particles delays the onset of cracking by providing an environment for localized plastic flow around the carbide particles[124] however, as a significant local volume fraction of the alloy essentially becomes single phase γ', this may become less resistant to creep deformation. The high strain compressive specimens showed strain induced phase coarsening occurring at short times, see Figure 62. This is analogous to the strain induced denudation observed in Nimonic 90, however, in the present case there is a sufficiently high volume fraction of the γ' phase to make it the major constituent. Unlike Nimonic 90 it is not coherent and therefore has a low misfit energy, and so cannot easily go back into solution. The massive coarsening shown in Figure 62 illustrates an alternative weakening process (overageing). Evidence has recently become available which indicates that this leads to an effective reduction in anti-phase boundary energy as dislocations

traverse the γ' particles[127]. It follows that tertiary deformation should be more closely related for conventionally cast and directionally solidified tests under compression than under tension. This is confirmed by the experimental results as can be seen by comparing Figures 34 and 38.

6.2.3 Comparison of triangular and rectangular creep properties of Mar M246

In rectangular tensile creep, the anelastic recovery effects are similar to those found for Nimonic 90, as can be seen for the conventionally cast material in Figure 43. An equation of the form $\Delta\sigma - \sigma_0' = K\ \varepsilon_a$ could be fitted to the data.

Although insufficient material was available to carry out rectangular creep tests on single crystals, stress reduction tests confirmed that anelastic recovery could occur. Grain boundary sliding could not be the cause of the recovery exhibited in these tests and so it is considered that anelastic effects during the unloaded phases of the rectangular creep tests is due to some other mechanism. The anelastic component alternates during cyclic stressing and makes no cumulative contribution to deformation behaviour.

6.2.4 Triangular tensile creep

In the triangular tension data shown in Figure 44 both conventionally cast and directionally solidified specimens tested at 300 c/hr exhibited fatigue failures close to the extensometer ridges. This appears to reduce the lives of the directionally solidified specimens but has less effect on the conventionally cast material. Directionally solidified specimens without ridges were tested at 300 c/hr. This produced longer lives that correlated with the predictions from Equation (128). However Figure 63 shows that the failure was still initiated by a fatigue process.

6.2.5 Push-pull triangular and rectangular creep

The effects of compressive hold periods on Mar M246 appear to be similar to those found for Nimonic 90. In Figure 45 it can be seen that the compressive phase of cycling is apparently as damaging as the tensile phase, the total times to rupture under push-pull stressing being similar to those of static creep. However, strain predictions using Equation (139) are not very accurate as illustrated in Figure 46. This led to the development of an improved empirical correlation based

on the assumption that the compressive phases do not contribute to net strain but still cause damage. This assumption produces better rupture predictions both for rectangular and triangular push-pull cycling (see Figure 45) and also much better strain predictions under rectangular push-pull cycling. It is considered that during push-pull cycling the stress range is increased and this may control the amount of tensile anelastic recovery which can occur during any compressive period, strength differential effects between tension and compression causing the net effect to be an enhanced strain accumulation during the subsequent tensile phase.

6.3 The effect of stress changes on subsequent creep deformation

6.3.1 Assessment of the validity of using stress reduction measurements in developing theories for creep

Considering the effect of small stress reductions made during nominally constant stress tests, experimental observations of strain response show that incubation periods, or at least periods of low creep rates, always follow small reductions in stress. However it was also pointed out in Section 2.2.4 that recently the whole concept of stress reduction tests as a means of obtaining information on deformation mechanisms has been criticised[89]. Since much of the experimental evidence in this programme comes from the above type of test the criticism requires investigation.

Stress reduction tests have been discussed in Section 2.2.4 and summarising current opinion on the experimental observations, three explanations can be given.

(a) Incubation periods occur for one level of stress reduction only, namely that where the applied stress is reduced by an amount equal to the level of the effective stress causing deformation. For smaller reductions in stress, positive creep is considered to commence from the instant of unloading. The rate controlling mechanism is suggested to be the glide of dislocations.

(b) Incubation periods occur over a range of stress reductions. They are considered to be due to the requirements of metallurgical recovery and the rate controlling process

is assumed to be the climb of dislocations or the growth of dislocation link lengths in a three-dimensional network to a size at which further dislocations can be emitted.

(c) Incubation periods occur if the net effect of the new creep rate at the reduced stress and the anelastic recovery which follows all stress reductions is zero. This explanation attaches little or no importance to the actual experimental observation of whether zero strain rates or small positive strain rates immediately follow stress reductions.

An important factor in support of model C is the experimental observation by Lloyd and McElroy[89] that anelastic strain is linear with respect to stress decrement and extrapolates to zero. This indicates that anelastic deformation accompanies any stress reduction and if this is a general finding allowance for anelastic components would have to be made in models A and B.

In all the models it is accepted that, provided the materials are polycrystalline, large stress reductions during creep are followed by periods of time dependent contraction termed either backwards creep or anelastic recovery. The crux of the discrepancy concerns what happens to the strain time relationship after small stress reductions are made during a creep test. An experimental difficulty is that, when very small reductions in stress are made, non-elastic strains can be as small as 10^{-6} and so absolute proof cannot be obtained from experimental observations.

In Nimonic 90 and Mar M246, Figures 28 and 34 show that although ε_a is linearly related to the stress reduction $\Delta\sigma$, the data do not extrapolate to zero and for temperatures tested have positive intercepts with the stress axis. This implies that for stress reductions less than the respective intercept values on the stress reduction axis, anelastic recovery does not contribute to deformation behaviour. Measurement of the critical stress decrement for negative flow ($\sigma_A - \sigma_c$) confirms this fact as shown in Figures 47a and b. This figure also shows that at any temperature for low applied stresses, the stress reduction for negative flow is constant. Whether anelastic recovery is due to viscous unbowing of dislocations under line tension forces[128],

to time dependent relaxation of dislocation pile-ups[129], or to any other mechanism, the implication is that in precipitation hardened alloys at least, a friction stress σ_o' exists which prevents these processes occurring for small stress reductions.

From recently available data[130], a metallurgical recovery parameter $r\ (=\Delta\sigma/\Delta t)$ has been calculated from the incubation periods following small stress reductions made during creep. As shown in Figure 77a for Nimonic 90 and Figure 77b for Mar M246, recovery is found to be linearly related to the creep rate prior to the stress change. These figures include recovery values made throughout primary and secondary creep and for a range of stress reductions. The simple relationship contrasts with the more complex anelastic model (model C) where recovery depends on creep rate following the stress reduction.

If dislocation flow occurs under an effective stress $(\sigma_A - \sigma_i)$, model A, then reducing σ_A to a level still greater than σ_i should give a positive effective stress and hence positive creep rates should be maintained immediately after reducing the applied stress. However the occurrence of incubation periods of zero creep rate indicates that the total internal stress opposing deformation during creep must be equal to the applied stress, and so must change by recovery prior to the recommencement of creep at a lower stress level.

Included in Figure 77a are recovery rates obtained from small increases in stress made during anelastic recovery or backwards creep. It can be seen that the anelastic recovery rates are again controlled by the rates of metallurgical recovery, and hence it follows that the same processes may control strain accumulation both in the forwards and backwards directions.

The current observations show that models A and C do not apply to precipitation hardened alloys and in these alloys at least, incubation periods are a true reflection of creep behaviour and are not influenced by anelastic effects.

6.3.2 Significance of stress reduction results

(a) Nimonic 90

Figure 19 shows that for Nimonic 90 changes in stress dependence of the minimum creep rate, $\dot{\varepsilon}_s$, occur at stress levels which are temperature dependent. The value of n in the equation

$$\dot{\varepsilon}_s = A \sigma^n e^{-Q/RT} \quad \ldots.(148)$$

changes from 4 at low stresses to 8 at high stresses. (Here the steady-state equation is written in full and includes a temperature term.) If the secondary creep rate in Figure 19 is plotted against $\frac{1}{T}$ K^{-1}, for constant stress and constant exponent n in the above equation, activation energies of 493 KJ/mole (108 K cals/mole) and 752 KJ/mole (180 K cals/mole) are obtained for n = 4 and 8 respectively. As stated earlier, many models have been proposed to account for the change in stress dependence of $\dot{\varepsilon}_s$. However recently[86,87] it has been found that high values of n can be related to creep recovery using a friction stress term, σ_o. Typical results of friction stress measurements on Nimonic 90 are presented in Figure 51a. It can be seen that at low applied stress levels, the friction stress, σ_o, is proportional to the applied stress, but as the applied stress is increased σ_o reaches a limiting maximum value. If the minimum creep rate data in Figure 19 are replotted against $(\sigma_A - \sigma_o)$ as in Figure 52a, a single value of n = 3.5 is obtained. This value applies over the whole range of testing. Further, as discussed in Section 2.3.2.1 it is possible to use $\sigma_A - \sigma_o$ in the calculation of activation energies. The data in Figure 52a can be used to calculate a single activation energy for creep over the whole stress and temperature range employed in the current investigation and a value of 280 KJ/mole (67 K cals/mole) is obtained as illustrated in Figure 78. This is close to the value for self-diffusion of nickel and also for creep of a simple nickel, 20 per cent chrome solid solution alloy[58]. It indicates that the improved creep resistance of the γ' precipitation hardened alloy Nimonic 90, may be due at least in part to the introduction of a friction stress exerted by these particles. This friction stress reduces the effective stress acting on the dislocations. The implication of the high activation energies obtained in previous measurements is that they are calculated for conditions under which the structure is not constant, ie since σ_o is temperature dependent, at constant applied stress $(\sigma_A - \sigma_o)$ varies.

Figure 20 shows that for Nimonic 90 there is no change in the stress dependence of the initial creep rates with increasing stress, a

value of 4 applying over the whole range of testing. Combining the 1123K results from Figures 15 and 20 to form Figure 79a, shows that initial creep rates can be up to 17 times faster than steady-state values. (Some additional steady-state creep rates at high stresses have been added.) However Figure 51 shows extrapolated limiting values of the friction stress at an applied stress of zero. This indicates minimum values of the friction stress, $\sigma_{o\,I}$, and it is reasonable to suppose that these values would apply at time t = 0 independent of applied stress, σ_A, ie these are inherent friction stresses due to precipitate alone. If the initial creep rates are now plotted against $(\sigma_A - \sigma_{o\,I})$, where $\sigma_{o\,I}$ is the inherent friction stress value at any specific temperature, it can be seen in Figure 79b that for the same effective stress, initial and steady-state creep rates can be superimposed. It follows that the activation energy for initial creep is also 280 KJ/mole (67 K cals/mole). However, from experimental determination of the friction stress, σ_o, it would appear that σ_o builds up extremely rapidly and so can commence rising during loading to higher stress values. The net effect of this is that initial creep rates of high stress tests could be slightly lower than if loading had been instantaneous.

If maximum steady-state friction stress, σ_o, and the inherent friction stress $\sigma_{o\,I}$ are both plotted against temperature, as shown in Figure 80, they have extrapolated zero values at 1223K. This is within the range 1210K to 1235K obtained for the γ' solvus range from differential thermal analysis[130].

The difference in the ratios of $\dot{\varepsilon}_i/\dot{\varepsilon}_s$ for n = 4 and n = 8 in Equation (148) may be explained by the fact that for n = 4 the steady-state friction stress, σ_o, has not reached the maximum attainable value. Over this range it is proportional to the applied stress and so possible damage due to increase in applied stress is partially off-set by increase in friction stress, σ_o. The high values of the ratio σ_o/σ_A results in low effective stresses operating under steady-state conditions and hence a large reduction in the creep rates from initial to steady-state values. When n = 8 the friction stress has reached its maximum value and so further increase in applied stress is not accompanied by increase in σ_o, the effective stress operating becomes larger and consequently the eventual steady-state creep rates are much higher and closer to initial values.

In Figure 47 the steady-state critical stress, σ_c, (the applied stress minus the stress reduction to just cause negative flow) is plotted against the original applied stress for a range of stresses and temperatures. Also included in this figure are the critical stress reductions to cause negative flow, $\Delta\sigma_c$. It can be seen that at low stress levels $\Delta\sigma_c$ is constant, independent of stress, but at high stresses progressively larger stress reductions are required to cause negative flow. The effect of this is that as applied stress increases, the value of σ_c increases at a decreasing rate, and eventually begins to fall as stress is increased further. The present work has shown that the change in stress dependence of the minimum creep rate is related to the change in stress dependence of the friction stress σ_0. Although σ_c is currently widely used as a basis for understanding creep deformation mechanisms (as illustrated in Section 2.2.4 where $\sigma_c \equiv \bar{\sigma}_I$) agreement between minimum creep rate and critical stress, σ_c, is impossible since, over a wide range of applied stresses, the effective stress $(\sigma_A - \sigma_c)$ is constant.

(b) Mar M246

For Mar M246 the value of n in the Equation (148) is found to vary slightly with temperature and so activation energies for creep could not be calculated from a graphical analysis of steady-state creep rates, however other work on research alloys similar to Mar M246 (Reference 131) indicates that a value of 830 KJ/mole (200 K cals/mole) is reasonable. Typical results of friction stress measurements are presented in Figure 51b. As for Nimonic 90, replotting minimum creep rates against $(\sigma_A - \sigma_0)$ yields a value for n of about 3.5 (see Figure 52b). Activation energies calculated for a constant effective stress of 154 MN/m^2, are reduced to 290 KJ/mole (69 K cals/mole) which is close to that found earlier for Nimonic 90.

Over the stress range investigated, initial creep rates were found to have stress exponents of 8, as were steady-state rates, however relatively slow loading rates were employed and in order to super-impose initial and steady-state creep rates it is necessary to assume that the friction stress has risen to about $2\sigma_{0_I}$ at the end of loading. With these assumptions initial and steady-state creep rates can be super-imposed.

If the maximum friction stress and inherent friction stress levels are plotted against temperature of testing as shown in Figure 78, a zero value is predicted at 1350K. Differential thermal analysis shows an isotherm in the range 1330K to 1370K which is probably due to resolution of fine γ' precipitate[130].

In Figure 47b the critical stress, σ_c, is plotted against the original applied stress. Included in this figure are the critical stress reductions to cause anelastic recovery. As for Nimonic 90 no correlation could be obtained with either of these values and minimum creep rate.

(c) General implications

The correlation between friction stresses and γ' solvus temperatures of Nimonic 90 and of Mar M246, together with the observations on activation energies for creep, provide substantial evidence indicating that in both these alloys the inherent friction stress, σ_o, is due to γ' precipitate, and in the case of the maximum friction stress σ_o, since this is stress dependent, dislocation-precipitate interaction can presumably increase friction stress levels until limiting maximum values are reached.

Using the effective stress concept, the Nimonic 90 and Mar M246 steady-state creep rates at 1173K are both shown (Figure 52) to have stress exponents between 3.5 and 4 but to be offset in creep rates for the same effective stress. However if a normalised effective stress $(\sigma_A - \sigma_{oc})/\sigma_{\text{proof stress}}$ is used the data super-impose. Extending this concept to the various temperatures at which Nimonic 90 and Mar M246 tests were conducted it can be seen by comparing Figures 81a and b that all the data super-impose without invoking diffusion or activation energy terms, unless these are inherent in the proof stress correction. Assuming constant loading rates and a stress exponent of 4, as was found for initial creep rates, activation energies can be calculated from manufacturer's proof stress data. Values obtained are close to those for self-diffusion and currently this is being investigated more fully. Subsequent data for Nimonic 75 and Nimonic 80A are also found to lie on the normalised curve[113]. The significance of this is that where n is approximately 4 or 8 in the minimum creep rate equation, it should be possible to predict minimum creep rates for all

precipitation hardened nickel based alloys for any stress and temperature, provided the proof stress is known at that temperature. Of even greater significance the concept is being extended to two titanium alloys and a niobium stabilised stainless steel. These data also lie on the normalised line, as shown by comparing the applied stress-minimum creep rate data given in Figure 82a with the normalised effective stress-minimum creep rate data given in Figure 82c.

In an extension of these ideas to conditions under which the stress exponent has a value of about 14 as illustrated for Nimonic 90 in Figure 19, friction stress measurements show that in this high stress region, σ_o progressively decreases as stress increases. Again plotting the effective stress against minimum creep rate reduces the stress exponent n from 14 to about 3.5 and dividing by the flow stress allows this data to be super-imposed on the normalised line.

The simplicity of the current approach can be seen by comparing this equation for steady-state creep rate with some of those discussed earlier, namely

(i) $\dot{\varepsilon}_s = A\,\sigma^n\, e^{-Q/RT}$ (Reference 15)

where for a range of stress and temperatures A, n and Q vary,

(ii) $\dot{\varepsilon}_s = 2\,\varepsilon_o \sinh \frac{\nu'\sigma}{KT} \exp^{-Q/RT}$ (References 39 to 43)

where for a range of stress and temperatures ν' and Q vary,

(iii) $\dot{\varepsilon}_s = A\,\sigma_f^3\, D_o\, e^{-Q_D/RT}$ (References 60, 61 and 74)

where for a range of stress and temperatures A, Q_D vary,

(iv) $\dot{\varepsilon}_s = B'(T)\,\bar{\sigma}_e^{\,n}\,\bar{\sigma}_i^{\,\ell}$ (References 64, 65 and 80)

where for a range of stress and temperatures B'(T), n and ℓ vary.
the current equation being

$$\dot{\varepsilon}_s = B\left(\frac{\sigma_A - \sigma_o}{\sigma_{proof}}\right)^{3.5}$$

where σ_o varies but B is a constant independent of material.

6.3.3 Implication of stress reduction observations to current physical theories of creep

In Nimonic 90 at the temperatures of the current investigation it is found that equations[132] for determining the rate controlling event in the creep process give stresses required for dislocation pairs cutting γ' precipitate or for dislocation pairs looping between γ' precipitates which are similar and the exact mechanism is uncertain. However, it seems reasonable to propose that for very high stresses single dislocation cutting of γ' precipitate is probably the dominant deformation mechanism.

In the current investigation the detailed processes by which the friction stress achieves its steady-state level are not important since this value has been measured experimentally. However processes do become important if attempting to improve understanding of the physical mechanisms of creep and also if attempting to predict friction stress from fundamental concepts. For a γ' nickel base alloy similar to Nimonic 90, Lagneborg[120] has found that at stresses below the break in the steady-state creep rate graph (ie where $n = 4$), dislocations by-pass particles by a combination of cross slip and climb. Above the break (where $n = 8$) he found that dislocations by-passed particles by an Orowan mechanism. More recently he has developed a creep theory for γ' precipitation nickel base alloys based on the extra dislocation length produced during climb over particles[133]. For simplicity the alloy is assumed misfit free. He considers that the dislocation experiences a back stress from precipitate particles and that this increases as the applied stress increases, until a constant back stress is achieved at a level sufficient for Orowan looping.

Although Lagneborg has attempted to relate his findings to the internal stress theories of Nix et al[64,65], they are more in line with friction stress concepts[86-88] where it has been suggested that higher applied stresses result in higher mobile dislocation densities and correspondingly decreased three-dimensional dislocation mesh sizes. In this approach $(\sigma_A - \sigma_o)$ is considered to be responsible for determining the steady-state mesh size of the dislocation network. The theory has been formulated to give the equation[134]

$$(\sigma - \sigma_o) = \alpha u b \sqrt{\rho_N} \qquad \left(\alpha u b \sqrt{\rho_N} = \sigma_N\right)$$

from which it is considered that immediately following a small reduction in applied stress, the mobile dislocation density is too high and so mesh size must grow by recovery until lengths are again capable of acting as dislocation sources. This model provides a suitable explanation of the experimentally observed incubation periods.

Combining the two approaches, extended climb of dislocations can be considered to occur for low applied stress. This implies that the effective stresses operating are insufficient to cause dislocation loops to form. For higher applied stresses Lagneborg suggests from his electron micrograph observations that bowing of dislocations between precipitate particles occurs. On this basis the breaks in the stress creep rate curves in Figure 19 indicate the critical stresses for dislocation bowing such that it is sufficient to cause loops to form around the particles. Although Lagneborg has produced no experimental evidence in support of this theory current observations confirm that when the steady-state stress exponent n has a value of 8, the friction stress, σ_0, attains a constant value. In terms of Lagneborg's model this implies that further increase in the applied stress cannot increase the friction stress but will simply increase the effective stress, $(\sigma_A - \sigma_0)$, being supported by the network dislocations. However as found by Wilshire et al and confirmed by the results in Figure 52 for example, apparent differences in both stress exponent, n, and activation energy, Q, for low and high stress levels can be eliminated by allowing for stress and temperature dependence of σ_0. This suggests that the rate controlling mechanism is essentially the same over this entire stress range. Figure 78 shows that the activation energies for Nimonic 90 and for Mar M246 are almost identical, both being very close to published data for a simple nickel solid solution alloy[58] and for pure nickel[135]. This indicates that processes occurring in the matrix may be rate controlling during creep of two-phase alloys.

Although the friction stress concept has been used previously to explain steady-state creep rates, the current results can extend this concept to the primary stages of creep. Since initially in a creep test, the friction stress is low and has a value equal to or very close to an inherent level due to precipitate particles, it follows that the effective stress, $(\sigma_A - \sigma_{0c})$, where σ_{0c} is the current value of the

friction stress at any instant, will be high. These high stresses will be supported by network dislocations and therefore rapid network growth will take place. This is indirectly confirmed from experimental measurements of rates of recovery. Under these conditions rapid dislocation flow will occur and this will result in dislocation/precipitate and dislocation/dislocation interaction. Dislocation flow increases the friction stress, reduces the effective stress and leads eventually to the conditions for steady-state creep.

This provides an explanation for the measured decrease in the rate of recovery during primary creep since, although the total dislocation density increases, the current experimental results provide evidence suggesting that part of the increase is due to the added dislocation lengths required to overcome precipitates and so contributes to the friction stress, σ_o, therefore reducing the stress being supported by the network dislocations. It should follow from this model that, whether in the primary or secondary stages of creep, the rate of growth of the network will depend solely on the effective stress operating. Also, whether extended climb, loop annihilation or particle cutting is the detailed mechanism by which dislocations flow through the lattice, is important only in the sense that this controls the level of the friction stress which is operating at any instant.

Figure 51 shows that a drop in σ_o occurs after the stress exponent n in the equation $\dot{\varepsilon}_s = A\,\sigma^n$, rises to values greater than about 8. Some evidence of dislocation cutting of γ' precipitates has been found under these conditions. The effect of this will be to reduce the friction stress due to the precipitates, although this will be replaced, probably less effectively, by anti-phase boundary energy required to cut precipitates. Since, through this deformation process, less extra length of dislocation is required to by-pass precipitate particles, the friction stress will be lower and the effective stress being supported by the network dislocations will be proportionately greater. This is in agreement with observed faster creep rates.

It has been suggested earlier that under conditions of creep deformation, a dislocation cannot be emitted in the forwards direction unless the applied stress is greater than the inherent friction stress due to the γ' precipitate. For dislocation flow to be maintained it is considered that segments of the dislocation line are concave to the

applied stress and are at a critical size to emit dislocations. For stress reductions sufficient to just cause instantaneous negative flow it follows that segments concave to the effective stress are at a critical size to emit a dislocation. This condition could be achieved if the difference between the effective stress operating under the original applied stress and the effective stress required to maintain forwards flow under the reduced applied stress is greater than the inherent friction stress to cause dislocation flow. Since the driving stress would now act in the back direction, anelastic recovery should be observed. This model predicts a constant stress reduction for anelastic recovery (independent of applied stress), the level depending on the inherent friction stress at the temperature concerned.

The model requires further refinement to take account of the increased stress reductions required to cause anelastic recovery at very high applied stresses. If γ' precipitates are now considered to be sheared by dislocations[136], this process will reduce the additional length of dislocation required at lower stresses to climb over precipitates, ie σ_0 will be reduced, but replaced by the stress supported through the anti-phase boundary energy created by dislocations passing through an ordered structure. This means that for anelastic recovery to just occur larger stress reductions are required the greater the amount of precipitate cutting since additional stress is required to 'unpin' dislocations from precipitates. The above model can account for the experimental agreement found between the inherent friction stress and the stress reduction to cause negative flow, see Figures 51 and 47.

Again for Mar M246, any model would have to be more complex because of the two distinct sizes of precipitate which are present. Although insufficient evidence is available to allow a detailed model to be proposed, it has been found that in this case the stress reduction for negative flow is less than the inherent friction stress which suggests that most of the dislocation-precipitate interaction which occurs, is with the smaller size of precipitates.

In the present results two further points of significance should be noted.

(1) For Nimonic 90 initial creep rates have a stress exponent of 4 for all applied stress levels tested, see Figure 20, even those where the steady-state level is 8.

(2) Using the friction stress concept the initial and steady-state creep rates are found to be identical for the same effective stress - even although dislocation distributions may be different.

The observations by Lagneborg[120], that the change in stress dependence of the steady-state creep rate graph from a value of 4 to one of 8 could be attributed to change in deformation mechanism, were made on test pieces stopped in the steady-state deformation region. However if these observations are attributed to changes which may occur during initial creep deformation then some significant correlations can be made of the current data as shown in Table VI on page 117.

Considering the limiting applied stresses at which the stress dependence of the steady-state creep rate data changes from n = 4 to n = 8 in Figure 19, case 1 in Table VI, if for the three temperatures the higher stress mechanism operates from the commencement of creep then it occurs under an effective stress equal to the applied stress σ_A minus the inherent friction stress σ_{oI}, case 2. For effective stresses greater than the limiting values given in case 2, the higher stress deformation mechanism will operate. However as primary creep progresses the friction stress builds up towards its steady-state value and if the effective stress operating falls to or below the levels given in case 2, transition to the lower deformation mechanism will take place. It follows that over a range of high stresses, the current effective stresses operating will reach the limiting values given in case 2 during primary creep. It also follows that for this stress range a change in deformation mechanism will occur during primary creep.

The maximum increase in friction stress is to the peak steady-state level $\sigma_{o\,max}$. Case 3 illustrates values for $\sigma_{o\,max}$ taken from Figure 51. It follows that when the friction stress operating has achieved this value during loading, there should be no primary creep and $\dot{\varepsilon}_i$ should equal $\dot{\varepsilon}_s$. From Figures 19 and 20 the extrapolated values for the intersections of the initial and steady-state creep rates can be obtained. These applied stress levels are given in case 4. It is interesting to note the agreement between the values in case 4 and transitions in σ_o measured during secondary creep deformation, case 5, transition in $\Delta\sigma_c$, case 6, and further transition in steady-state stress exponent n from a value of 8 to a value of 14, case 7.

TABLE VI

Summary table of transition stress levels in Nimonic 90

Case	Detailed conditions All stresses in MN/m^2	Temperature		
		1073K	1123K	1173K
1	Applied stress for transition in steady-state creep rate (Figure 19) from n = 4 to n = 8	316	223	154
2	Equivalent effective stress at commencement of test	(316 - 77) = 239	(223 - 49) = 174	(154 - 31) = 123
3	Maximum friction stress values	216	142	77
4	Applied stress at which extrapolated values for $\dot{\varepsilon}_i$ and $\dot{\varepsilon}_s$ are equal	477	339	220
5	Applied stress corresponding to σ_o falling	Not measured	300	185
6	Applied stress corresponding to $\Delta\sigma_c$ increasing with applied stress	462	323	208
7	Applied stress for transition in steady-state creep rate n = 8 to n = 14	Not measured	293	Not measured
8	Applied stress for change in deformation mechanism to be maintained in steady-state (case 2 and case 4)	(216 + 223) = 439	(174 + 142) = 316	(123 + 77) = 200

Case 2 gives the minimum effective stress to cause the high deformation mechanism to operate. If this deformation mechanism is maintained under steady-state conditions the effective stress must be equal to or greater than these levels. However the maximum friction stresses will now operate. For the three temperatures tested these stresses are given in case 3. Adding values in cases 2 and 3 gives the minimum applied stress necessary to maintain the higher deformation mechanism, case 8. The agreement in stress levels with cases 4, 5, 6 and 7 suggest that under steady-state conditions there may be a unique effective stress at which dislocation bowing can be maintained since higher effective stresses may cause further change in deformation mechanism, probably cutting of γ' precipitate particles.

Since creep rate can be shown to be proportional to rate of recovery, Figure 77, and since it is also proportional to effective stress, Figure 52, it follows that a correlation may exist between effective stress and rate of recovery, ie effective stress and rate of growth of the dislocation network to the critical size to emit a dislocation. From this and the discussion on the data given in Table VI it follows that changes in the slopes of the applied stress versus minimum creep rate graphs do not necessarily indicate that different deformation mechanisms are operating below and above the transitions but that different mechanisms may have operated during earlier stages of primary creep. Also creep rates increase progressively as effective stress increases but, unlike creep rate versus applied stress correlations, these do not show transition in rate with possible change in method of dislocation by-passing precipitates. This supports the earlier proposal that the detailed mechanism by which dislocations by-pass precipitate particles is important only in determining the level of the friction stress operating. It also helps to confirm the suggestion that ultimately deformation of the matrix material is rate controlling.

Insufficient data is available on the more complex alloy, Mar M246, and no detailed model can be proposed at present. However general deformation processes appear to be similar to those for Nimonic 90 and even without a detailed model, the effective stress concept allows the current data on Mar M246 and on Nimonic 90 to be explained on a general creep recovery basis.

6.4 Implications of friction stress concepts to variable stress creep

(a) Frequency effect in cyclic creep

A physically acceptable explanation of this effect can be developed based on the incubation periods which are observed when small instantaneous stress reductions are made during an essentially constant stress creep test. The occurrence of these incubation periods implies that for any applied stress level, work hardening will create a friction stress level as illustrated by σ_0 in Figure 51. The result of this is to reduce the damaging effect of the applied stress. If part of the applied stress is removed, initially the three-dimensional network size is too refined to maintain dislocation emission and must grow by recovery to a value consistent with the new applied stress. Prior to true equilibrium being established no net creep flow occurs and it is reasonable to suppose that no damage is incurred. The effect is considered to be that illustrated schematically in Figure 76.

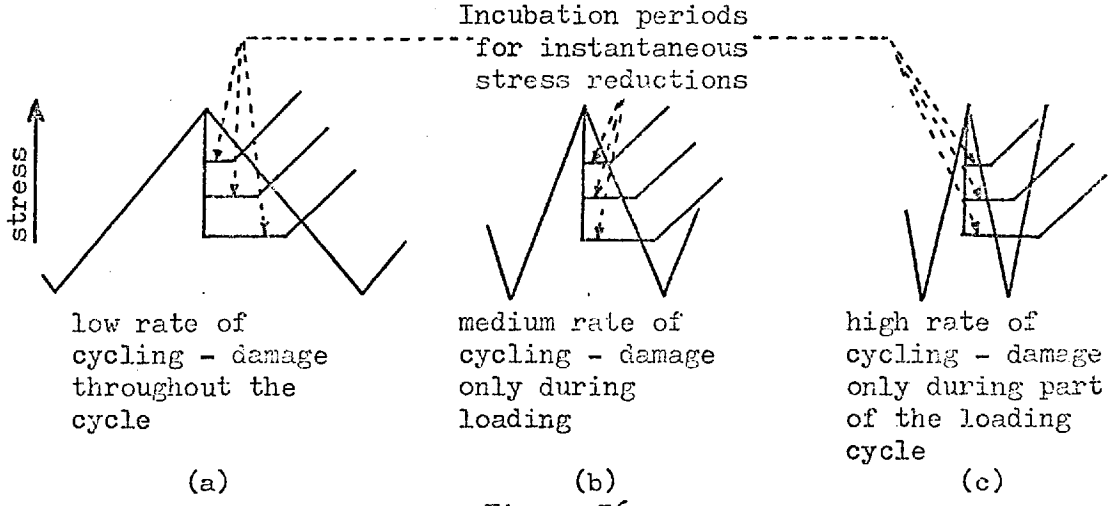

Figure 76

If the rate of cycling is 'slower' than the rate of network growth (represented through the incubation periods), Figure 76a, then during unloading full damage will be incurred, ie throughout the whole of the unloading cycle. If the rate of cycling is slightly faster, Figure 76b, since the rate of network growth is constant, now incubation periods can be of sufficient duration that during unloading they are longer than the unloading time and so damage is incurred during part of the cycle only. The situation is slightly more complex since once the

stress level is reduced to below the critical stress for negative flow, anelastic recovery effects will aid recovery such that incubation periods tend to be destroyed, the net effect being that although no effective damage is incurred during fast unloading the friction stress has been reduced and the network has grown to sufficient size that damage is incurred throughout the whole of the next loading cycle.

Since anelastic recovery is time dependent, for very high cycle frequencies Figure 76c, it has had insufficient time to reduce the friction stress and so damage is incurred only during the final stages of loading.

It follows therefore that over a wide range of relatively low frequencies, Equation (128) will adequately predict the cyclic life, however over a range of slightly faster frequencies damage will be incurred during the loading cycle only and lives will now be about twice those predicted by this equation. For very fast frequencies lives will be even greater than twice the value predicted by this equation. Under these conditions it will be necessary to incorporate a frequency term into the prediction as has been developed in Equation (131). There appears to be an upper limit to the life obtained experimentally as illustrated by the close agreement between the times to failure for the 100 and 1000 c/min tests given in Figure 30.

(b) Equation of state life predictions for stress variations during creep

Previously the friction stress concept has been applied to single stress change tests in the steady-state region[86]. The experimental results showed that the creep rate after an incubation period may be lower than would be found during steady-state creep at the lower stress level. The current investigation allows the friction stress concepts to be extended to repeated stress variations during creep.

(1) Considering the stress range in which a stress exponent of 8 applies in the original steady-state creep rate correlation $\dot{\varepsilon}_s = A\sigma^n$ (a) for small stress reductions less than the critical stress for backwards flow (for example 45 MN/m^2 for Nimonic 90 at 1123K) no anelastic recovery occurs, incubation periods are very short and the re-established creep rate at the lower stress level is identical to that obtained from a constant stress test at the lower stress, see Figure 48. Since σ_o remains constant for both stress levels, this

indicates that no large structural changes take place. (b) For stress reductions greater than critical stress to cause backwards flow the creep rate immediately after the stress reduction is negative. The eventual forwards creep rate is found to be slightly faster than obtained in constant stress creep tests at the lower stresses. From a series of stress reductions causing initial negative flow it can be seen for both Nimonic 90 and for Mar M246 that the creep rates are all faster than in the equivalent constant stress tests at the lower stress levels. The implication of these results is that if anelastic recovery occurs on reducing the applied stress then it would appear that this destroys part of the dislocation contribution to the friction stress such that creep re-commences under a higher effective stress and hence creep rates tend towards initial values.

(2) Considering the region in which a stress exponent of 4 applies in the equation $\dot{\varepsilon}_s = A\sigma^n$, (a) for small stress reductions less than the critical stress for negative flow, as found previously, incubation periods are observed and the creep rates after the incubation period are lower than obtained in corresponding static creep tests. From a series of stress reductions in Nimonic 90 and Mar M246 the value of n is found to be greater than 4 as can be seen in Figure 48. (b) For large stress reductions greater than the critical stress for negative flow, anelastic recovery accompanies each stress reduction but under these conditions, for a series of stress reductions the value of n obtained from the eventual forwards creep rates is found to be much lower than 4 but the greater the stress reduction the closer the creep rate comes to that obtained in a static creep test.

Applying the friction stress concept to explain the results obtained in (2)(a) and (b), in these cases under the original applied stress the friction stress is stress dependent. In case (a), on re-commencement of forwards creep at the lower stress level, the friction stress is still close to its original value, is higher than the monotonic creep value for the lower stress level, and so creep occurs under a lower effective stress than in the static creep test. For large stress reductions as in case (b) the effect of anelastic recovery is to reduce the friction stresses to levels which are close to those operating under steady-state monotonic creep conditions.

Applying the broad implications of the friction stress concept to damage predictions made using equation of state theories, the four conditions discussed above will be considered separately.

(1) For regions in which the stress exponent n is 8

(a) for small stress reductions the 'correct' creep rate for the new applied stress is established immediately after the incubation period and so strain hardening would be expected to predict damage reasonably accurately and experimental life fractions would be expected to sum to unity.

(b) for larger stress reductions a faster creep rate is established at the lower stress level and so strain hardening would be expected to give slightly optimistic predictions and experimental life fraction determinations would be expected to sum to less than unity. However since the damage under peak stress conditions is very much greater than at the lower stress this could result in an experimental life fraction which could still be close to unity.

(2) For regions in which the stress exponent n is 4

(a) for small stress reductions the creep rate following the incubation period is lower than the 'correct' creep rate for the new applied stress and so strain hardening would be expected to give pessimistic predictions of damage. Experimental life fractions would be expected to sum to greater than unity.

(b) for large stress reductions creep rates after the incubation periods are found to be closer than in case (a) and so strain hardening predictions should be more accurate and experimental life fraction determinations should be closer to unity than in case (a).

The predictions above are difficult to prove in short time testing, however a programme of tests is currently being conducted to test these proposals[130]. The two main points in the above predictions have been tentatively verified, namely (i) under conditions where the stress exponent n is 8, for small stress reductions lives are close to predictions made by strain hardening or life fraction methods.
(ii) Under conditions in which the stress exponent n is 4 for small stress reductions the lives are greater than predicted by strain hardening or life fraction and in cyclic tests having longer hold periods at the lower stress level, lives at these lower stresses are found to be greater than under static creep, even without consideration of the time spent at the higher stress levels.

These results are in agreement with friction stress observations and indicate the potential of this concept when applied in conjunction with equation of state theories. Although further work is necessary prior to quantitatively including friction stress in equation of state predictions the approach gives a possible physical explanation for the wide differences in the degree of success recorded in the technical literature when applying equation of state concepts to life predictions under conditions of variable stress.

6.5 Main findings and conclusions

The work conducted in this thesis can be divided into

(a) extension of empirical life prediction methods and

(b) extension of the understanding of high temperature deformation.

Findings relating to the former category have been presented in Section 5 but for completeness are summarised here. The main conclusions are as follows.

(1) Power law equations can be used to predict initial creep rates and an appropriate expression has been derived.

(2) Based on the Graham and Walles creep equations, computer programs have been written which allow analysis of basic creep data and regeneration of any required creep curve, within the original range of data, to a high degree of accuracy.

(3) Equations have been developed which allow strain accumulation and times to fracture under various cyclic loading conditions to be predicted from monotonic creep. The equations derived for the various predictions are summarised in Section 5.7.

(4) The advantage of directionally solidified and single crystal forms of Mar M246 over conventionally cast structures is not due to a reduction in minimum creep rate, but to a slight retardation of the onset of tertiary deformation and an increased contribution from this stage. Specimen size effects are much more significant in conventionally cast than in directionally solidified and single crystal forms of Mar M246.

(5) The laws for compressive creep are similar to those for tensile creep. Conventionally cast Mar M246 has slightly superior resistance to compressive deformation than to tensile deformation, however no further improvement in compressive creep resistance is achieved in directionally solidified or single

crystal forms of the material. Both for Nimonic 90 and for Mar M246 tertiary creep in compression is accompanied by strain induced phase transformations.

(6) A critical stress reduction must be exceeded for anelastic recovery to occur. Over a range of applied stresses the reduction required is constant.

(7) The experimental results obtained from Nimonic 90 and Mar M246 are best fitted by the recovery creep/friction stress model, creep rates in both the forwards and backwards directions being controlled by metallurgical recovery.

(8) The steady-state friction stress, σ_0, has been shown to have an inherent contribution due to second phase precipitate particles and a stress dependent contribution due to dislocation/precipitate interaction. The application of an effective stress $(\sigma_A - \sigma_0)$ to the relationship between stress and minimum creep rate has reduced the several stress exponents previously required to a single value. The inherent friction stress can also be used to calculate initial effective stresses and this has permitted initial and minimum creep rates to be superimposed.

(9) By the use of the friction stress concept, activation energies for initial and steady-state creep rates of Nimonic 90 and Mar M246 can be reduced to that of a basic Ni-Cr solid solution alloy.

(10) The normalised effective stress $\left(\sigma_A - \sigma_0/\sigma_{\text{proof stress}}\right)$ allows the steady-state creep rate data for several materials at a variety of temperatures to be superimposed without the use of separate activation energy or diffusion rate constants.

(11) For Nimonic 90 at 1173K, even under cyclic loading, creep is the major deformation mechanism, higher frequencies increasing both the number of cycles to failure and the times to failure. The friction stress concept provides a satisfactory explanation of this effect.

7.0 Relevance of the current research programme to the practical problem of thermal fatigue

An objective of the various programmes on static and cyclic properties of materials at elevated temperature has been to provide data which might allow an assessment of the resistance of materials to

thermal fatigue, where thermal fatigue is considered to be due to the repeated application of stresses that are thermal in origin. This type of damage is experienced by gas turbine components such as turbine blades, as a consequence of the rapid change in the temperature of the environment on start-up or shut-down of an engine.

7.1 Choice of materials

Nimonic 108 was selected as being a typical wrought material used for turbine blades. Its characteristics have been discussed earlier.

7.2 Experimental technique

The stress-temperature history experienced by the most damaged element of a Nimonic 108 blade in a current engine has been calculated in another research programme. A typical history is given in Figure 84a. The cycle demands heating in 4 seconds and cooling in 3 seconds. However it has been found experimentally that natural cooling of the hollow specimen employed in these tests takes about 20 seconds and that forced cooling, by passing air down the centre of the specimen, introduces temperature gradients such that very high transient strain damage is developed at low temperatures under theoretically elastic conditions. The cycle time has therefore been extended such that it is about 15 times slower than calculations of practice.

A commercial testing machine has been adapted to cycle specimen load and temperature simultaneously. A schematic representation of the operational functions of the machine is given in Figure 83. Load is sensed by a transducer, compared with a theoretical function in a summing amplifier and the resulting error signal used to activate a hydraulic servo valve. The desired function can be maintained to within an accuracy of 0.1 per cent. Specimen temperature is sensed by a thermocouple spot welded to the gauge length. The rapid heating rates required can be achieved with silicon controlled rectifiers and resistance heating, and can be maintained to within 2K of the desired temperature throughout the cycle, peak temperature being maintained to within ±0.5K. Thermocouples were found to give low millivolt outputs (for example 50K at 1273K) and were calibrated against a total radiation pyrometer.

Manufacturers creep rupture data was used to obtain an appreciation of general damage characteristics. The theoretical stress-temperature combinations of the cooling phase were superimposed on

stress-rupture curves as shown in Figure 85. If it is assumed that compression is as equally damaging as tension, damage incurred during compression can be assessed in this manner and so this figure includes representation of the tensile equivalent of compressive damage during heating.

This plot gives little indication of the actual damage experienced by the blade due to the various stress-temperature combinations since exposure times are not quantified. If the transient stress and temperature cycles are split into a large number of equal time intervals, Δt, within each of which it is assumed that both stress and temperature are constant, and if creep life fraction theory is assumed to apply, then the relative damage contributions of each stress-temperature combination can be assessed. At any stress and temperature, damage, d, will be directly proportional to the time interval, Δt, but inversely proportional to the time to fracture t_f

$$\text{ie} \qquad d \propto \frac{\Delta t}{t_f}$$

Using the data from Figures 84a and 85, Figure 84b can be obtained. This allows the most damaging regions to be specified and hence allowed effort to be concentrated on achieving greatest experimental control over these regions. This information was also used in cutting stress and temperature cams to their required profiles. Reproducible heating and cooling cycles were obtained which had apparent surface variations of less than ±1K, maximum and minimum temperatures being achieved to within ±0.5K. A temperature gradient from the ridge to the centre of the gauge length of about 30K was a necessary consequence of using resistance heating and water cooled ends. A scissors type extensometer, located on ridges on the specimen, allowed strain discrimination to 2×10^{-5} when monitoring a complete damage cycle on a chart recorder. These tests were conducted under load control and not stress control since temperature gradients along the specimen would upset systems developed for maintaining constant stress.

7.3 Analysis of thermal fatigue damage

Applying strain hardening hypotheses to the Graham and Walles creep equations, if the stress σ_1 has been applied at temperature T_1 for time t_1 the equivalent damage time t_2 for stress σ_2 and temperature T_2 can be calculated from

$$\varepsilon = c_1 \sigma_1^{\beta} t_1^{\kappa} \psi_1^{\kappa} = c_2 \sigma_2^{\beta} t_2^{\kappa} \psi_2^{\kappa}$$

where $\psi = (T' - T)^{-20}$

and if no transition in stress exponent β occurs over the change in test condition, it follows that

$$t_2 = t_1 \left(\frac{\sigma_1}{\sigma_2}\right)^{\frac{\beta}{\kappa}} \frac{\psi_1}{\psi_2} \qquad \ldots.(149)$$

From this the total damage incurred over a range of stress and temperature conditions can be converted to an equivalent damage under any selected stress and temperature.

If the subscript 'L' denotes the last stress/temperature/time combination in the damage sequence, it follows that the damage per cycle, expressed as strain accumulation, can be presented in the form

$$\Sigma_1^L \Delta\varepsilon = \Sigma c \, \Delta t^{\kappa} \left[\sigma_L^{\frac{\beta}{\kappa}} \psi_L + \sigma_{L-2}^{\frac{\beta}{\kappa}} \psi_{L-2} + \ldots. \sigma_1^{\frac{\beta}{\kappa}} \psi_1\right]^{\kappa} \qquad \ldots.(150)$$

However converting the form of this equation to the equivalent time concept which has been developed for the various isothermal cases in Section 5, it follows that

$$\Sigma_1^L \Delta\varepsilon = \Sigma c \, \sigma^{\beta} t_{L*}^{\kappa} \qquad \ldots.(151)$$

where t_{L*} is the equivalent time of 1 cycle at σ_L and T_L, and is given by

$$t_{L*} = \Delta t \left[1 + \left(\frac{\sigma_{L-1}}{\sigma_1}\right)^{\frac{\beta}{\kappa}} \left(\frac{\psi_{L-1}}{\psi_L}\right) + \left(\frac{\sigma_{L-2}}{\sigma_L}\right)^{\frac{\beta}{\kappa}} \left(\frac{\psi_{L-2}}{\psi_L}\right) + \ldots.\right]$$

It follows that the equivalent total time is given by Nt_{L*} and hence the constant c in the equation above need not be evaluated if the rupture time t_{Lf} of a monotonic creep test at stress σ_L and temperature T_L is known. The number of cycles to failure can therefore be given by

$$N = t_{Lf}/t_{L*} \qquad \ldots.(152)$$

Using this equation the number of cycles to failure for the theoretical cycle have been calculated assuming (i) damage occurs during heating only and (ii) damage occurs during cooling only. The predictions are given in Table VII for a variety of time increments.

The damage range specified to calculate the number of cycles to failure N_f in Table VII includes an arbitrary chosen maximum damage region. Using a time increment of 0.2 the damage range was increased by about 66 per cent relative to that of the results given in Table VII and the effect on the predicted number of cycles is shown in Table VIII.

The method used above has calculated damage in terms of a minor damage combination, stress σ_L and temperature T_L, however any stress-temperature combination could be chosen in the equations and so converting to equivalent time under peak damage stress and temperature (σ_M, T_M) and using a value of time increment of 0.2 seconds the new prediction is compared with the data from Table VIII in Table IX.

7.4 Discussion of thermal fatigue analysis and comparison with experimental results

By using available monotonic creep rupture data to calculate the various constants associated with the equation derived to predict thermal fatigue, it has been possible to assess several properties of the equation.

Table VII shows that, provided the damage region is divided into intervals of 0.25 seconds or less (for example, 12 or more steps) the predicted results will be close to continuous change predictions. From Table VIII it can be seen that increasing the damage range by about 60 per cent decreases the predicted cyclic life by about 20 per cent.

Relative to the effects of other variables, changing the equivalent time from last stress and temperature conditions to maximum damage stress and temperature conditions, has had the most marked difference on the predicted number of cycles to failure. This is due

mainly to the method employed in the analysis. Since only limited monotonic creep data with large scatter factors was available, in the initial creep analysis of this data, effort was concentrated in obtaining constants which on regeneration would give the best fit over the peak damage region. It follows therefore that the other regions were slightly less accurately specified and, in the initial thermal fatigue analysis, the methods adopted converted damage to stresses and temperatures in the less accurately specified regions and hence predictions would also have a larger error factor. This is more significant on cooling than on heating because in the latter case the last stress-temperature combination is close to the maximum damage stress-temperature condition and hence will still be accurately predicted.

The analysis has the advantage that by conducting two or three sorting tests at maximum stress-temperature damage conditions, data derived on other equipment or on different casts of materials can be partly normalised, the original data allowing the remaining constants to be calculated to a degree of accuracy within that of general testing techniques employed. These equations should therefore give the most accurate predictions of thermal fatigue but this can only be verified further by comparing predicted and experimentally obtained data.

From basic monotonic creep data on Nimonic 108 the values calculated for the various constants were found to be such that $\frac{\beta}{\kappa} = 8$, $T' = 1520K$ and for rupture $\kappa = 9$. Predicted and experimental cycles to failure are compared in Figure 86. The predicted rupture lives are found to be within a factor of 2 of those obtained experimentally, largest deviations occurring in early tests. This accuracy is considered to provide satisfactory evidence that Nimonic 108 blades subjected to transient stress and temperature fail by creep dominated deformation mechanisms and also that laws developed to predict isothermal transient stress damage can be extended to cover concurrent temperature variations.

Internal friction concepts have not been applied to the analysis of thermal fatigue results, however, current work indicates that in constant strain rate tests subsequently held at constant strain, materials relax to stress levels close to the friction stress which was initially operating. In extending the work to strain controlled cycling it may be possible to include friction stress concepts.

7.5 Main findings and conclusions

(1) A machine has been developed which allows rapid but accurately controlled changes in stress and temperature.

(2) The empirical analysis applied to isothermal testing has been extended to the transient temperature situation. Lives experienced in this latter situation can be predicted to within a factor of 2 using monotonic creep rupture data and the equation

$$N = \frac{t_{Lf}}{t_{L^*}}$$

ACKNOWLEDGEMENTS

The author wishes to acknowledge with thanks the help and encouragement given throughout the period of this research by both his supervisor, Dr G P Tilly, and his director of studies, Dr G A Webster.

Gratitude is expressed to the Director of NGTE for use of facilities. Appreciation is also expressed to his colleague, Dr W J Evans, for helpful discussion.

REFERENCES

No.	Author(s)	Title, etc
1	E N C Andrade	Proc Roy Soc, Vol. A84, p.1, 1910
2	J B Conway M J Mulliken	Paper presented at AIME meeting Detroit, Mich, 1965
3	J de Lacombe	Rev Met, Vol. 36, p.178, 1939
4	R Lagneborg	International Met Reviews Vol. 17, p.130, 1972
5	K E Amin A K Mukherjee J E Dorn	J Mech Phys Solids Vol. 18, p.413, 1970
6	P G McVetty	Mech Eng, Vol. 56, p.149, 1934
7	B Wilshire P L Threadgill	Proc I.S.I. Conference on the creep strength of steels Sheffield 1972
8	J B Conway M J Mulliken	Trans AIME, Vol. 236, p.1629, 1966
9	J B Conway	Numerical methods for creep and rupture analysis London (Gordon and Breach) 1968
10	W J Evans	Ph.D Thesis, Wales, 1969
11	A J Kennedy	Processes of creep and fatigue Oliver and Boyd, Edinburgh and London 1962
12	A Graham K F A Walles	J I.S.I., Vol. 179, p.105, 1955
13	F H Norton	The creep of steel at high temperatures McGraw Hill, New York, 1929
14	R W Bailey	Engineering, Vol. 129, p.265, 1930
15	J E Dorn	J Mech Phys Solids, Vol. 3, p.85, 1955
16	P Feltham	Proc Phys Soc London B, Vol. 66, p.865 1953
17	J Weertman	J Applied Phys, Vol. 28, p.362, 1957
18	F Garofalo	Fundamentals of creep and creep-rupture in metals New York 1965

REFERENCES (cont'd)

No.	Author(s)	Title, etc
19	F R Larsen J Miller	Trans Amer Soc Mech Engineers (Macmillan) Vol. 74, p.765, 1952
20	S S Manson A M Haferd	NASA Tech Note 3195 1954
21	A Graham	Engineer, Vol. 193, p.198, 1952
22	F J Clauss	Deformation and fracture at elevated temperatures MIT Press, Cambridge Mass, 1965
23	P K Raut W R Clough	J Basic Engineering p.8, March 1972
24	Y N Rabotnov	Some problems on the theory of creep NACA Tech Memo 1353, 1948
25	Y N Rabotnov	Joint International Conference on Creep Vol. II, p.117, 1963
26	H R Voorhees J W Freeman	Wright Air Development Centre Tech Report, January 1959 (reviewed by M M Aboelata and I Finnie)
27	D L Marriott F A Leckie	Conference of thermal loading and creep in structures and components 1964
28	I Finnie W R Heller	Creep of engineering materials McGraw Hill 1959
29	A E Johnson	Proc Inst Mech Eng, 1941
30	J D Lubahn R P Felgar	Plasticity and creep of metals McGraw Hill, 1959
31	A S Norwick B S Berry	Anelastic relaxation in crystalline solids Academic Press, 1972
32	R Lagneborg	Met Sci J, Vol. 3, p.18, 1969
33	H Clauer B A Wilcox J P Hirth	Acta Met, Vol. 18, p.381, 1970
34	R Lagneborg B Modeer	Jerkontorets Ann Vol. 155, p.363, 1971

REFERENCES (cont'd)

No.	Author(s)	Title, etc
35	J E Bird A K Mukherjee J F Dorn	Proc International Conference on quantitative relationships between props and microstructure Jerusalem, Israel Univ Press, p.255 1969
36	C R Barrett C N Ahlquist W D Nix	Met Sci J, Vol. 4, p.41, 1970
37	Y Ishida	Trans Jap Inst Met Vol. 9, p.120, 1968
38	W Kauzmann	Trans AIME, Vol. 143, p.57, 1941
39	N F Mott	Creep and fracture of metals at high temperatures London HMSO, p.21, 1956
40	P B Hirsch D H Warrington	Phil Mag, Vol. 6, p.735, 1961
41	J E Dorn J D Mole	Proc of 3rd Symposium on naval structural mech p.95, 1964
42	L Raymond J E Dorn	Trans AIME, Vol. 220, p.560, 1964
43	C R Barrett W D Nix	Acta Met, Vol. 13, p.1247, 1965
44	J Weertman	Trans AIME, Vol. 233, p.2069, 1965
45	A H Cottrell	Dislocations and mechanical properties of crystals Ed J C Fisher et al New York, John Wiley, 1957
46	D McLean K Hale	Structural processes on creep London J I.S.I., p.19, 1961
47	J C M Li	Trans AIME, Vol. 227, p.1474, 1963
48	J C M Li	Acta Met, Vol. 11, p.1269, 1963
49	W G Johnston J J Gilman	J Applied Phys, Vol. 30, p.129, 1959
50	N S Akulov	Acta Met, Vol. 12, p.1195, 1964
51	C R Barrett W D Nix O D Sherby	TASM, Vol. 59, p.3, 1966

REFERENCES (cont'd)

No.	Author(s)	Title, etc
52	G A Webster	Phil Mag, Vol. 14, p.775, 1966
53	G A Webster A P D Cox J E Dorn	Met Sci J, Vol. 3, p.201, 1969
54	R N Bailey	J Inst Metals, Vol. 35, p.27, 1926
55	E Orowan	J West Scotland Iron and Steel Inst Vol. 54, p.45, 1946-47
56	A H Cottrell V Aytekin	J Inst Metals, Vol. 77, p.389, 1950
57	Y Ishida D McLean	J Iron and Steel Inst Vol. 205, p.88, 1967
58	D Sidey B Wilshire	Met Sci J, Vol. 3, p.56, 1969
59	B L Jones C M Sellars	Met Sci J, Vol. 4, p.96, 1970
60	N F Mott	Proc Roy Soc London A220, p.1, 1953
61	J Weertman	J Appl Phys, Vol. 26, p.123, 1955
62	J S Koehler	Phys Rev, Vol. 86, p.52, 1952
63	J Weertman	J Appl Phys, Vol. 28, p.362, 1957
64	R Gasca-Neri C N Ahlquist W D Nix	Acta Met, Vol. 18, p.655, 1970
65	R Gasca-Neri C N Ahlquist W D Nix	Acta Met, Vol. 18, p.655, 1970
66	A K Mukherjee J E Bird J E Dorn	Proc of Symposium on interaction between dislocations and defects Vol. II, Part III, p.422, 1968
67	J C M Li	Discussions of Faraday Soc Vol. 38, p.138, 1964
68	P M Hazzledine	J D Physique, Vol. 27, Supplement C3, p.210, 1966
69	D McLean	Met Rev, Vol. 7, p.481, 1962
70	G S Ansell J Weertman	Trans AIME, Vol. 215, p.838, 1959

REFERENCES (cont'd)

No.	Author(s)	Title, etc
71	G S Ansell	Precipitation on iron base alloys AIME Gordon and Breach, New York, 1965
72	D McLean	Rep Progress Physics, Vol. 29, p.1, 1966
73	J Friedel	Dislocations Pergamon Press, Oxford, 1964
74	S K Mitra D McLean	Proc Roy Soc, Vol. A295, p.288, 1966
75	D McLean	Trans AIME, Vol. 242, p.1193, 1968
76	R Lagneborg	Metal Sc J, Vol. 4, p.89, 1970
77	P W Davies K R Williams	J Inst Metals, Vol. 97, p.337, 1969
78	C R Barrett C N Ahlquist W D Nix	Met Sc J Vol. 4, p.41, 1970
79	W J Evans B Wilshire	ibid, Vol. 4, p.89, 1970
80	C N Ahlquist W D Nix	Acta Met, Vol. 19, p.373, 1971
81	E Orowan	Proc Phys Soc, Vol. 52, p.8, 1940
82	C R Barrett	Trans Metal Soc AIME, Vol. 239, p.1927 1967
83	T Vreeland Jr	Dislocation dynamics ed by J C M Li McGray Hill, p.487, 1968
84	N F Mott	Phil Mag, Vol. 44, p.742, 1953
85	P W Davies R W Evans	Acta Met, Vol. 13, p.353, 1970
86	P W Davies G Nelmes K R Williams B Wilshire	Met Sc J, Vol. 7, p.87, 1973
87	P L Threadgill B Wilshire	Met Sc J, Vol. 8, p.117, 1974
88	K R Williams B Wilshire	Met Sc J, Vol. 7, p.176, 1973

REFERENCES (cont'd)

No.	Author(s)	Title, etc
89	G J Lloyd R S McElroy	Acta Met, Vol. 22, p.339, 1974
90	H Z Suzuki	Dislocations and mechanical properties of crystals ed J C Fisher, W G Johnston, R Thomson and T Vreeland John Wiley and Sons, New York, 1957
91	A H Cottrell	Relation of properties to microstructure ASM, Clevedon, p.131, 1954
92	A H Cottrell C S Hunter F R N Nabarro	Phil Mag, Vol. 44, p.1064, 1953
93	G Schnoech Seeger	Acta Met, Vol. 7, p.469, 1959
94	N F Mott F R N Nabarro	Report on Bristol Conference Strength of solids Phys Soc London, p.1, 1948
95	J C Fisher	Acta Met, Vol. 2, p.2, 1954
96	C K L Davies P W Davies B Wilshire	Phil Mag, p.12, 1965
97	J Friedel	Conference on internal stresses and fatigue Elsevier Publishing Co, Amsterdam p.220, 1959
98	J P Dennson R J Llewellyn B Wilshire	J Inst Metals, Vol. 95, p.115, 1967
99	E Orowan	Symposium of internal stresses in metals and alloys London Inst Metals, p.451, 1948
100	P M Kelly	Int Met Reviews, Vol. 18, p.31, 1973
101	A J E Foreman M J Makin	Canad. J Phys, Vol. 45, p.511, 1967
102	E A Fell	Metallurgia, Vol. 63, p.157, 1961
103	W I Mitchell	Z Melalk, Vol. 55, p.613, 1964
104	E A Fell W I Mitchell D Wakeman	Structural processes in creep Sp Report 70, I.S.I. London, p.136, 1961

REFERENCES (cont'd)

No.	Author(s)	Title, etc
105	M Hillert	Acta Met, Vol. 13, p.227, 1965
106	R Lagneborg	J Mat Sci, Vol. 3, p.596, 1968
107		Trans AIME, Vol. 236, p.519, 1966
108	R K Ham	Ordered alloys - structural application and physical metallurgy Proc 3rd Bolton landing conference Clacton's Publishing Division Balon Rouge, 1970
109	M J Fleetwood	J Inst Metals, Vol. 81, p.25, 1952
110	R Lagneborg	Jernkont Ann, Vol. 155, p.368, 1971
111	G P Tilly G F Harrison	J Strain Analysis, Vol. 7, No. 3, 1972
112	G P Tilly	J Phys (E), Vol. 3, p.292, 1970
113	D McLean	J Inst Metals, Vol. 85, 1956
114	G P Tilly	J Strain Analysis, Vol. 7, No. 1, 1972
115	S C Monkman N J Grant	Proc Am Soc Test Malv, Vol. 56, 1956
116	E L Robinson	Trans ASME, Vol. 60, 1938
117	G P Tilly	J Strain Analysis, Vol. 7, No. 4, 1972
118	W I Mitchell	Z Metallkunda, Vol. 57, 1966
119	S L Manman P Rodriguez	Sci Met, Vol. 5, 1971
120	R Lagneborg B Bergman	Jernkont Ann 155, p.368, 1971
121	D A Woodford	Met Sc J, Vol. 3, p.50, 1969
122	C T Sims	J.O.M., Vol. 18, 1966
123	H E Gresham	Metals and Materials, Vol. 11, p.433, 1969
124	J E Doherty B H Kear A F Giamei	J.O.M., Vol. 23, 1971
125	P W Davies	Jernkont Ann, Vol. 155, p.302, 1971

REFERENCES (cont'd)

No.	Author(s)	Title, etc
126	P W Davies J P Dennison D Sidey	JIM, Vol. 101, p.153, 1973
127	G R Leverant D H Kear J M Oblak	Met Trans, Vol. 4, p.355, 1973
128	J H Gittus	Scripta Met, Vol. 6, p.247, 1972
129	P W Davies B Wilshire	Scripta Met, Vol. 5, p.457, 1971
130	G F Harrison W J Evans	Current work at NGTE
131	J E Restall	Private communication
132	D Raynor J M Silcock	Met Sci J, Vol. 4, p.121, 1970
133	R Lagneborg	Scripta Met, Vol. 7, p.605, 1973
134	H E Evans K R Williams	Phil Mag, Vol. 25, p.199, 1972
135	J P Dennison R J Llewellyn B Wilshire	Met Sc 5, Vol. 7, p.87, 1973
136	S M Copley B H Kear	Trans AIME, Vol. 239, p.984, 1967

TABLE I

Chemical composition and heat treatment

Alloy	C	Cr	Co	Fe	W	Mo	Ta	Ti	Al	Ni	Heat treatment
Nimonic 90	.1	20	18	3	-	-	-	2.5	1.5	bal	8h 1153K a.c. 16h 973K a.c.
Nimonic 108	.2	15	20	2	-	5	-	1.5	4.5	bal	8h 1153K a.c. 16h 973K a.c.
Mar M246	.15	9.0	10	-	-	2.5	1.5	1.5	5.5	bal	As cast

TABLE II

Schematic illustration of test programme

In text - see page 54

TABLE III

Electron-probe microanalysis of the distribution of elements in Nimonic 90 after high compressive strain

Position	Fe	Cr	Ti	Al	Co	Ni	C
Centre of grains	0.5	21.9	2.4	0.9	16.7	56.4	-
Matrix in wide denuded grain boundary	0.6	22.4	0.9	1.7	18.9	53.5	-
Matrix in narrow denuded grain boundary	0.4	22.0	1.6	1.5	17.6	55.9	-
Carbides in wide denuded grain boundary	0.3	20.6	35.2	0.7	10.9	12.2	bal
Carbides in narrow denuded grain boundary	-	17.1	47.3	-	10.1	10.9	bal
Chemical analysis of 'as received' material (0.395 Si, 0.04 Mn)	0.65	19.05	2.62	1.43	16.7	bal	0.1

TABLE IV

Summary of metallographic examination of selected test specimens

	Temp.	Stress (MN/m^2)	Type of cracking	Crack distribution (per mm)	Crack length (mm)	γ' precipitate size (μ)	Total time of test hours
Monotonic creep	900	80	wedge/ cavity	10	0.05 to 0.1	0.045	129
	900	123	wedge/ cavity	6	0.1 to 0.15	0.03	24.9
	850	161.5	wedge	7	0.1 to 0.3	0.045	100.6
	800	357	wedge	7	0.15 to 0.25	0.02	11.1
Rectangular tension	900	80	wedge/ cavity	20	0.07 to 0.15	0.055	208.6
	900	138.5	wedge/ cavity	10	0.07 to 0.15	0.045	27.8
	850	154	wedge	10	0.05 to 0.15	0.02	199.6
	800	346	wedge	10	0.05 to 0.18	0.025	39.2

TABLE V

Statistical analysis of Nimonic 90 creep data

Test	Standard deviation (log time)			
	$t_{\frac{1}{3}}$	t_1	t_3	t_r
Monotonic tensile creep	0.33	0.22	0.10	0.10
Monotonic compressive creep	0.27	0.20	0.09	-
Rectangular tensile creep	0.35	0.15	0.10	0.09
Rectangular tensile creep (combined time-temperature function)	0.4	0.15	0.11	0.09

TABLE VI

Summary table of transition stress levels in Nimonic 90

In text - see page 117

TABLE VII

Life predictions for various time intervals

Analysis employed	Region of cycle analysed	N_f for time interval Δt (seconds)				
		0.1	0.15	0.2	0.25	0.3
Equation (152)	Cooling	1424	1460	1403	1394	1196
Equation (152)	Heating	3517	3455	3424	3542	3539

$T' = 1210$ σ_L cooling $= 26.3$ T_L cooling $= 842^{\circ}C$ $c = 10^{355}$

σ_L heating $= 9.6$ T_L heating $= 952^{\circ}C$

TABLE VIII

Life predictions for several assumed damage regions

Analysis employed	Time interval Δt	Region of cycle analysed	No. of points analysed	No. of cycles to failure N_f
Equation (152)	0.2	Cooling	15 23	1403 1167
		Heating	15 24	3426 2889

TABLE IX

Comparison of life predictions based on final stress and temperature and peak damage stress and temperature

Analysis employed	Time interval Δt	Region of cycle analysed	No. of cycles to failure N_f	Damage condition for equivalent time
Equation (152)	0.2	Cooling	1403 780	σ_L, T_L σ_M, T_M
		Heating	4424 4200	σ_L, T_L σ_M, T_M

σ_L and T_L is the last stress and temperature combination in the damage region.

σ_M and T_M is the stress and temperature combination to give peak damage.

APPENDIX I

The Graham and Walles method for analysis of creep data

The basis of this method is to employ a very general solution and by a process of simplification, to use the minimum number of terms compatible with the experimental results. It is assumed that the total creep strain is the sum of a number of separate mechanisms each of which can be expressed by a Nutting type equation and so in the general form,

$$\varepsilon_c = \Sigma\, c\, \sigma^{\beta}\, \phi^{\kappa} \qquad \ldots.(153)$$

where $$\phi = t(T' - T)^{-20}$$

During any constant stress creep test, two of the four parameters are held constant and so Equation (153) can be written

$$(\varepsilon)_{\sigma,T} = \varepsilon_0 + c_1\, \sigma^{\beta_1}\, \phi^{\kappa_1} + c_2\, \sigma^{\beta_2}\, \phi^{\kappa_2} + c_3\, \sigma^{\beta_3}\, \phi^{\kappa_3} + \ldots \qquad \ldots.(154)$$

where κ has the values of the series $\frac{1}{3}$ .... 1 .... 3 .... and for constant temperature this can reduce to the well established empirical equation

$$(\varepsilon)_{\sigma,T} = at^{\frac{1}{3}} + bt + ct^3 \qquad \ldots.(155)$$

To evaluate the constants associated with each term of Equation (155), times to a convenient standard strain are measured and cross plotted against the corresponding stress. These times are designated the $t_{\frac{1}{3}}$, t_1 and t_3 components and the displays obtained are similar to conventional stress-rupture cross-plots.

It is found from experimental creep results that a series of curves is obtained and these become asymptotic to straight line segments, the effect of increasing temperature being to displace the segments leftwards and downwards, ie to shorter times and lower stresses. In the Graham and Walles analysis the segments have slopes within the series 2^{-n} and each segmental mode effectively defines

limits of applicability of a particular equation of state. Within one segmental mode $\left(\frac{\partial \psi}{\partial \log t_\kappa}\right)$ is independent of stress and temperature and is associated with a particular differential $\left(\frac{\partial \psi}{\partial T}\right)$ which is a function of temperature only, parallel straight lines displaced in time due to the effect of temperature. The full Graham and Walles form is given by

$$\log(\sigma)_\varepsilon = -\log\left(\frac{c}{\varepsilon}\right)^{\frac{1}{\beta}} - \frac{\kappa}{\beta}\log t_\kappa + 20\frac{\kappa}{\beta}\log(T' - T) \qquad \ldots.(156)$$

However the curved nature of the $\log\sigma - \log t_\kappa$ cross-plots for low κ values, makes solutions of Equation (154) more difficult.

The Graham and Walles analysis overcomes these difficulties by making the component terms of Equation (154) compound, such that this compound form specifies the two regions where $\left(\frac{\partial \psi}{\partial \log t_\kappa}\right)$ is independent of time and temperature, ie where it is linear and can be solved by Equation (155). The curvature between these regions is then absolutely specified by the two sets of $\frac{\kappa}{\beta}$ and related constants and by the time exponent, κ, of the term being evaluated, the equation being of the form

$$(\varepsilon)_{\kappa,\sigma,T} = \left[c_1\,\sigma^{\beta_1}\,(T' - T)^{-20\kappa} + c_2\,\sigma^{\beta_2}\,(T' - T)^{-20\kappa}\right] t^\kappa \qquad \ldots.(157)$$

Although the method described allows a solution of Equation (157) this equation (one term of Equation (155)) includes four unknown constants and three known constants making a mathematical solution of limited experimental data virtually impossible. However a feature of the logarithmic-graphical presentation of the data is that for specified κ's and β's all solutions of Equation (157) are geometrically similar and for transition between any two sets of $\frac{\kappa}{\beta}$ values a master curve can be constructed for each κ. Simple location of sets of curves on the experimental data allow the β_1 and β_2 constants to be solved prior to any attempt to solve the c and T' constants. This in effect specifies temperature independent regions and allows solution of the corresponding c and T' constants.

Briefly summarising it follows therefore that in stress-time cross-plots, for segmental modes wherein linear equations can be applied, lines of slope 2^{-n} are in evidence, monotonic behaviour exists and single time terms are employed in the various creep equations. However where curvature exists bimodal deformation mechanisms are considered to operate over the transition region and the compound form of the various equations must be employed.

APPENDIX II

Programme for component analysis of creep curves

```
LIST
0010
0020
0030 PRINT "INPUT STRESS,TIME, MATERIAL"
0040 DIM T[20],E[20],G[100],H[100]
0050 DIM U[20],T[20],F[20],Y[20],X[20]
0060 INPUT S,T,M
0070 PRINT "INPUT N"
0080 INPUT N
0090 LET X[I]=0
0100 LET Y[I]=0
0110 PRINT "INPUT TIME AND STRAIN"
0120 FOR I=1 TO N
0130  INPUT T[I],E[I]
0140 NEXT I
0150 LET L=1
0160 FOR M=-1 TO 2
0170  LET K=(3↑M)
0180  LET J=1
0190  LET I=L
0200  LET X1=0
0210  LET Y1=0
0220  LET X1=X1+LOG(T[I])
0230  LET Y1=Y1+LOG(E[I])
0240  LET X3=X1/J
0250  LET Y3=Y1/J
0260  LET G=Y3-K*X3
0270  LET H=EXP(G)
0280  LET A=(.1/H)↑(1/K)
0290  LET I=I+1
0300  LET J=J+1
0310  LET L=I
0320  LET S=H*T[I]↑K
0330  IF I=N THEN GOTO 0440
0340  IF (E[I]-S)/S<.1 THEN GOTO 0220
0350  PRINT "TOTAL POINTS =";I-1
0360  PRINT "T";K"COMP=";A
0370  FOR I=1 TO N
0380    LET E[I]=E[I]-H*T[I]↑K
0390    PRINT T[I],E[I]
0400  NEXT I
0410 NEXT M
0420 DATA .06,.012,.12,.016,.25,.021,.40,.029,1,.041,2,.061
0430 DATA 8,.15,16,.241,26,.551,35,1.271,43,3.29,61,6
0440 PRINT "TOTAL POINTS=";I
0450 PRINT "T";K"COMP=";A
```

APPENDIX III

```
LIST
0010      Programme for master curve presentation of analysed data
0020 DIM V[5],X[5],Y[5],Z[5],U[5],P[5,2]
0030 FOR N=0 TO 5
0040  READ V[N],X[N],Y[N],Z[N],U[N]
0050 NEXT N
0060 FOR N=0 TO 5
0070  FOR M=0 TO 2
0080    READ P[N,M]
0090  NEXT M
0100 NEXT N
0110 FOR N=0 TO 5
0115  PRINT "K=";V[N],"K/B=";X[N],"T1=";Y[N],"C=";Z[N];"EXP";U[N]
0120  FOR M=0 TO 2
0130    LET T=800+50*M
0135    PRINT "T=";T,"TIME","SIGMA"
0137    LET C1=EXP(1/V[N]*LOG(.001))
0140    LET C1=C1/(EXP(1/V[N]*LOG(Z[N]))+U[N]/V[N]*LOG(10))
0150    FOR J=1 TO P[N,M]
0160      READ T2
0170      LET C2=EXP(20*LOG(Y[N]-T))/T2
0180      LET S=EXP(X[N]*LOG(C1*C2))
0190      PRINT TAB(1),T2,S
0200    NEXT J
0210    PRINT
0220  NEXT M
0230  PRINT
0240 NEXT N
0250 PRINT
0260 PRINT
0280 DATA .333333,.125,1208,3.2,10
0290 DATA 1,.1875,1176,1.9,40
0300 DATA 3,.125,1130,1.43,113
0310 DATA 3,.25,1225,5,134
0320 DATA 9,.25,1286,1.6,420
0330 DATA 9,.125,1155,9.35,349
0340 DATA 6,12,6
0350 DATA 6,11,4
0360 DATA 2,2,2
0370 DATA 4,3,5
0380 DATA 8,8,8
0390 DATA 3,4,4
0400 DATA 4,7.5,25,44,58,265
0410 DATA .245,1.3,3,3.75,28,40,40,46,90,100,125,155
0420 DATA 16,195,160,520,500,2000
0430 DATA 12.2,21,36.5,60,75,80
0440 DATA .325,1.3,2.12,3.85,6.5,9,10,10,21,25,33
0450 DATA 1.25,4.6,12.5,11
0460 DATA 6.5,16.9
0470 DATA .75,3
0480 DATA 2.9,6.6
0490 DATA 37,31,53,115
0500 DATA 6.6,17.5,33
0510 DATA 6.2,24,22,2.7,6.6
0520 DATA 110,80,83,46.5,49,38,38,39
0530 DATA 87,64,64,83,34.5,14.5,8.5,7
0540 DATA 193,75,50,56,44,48,14.7,9
0550 DATA 22,17.8,6.2
0560 DATA 8.5,7,1.8,.79
0570 DATA 1,1,1,1
```

APPENDIX IV

```
LIST
0010        Programme for regeneration of creep curves
0020 DIM W[5],X[5],Y[5],Z[5],U[5],F[12,5],A[12]
0030 FOR N=0 TO 5
0040  READ W[N],X[N],Y[N],Z[N],U[N]
0050 NEXT N
0060 PRINT "INPUT S AND T"
0070 INPUT S,T
0080 FOR N=0 TO 5
0090  FOR J=0 TO 12
0100    LET T3=.1
0110    LET L=20*W[N]*LOG(Y[N]-T)
0120    LET F[J,N]=(LOG(Z[N])+U[N]*LOG(10)+(Y[N]/X[N])*LOG(S))
0130    LET F[J,N]=EXP(F[J,N]+W[N]*LOG(T3)-L)
0135    LET T2=.1*2↑J
0137    LET F[J,N]=F[J,N]*(T2/T3)↑W[N]
0140  NEXT J
0150 NEXT N
0160 IF F[0,2]>F[0,3] THEN GOTO 0200
0170 LET A=2
0180 LET B=3
0190 GOSUB 0470
0200 IF F[0,4]>F[0,5] THEN GOTO 0250
0210 LET A=3
0220 LET B=5
0230 GOSUB 0470
0240 GOTO 0280
0250 LET A=3
0260 LET B=4
0270 GOSUB 0470
0280 PRINT "STRESS=";S,"TEMP=";T
0290 PRINT "TIME","T1/3COMP","T1COMP","T3COMP","TRCOMP"
0300 FOR J=0 TO 12
0310  LET A[J]=0
0320 NEXT J
0330 FOR J=0 TO 12
0340  LET A[J]=F[J,0]+F[J,1]+F[J,2]+F[J,3]
0350 NEXT J
0360 FOR J=0 TO 12
0370  LET T2=.1*2↑J
0380  PRINT T2,F[J,0],F[J,1],F[J,2],F[J,3]
0390 NEXT J
0400 PRINT
0410 PRINT "TIME","TOTAL CREEP STRAIN"
0420 FOR J=0 TO 12
0430  LET T2=.1*2↑J
0440  PRINT T2,A[J]
0450 NEXT J
0460 GOTO 0060
0470 FOR J=0 TO 12
0480  LET F[J,A]=F[J,B]
0490 NEXT J
0500 RETURN
0510 DATA .333333,.125,1208,3.2,10
0520 DATA 1,.1875,1176,1.9,40
0530 DATA 3,.125,1130,1.43,113
0540 DATA 3,.25,1225,5,134
0550 DATA 9,.25,1286,1.6,420
0560 DATA 9,.125,1155,9.35,349
```

APPENDIX V

Strain accumulation under rectangular stress cyclic creep using time hardening assumptions

Considering

$$\dot{\varepsilon} = \frac{d\varepsilon}{dt} = \sum \kappa\, c\, \sigma^{\beta} t^{\kappa-1}$$

Integrating each term and calculating the strain accumulated during each cycle it follows that

$$\Delta\varepsilon_1 = \sum c\, \sigma^{\beta} \left(\lambda^{\kappa} - 0\right)$$

$$\therefore \quad \Delta\varepsilon_2 = \sum c\, \sigma^{\beta} \left[(3\lambda)^{\kappa} - (2\lambda)^{\kappa}\right]$$

$$\therefore \quad \Delta\varepsilon_i = \sum c\, \sigma^{\beta} \left[\left((N-1)\lambda\right)^{\kappa} - \left((N-2)\lambda\right)^{\kappa}\right]$$

where $\Delta\varepsilon_i$ = strain incurred in ith cycle and N = number of $\frac{1}{2}$ cycles.

$$\therefore \quad \sum_{i=1}^{i=N/2} \Delta\varepsilon_i = \varepsilon_r = \sum c\, \sigma^{\beta} \left[\left((N-1)\lambda\right)^{\kappa} - \left((N-2)\lambda\right)^{\kappa} + \left((N-3)\lambda\right)^{\kappa} - \ldots\right]$$

$$= \sum c\, \sigma^{\beta} \lambda^{\kappa} \sum_{p=1}^{\frac{1}{2}(N-1)} \left[(2p)^{\kappa} - (2p-1)^{\kappa}\right] \quad \ldots.(158)$$

and considering $(2p)^{\kappa} - (2p-1)^{\kappa}$ for large p.

$$\frac{(2p)^{\kappa}}{(2p-1)^{\kappa}} = \frac{1}{(1-\frac{1}{2}p)^{\kappa}}$$

$$\simeq 1 + \frac{\kappa}{2p}$$

$$\therefore \quad (2p - 1)^{\kappa} = (2p)^{\kappa} \Big/ \left(1 + \frac{\kappa}{2p}\right)$$

$$\therefore \quad (2p)^{\kappa} - (2p - 1)^{\kappa} = (2p)^{\kappa} \left(1 - \frac{1}{1 + \frac{\kappa}{2p}}\right)$$

$$= \kappa\ (2p)^{\kappa-1} \text{ for } p >> \kappa,$$

and substituting in Equation (158)

$$\varepsilon_r = c\ \sigma^{\beta} \lambda^{\kappa} \sum_{p=1}^{\frac{1}{2}(N-1)} \kappa\ (2p)^{\kappa-1}$$

But for n large

$$\sum_{p=1}^{\frac{1}{2}(N-1)} p^{\kappa-1} \rightarrow \int_{1}^{\frac{1}{2}(N-1)} p^{\kappa-1}\, dp \simeq \int_{0}^{\frac{1}{2}(N-1)} p^{\kappa-1}\, dp$$

$$\therefore \quad \varepsilon_r = c\ \sigma^{\beta} \lambda^{\kappa}\ 2^{\kappa-1} \left[p^{\kappa}\right]_{0}^{\frac{1}{2}(N-1)}$$

$$\therefore \quad \varepsilon_r = \sum c\ \sigma^{\beta} \lambda^{\kappa}\ 2^{-1}\ (N - 1)^{\kappa}$$

$$\simeq \sum c\ \sigma^{\beta} \lambda^{\kappa}\ 2^{-1}\ N^{\kappa}$$



(a) ×400

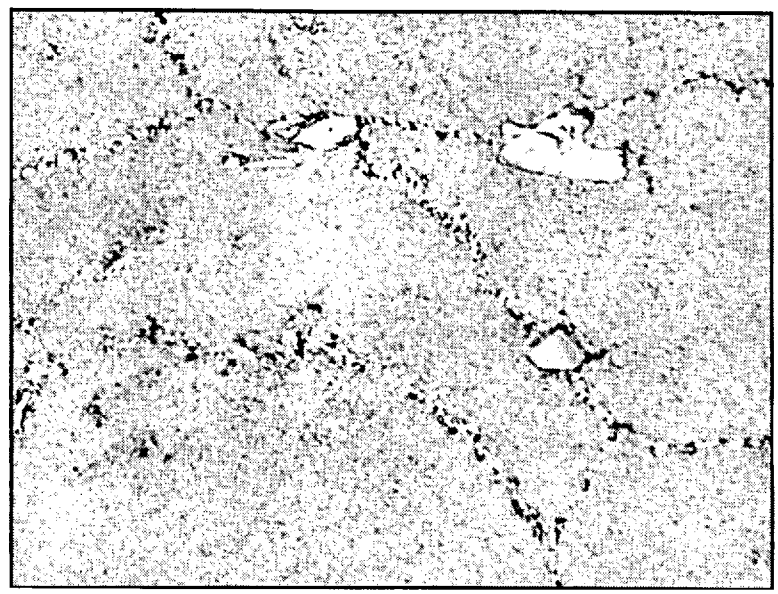

(b) ×400

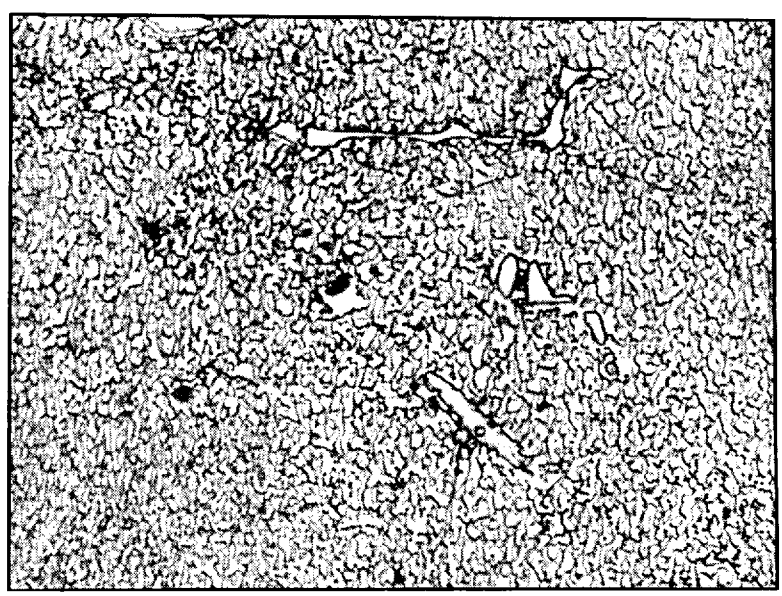

(c) ×400

FIG.6 TYPICAL MICROSTRUCTURES OF a) NIMONIC 90 b) NIMONIC 108 AND c) MAR M 246

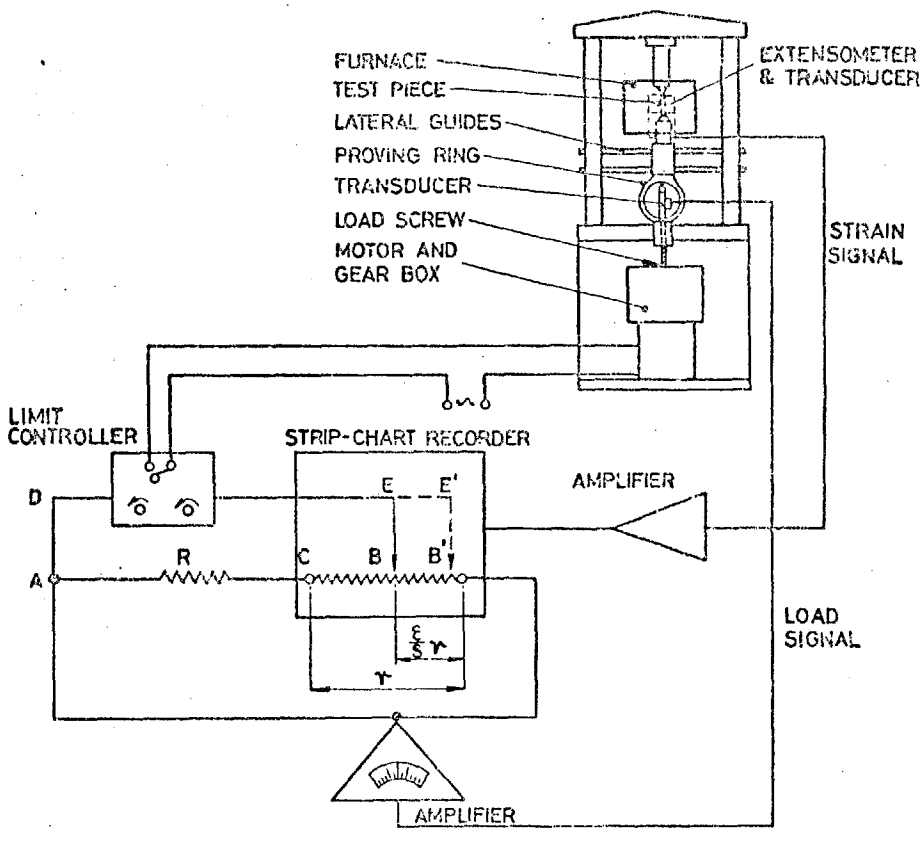

FIG. 8 CONTROL SYSTEM FOR COMPRESSIVE CREEP

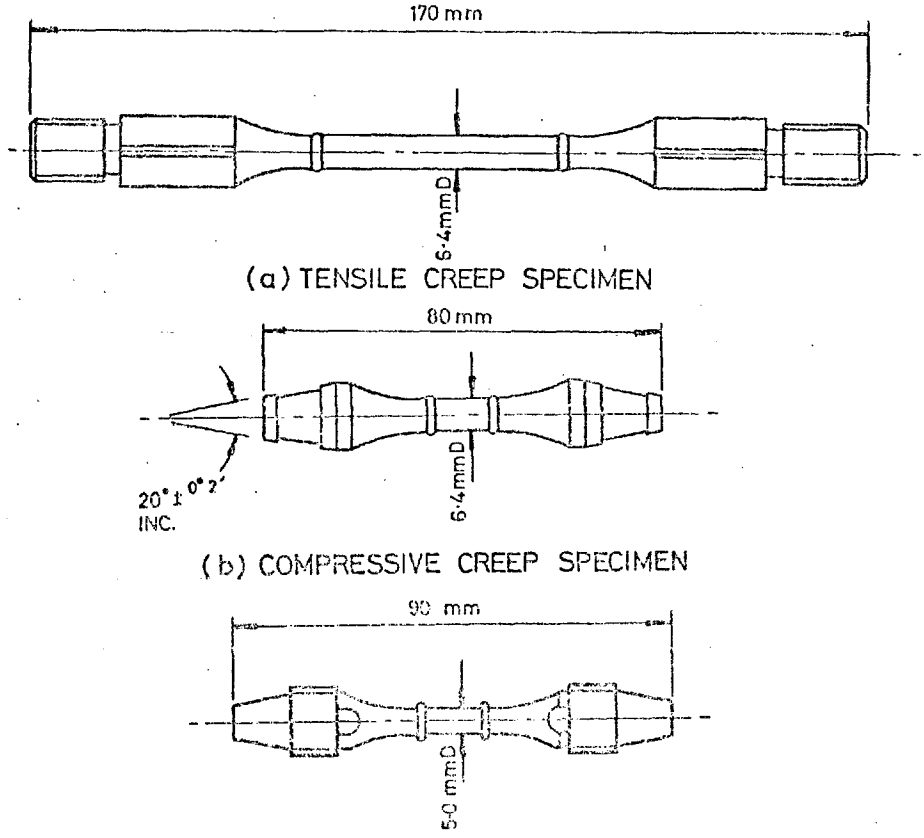

FIG. 9 SPECIMEN DESIGN

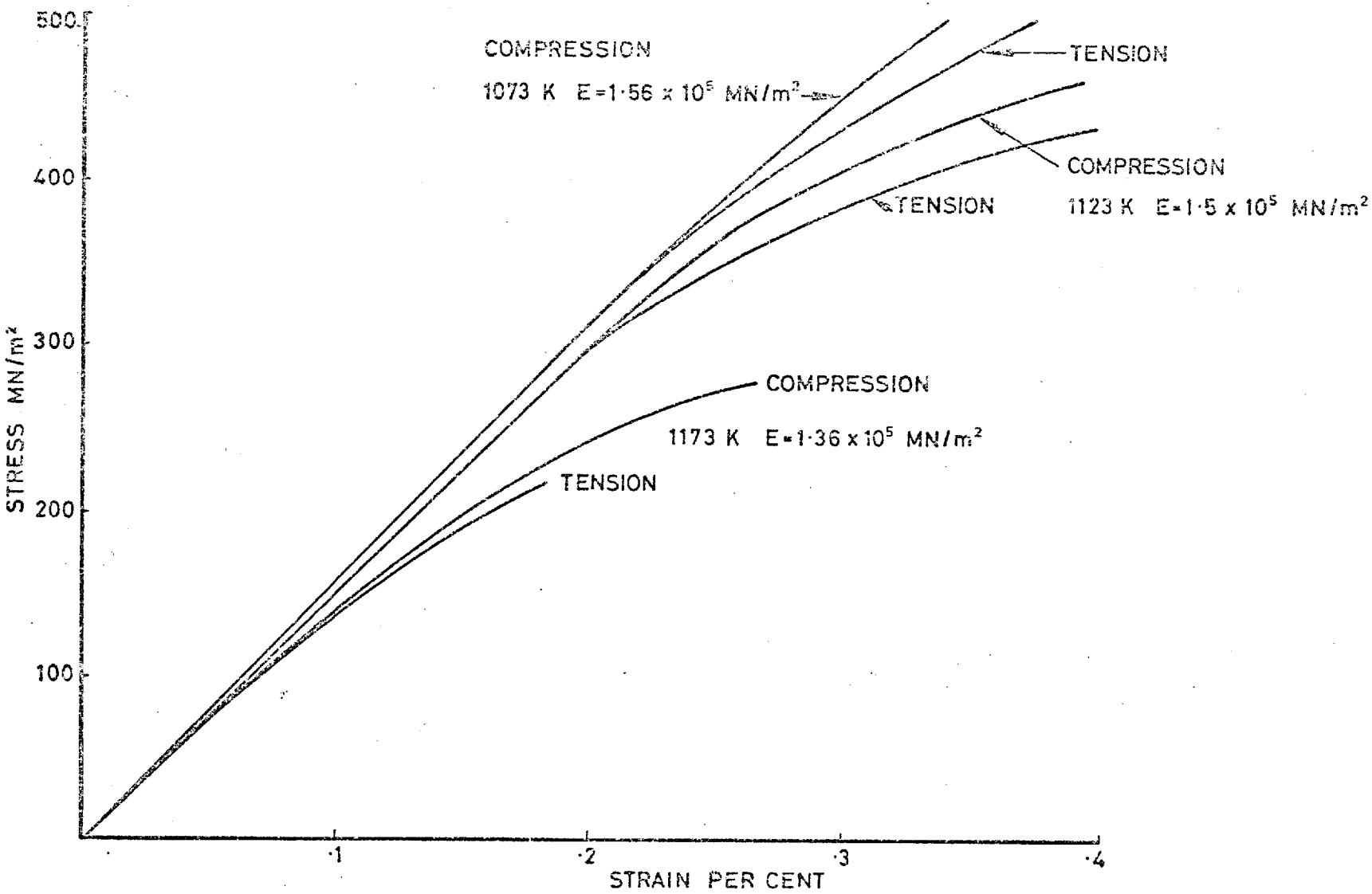

FIG.10 STRESS-STRAIN CURVES FOR NIMONIC 90 UNDER TENSILE & COMPRESSIVE LOADING

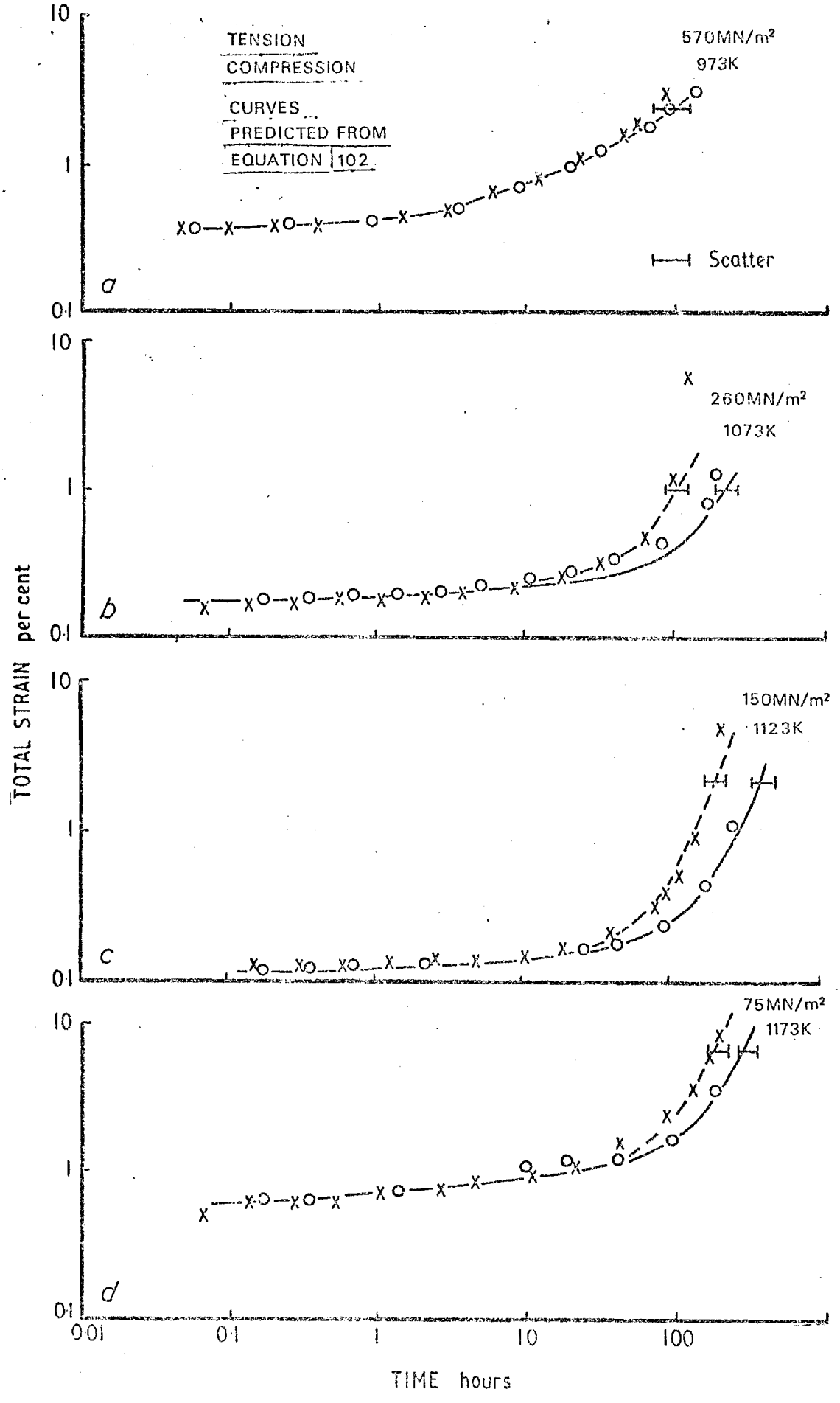

FIG.11 TENSILE AND COMPRESSIVE CREEP CURVES FOR NIMONIC 90

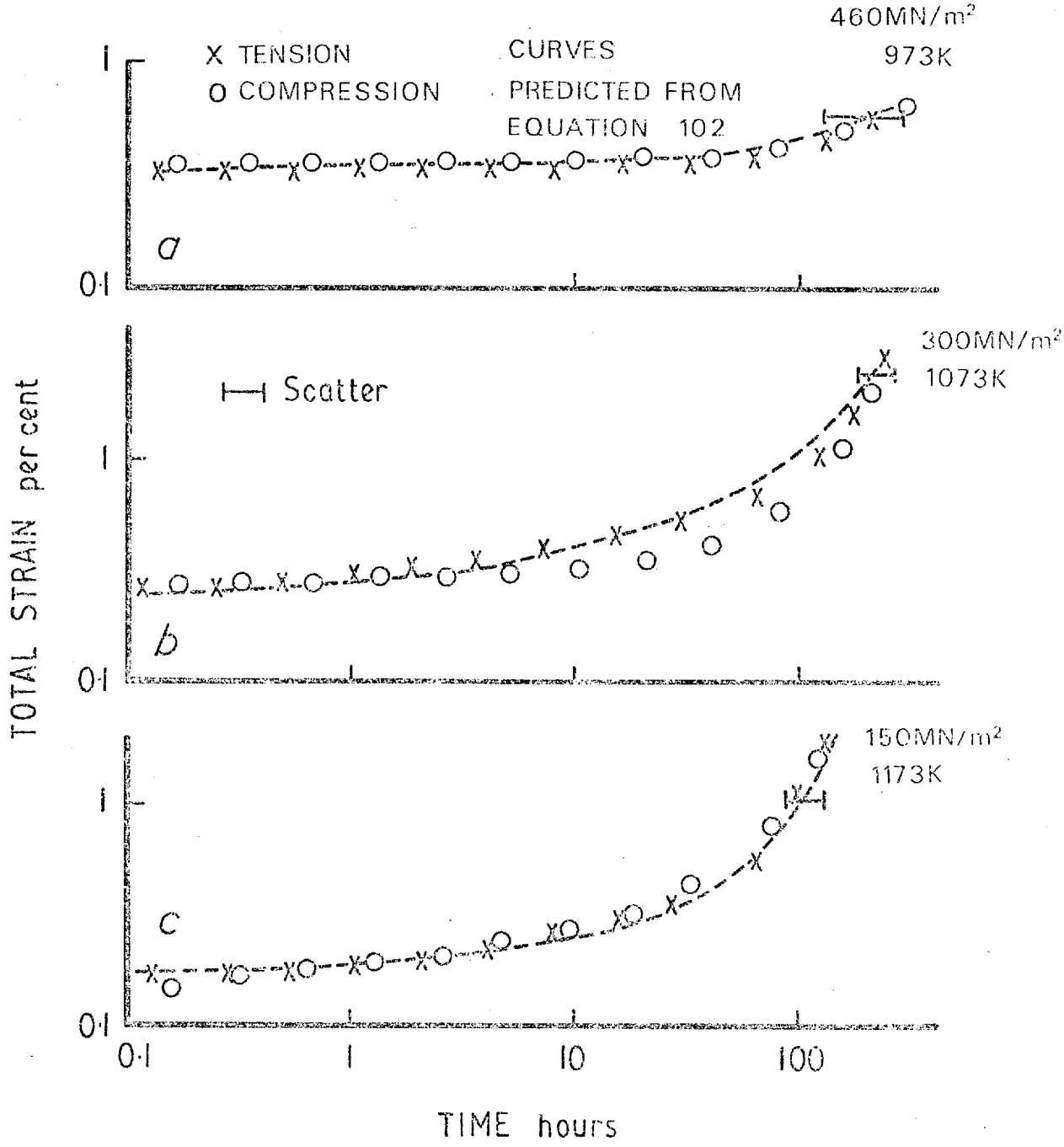

FIG.12 TENSILE AND COMPRESSIVE CREEP CURVES FOR NIMONIC 108

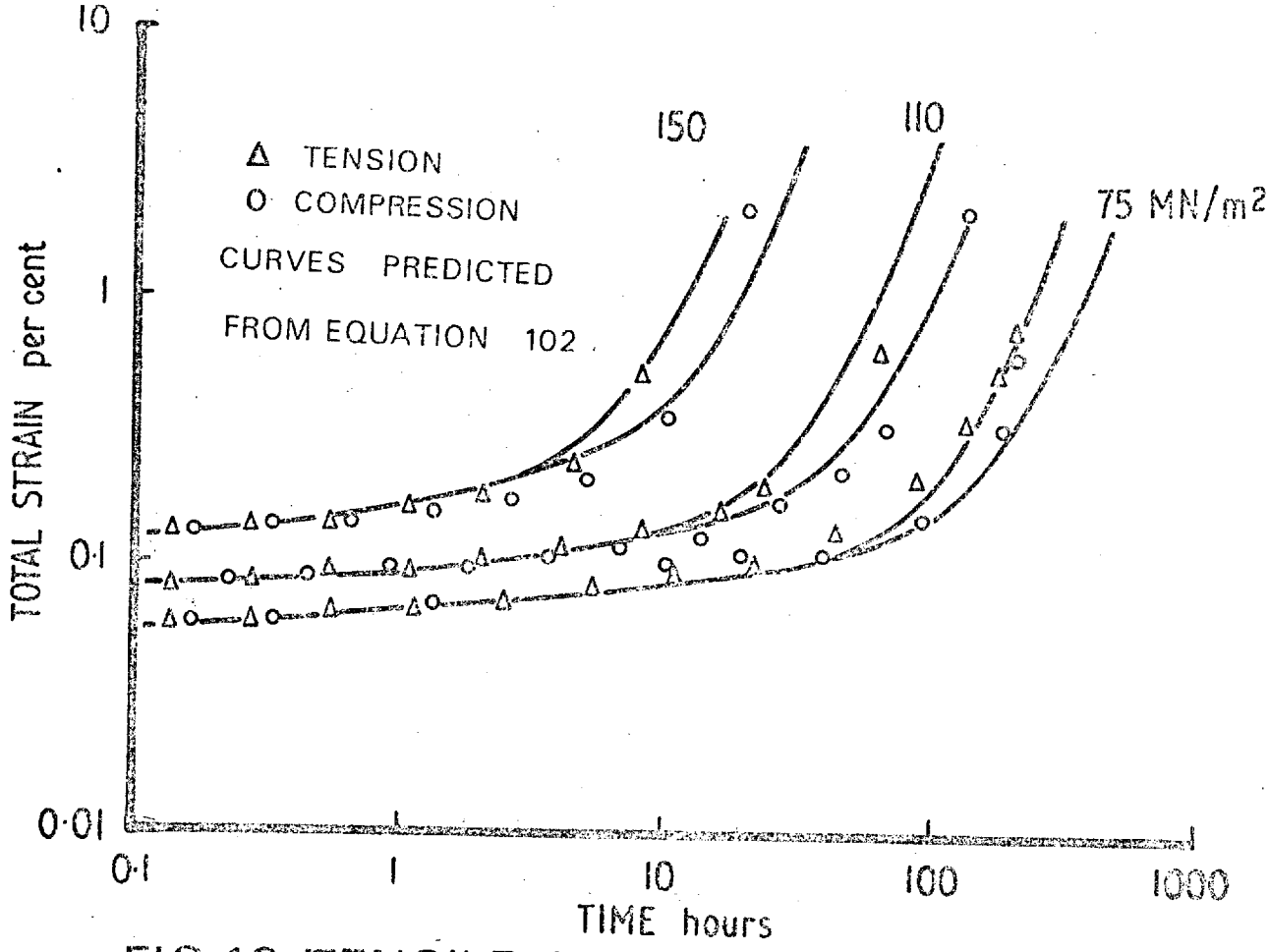

FIG.13 TENSILE AND COMPRESSIVE CREEP CURVES FOR NIMONIC 90 AT 1173K

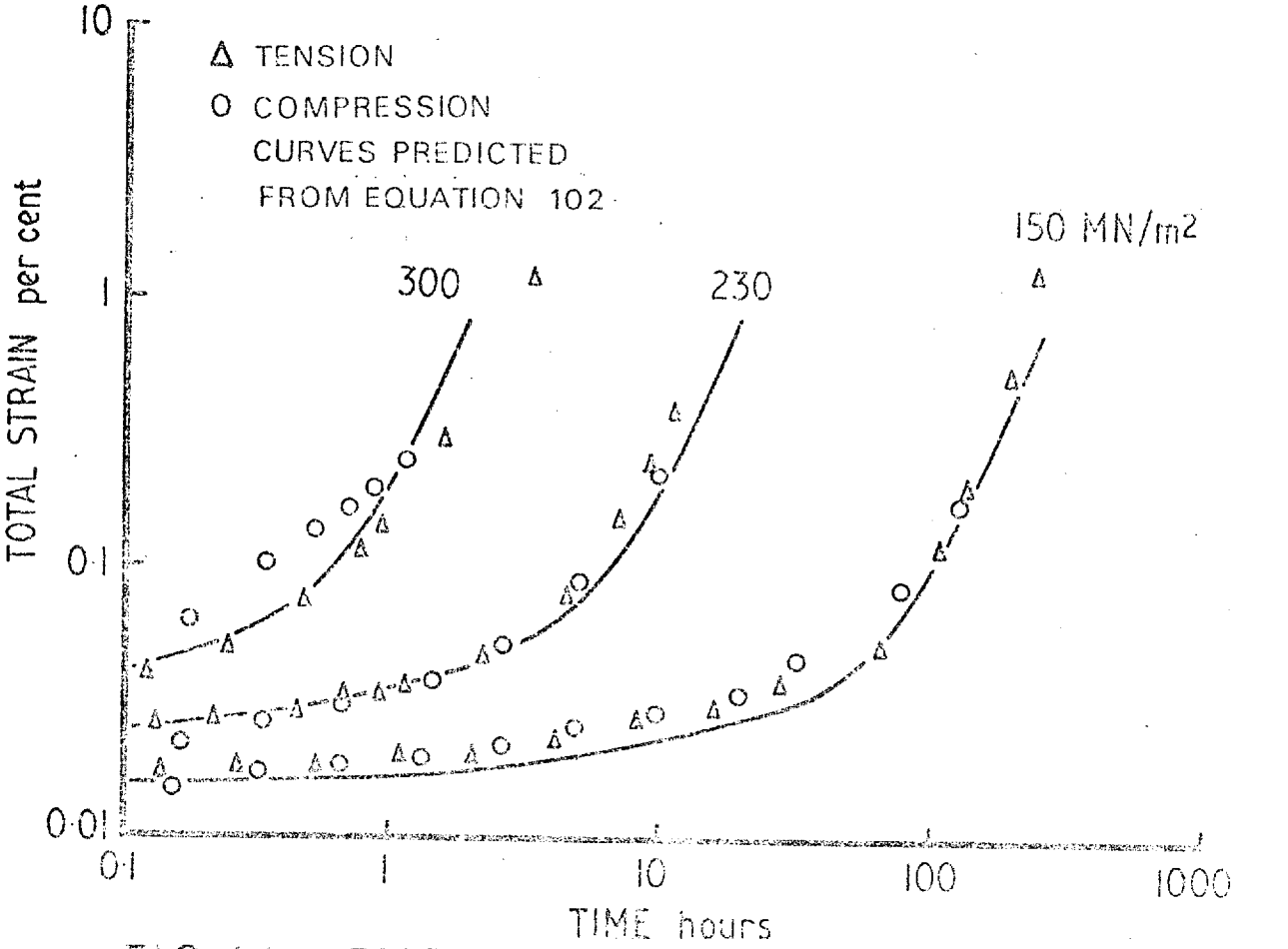

FIG.14 TENSILE AND COMPRESSIVE CREEP CURVES FOR NIMONIC 108 AT 1173K

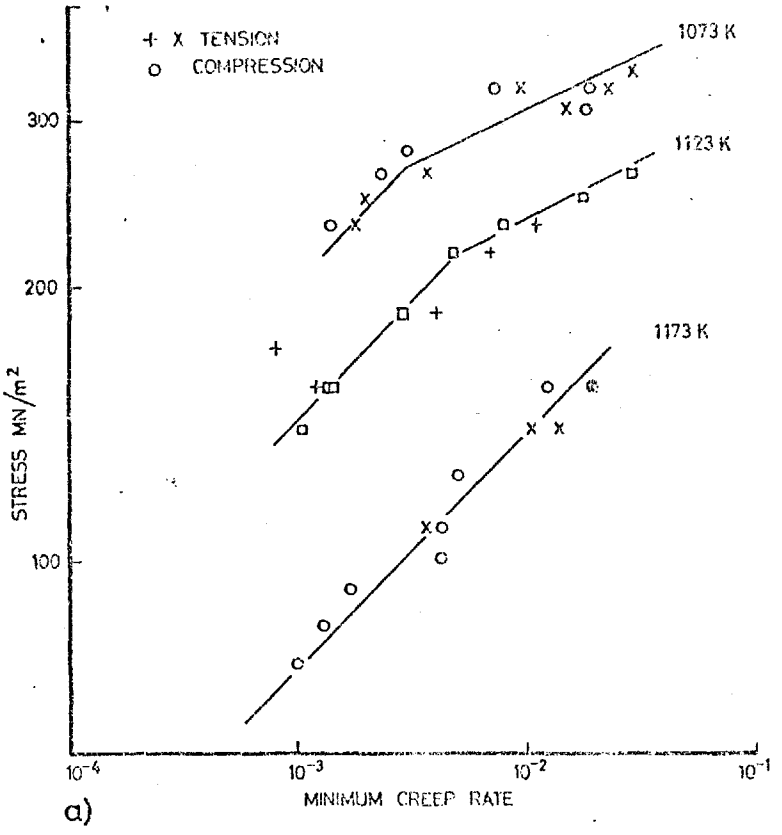

FIG. 15 MINIMUM CREEP RATES FOR NIMONIC 90 UNDER TENSILE AND COMPRESSIVE CREEP

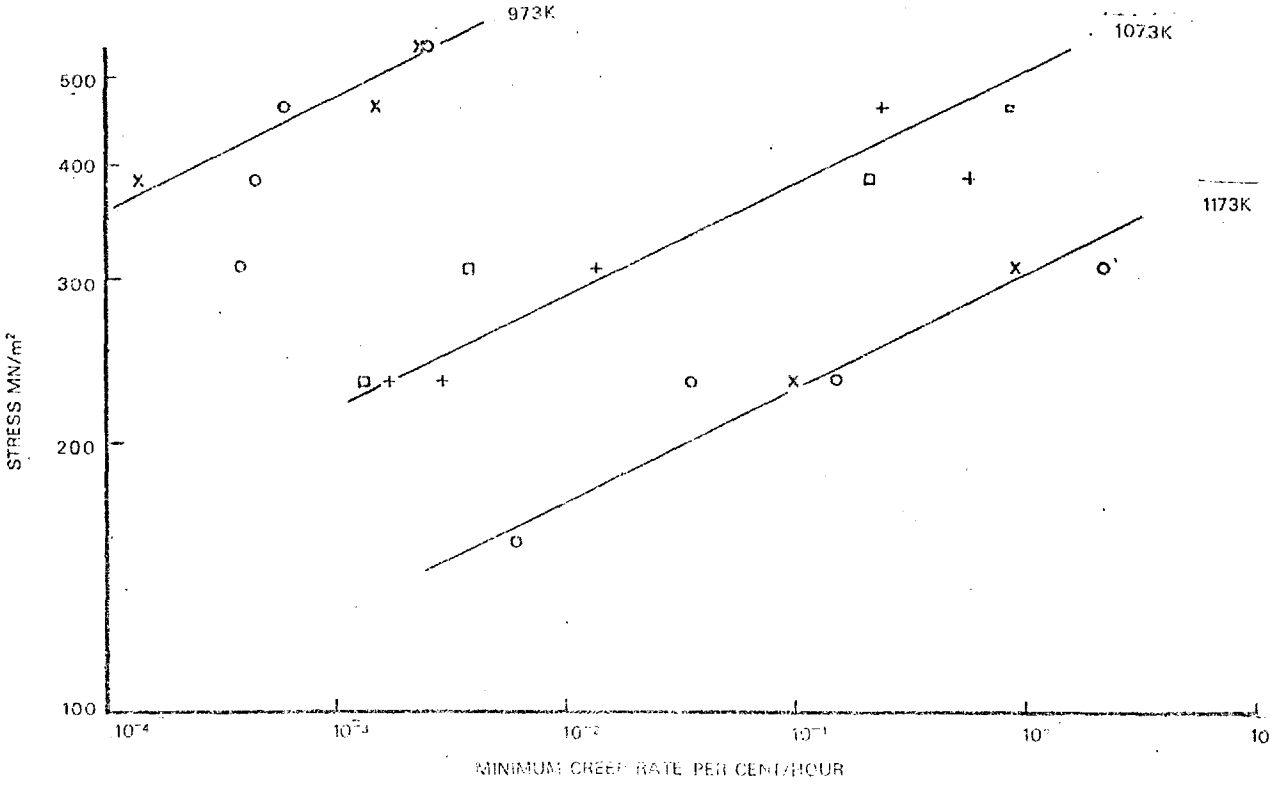

FIG.16 MINIMUM CREEP RATES FOR NIMONIC 108 UNDER TENSILE AND COMPRESSIVE CREEP

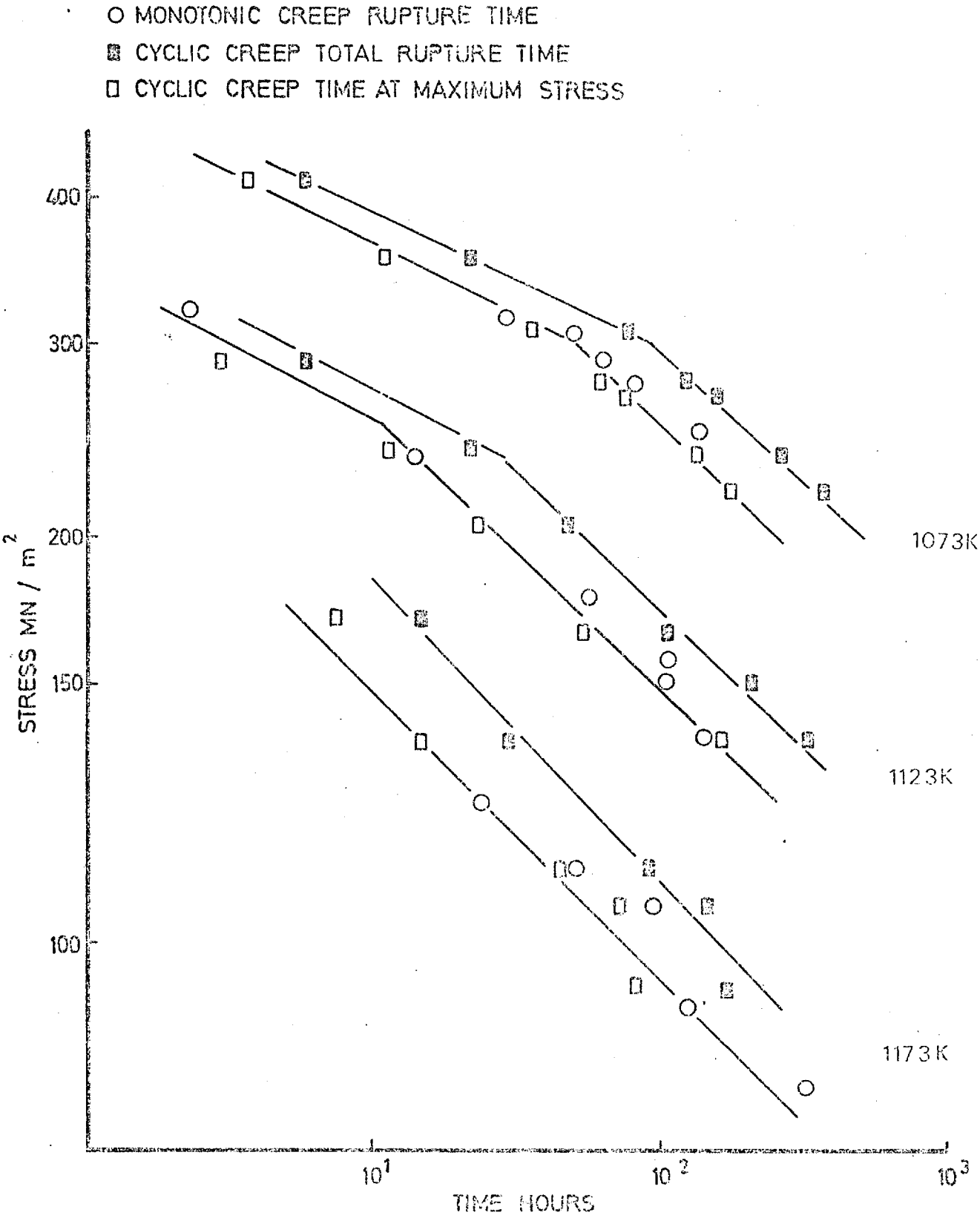

FIG.17 MONOTONIC & RECTANGULAR STRESS CYCLIC CREEP TIMES TO RUPTURE

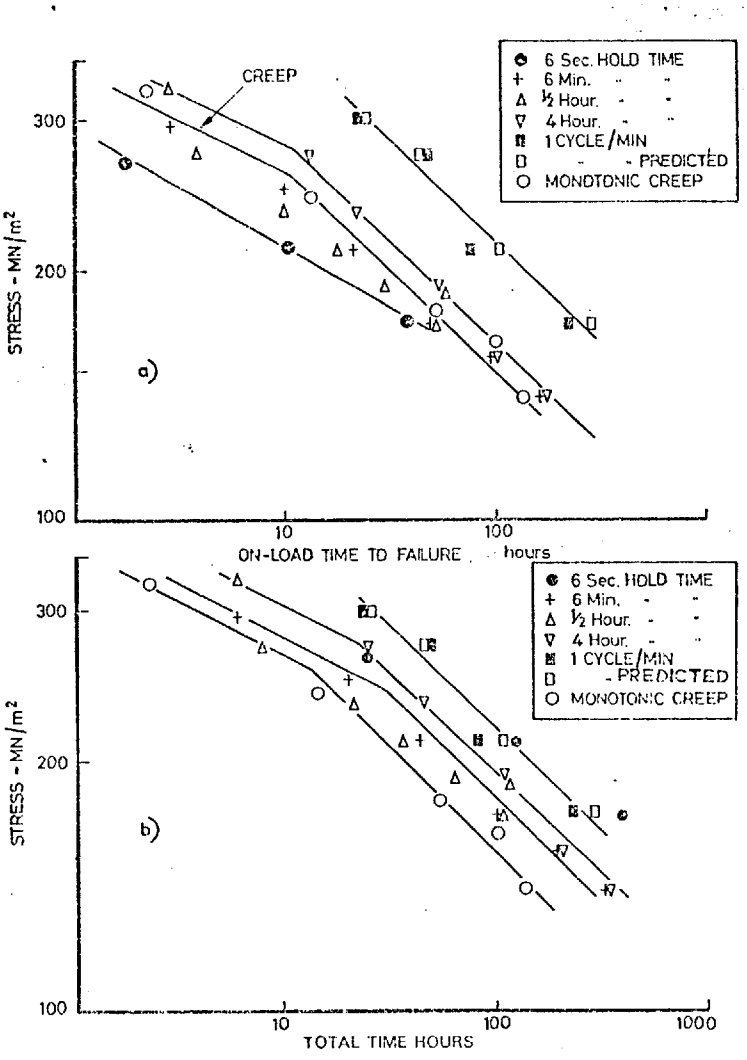

FIG.18 a&b EFFECTS OF CYCLE HOLD TIME AND FATIGUE ON TIME TO RUPTURE

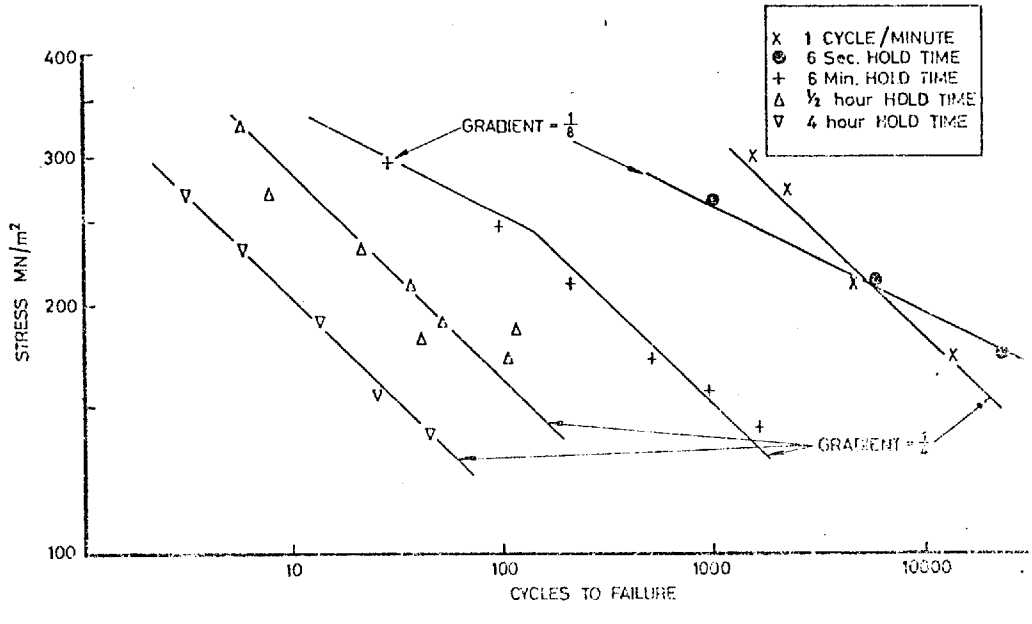

FIG.18c EFFECTS OF LOADING PATH ON CYCLES TO FAILURE

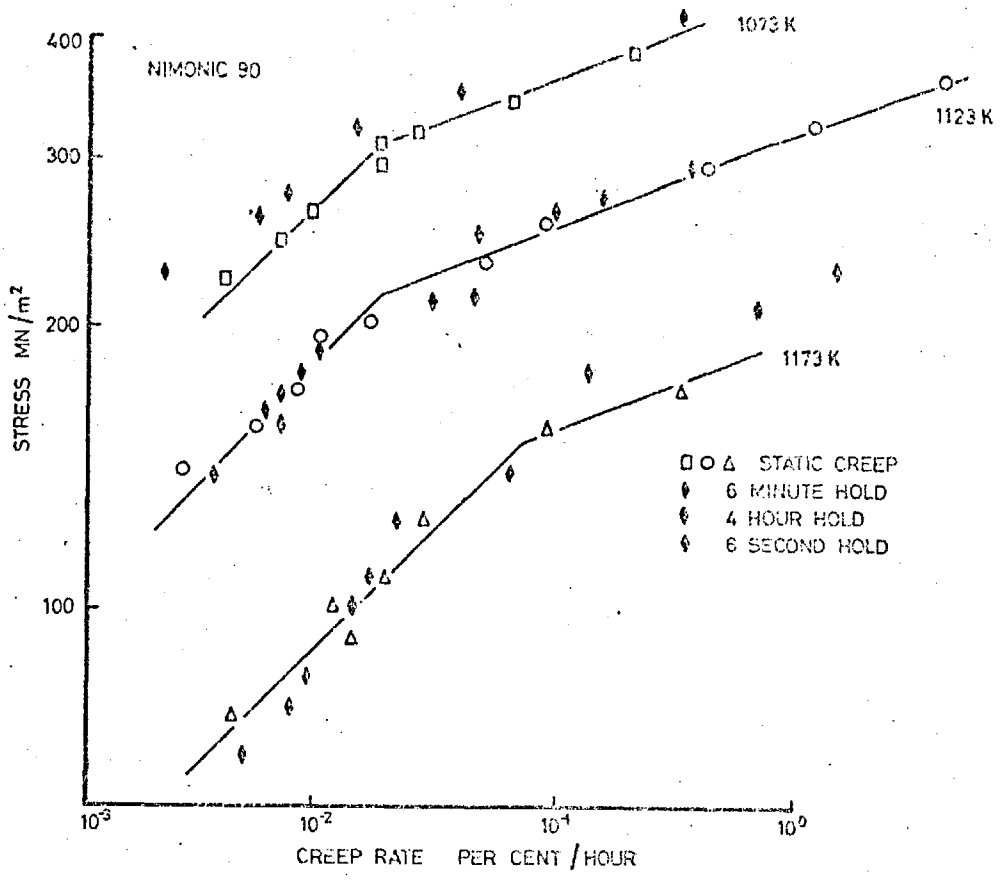

FIG.19 MINIMUM CREEP RATE UNDER STATIC AND CYCLIC LOADING

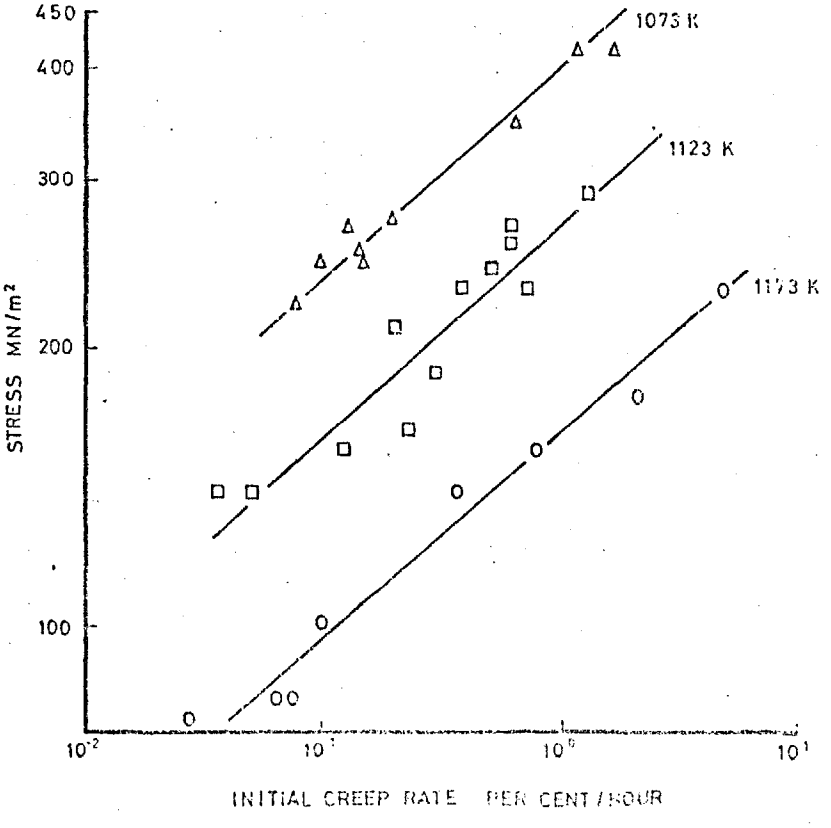

FIG. 20 INITIAL CREEP RATES FOR NIMONIC 90

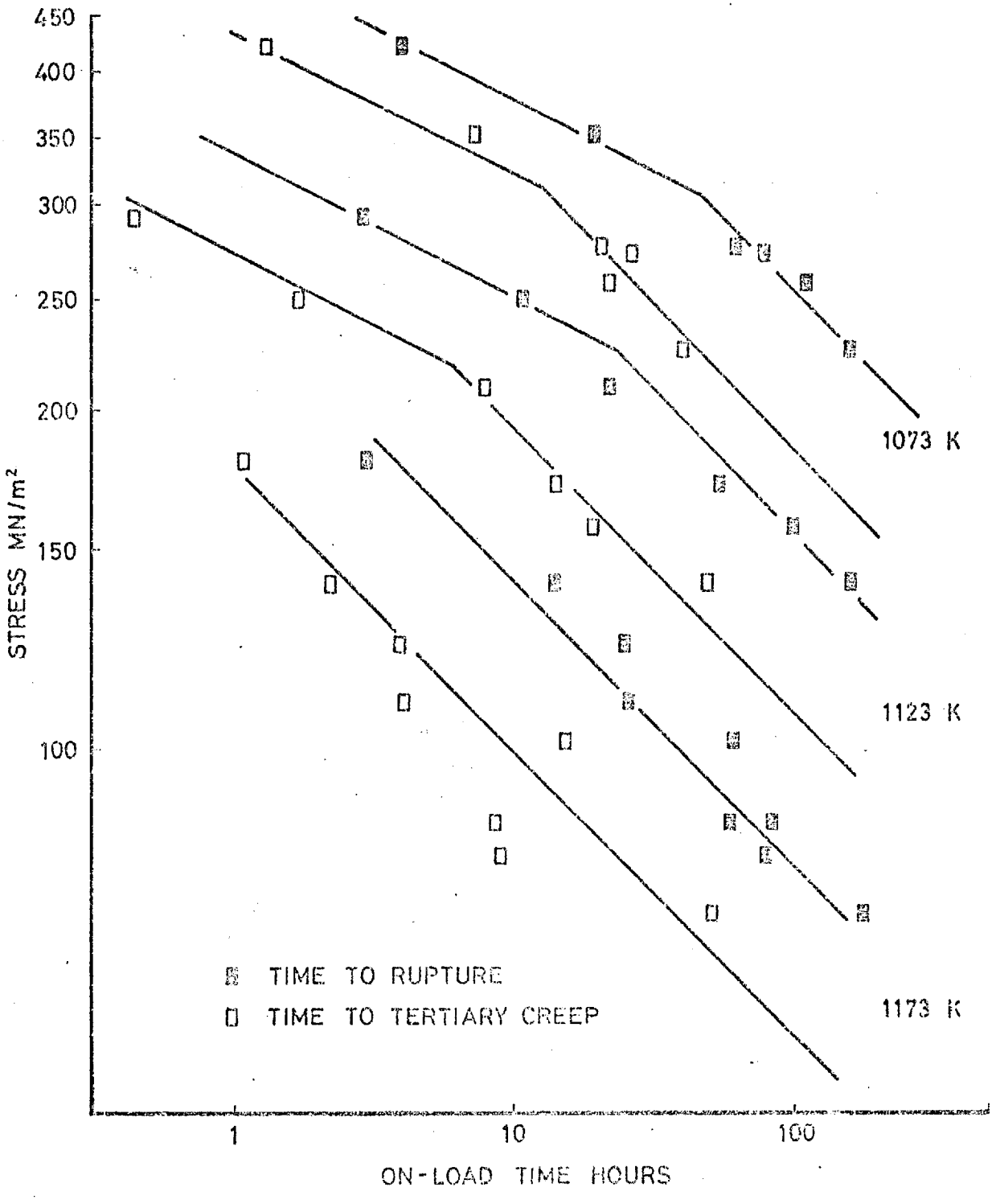

FIG. 21 TIMES TO TERTIARY AND TIMES TO RUPTURE FOR RECTANGULAR CREEP OF NIMONIC 90

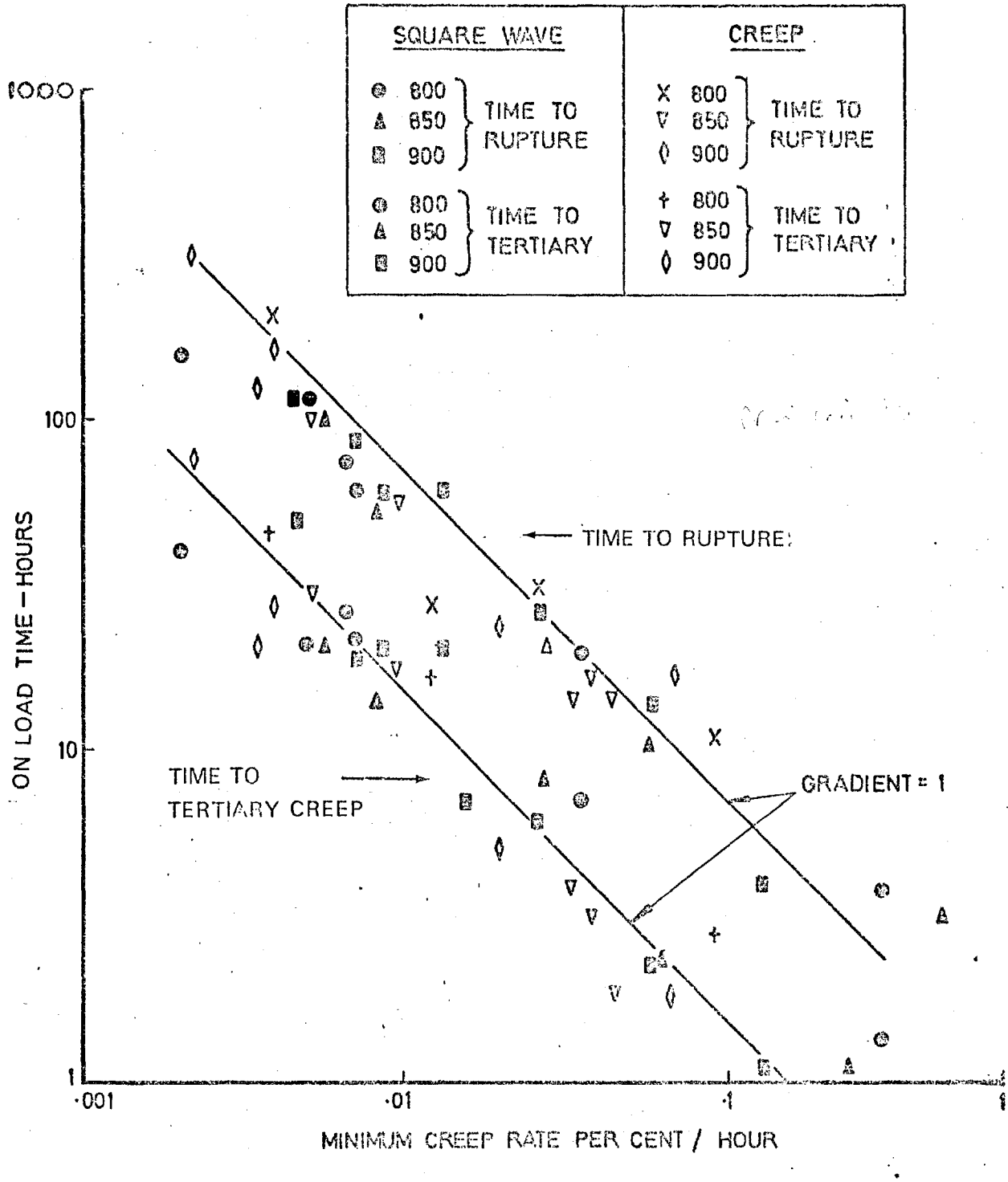

FIG.22 MINIMUM CREEP RATE/TIME CORRELATIONS FOR STATIC & CYCLIC CREEP

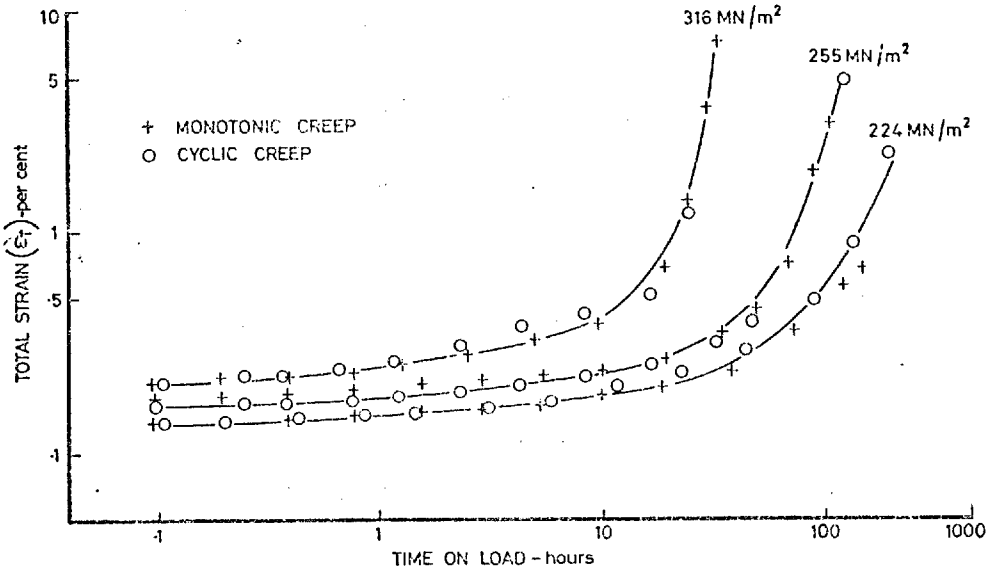

FIG.23 STRAIN-TIME CURVES FOR NIMONIC 90 UNDER STATIC AND CYCLIC STRESSES AT 1073K

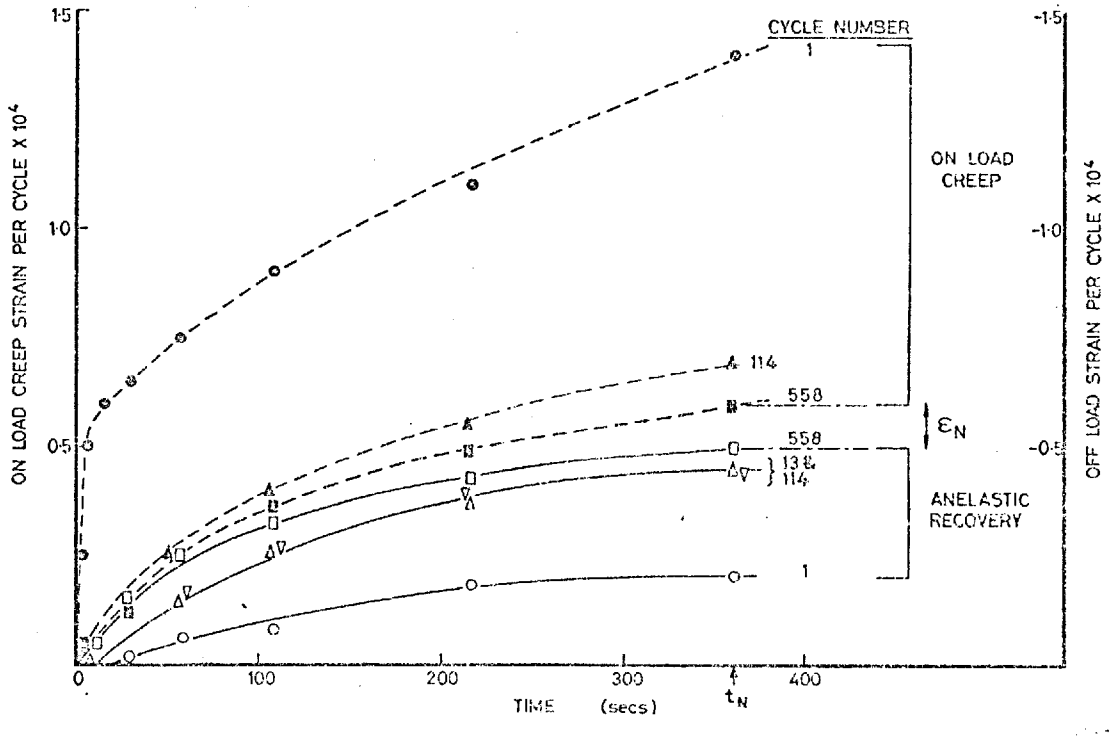

FIG.24 ON-LOAD CREEP STRAIN AND OFF-LOAD ANELASTIC RECOVERIES FOR SPECIFIED CYCLES OF NIMONIC 90 AT 1123K AND 170 MN/m^2

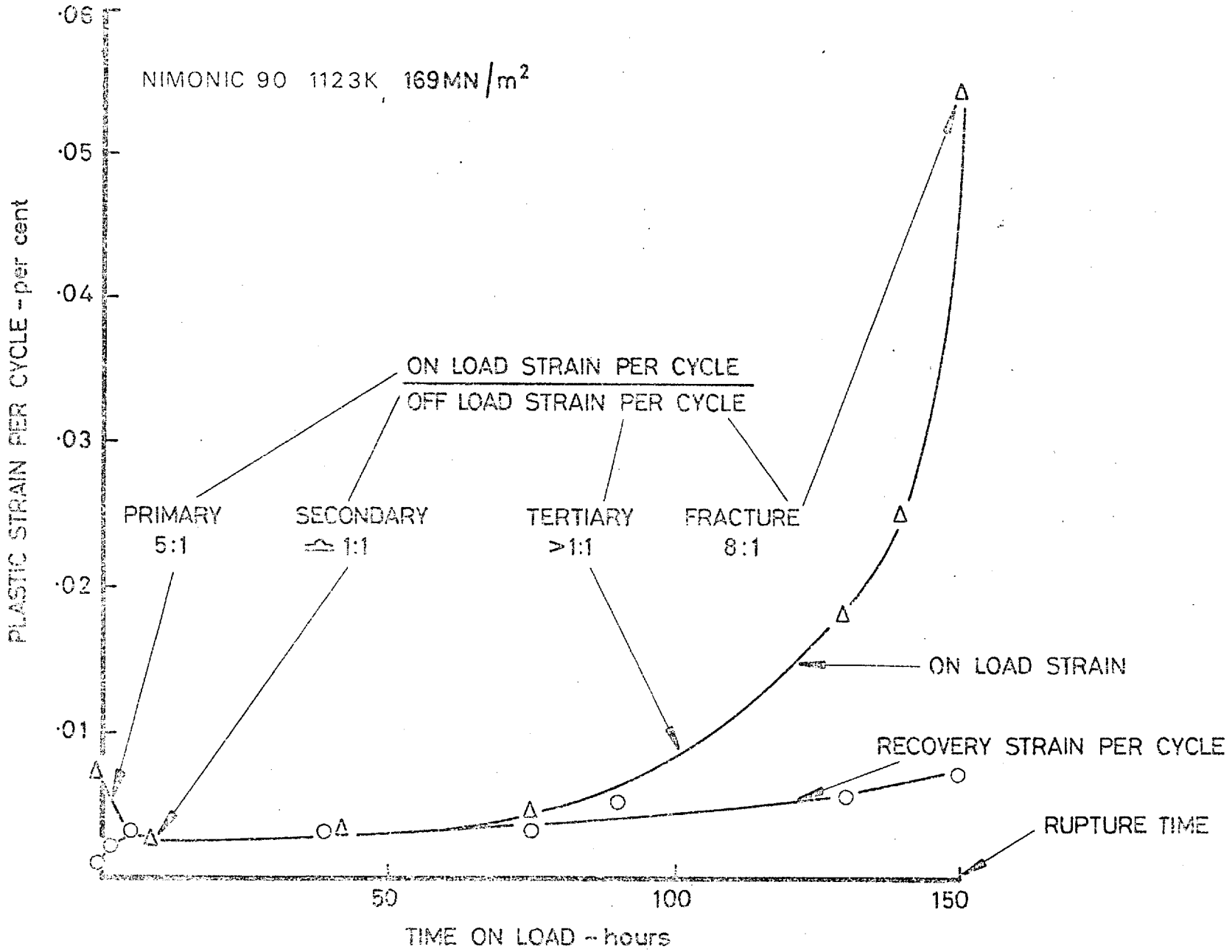

FIG.25 FORWARDS AND BACKWARDS CREEP STRAIN PER CYCLE

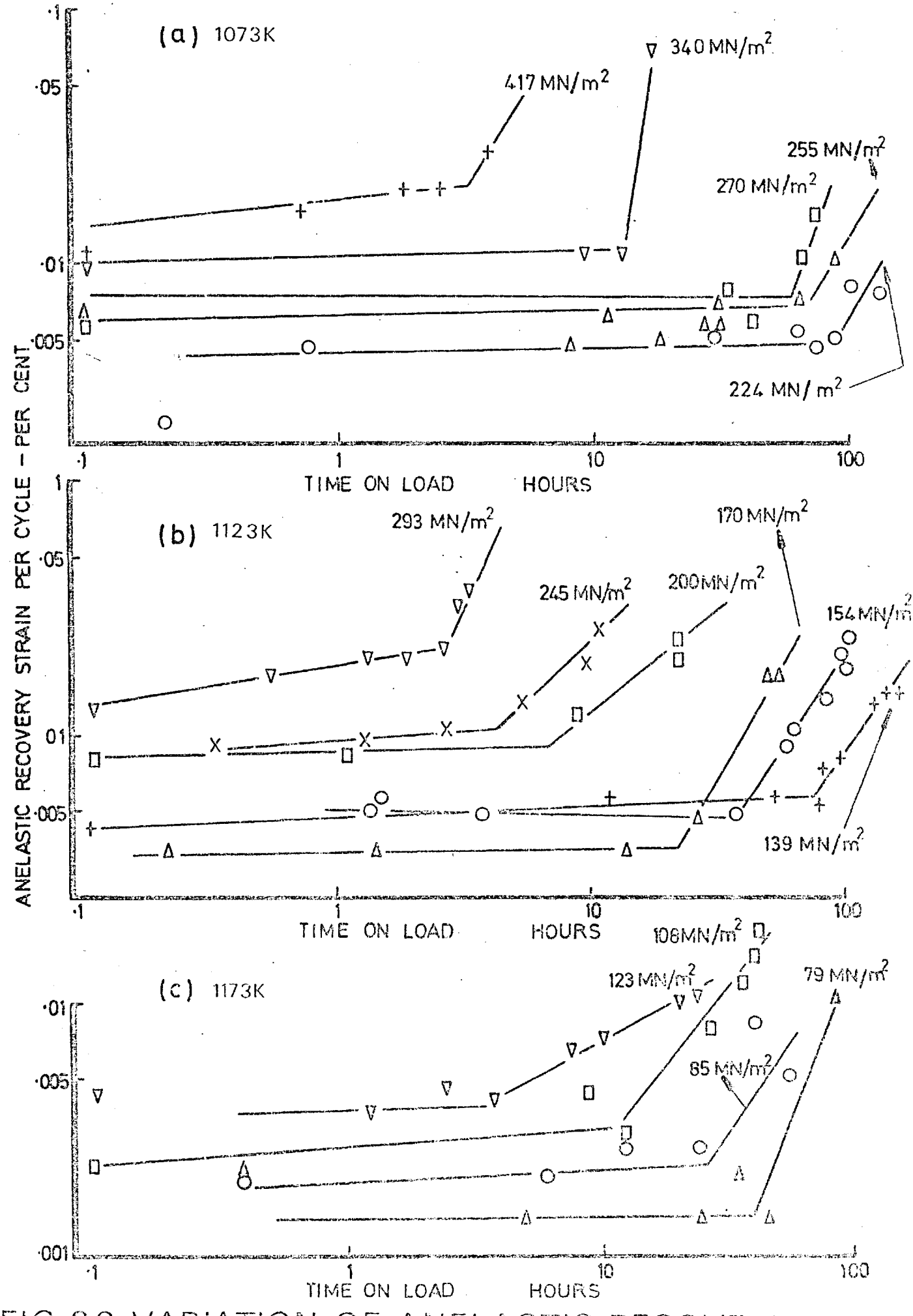

FIG. 26 VARIATION OF ANELASTIC RECOVERY PER CYCLE THROUGHOUT CREEP LIFE FOR NIMONIC 90

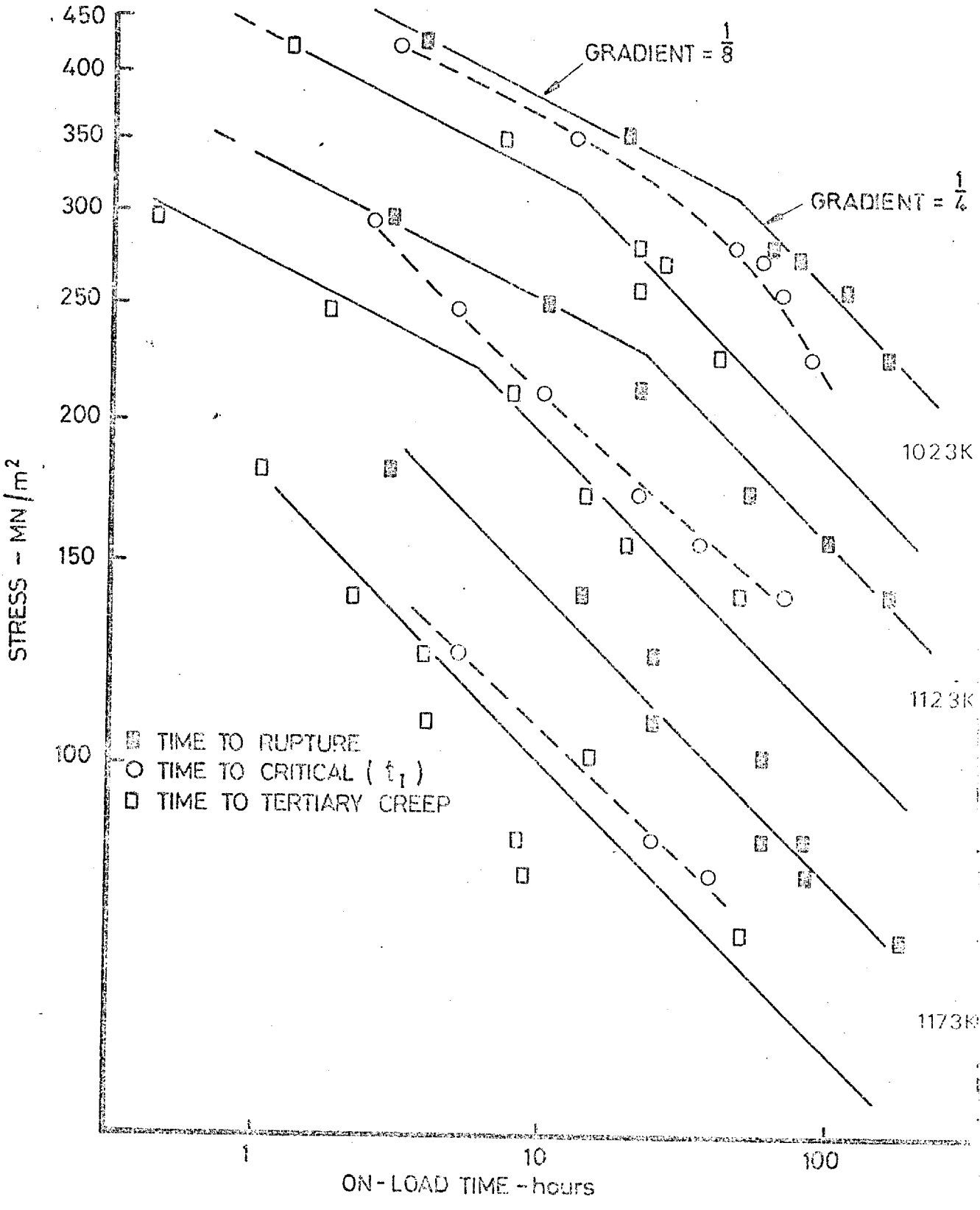

FIG.27 COMPARISONS OF CRITICAL TIME, TIME TO TERTIARY CREEP AND RUPTURE TIME FOR NIMONIC 90

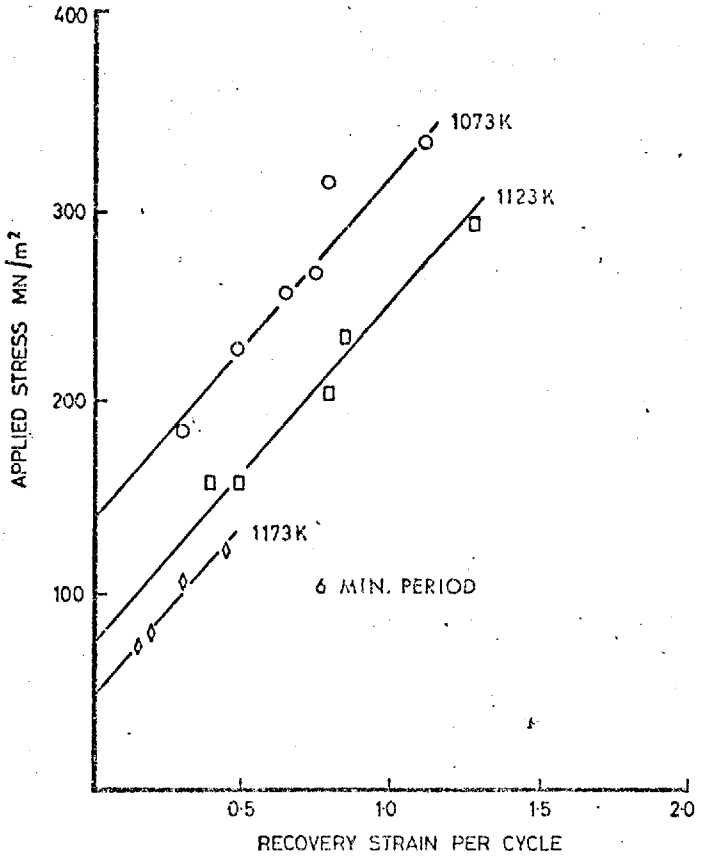

FIG. 28 STEADY STATE ANELASTIC RECOVERY OF NIMONIC 90 UNDER CYCLIC LOADING

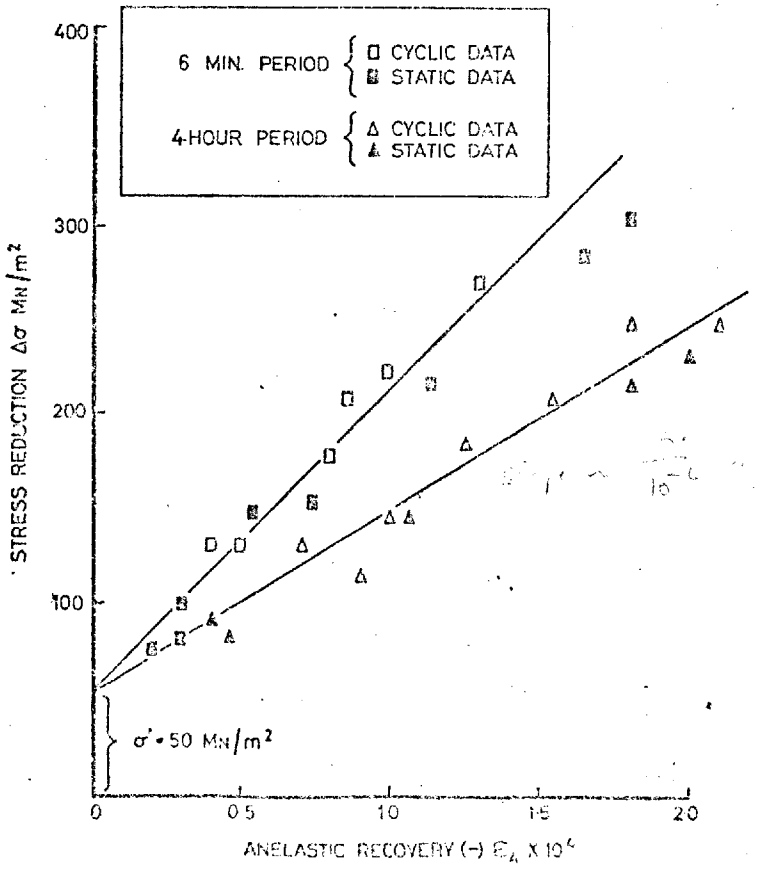

FIG. 29 EFFECT OF STRESS REDUCTION ON ANELASTIC RECOVERY OF NIMONIC 90 AT 1123K

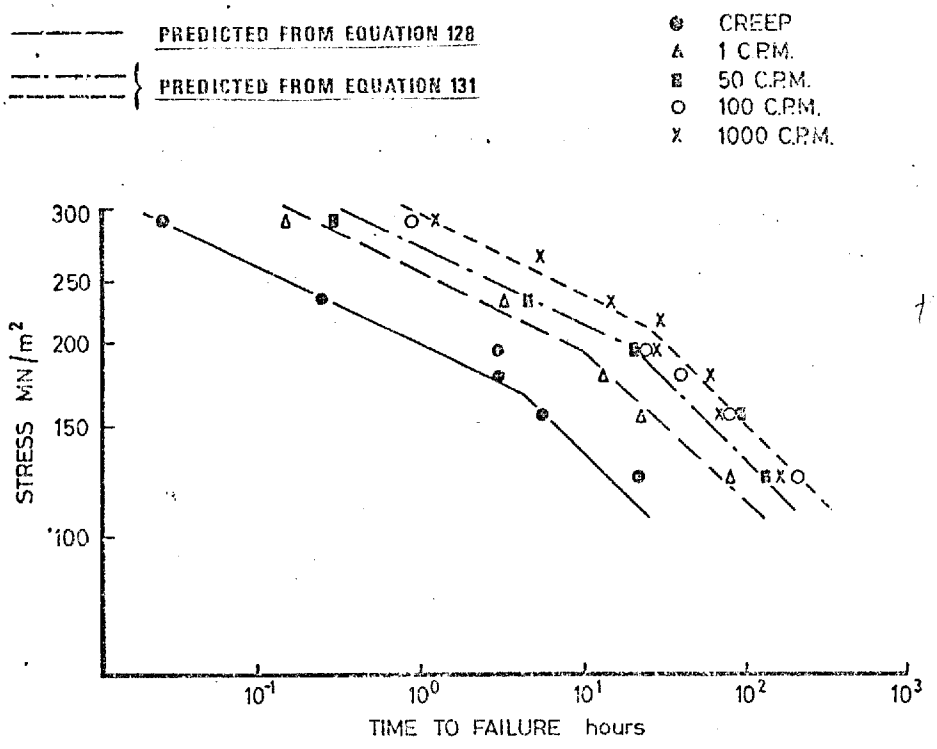

FIG.30 EFFECT OF FREQUENCY ON CYCLIC CREEP TIMES TO RUPTURE OF NIMONIC 90 AT 1173K

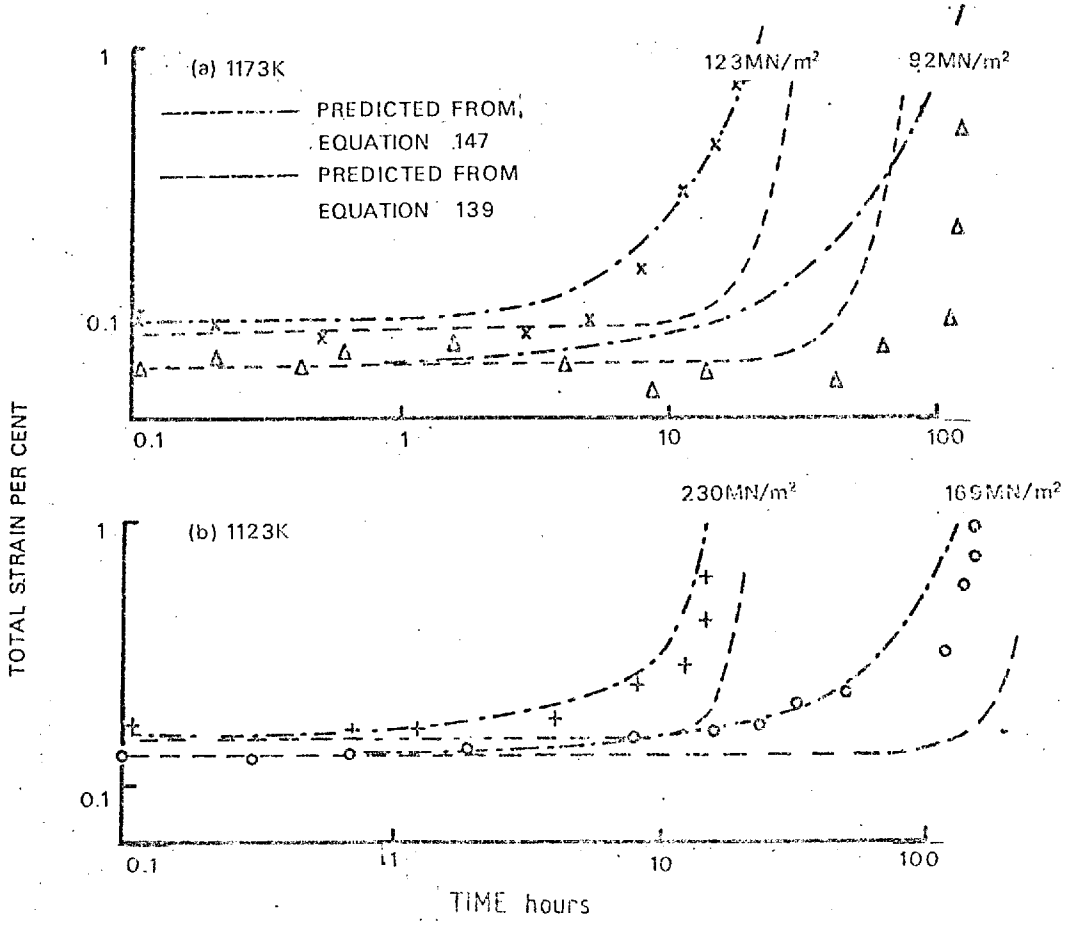

FIG.31 STRAIN ACCUMULATION UNDER RECTANGULAR PUSH-PULL STRESSING OF NIMONIC 90

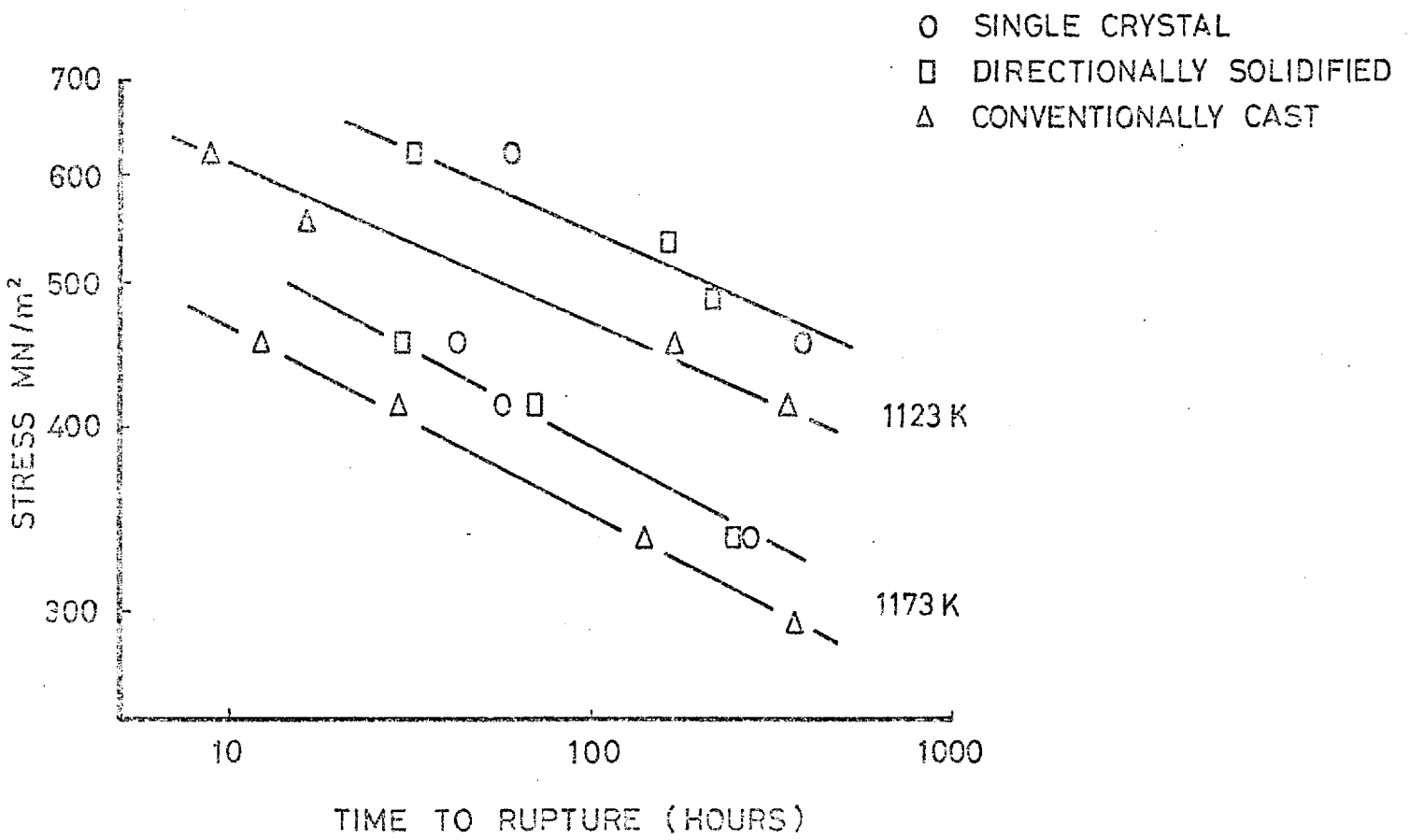

FIG.32 RUPTURE TIMES FOR THREE CAST FORMS OF MAR M246

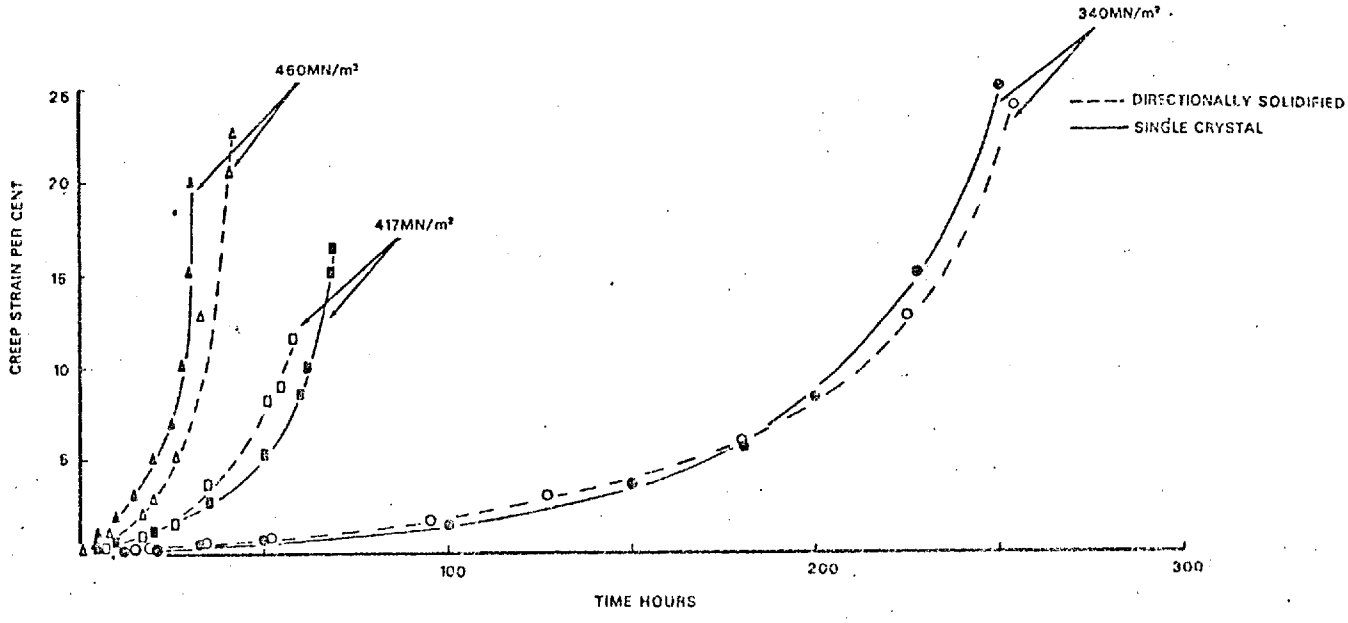

FIG.33 TENSILE CREEP OF DIRECTIONALLY SOLIDIFIED AND SINGLE CRYSTAL MAR M246 AT 1173K

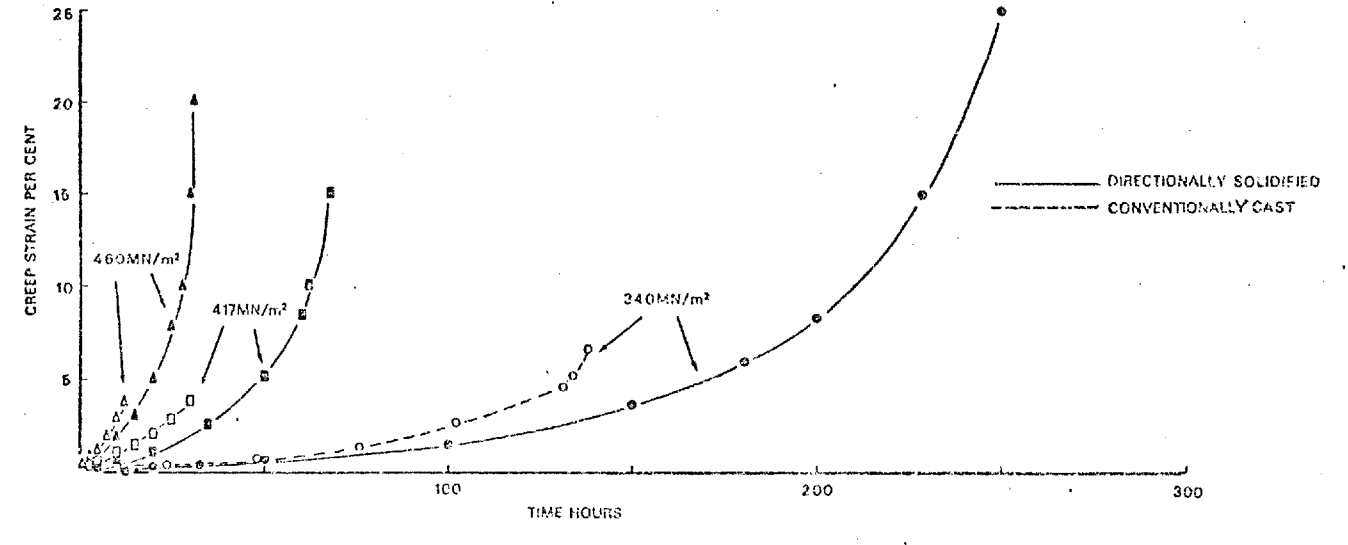

FIG.34 TENSILE CREEP OF DIRECTIONALLY SOLIDIFIED AND CONVENTIONALLY CAST MAR M246 AT 1173K

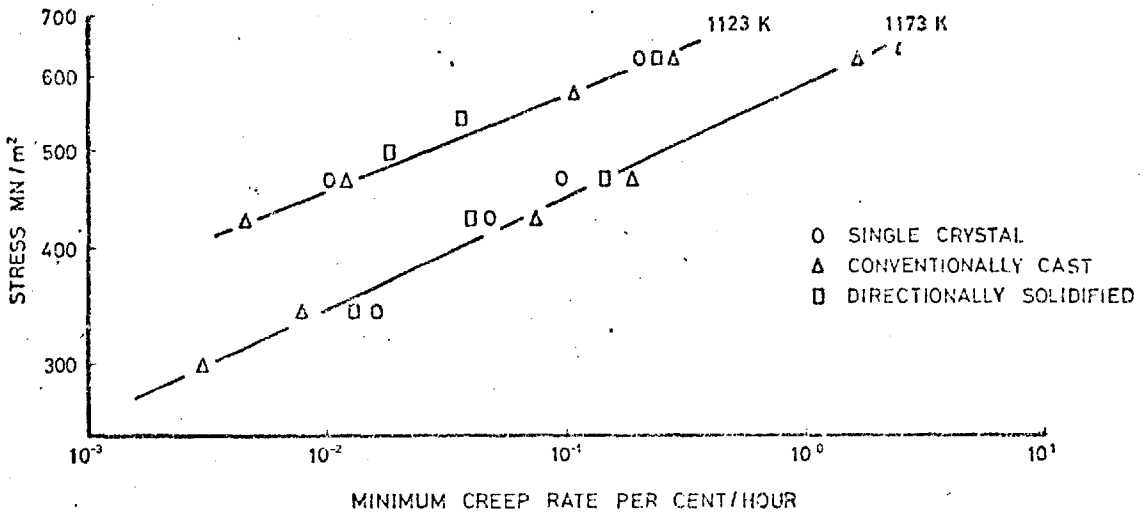

FIG. 35 THE EFFECT OF CAST FORM ON MINIMUM CREEP RATE

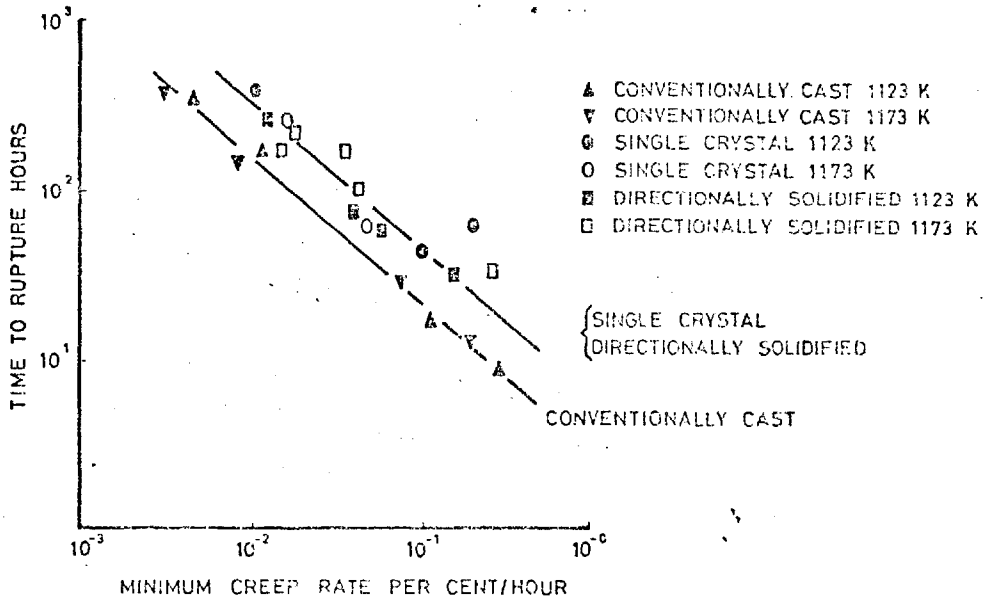

FIG. 36 CORRELATION BETWEEN MINIMUM CREEP RATE AND TIME TO RUPTURE

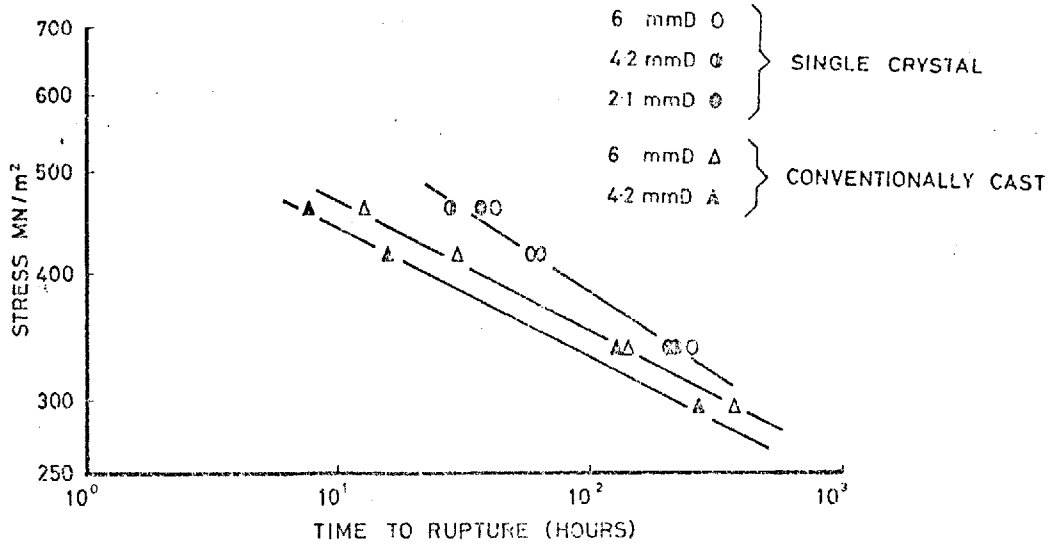

FIG. 37 THE EFFECT OF SPECIMEN SIZE ON TIMES TO RUPTURE OF SINGLE CRYSTAL AND CONVENTIONALLY CAST MAR M246 AT 1173 K

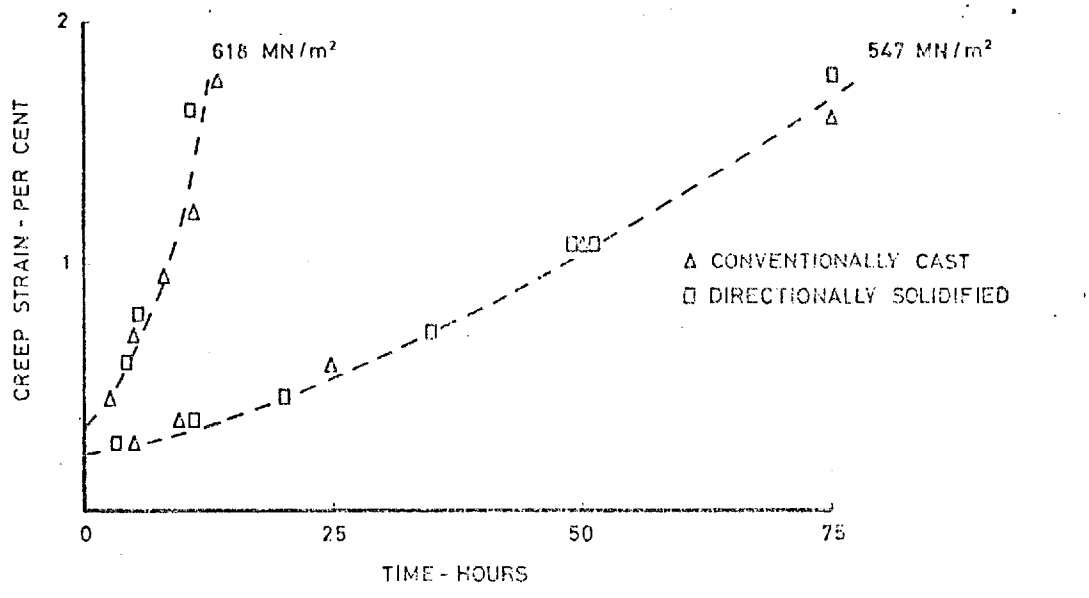

FIG. 38 COMPARISON BETWEEN CONVENTIONALLY CAST AND DIRECTIONALLY SOLIDIFIED MATERIAL UNDER COMPRESSIVE STRESS AT 1123K

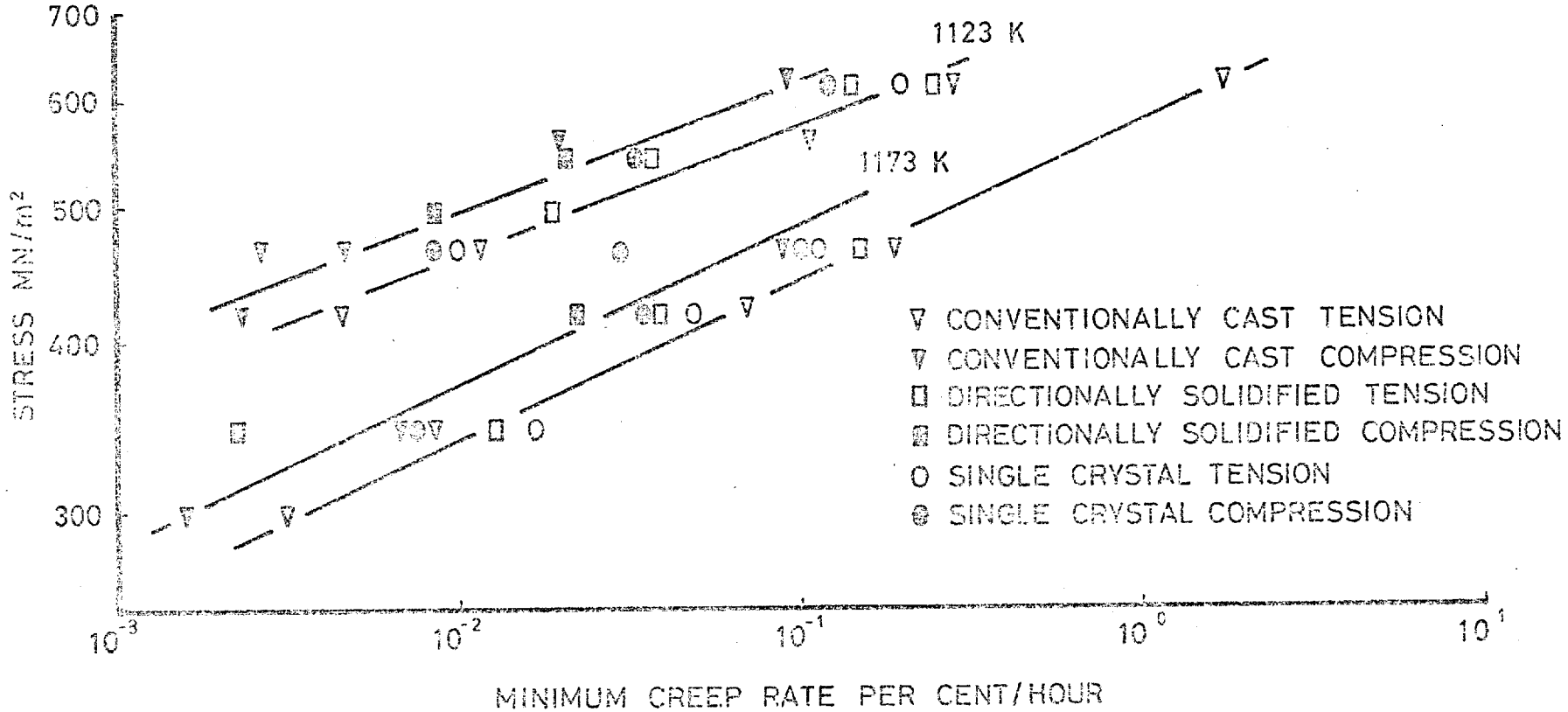

FIG. 39 COMPARISON OF MINIMUM CREEP RATE UNDER TENSILE AND COMPRESSIVE LOADING

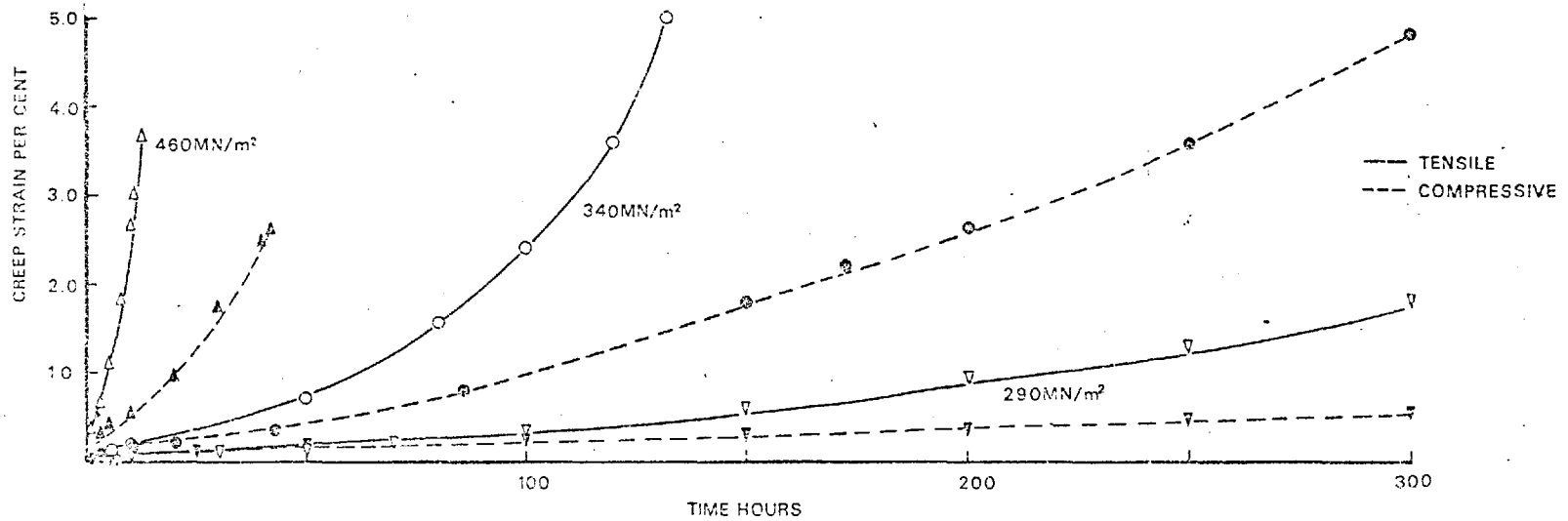

FIG.40 TENSILE AND COMPRESSIVE CREEP OF CONVENTIONALLY CAST MAR M246 AT 1173K

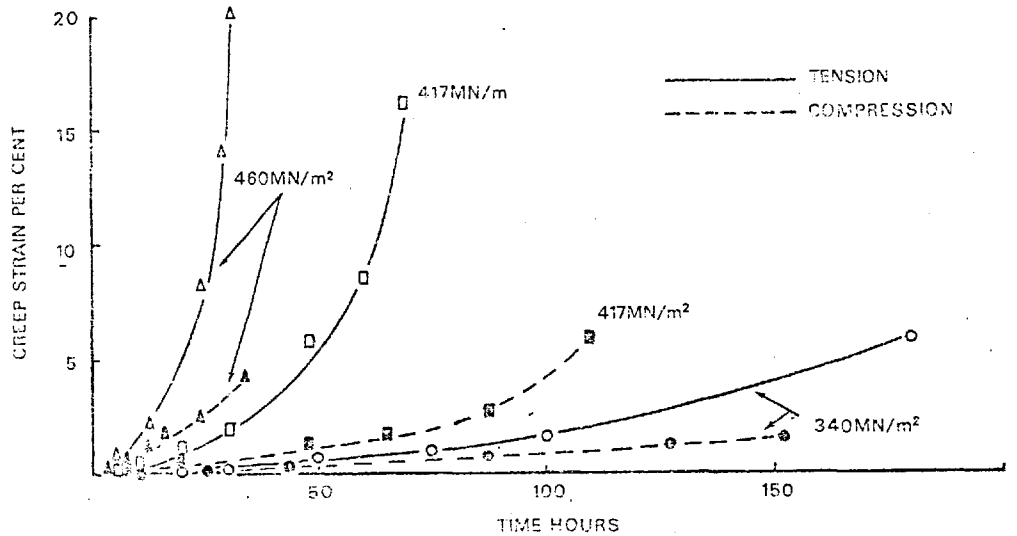

FIG.41 TENSILE AND COMPRESSIVE CREEP OF DIRECTIONALLY SOLIDIFIED MAR M246 AT 1173K

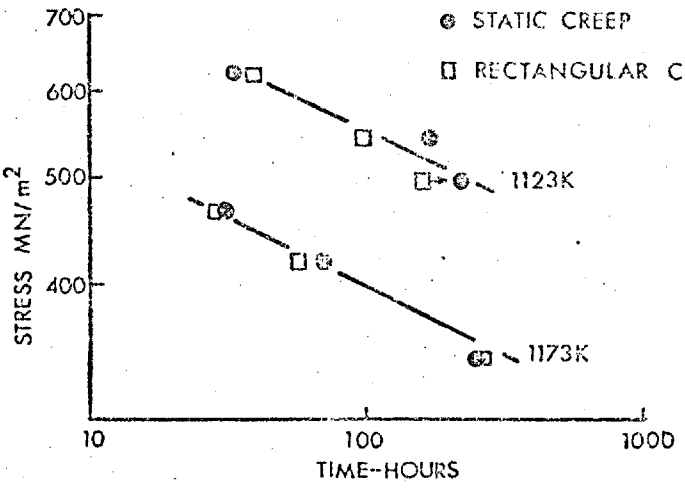

FIG.42 COMPARISON OF STATIC AND RECTANGULAR CREEP OF DIRECTIONALLY SOLIDIFIED MAR M246

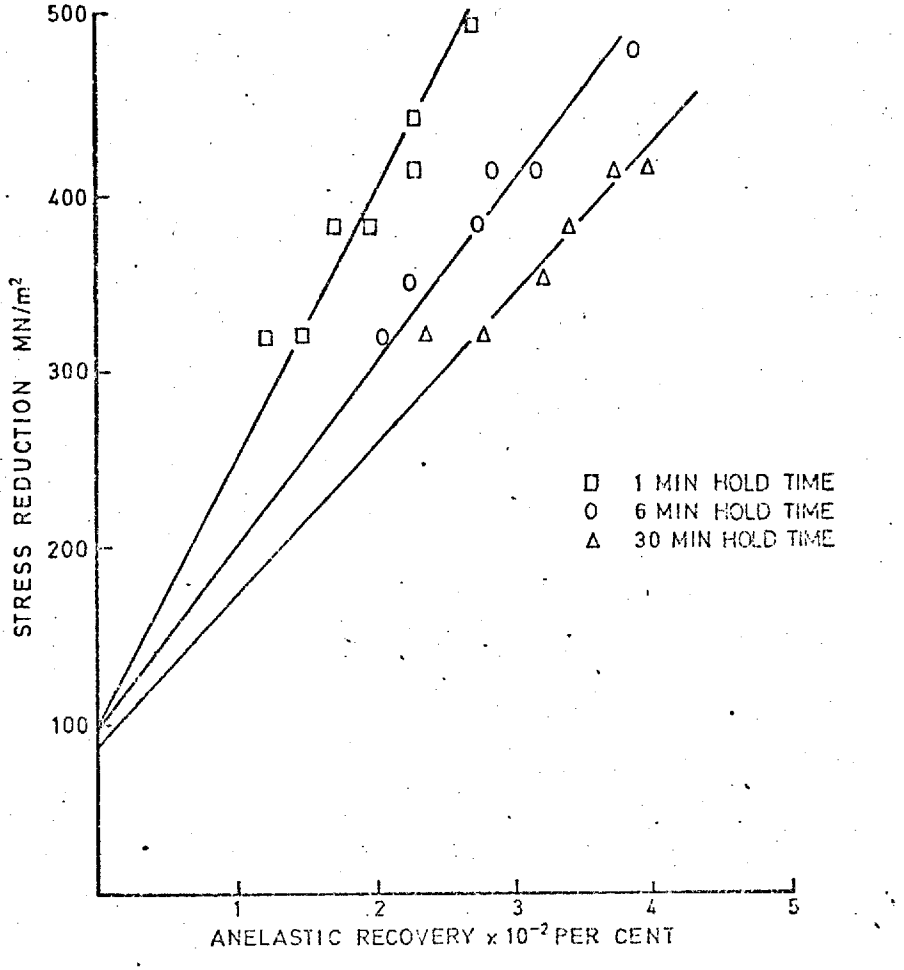

FIG. 43 ANELASTIC RECOVERY OF CONVENTIONALLY CAST MAR M246 AT 1173K

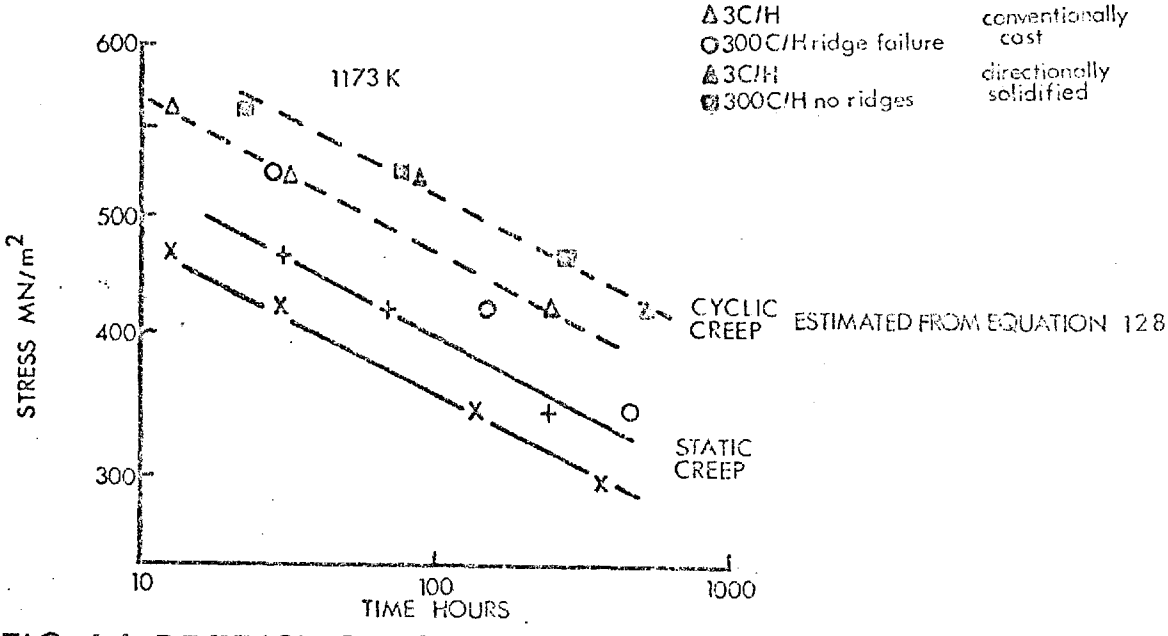

FIG.44 PREDICTION OF TRIANGULAR TENSION CREEP RUPTURE FROM STATIC CREEP DATA

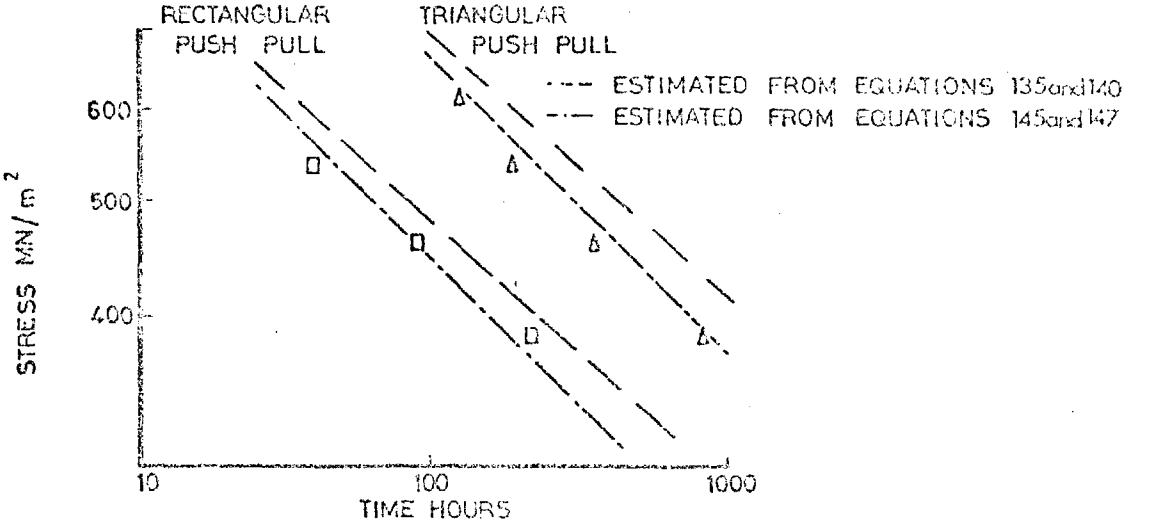

FIG.45 PREDICTION OF RECTANGULAR AND TRIANGULAR PUSH-PULL CREEP RUPTURE FROM STATIC CREEP DATA

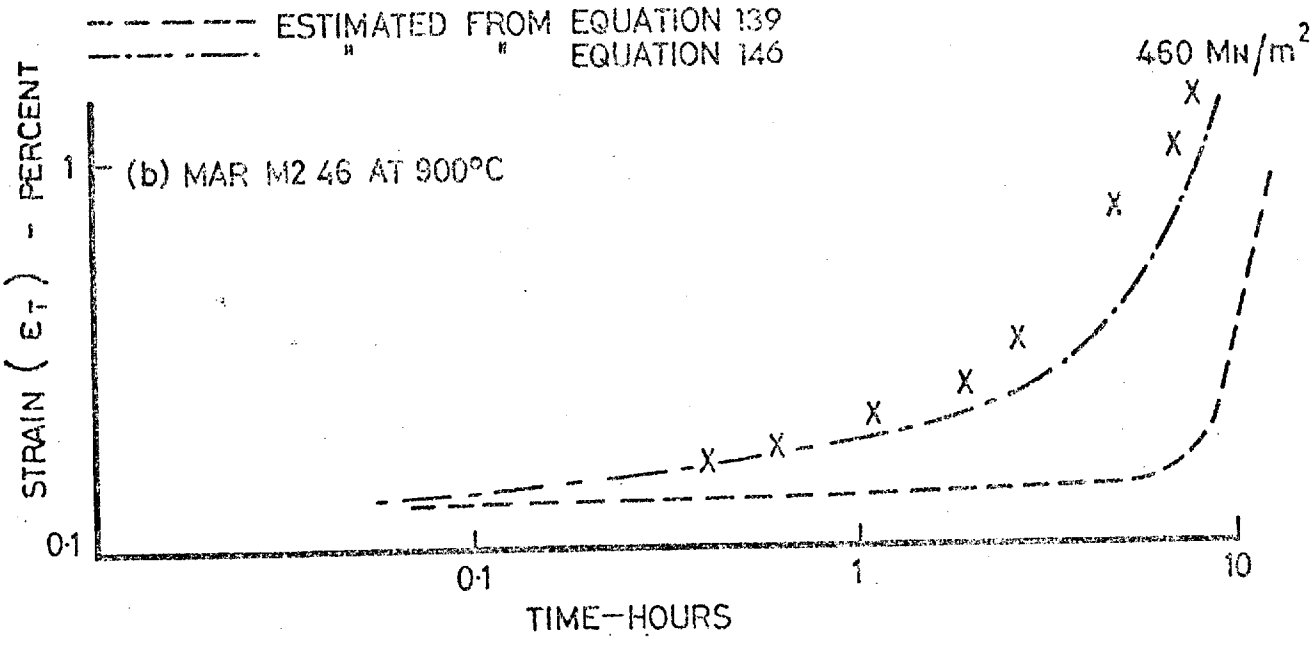

FIG.46 PREDICTION OF STRAIN ACCUMULATION UNDER RECTANGULAR PUSH-PULL CYCLING FROM STATIC CREEP DATA

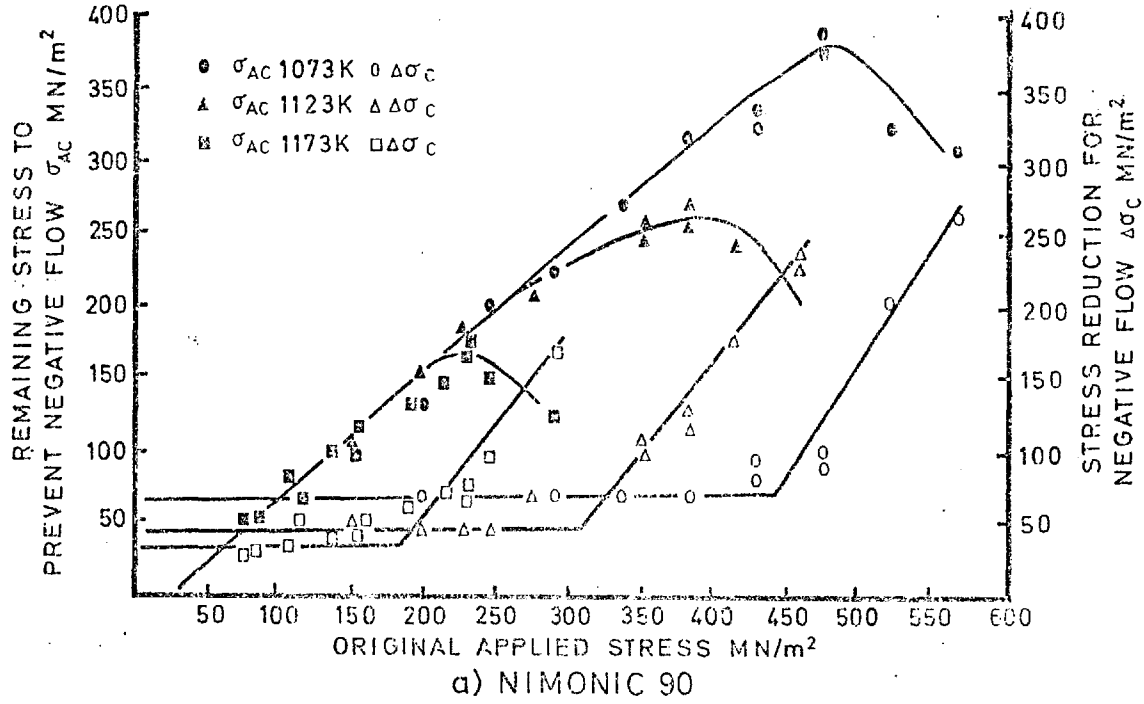

a) NIMONIC 90

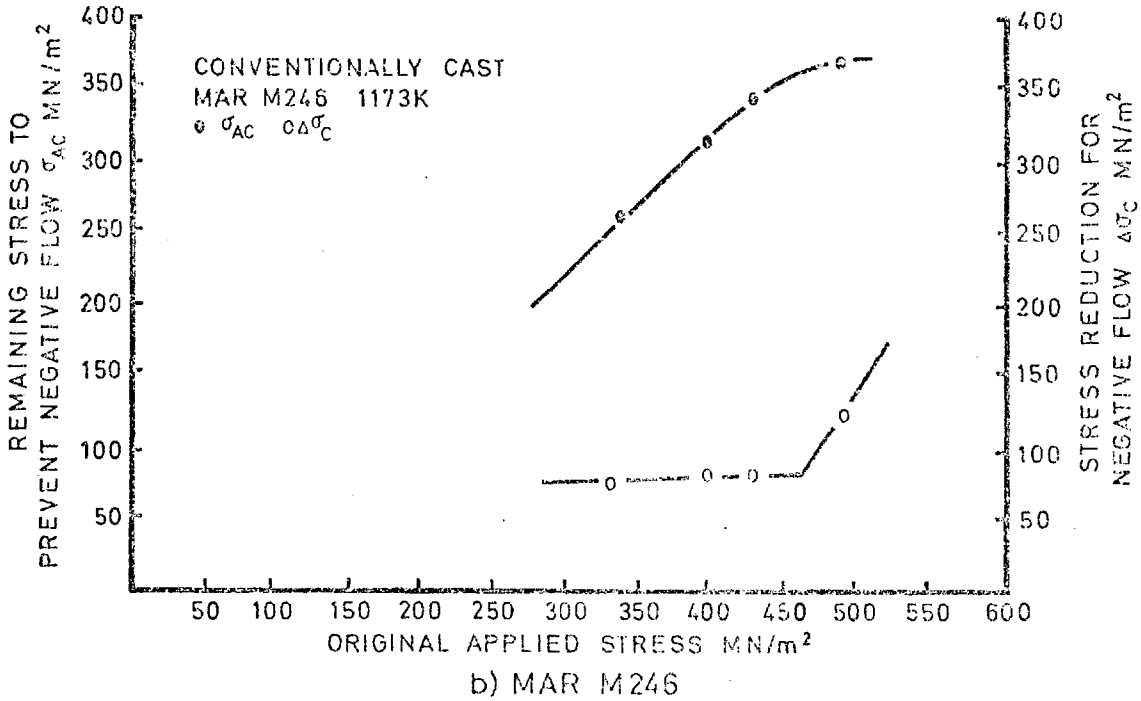

b) MAR M246

FIG.47 REMAINING APPLIED STRESS & CRITICAL STRESS REDUCTIONS REQUIRED TO INITIATE NEGATIVE FLOW IN a) NIMONIC 90 & b) CONVENTIONALLY CAST MAR M246

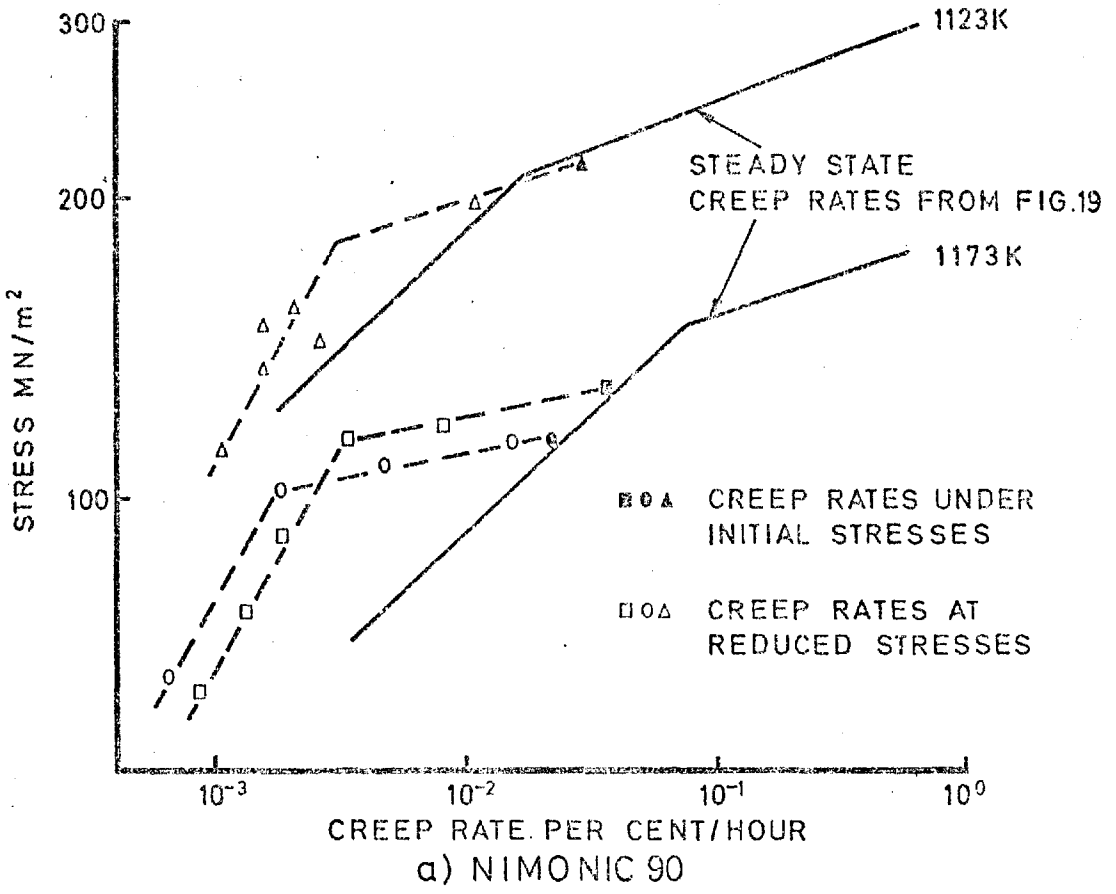

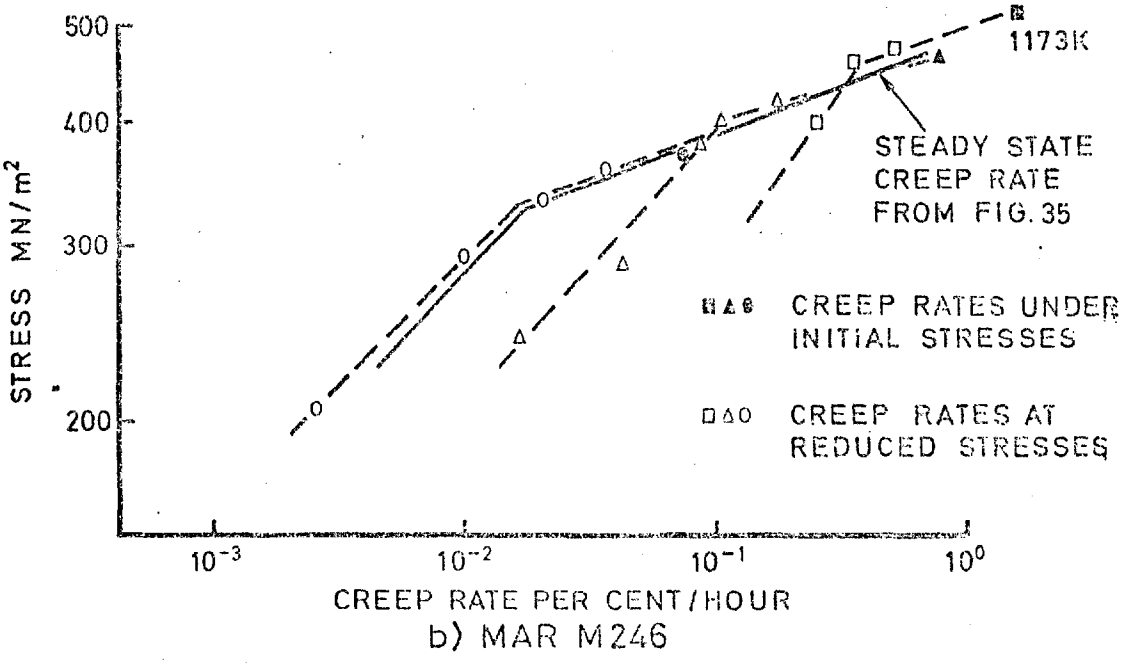

FIG.48 FORWARDS CREEP RATES FOR A SERIES OF STRESS REDUCTIONS FOR a) NIMONIC 90 & b) MAR M246

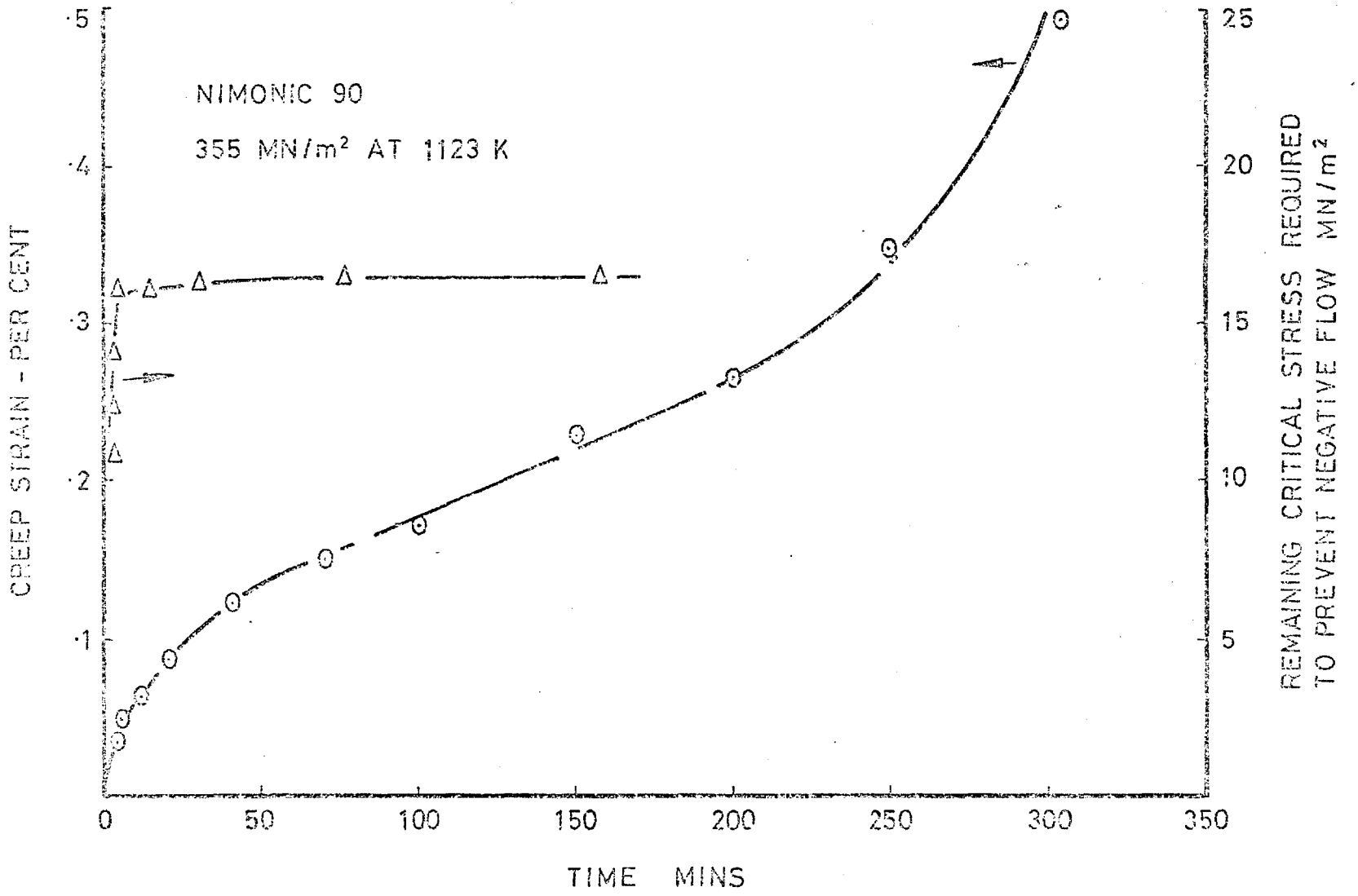

FIG.49 VARIATION IN CRITICAL STRESS THROUGHOUT CREEP LIFE

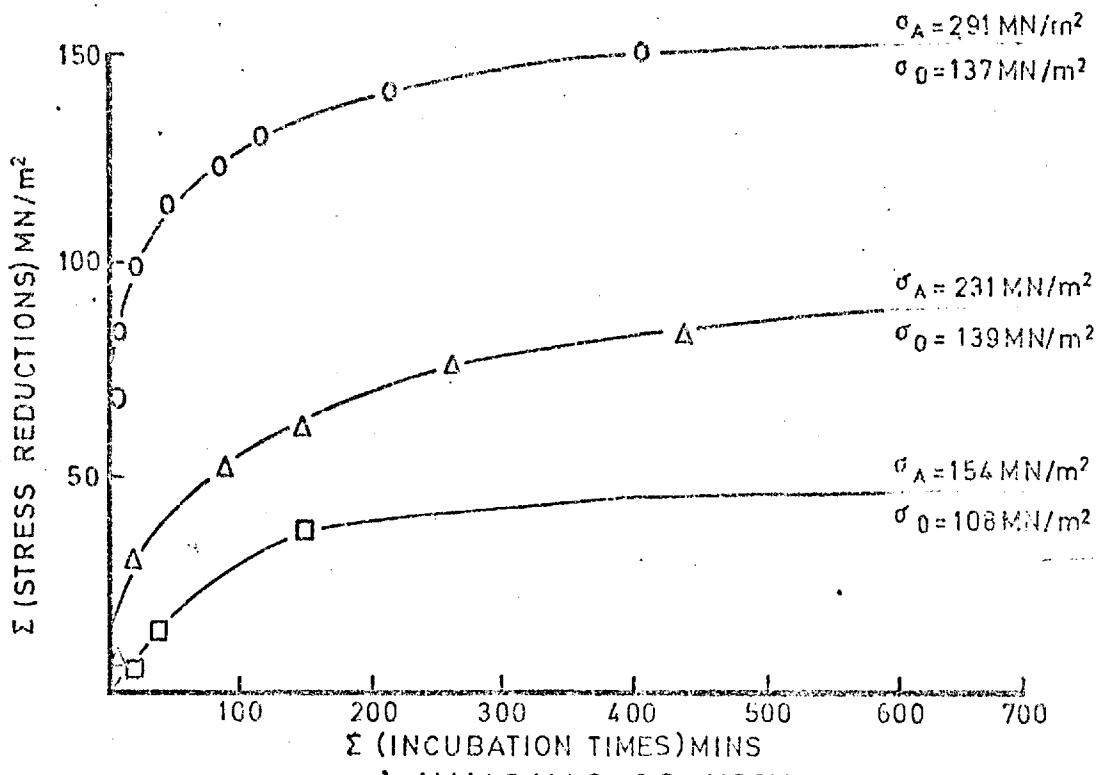

a) NIMONIC 90 1123K

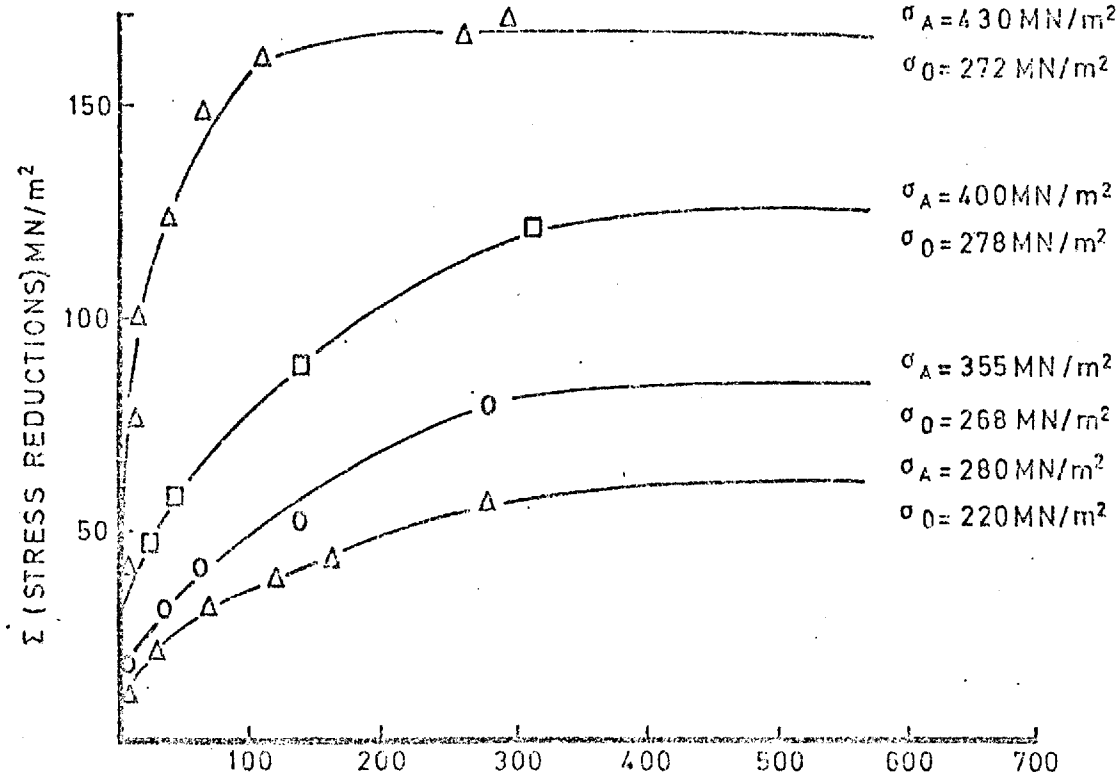

b) MAR M246 1173K

FIG.50 ACCUMULATED STRESS REDUCTIONS & INCUBATION PERIODS FOR a) NIMONIC 90 & b) MAR M246

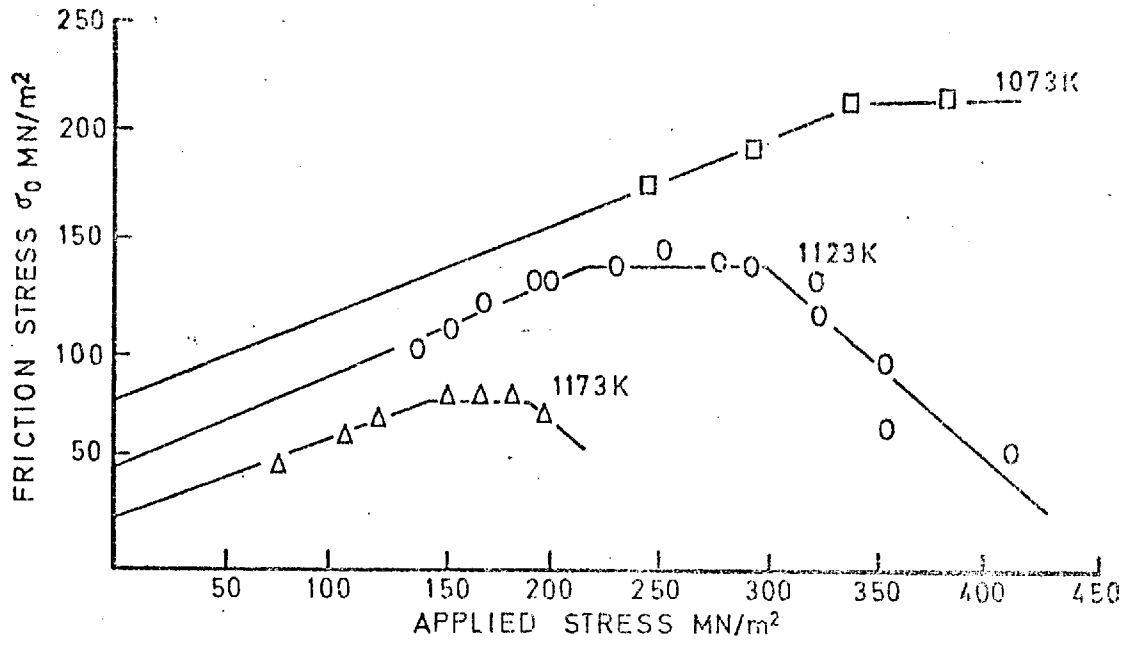

a) NIMONIC 90

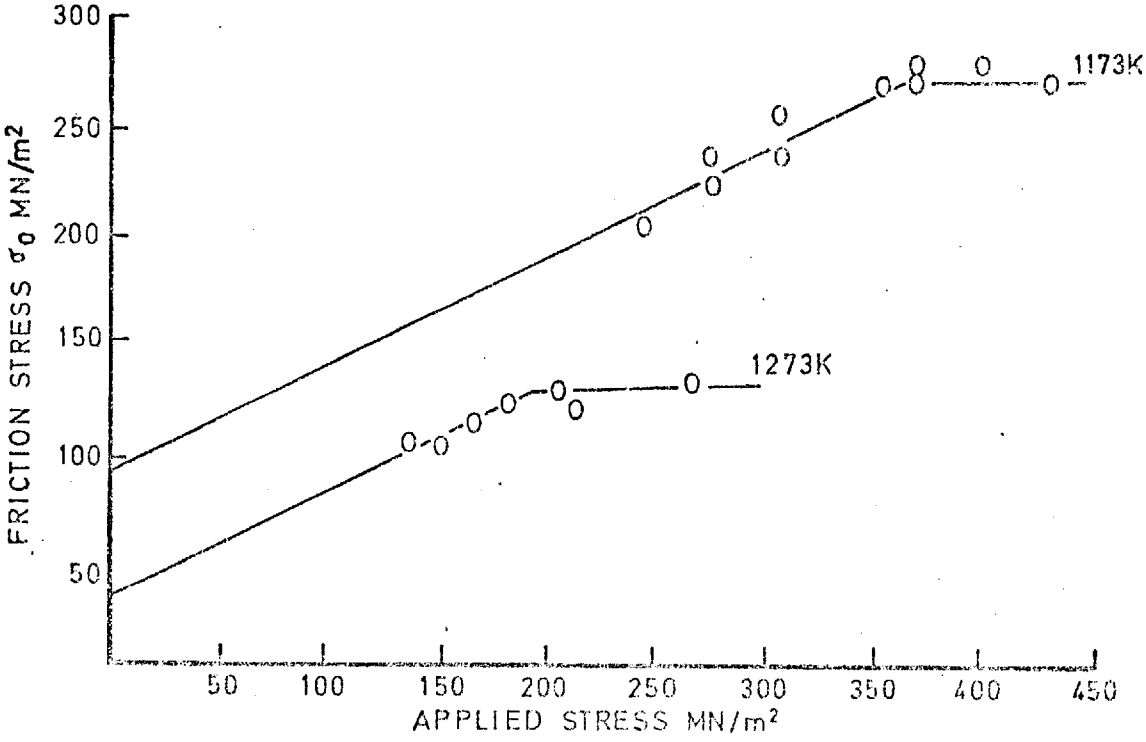

b) MAR M246

FIG.51 THE EFFECT OF APPLIED STRESS & TEMPERATURE ON FRICTION STRESS LEVELS OF a) NIMONIC 90 b) MAR M246

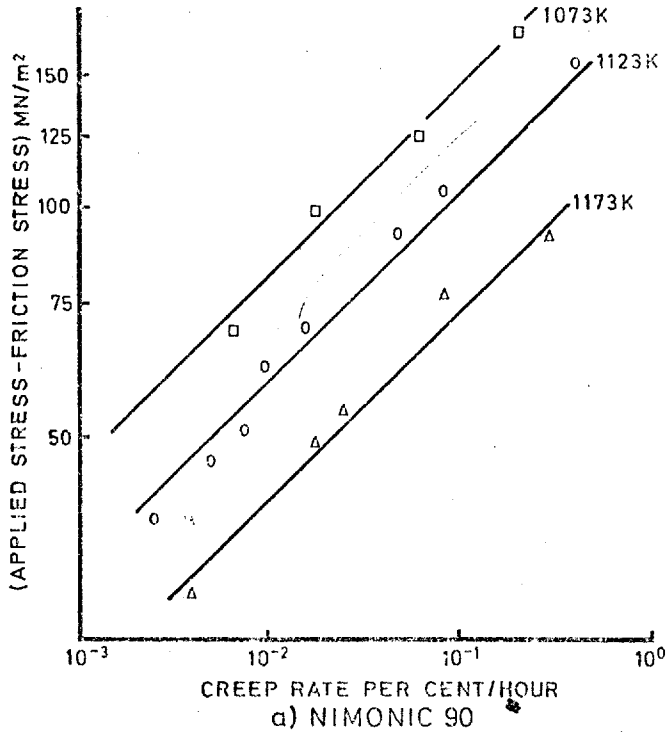

a) NIMONIC 90

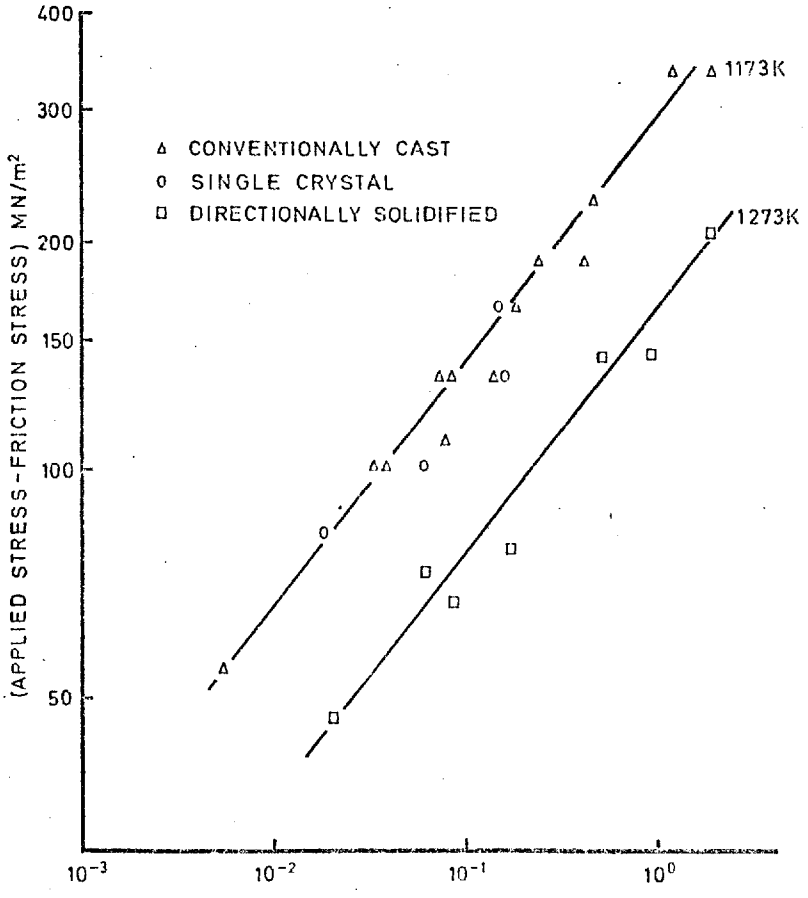

b) MAR M246

FIG. 52 EFFECTIVE STRESS-MINIMUM CREEP RATE CORRELATION FOR a) NIMONIC 90 & b) MAR M246

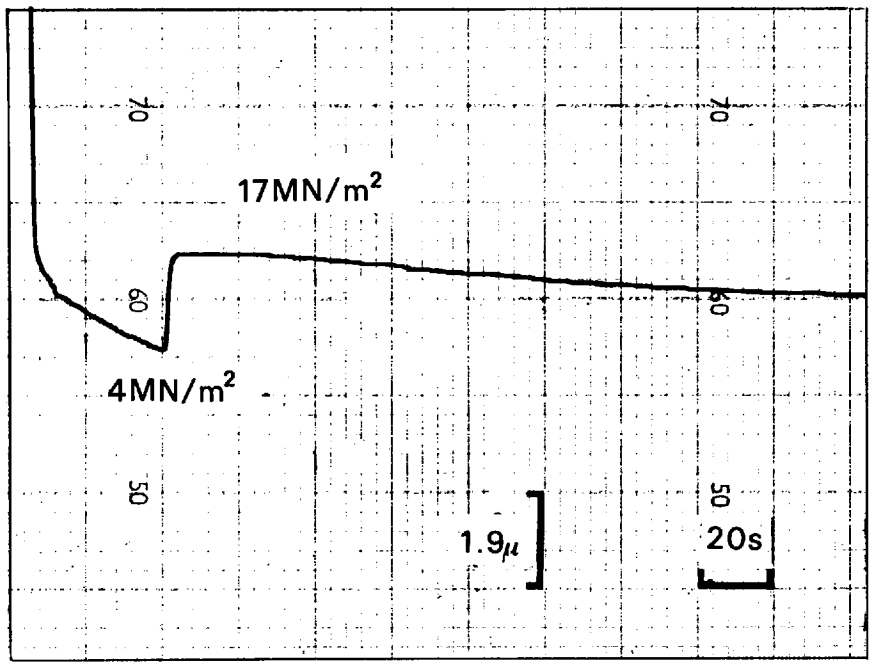

FIG.53 EFFECT OF STRESS CHANGE ON ANELASTIC RECOVERY OF NIMONIC 90



×500

FIG.54 STEREOSCAN MICROGRAPH OF INTERGRANULAR FRACTURE IN NIMONIC 90 AFTER 225MN/m² AT 1073K



×450

FIG.55 WEDGE CRACKING IN NIMONIC 90
AFTER 340MN/m^2 AND 1073K

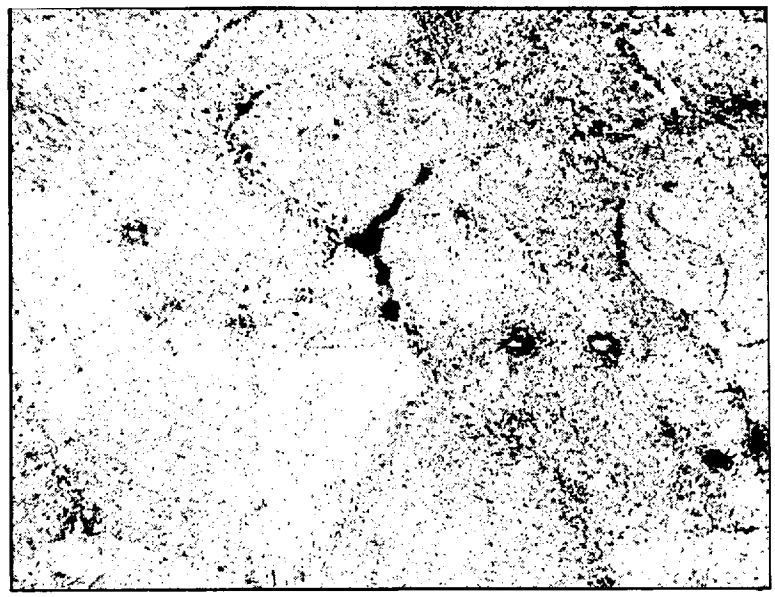

×450

FIG.56 CAVITY CRACKING IN NIMONIC 90
AFTER 70 MN/m^2 AND 1073K



×1000

FIG.57 STEREOSCAN MICROGRAPH OF CAVITY
NUCLEATION IN NIMONIC 90
AFTER 70 MN/m^2 AND 1173K

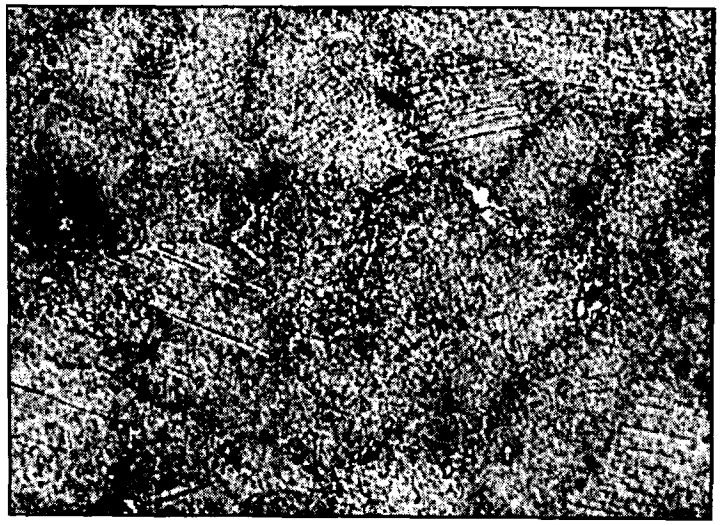

×500

(a) DEAD ZONE - LITTLE DENUDATION



×500

(b) CENTRE REGION - LARGE DENUDED AREAS

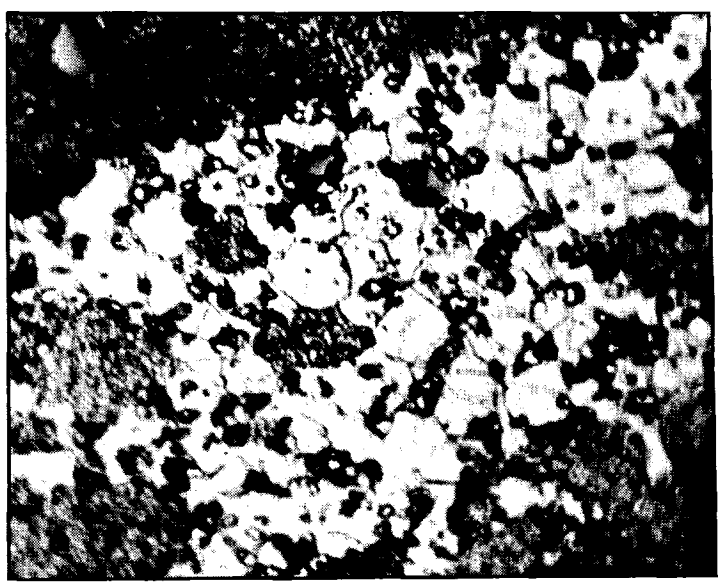

×1250

(c) RECRYSTALLISATION WITHIN DENUDED AREAS

FIG.58 COMPARISON OF DEAD ZONE AND CENTRE AFTER 30% COMPRESSION AT 1173K

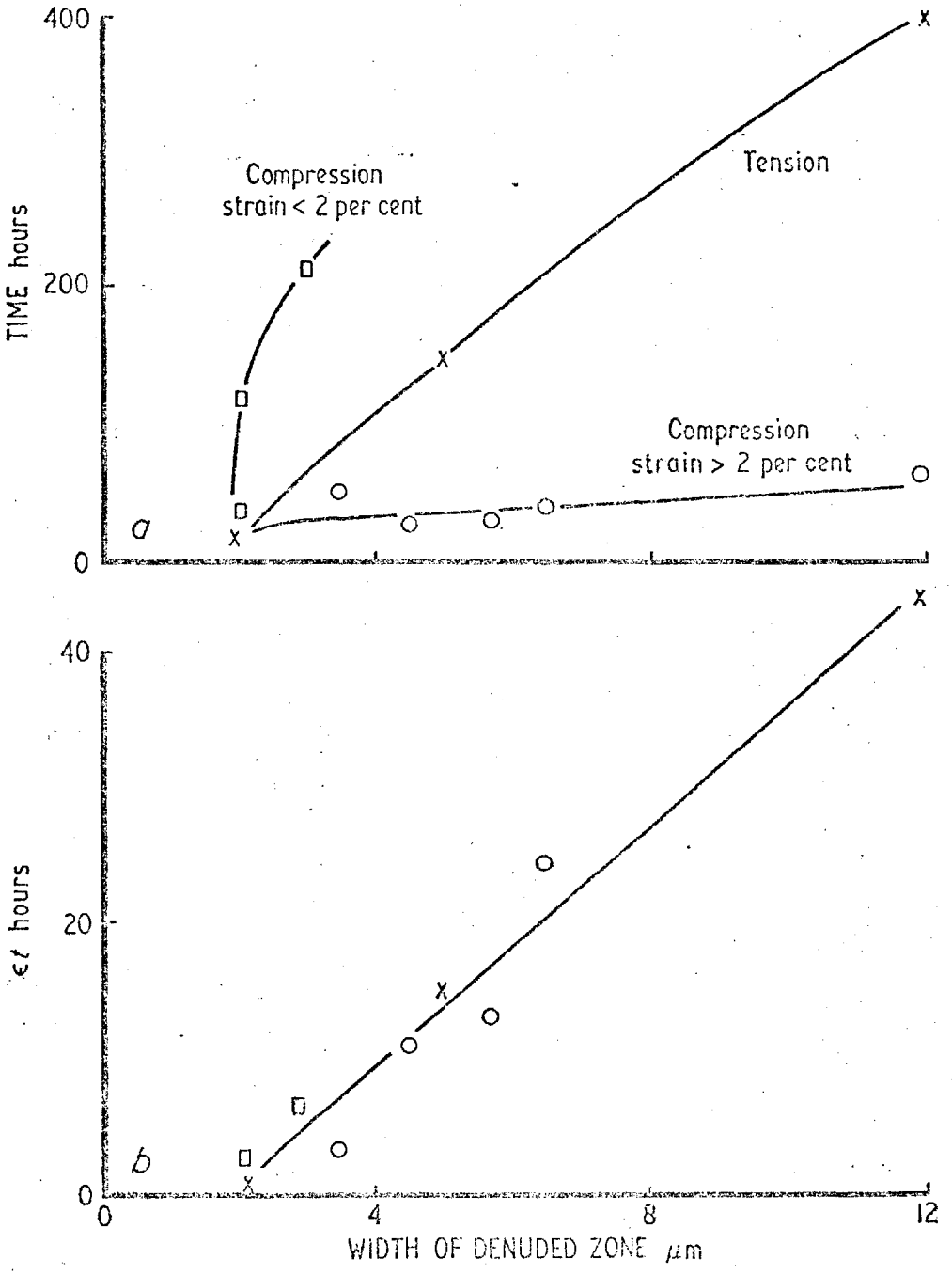

FIG.59 INFLUENCE OF TIME AND STRAIN ON GROWTH OF DENUDED ZONES IN NIMONIC 90 AT 1173K

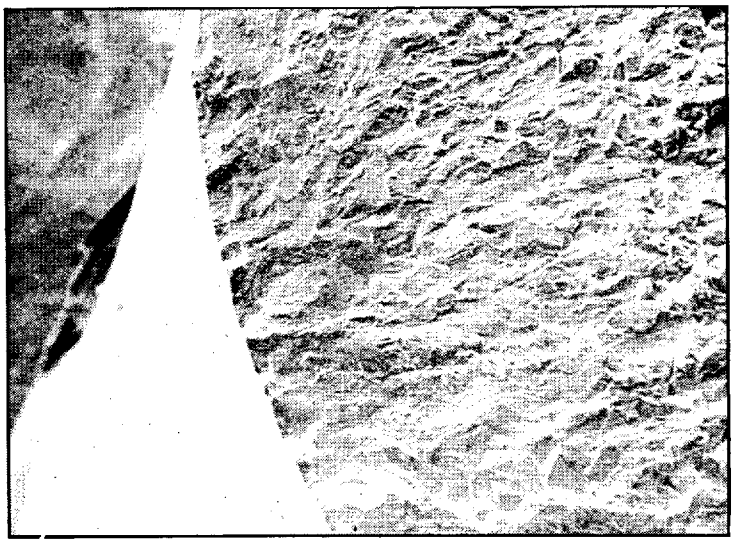

×50



×1000

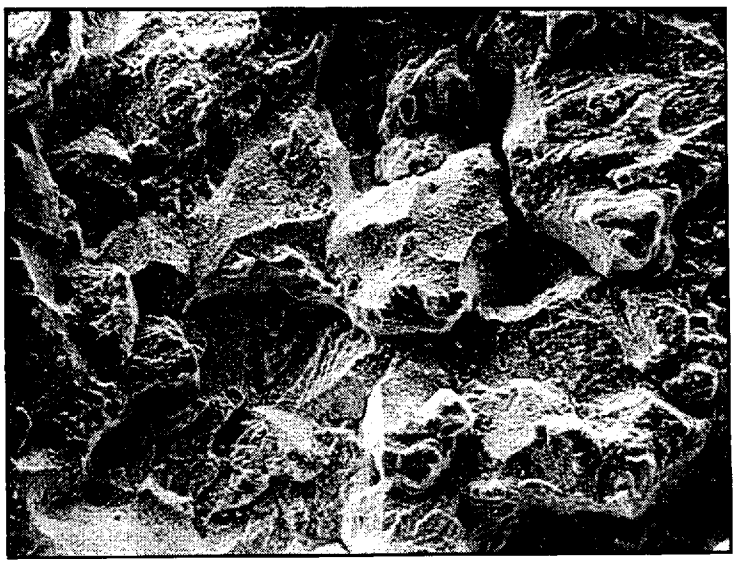

×200

FIG.60 FATIGUE FAILURE OF NIMONIC 90 AFTER 1000 c/m AT 1173K AND 270 MN/m^2

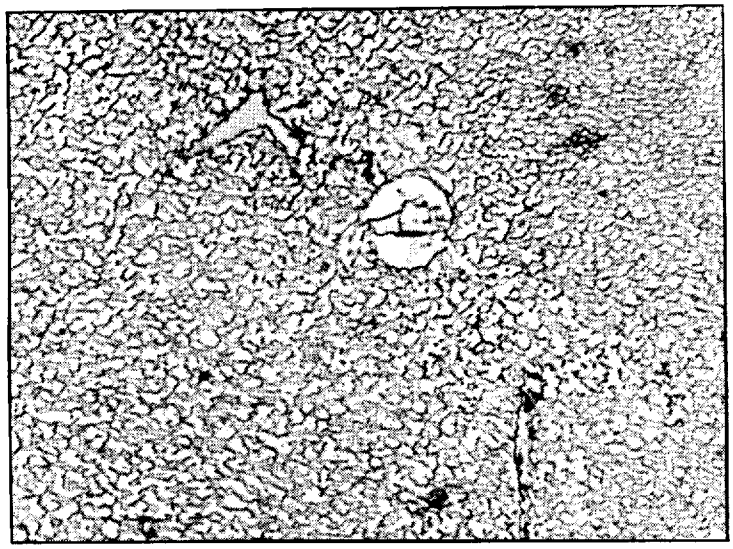

×600

(a) CONVENTIONALLY CAST

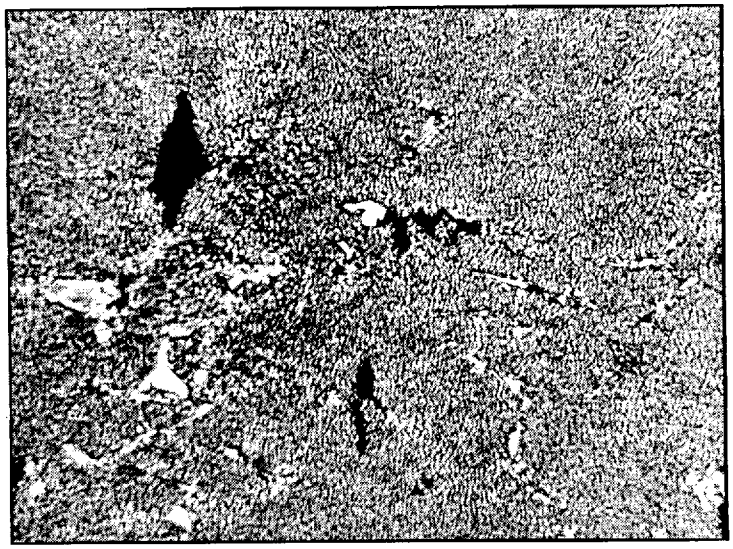

×400

(b) DIRECTIONALLY SOLIDIFIED

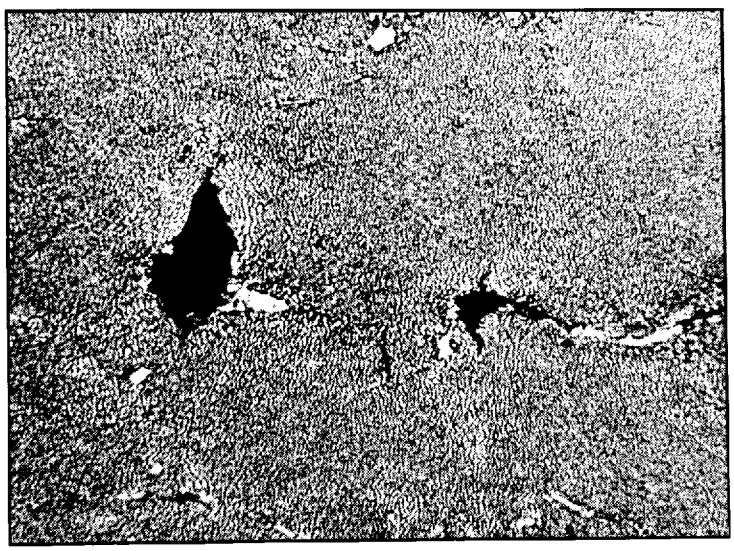

×400

(c) SINGLE CRYSTAL

FIG.61 CREEP CRACKING IN THREE FORMS OF MAR M246

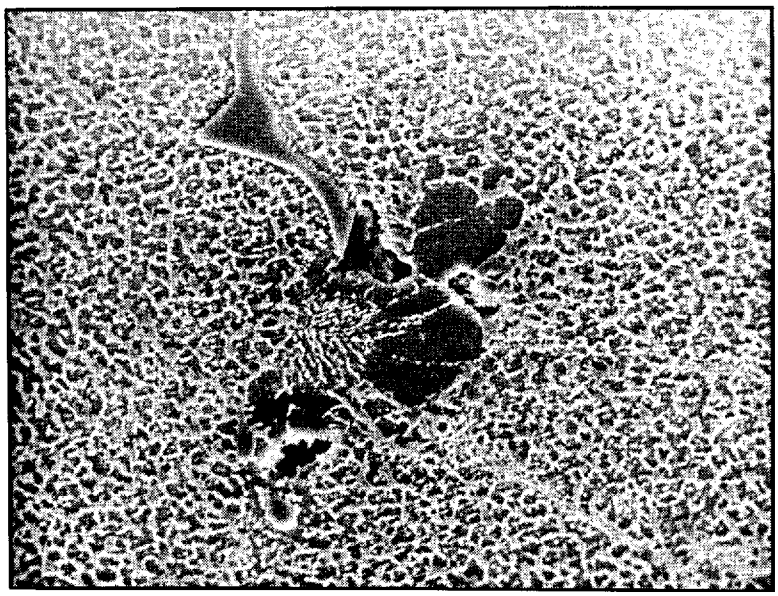

(a) ×2000

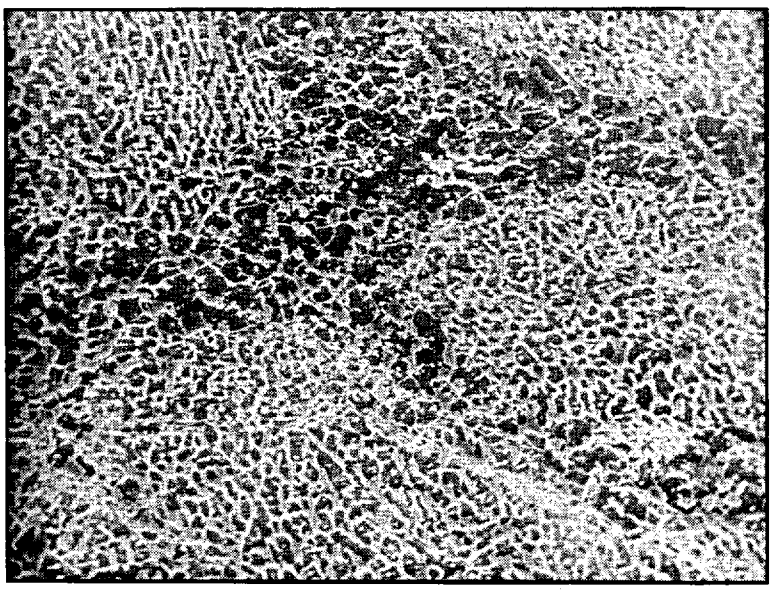

(b) ×2000

FIG.62 COMPARISON OF a) GENERAL STRUCTURE AND b) REGIONS OF STRAIN INDUCED COARSENING OF γ' PRECIPITATES IN MAR M246 AFTER COMPRESSIVE DEFORMATION



×25

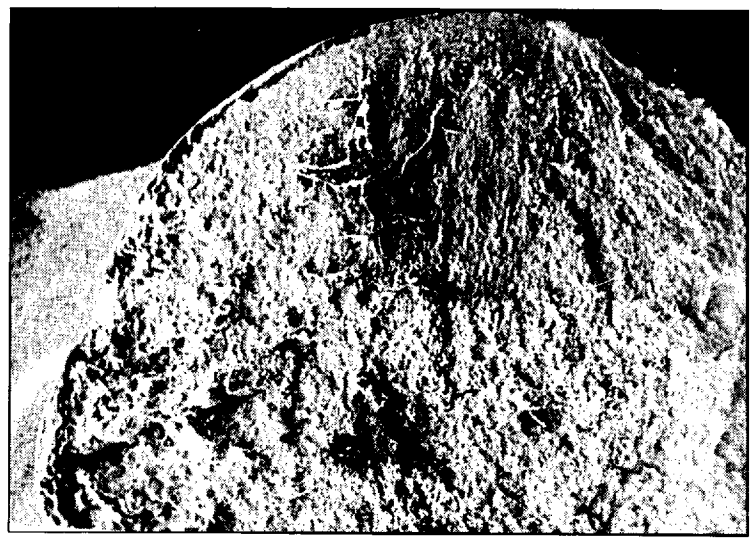

×25

FIG.63 CRACK INITIATION IN DIRECTIONALLY SOLIDIFIED MAR M246 AFTER 300 c/h AT 1173K AND 616 MN/m^2, 425 MN/m^2

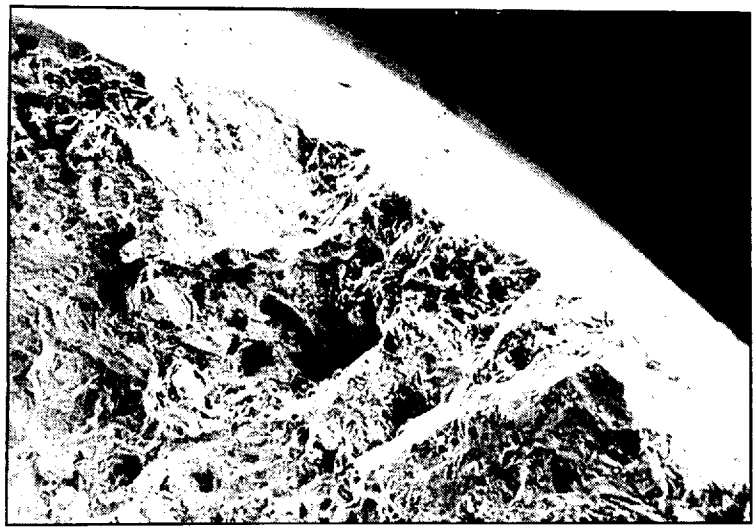

×100

FIG.64 CRACK INITIATION AFTER PUSH-PULL TRIANGULAR CYCLING OF CONVENTIONALLY CAST MAR M246 AT 450 MN/m^2 AND 1173K

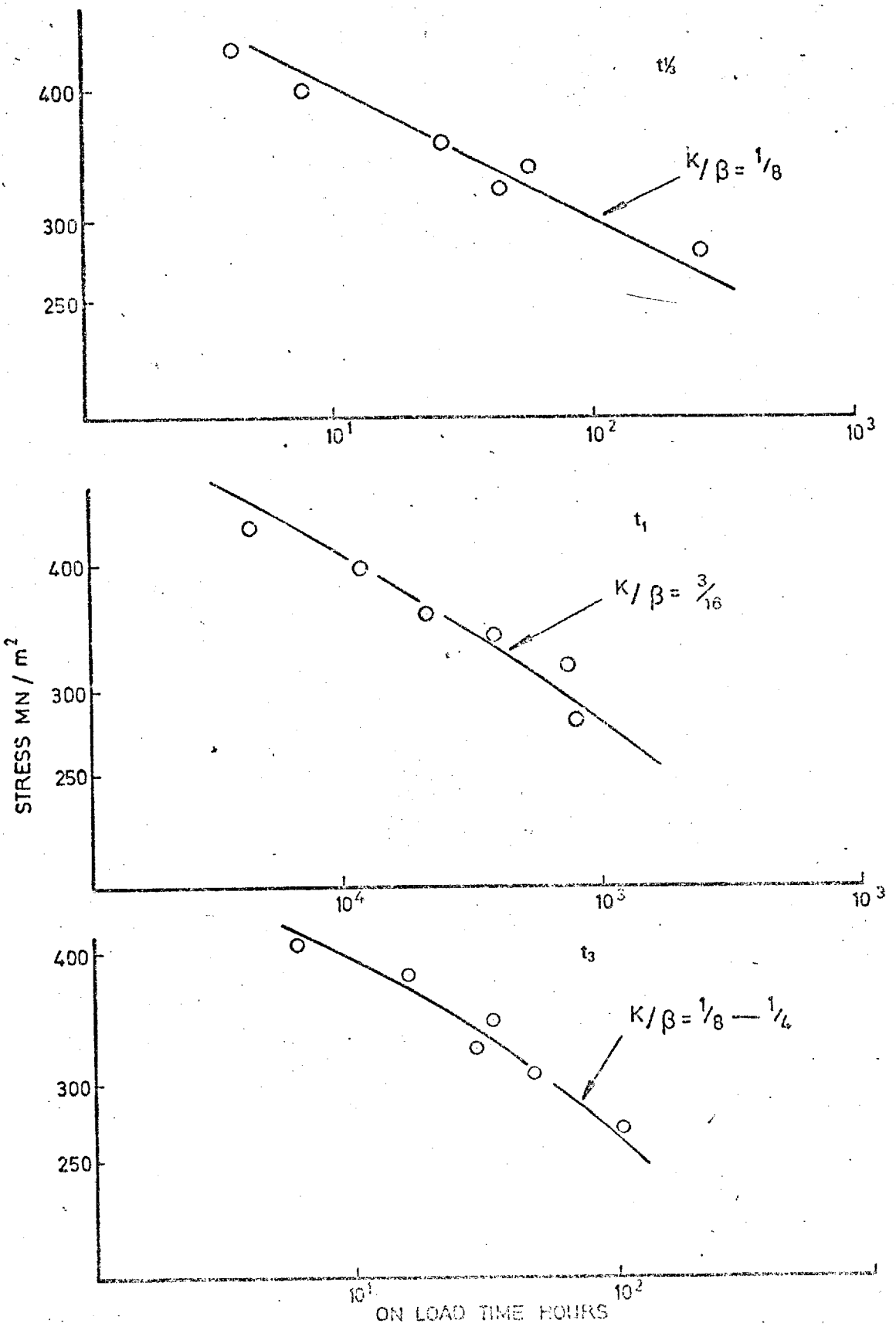

FIG.65 STRAIN COMPONENT CROSS PLOTS FOR CYCLIC TESTS ON NIMONIC 90 AT 1073K

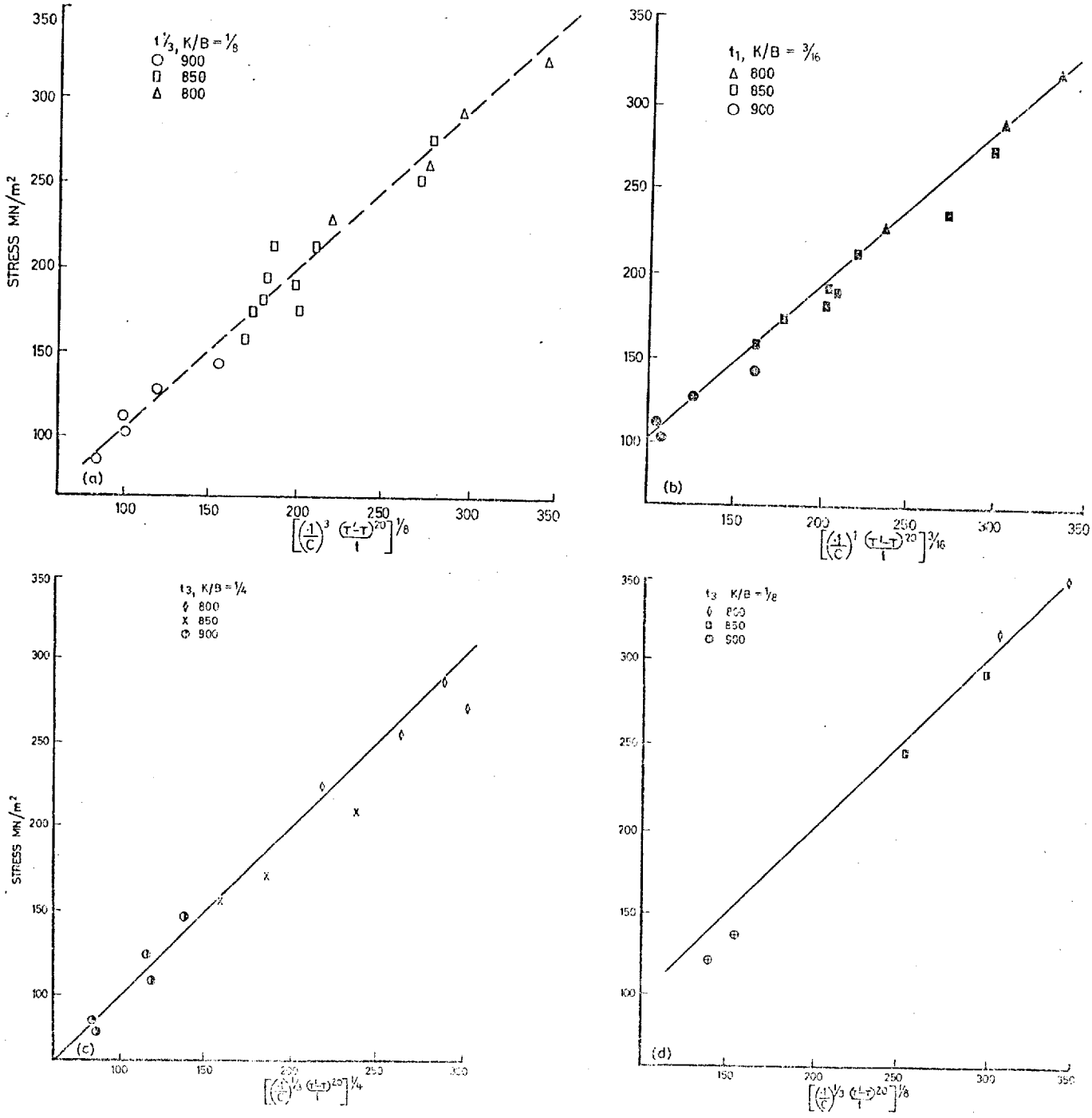

FIG.66 a–d GRAPHICAL DISPLAY OF COMPUTER ANALYSED COMPONENT TERMS OF NIMONIC 90 CREEP CURVES

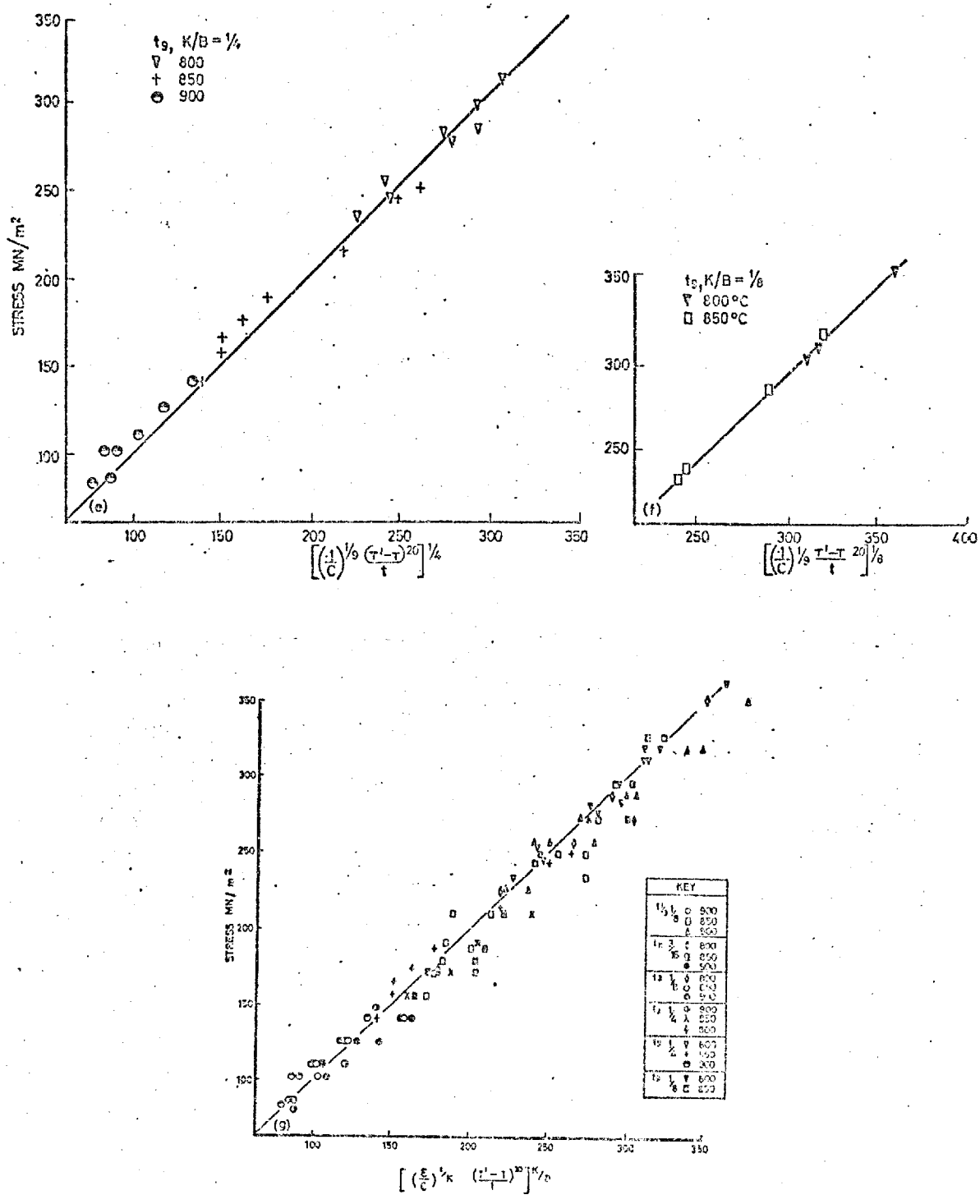

FIG.66 e–g GRAPHICAL DISPLAY OF COMPUTER ANALYSED COMPONENT TERMS OF NIMONIC 90 CREEP CURVES

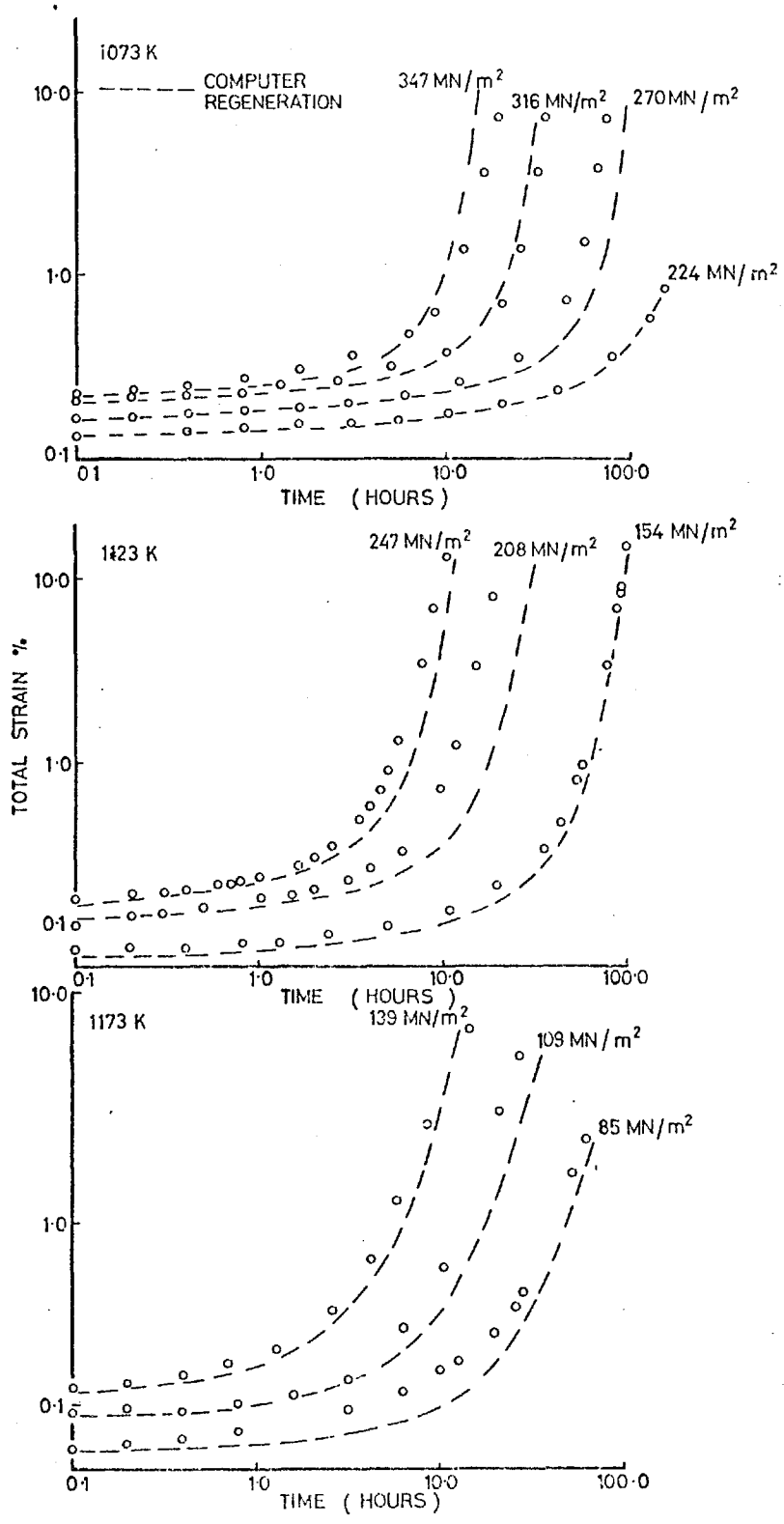

FIG. 67 COMPUTER REGENERATED CREEP CURVES FOR NIMONIC 90

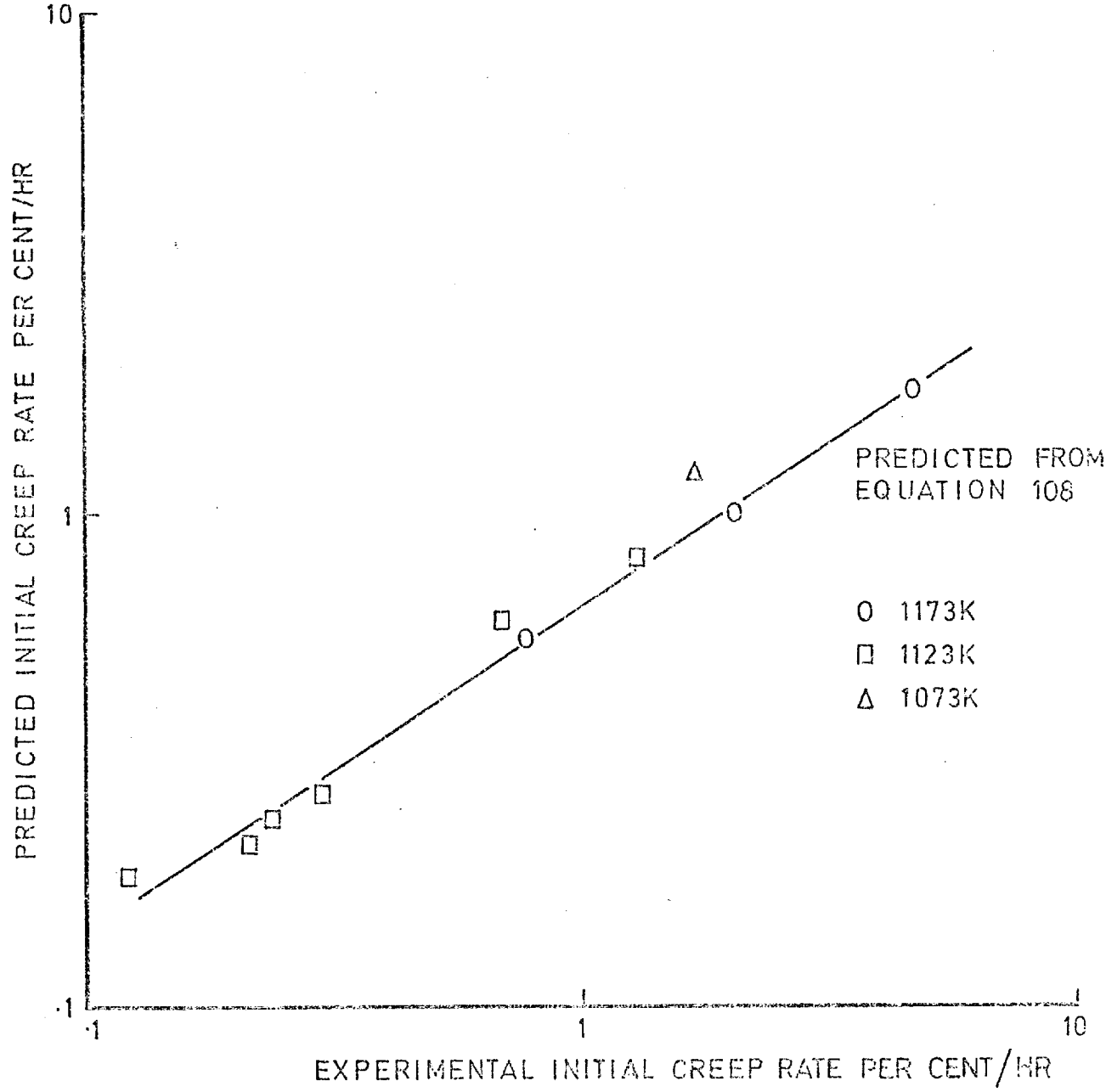

FIG.68 COMPARISON OF PREDICTED AND EXPERIMENTAL INITIAL CREEP RATES FOR NIMONIC 90

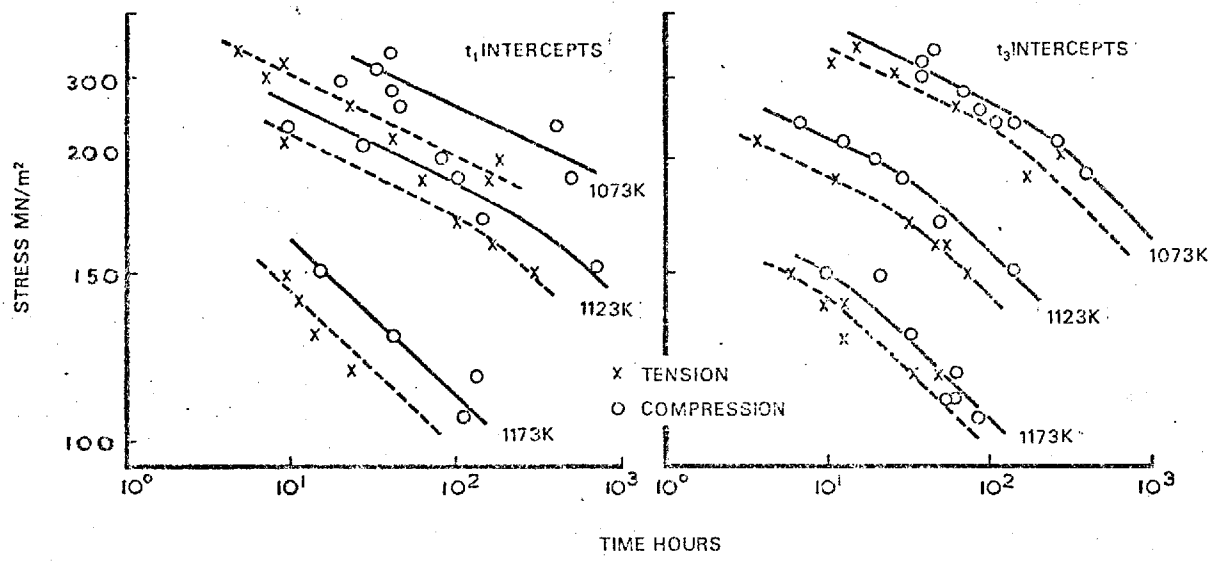

FIG.69 STRAIN COMPONENT CROSS PLOTS FOR NIMONIC 90

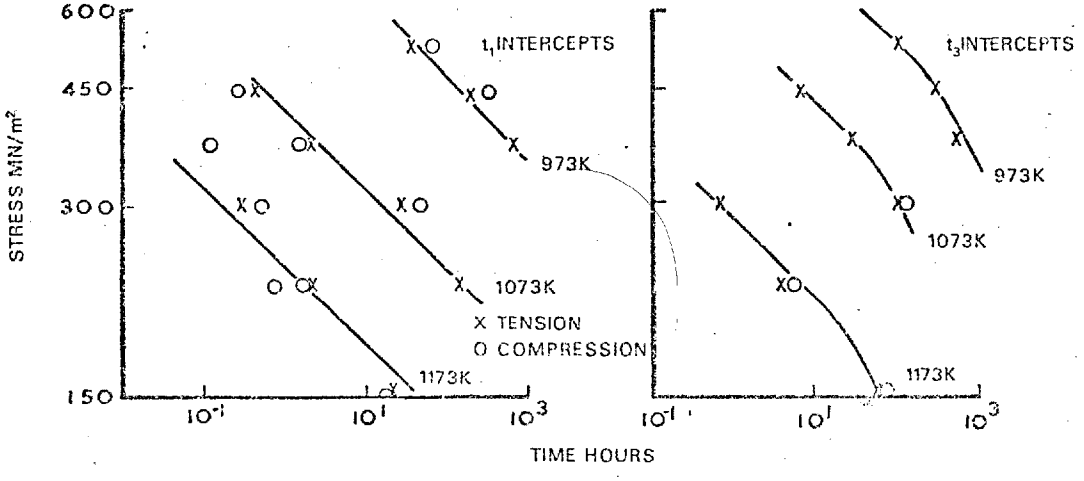

FIG.70 STRAIN COMPONENT CROSS PLOTS FOR NIMONIC 108

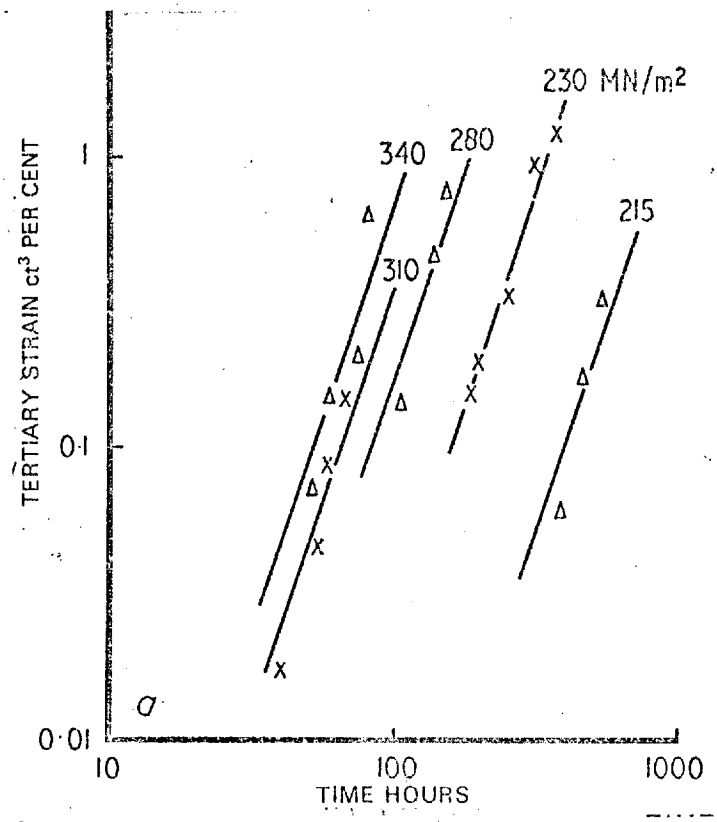

FIG.71 TERTIARY CREEP COMPONENTS OF NIMONIC 90 UNDER COMPRESSIVE STRESSES AT 1073K

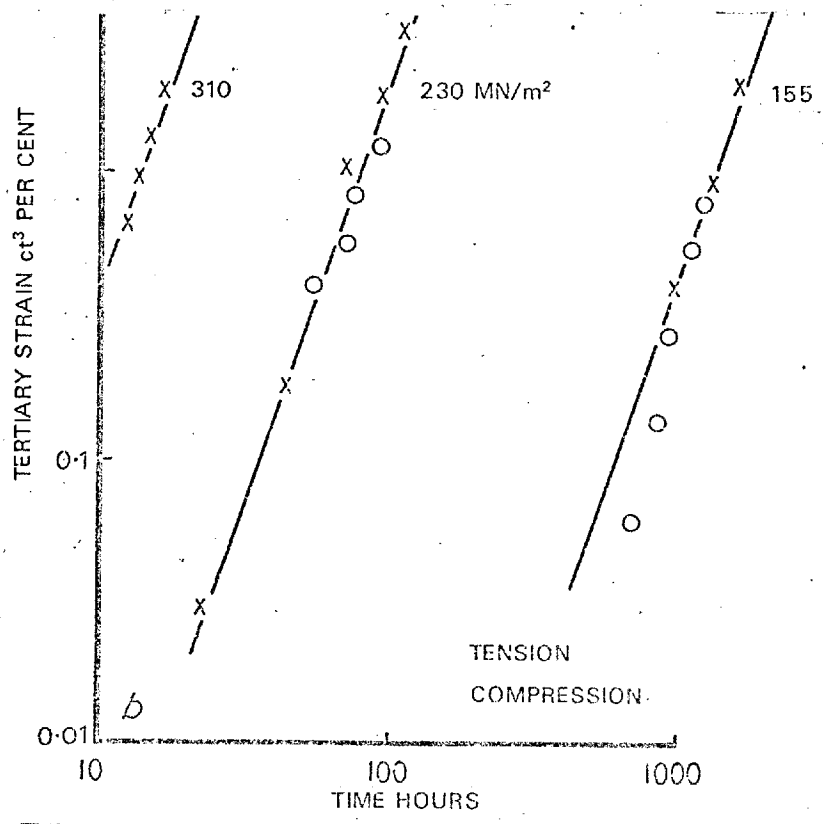

FIG.72 TERTIARY CREEP COMPONENTS OF NIMONIC 108 UNDER TENSILE AND COMPRESSIVE STRESSES AT 1073K

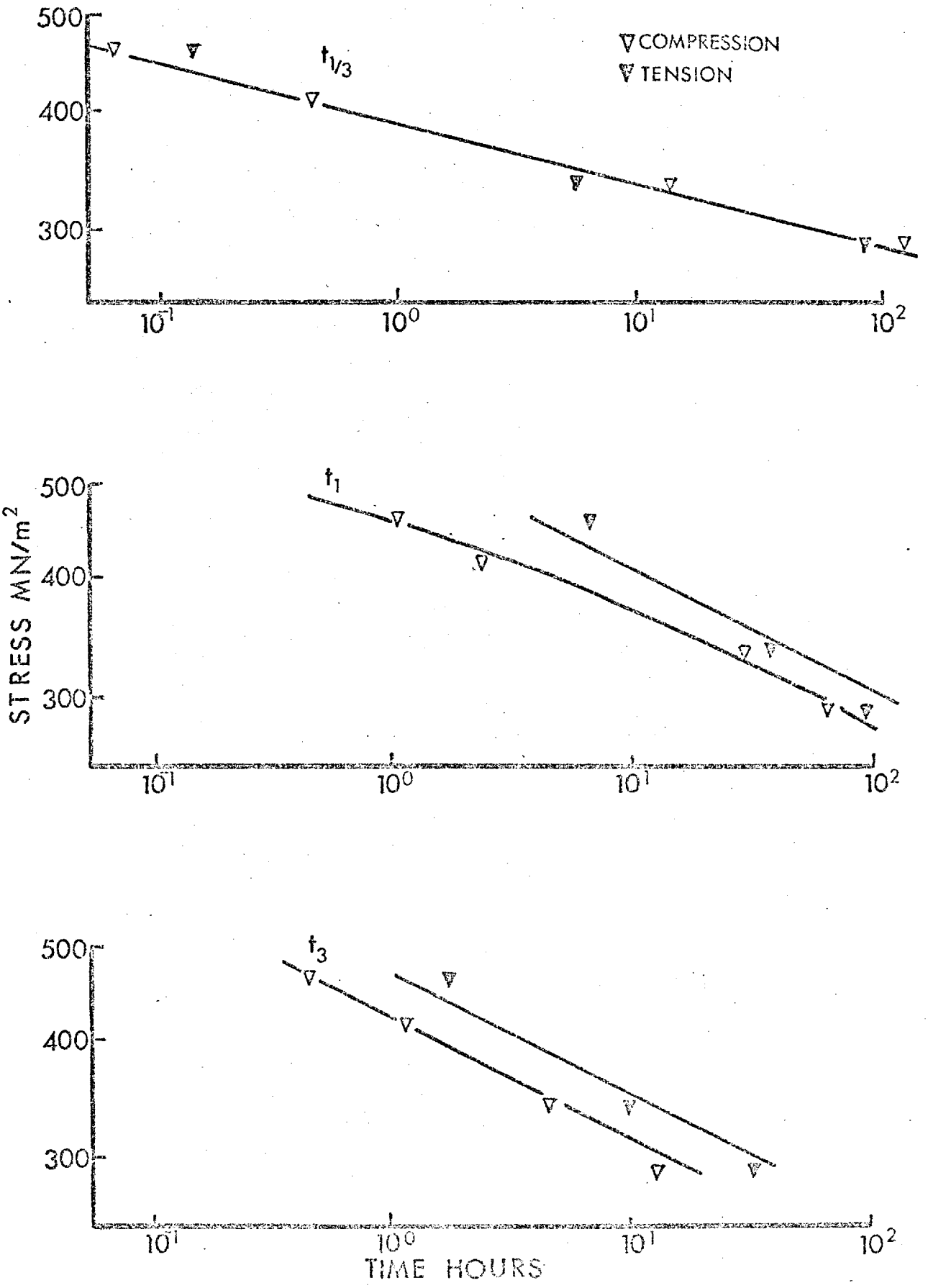

FIG. 73 STRAIN COMPONENT CROSS PLOTS FOR CONVENTIONALLY CAST MAR M 246 AT 1173K

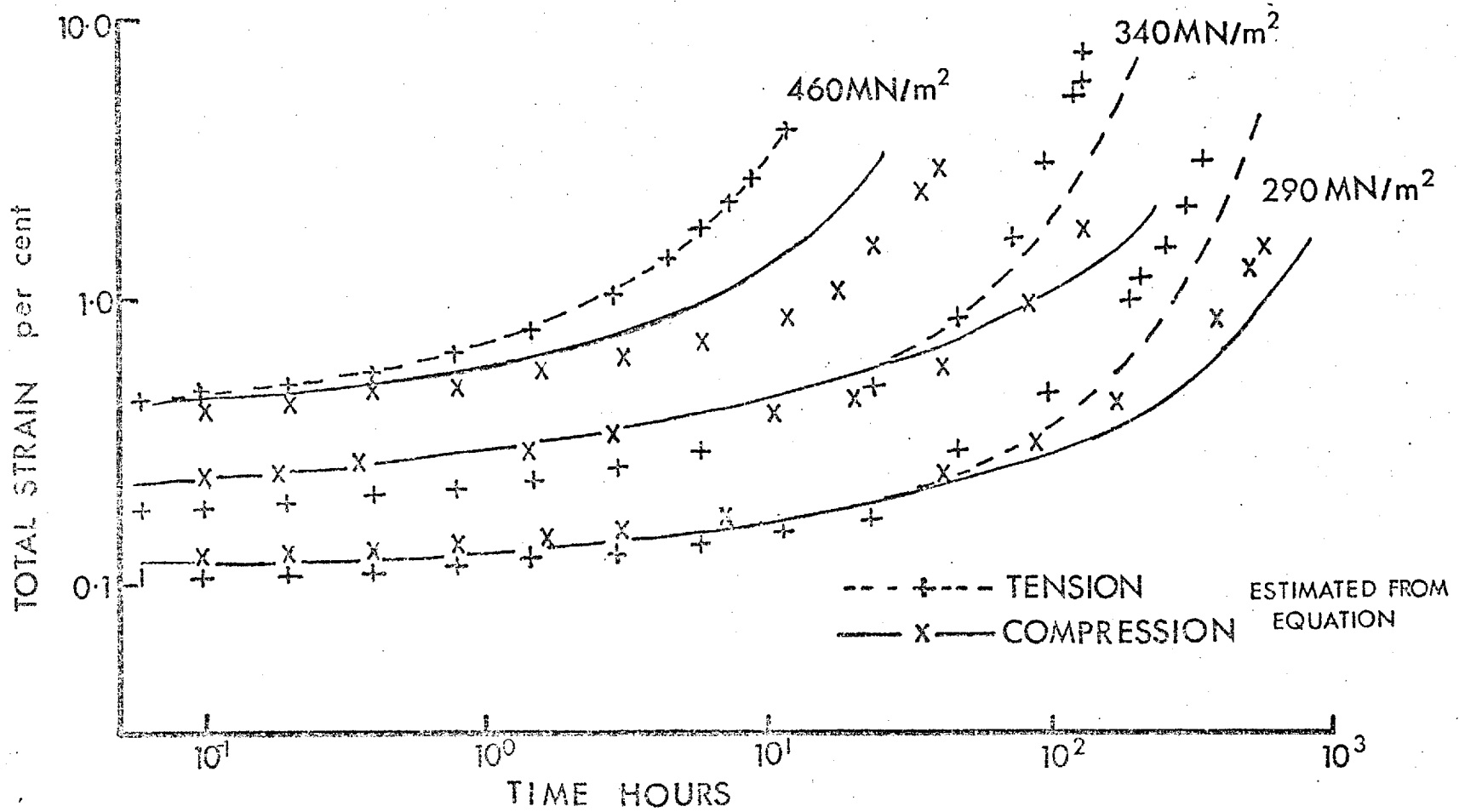

FIG.74 PREDICTED CREEP CURVES FOR CONVENTIONALLY CAST MAR M 246 AT 1173K

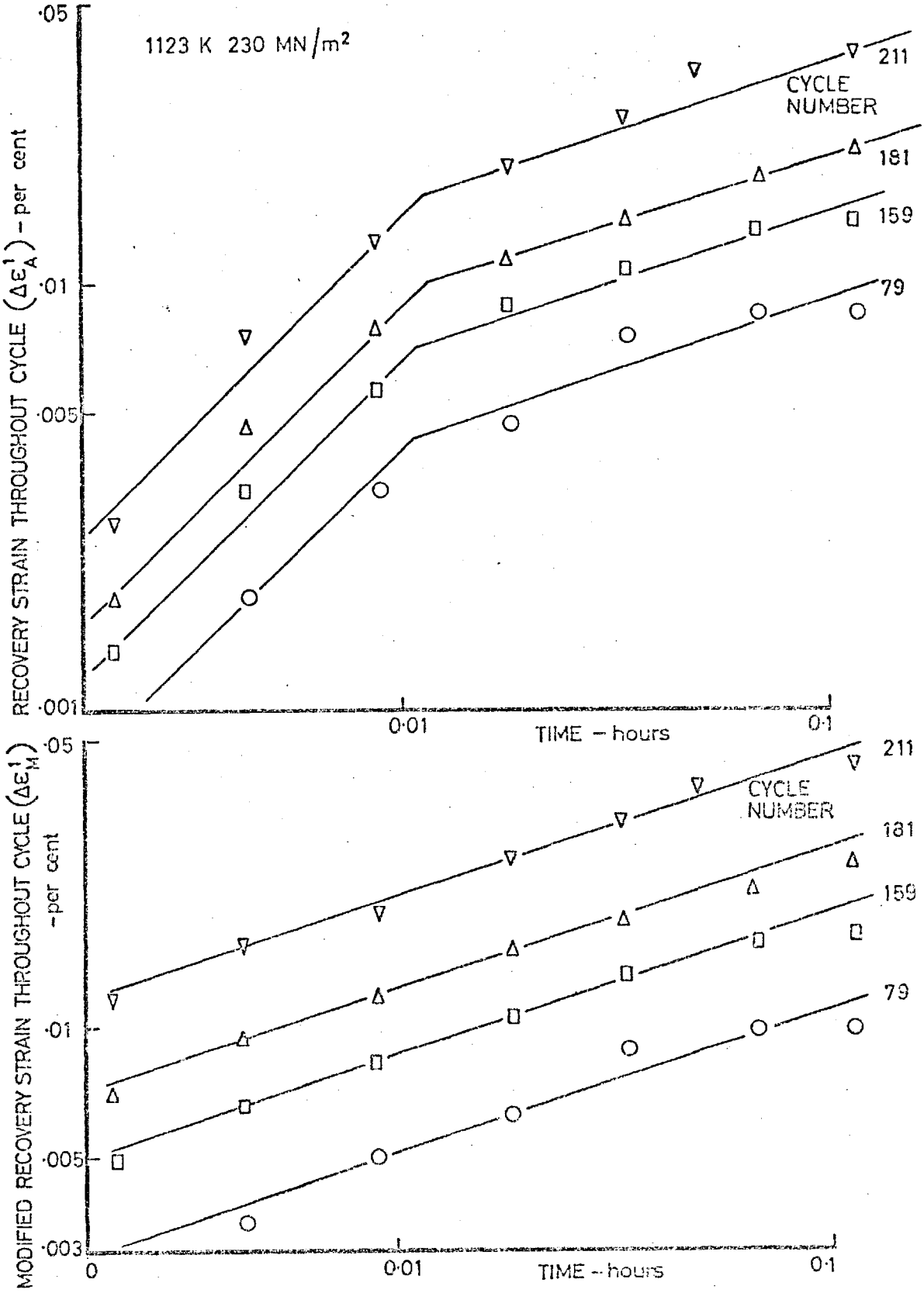

FIG.75 COMPARISON OF RECOVERY STRAIN AND MODIFIED RECOVERY STRAINS THROUGHOUT OFF-LOAD PERIOD

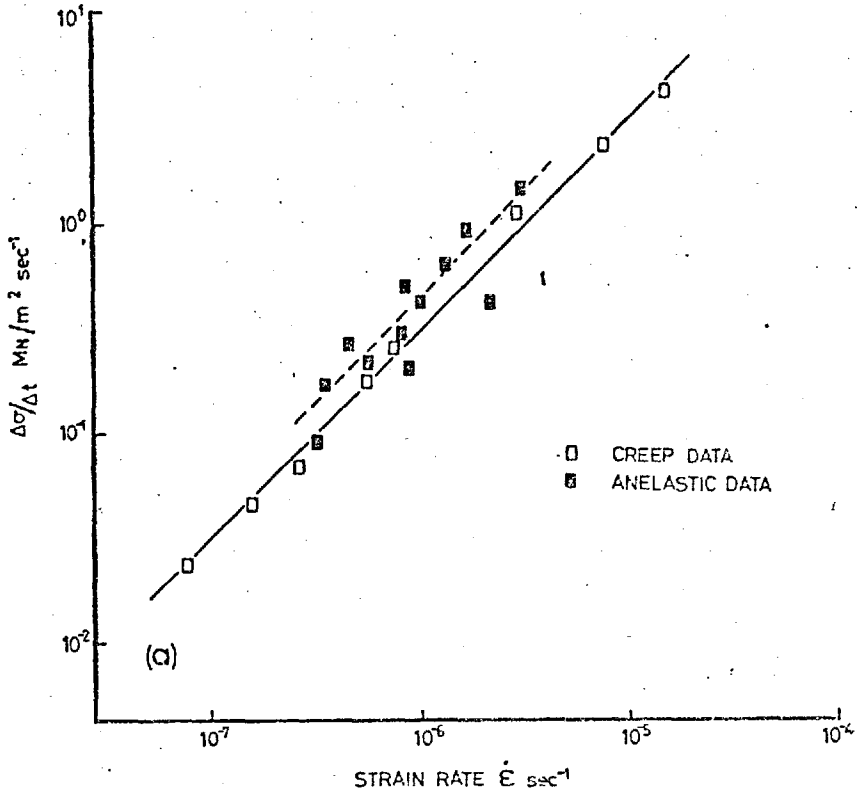

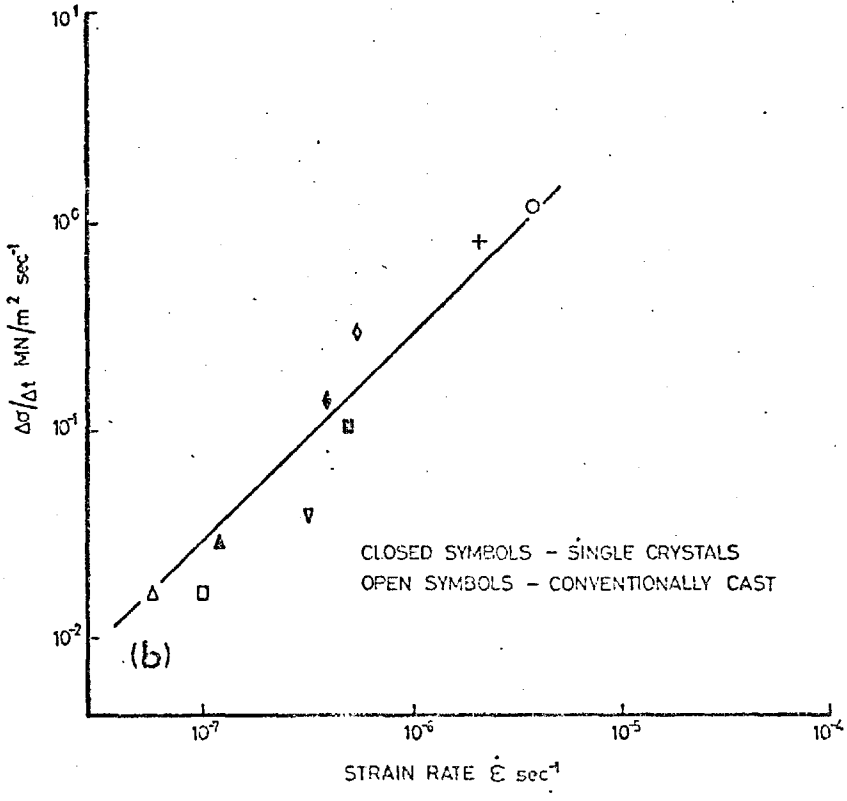

FIG. 77 CORRELATION BETWEEN METALLURGICAL RECOVERY AND PRIOR STRAIN RATE
a) FOR NIMONIC 90 AT 1123K AND
b) FOR MAR M 246 AT 1173K

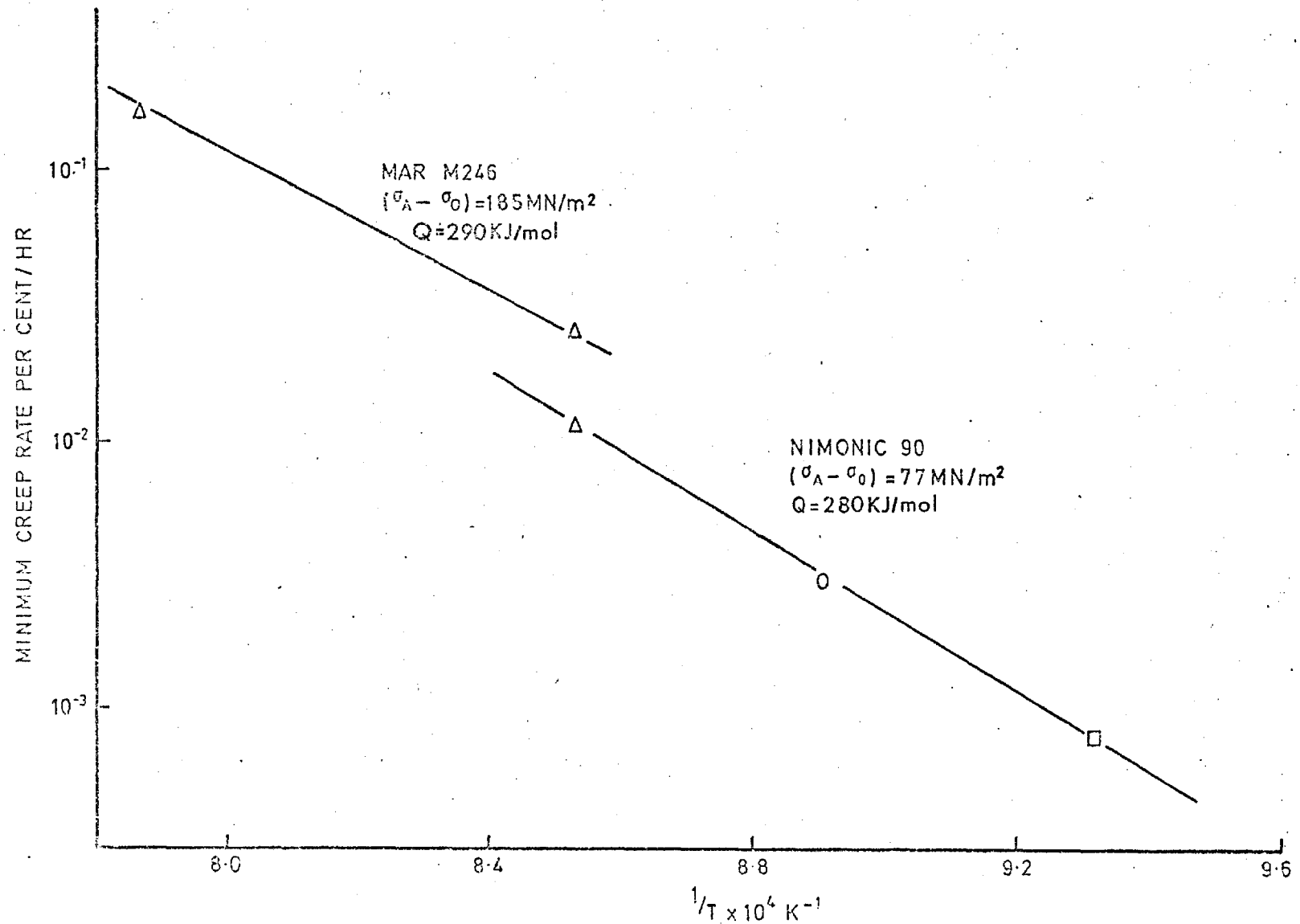

FIG.73 ACTIVATION ENERGIES FOR CREEP OF NIMONIC 90 AND MAR M246 CALCULATED AT CONSTANT EFFECTIVE STRESS

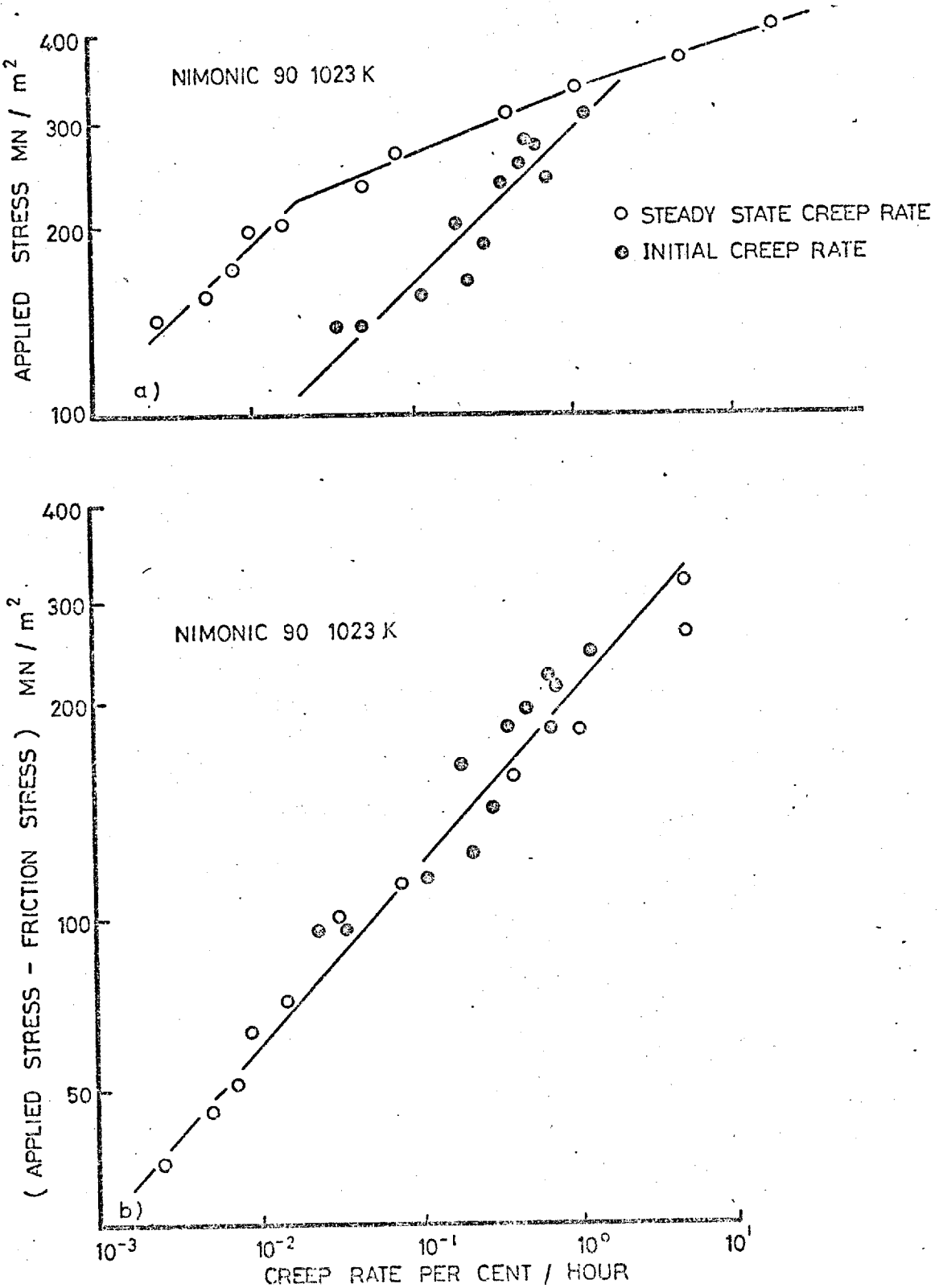

FIG.79 INITIAL & STEADY STATE CREEP RATE CORRELATIONS

a) WITH APPLIED STRESS AND

b) WITH EFFECTIVE STRESS

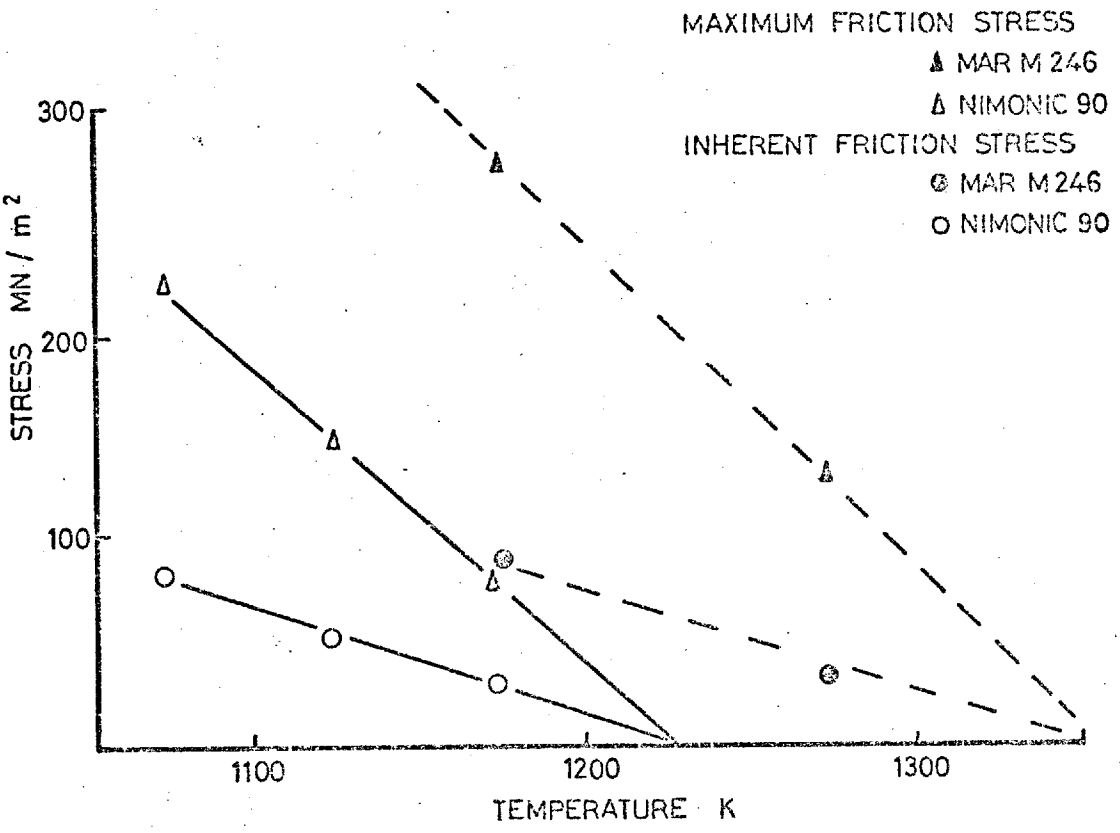

FIG. 80 TEMPERATURE DEFENDENCE OF INHERENT AND MAXIMUM FRICTION STRESS OF NIMONIC 90 AND MAR M 246

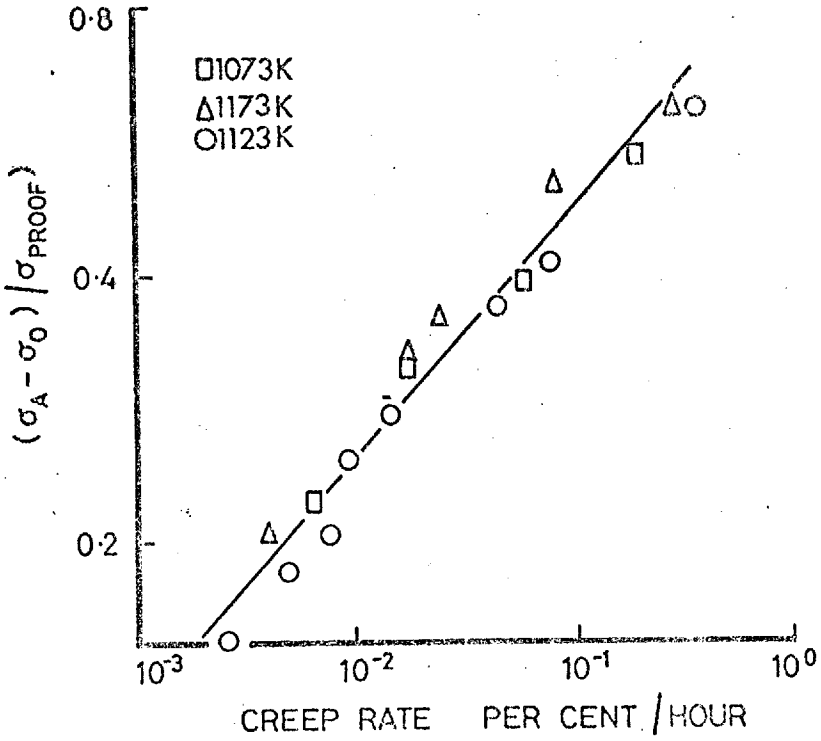

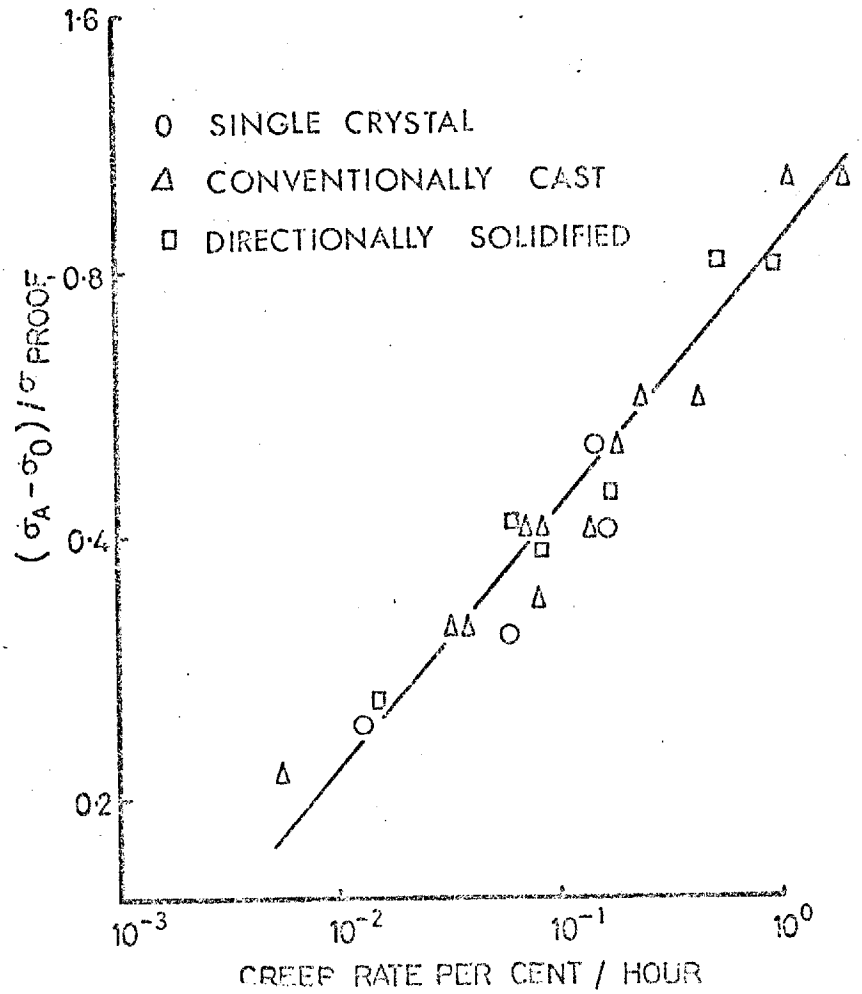

FIG.81 CORRELATION OF NORMALISED EFFECTIVE STRESS WITH MINIMUM CREEP RATES OF a) NIMONIC 90 AND b) MAR M246

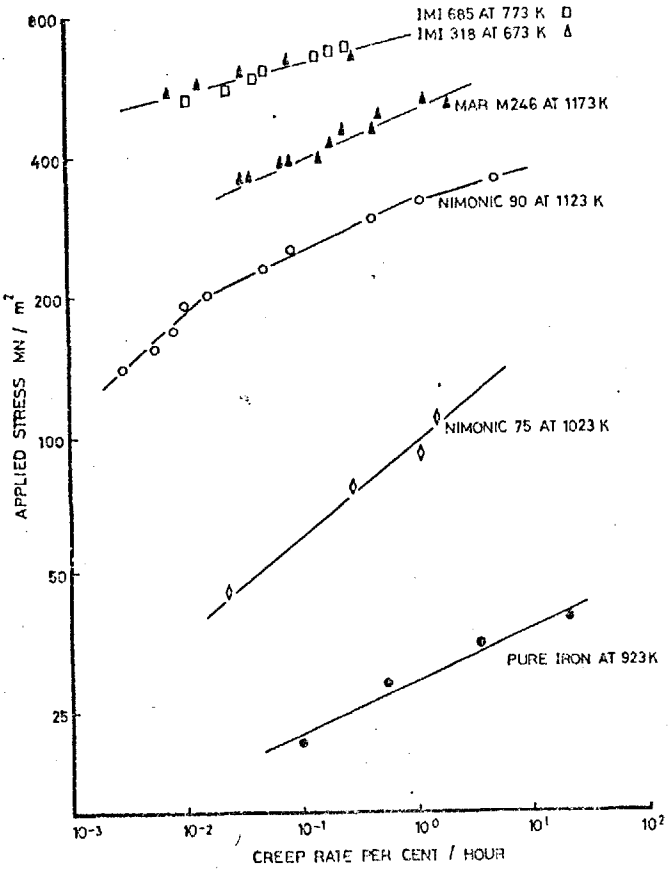

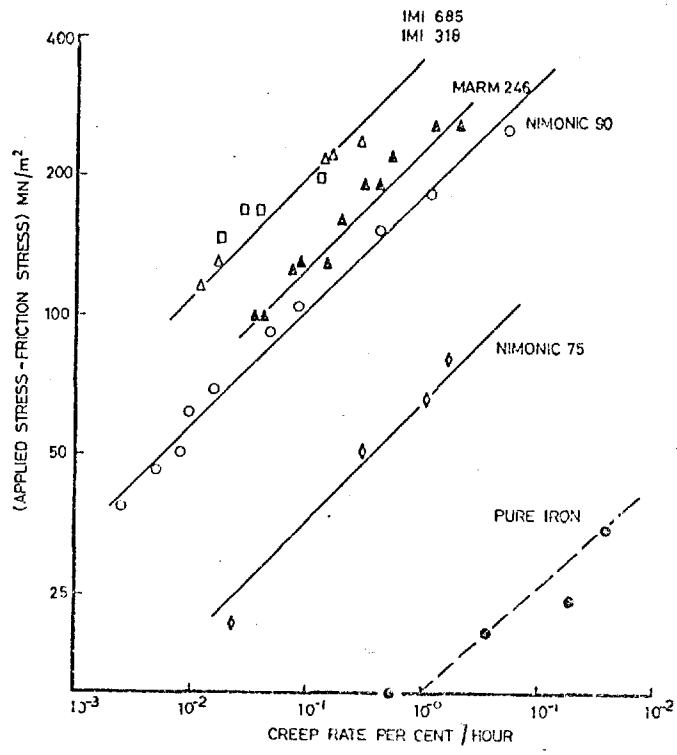

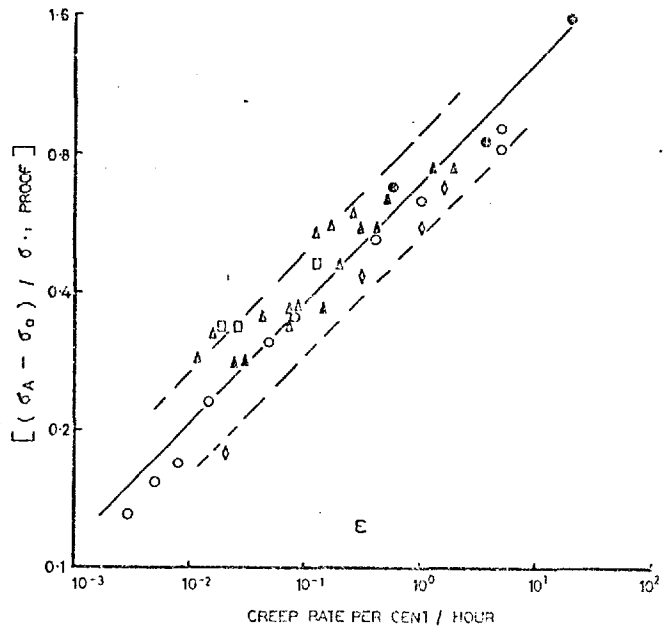

FIG.82 CORRELATION FOR SEVERAL ALLOYS OF a) APPLIED STRESS
b) EFFECTIVE STRESS AND c) NORMALISED EFFECTIVE STRESS
WITH MINIMUM CREEP RATES

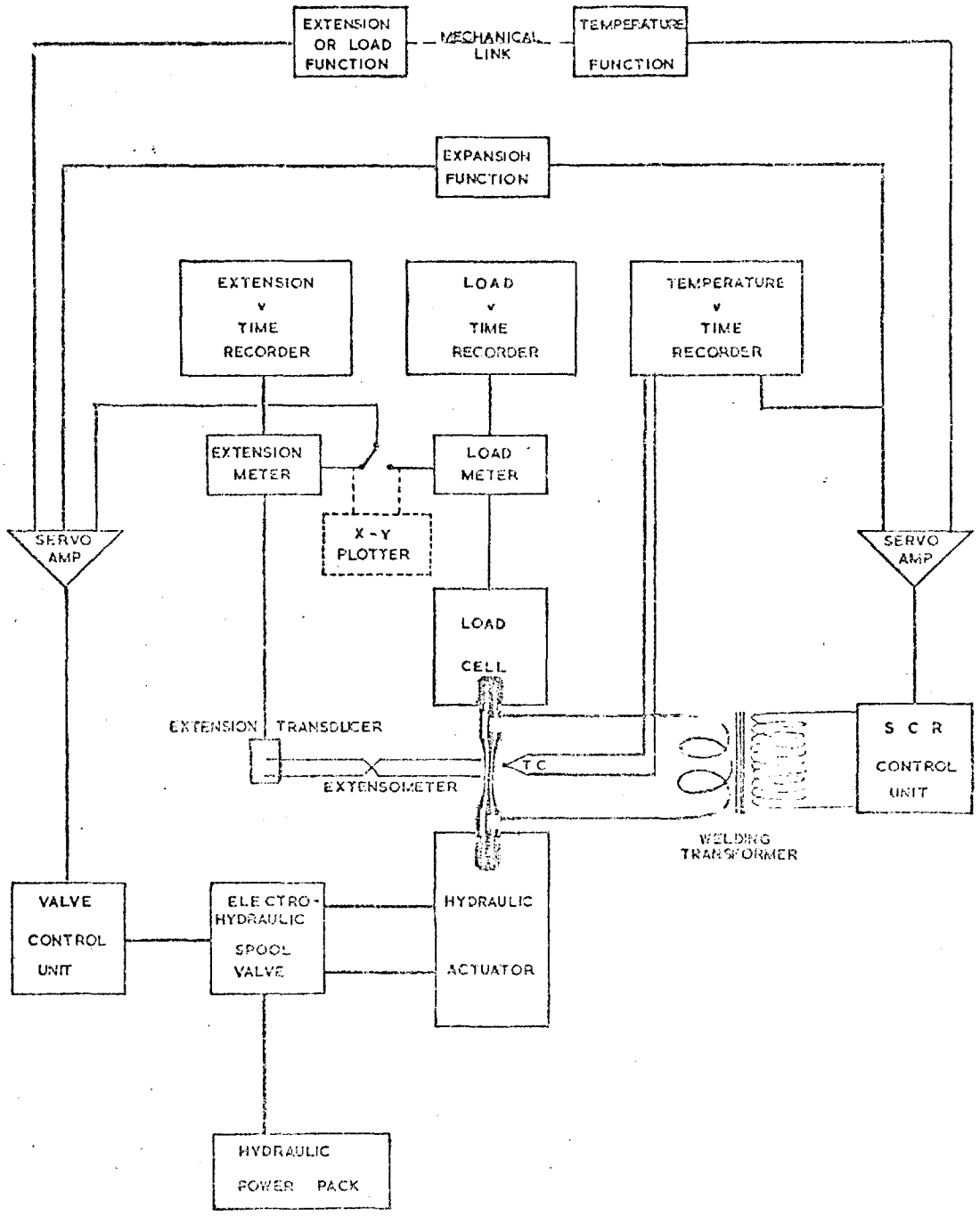

FIG. 83 SCHEMATIC LAY-OUT OF CYCLIC STRESS AND CYCLIC TEMPERATURE MACHINE

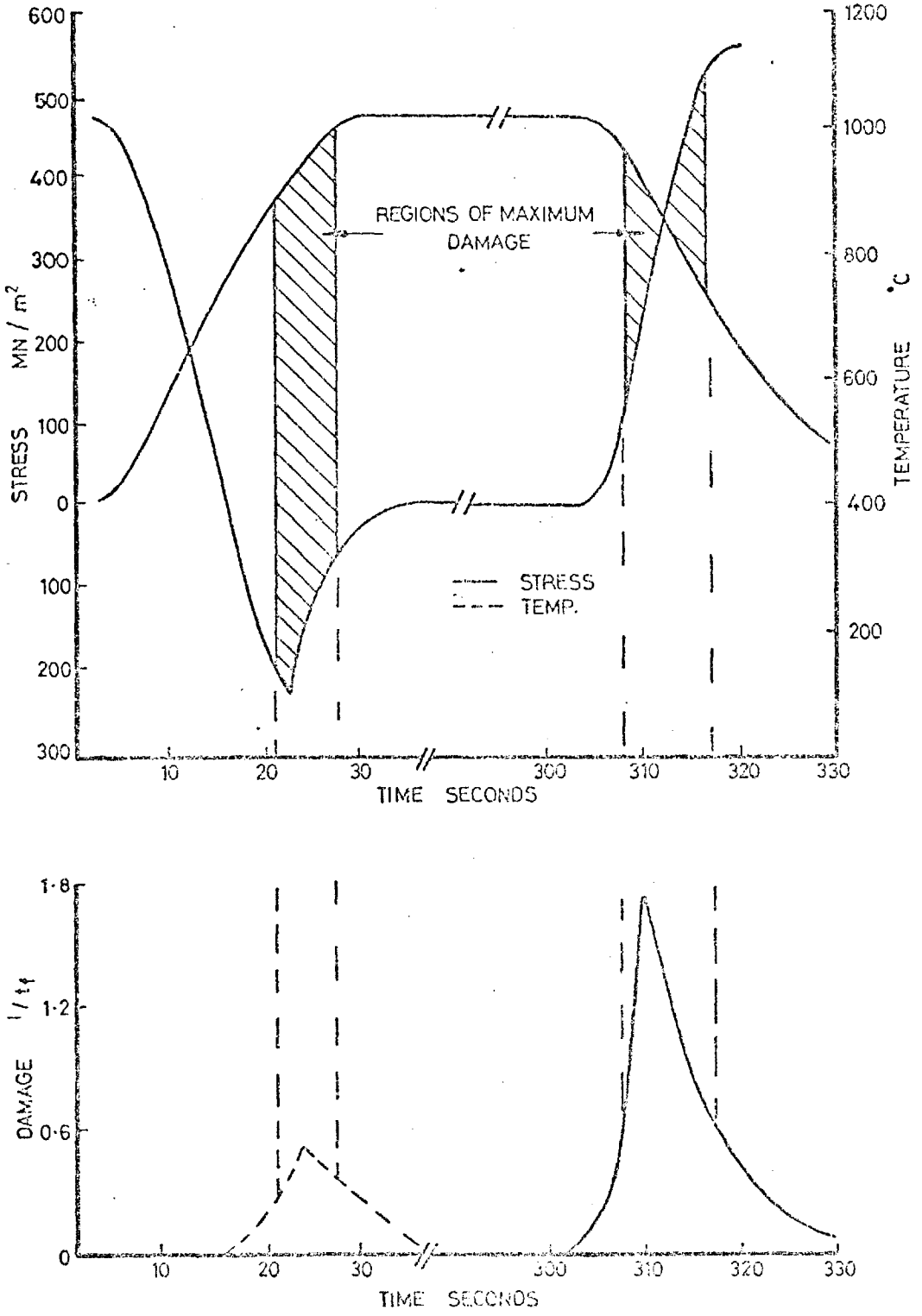

FIG.84 a) STRESS-TEMPERATURE HISTORY AND b) QUALITATIVE ILLUSTRATION OF DAMAGE EXPERIENCED BY A TURBINE BLADE DURING START-UP AND SHUT-DOWN OF AN ENGINE

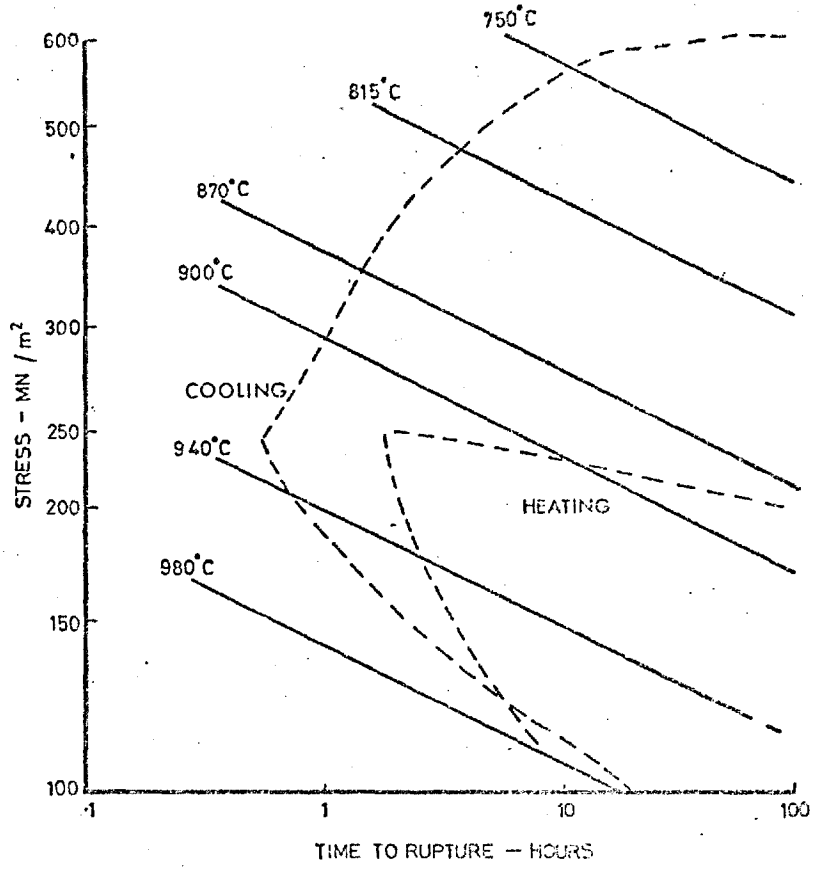

FIG.85 STRESS-TEMPERATURE COMBINATIONS EXPERIENCED DURING START UP AND SHUT DOWN SUPERIMPOSED ON A TENSILE STRESS-RUPTURE CROSSPLOT

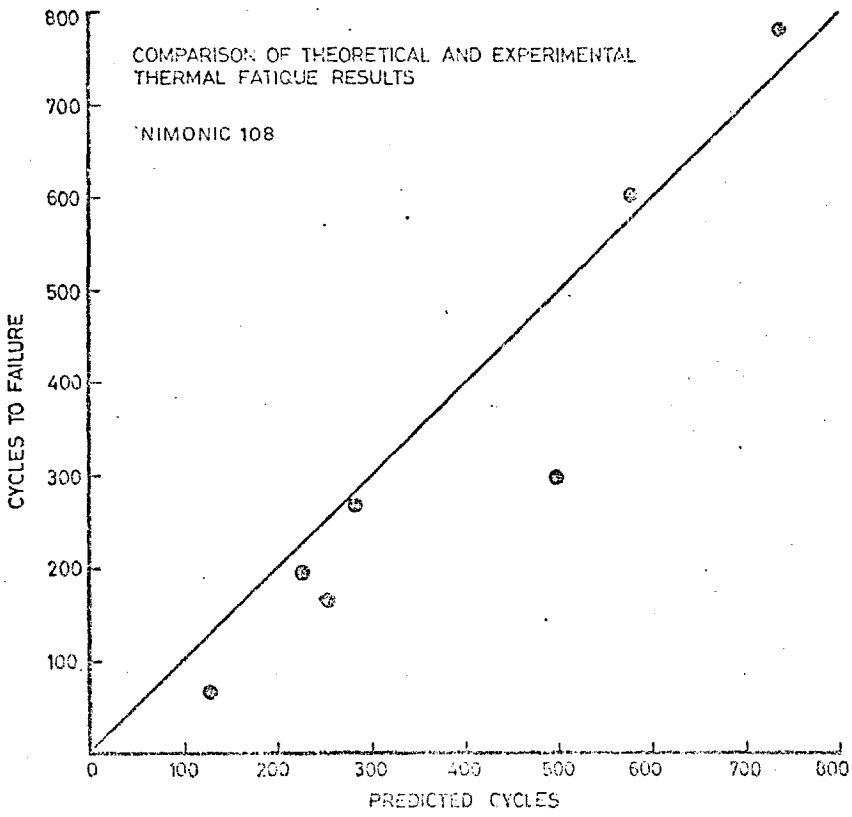

FIG.86 PREDICTED AND EXPERIMENTAL CYCLES TO FAILURE UNDER TRANSIENT STRESS AND TEMPERATURE